Wang, Linwei (2019) On the thermodynamics and dynamics of coal and biomass combustion. PhD thesis.

On the thermodynamics and dynamics of coal and biomass combustion

Linwei Wang

Submitted in fulfilment of the requirements for the
Degree of Doctor of Philosophy

School of Engineering
College of Science and Engineering
University of Glasgow

July 2018

Declaration

The author confirms that the work presented in this thesis is the results of the author's own research. This thesis is composed by the author. The standard referencing practices are applied to any ideas or techniques from published works.

. . . .

Linwei Wang
July, 2018

This thesis is delicated to my parents, my sister and my brother
for their continuous love and support.

Abstract

The combustion of solid fuels is a complex multi-phase, multi-scale and multi-component process. While oxy-fuel combustion is under development and given the promising future of biomass in energy generation, further research on oxy-fuel coal and biomass combustion is demanded. In particular, the combustion characteristics of coal and biomass in oxygenated environments need to be better understood. To respond to these needs, transient combustion of a single coal and biomass particle in a drop-tube furnace is investigated numerically. The burning process takes place in preheated O_2/N_2 and O_2/CO_2 atmospheres with varying concentration of oxygen and under either quiescent or active flows. The oxygen concentration varies from 20% to 100% in both nitrogen and carbon dioxide background environments. The simulations are rigorously validated against the existing experimental data by matching the particle ignition delay time, particle life time and particle temperature.

The unsteady temperature and species concentration fields are calculated in the course of transient burning process and the subsequent diffusion of the combustion products into the surrounding gases. The spatio-temporal evolutions of the temperature, major chemical species including CO, CO_2, O_2, H_2 and H_2O are obtained. It is shown that the homogenous combustion of the products of devolatilisation process dominates the temperature and chemical species fields at low concentrations of oxygen, and the rates of production and transport of chemical species reach their maximum level during the homogenous combustion of volatiles and decay subsequently. Yet, by oxygen enriching of the atmosphere the post-ignition heterogeneous reactions become increasingly more influential. However, the transient transfer of heat of combustion continues for a relatively long time after the termination of particle life time. It should be noted that, the results show that the combustion behaviours are different under CO_2 background gas compared with N_2 environments. Whether the volatiles and char burn simultaneously is distinguished in these two different gas atmospheres.

Through using the validated numerical combustion model, analysis of NO_x and SO_x emissions is conducted by investigating the overall NO_x and SO_x PPM emissions rate and formation process of nitrogen and sulphur pollutant species. It is shown that CO_2 has a significant inhibitory effect on NO_x formation, while it promotes SO_2 emissions generally. The overall NO and SO_2

PPM decrease in oxygenated conditions in both O_2/N_2 and O_2/CO_2 atmospheres. The emission rate of NO and SO_2 decreases when increasing oxygen concentration under both types of gas atmospheres. Further, oxygen concentration has a greater influence on the formation of NO_x in O_2/CO_2 gas conditions. Also, SO_x pollutants are sensitive to oxygen concentration in both O_2/N_2 and O_2/CO_2 environments.

Further, the numerical results are post processed to reveal the temporal rates of unsteady entropy generation by transport of heat and chemical species and through chemical reactions in the transient oxy-combustion of single coal and biomass particles combustion system. Analysis of the total entropy generation shows that the chemical entropy is the most significant source of irreversibility and is generated chiefly by the ignition of volatiles. However, thermal entropy continues to be produced well after termination of the particle life time through diffusion of the hot gases into the surrounding environment. Mass transfer irreversibility is found to have a negligibly small contribution. Most importantly, it is demonstrated that a slight oxygenation of the atmosphere results in major increases in the total chemical entropy generation and thus in the global irreversibility of the process. Nevertheless, upon exceeding a certain mole fraction of oxygen in the atmosphere, further addition of oxygen only causes minor increases in entropy generation. This trend is observed consistently in both quiescent and active flow cases.

In addition, an experimental work about the smouldering combustion of biomass packed bed under different ignition temperatures and air mass flow conditions is conducted. The instabilities and the speed of the smouldering combustion front, and the combustion temperature and heating rate during the smouldering combustion process are investigated in detail. The results show that, the smouldering reaction front keeps flat at lower ignition temperatures and slower air mass flow rate conditions, and the instabilities appear when the ignition temperature and air mass flow rate exceed a certain value. Increases in ignition temperature and air mass flow rate both lead to the increases in the reaction front speed, smouldering combustion temperature and heating rate. Moreover, the results indicate that the ignition temperature has a greater influence on the smouldering combustion of biomass packed bed than air mass flow rate.

Acknowledgements

First of all, I would like to express my profound gratitude to Dr Nader Karimi for being a great supervisor. You give me sufficient support and patient guidance during the past four years. This thesis cannot be completed successfully without your support and guidance. You console me and cheer me up when I was in a struggle and experience deep darkness. With your personality traits, you influence me unconsciously. You are also a role model for me. You are the best supervisor I could ever have wished for. I am also very grateful for the support and guidance received from Dr Manosh Paul. As my second supervisor, you always make me clear when I ran into obstacles with numerical simulations.Your valuable suggestions and comments contributed a great deal to my research work during my PhD time.

I am delighted to thank all my group members for their support, encouragement and all the good times. In particular, many thanks to Tata Sutardi, Graeme Hunt and Loizos Christodoulou. Further, thanks to the staff of School of Engineering, especially Cammie and Ken, who were always kind and helpful. Thanks to the friendly environment and efficient work thy provided which are conducive to my research work.

I sincerely appreciate the financial support provided by China Scholarship Council during the course of this PhD at the University of Glasgow.

A big thanks to my friends who supported me throughout my doctorate studies. Dr Zhang, sincere thanks for being with me through all the good and bad times. I feel quite fortunate to be blessed with having you. Thank you, Maomao, Xinyang and Ziyu. I am so glad to meet you here. The days we spent together were the most enjoyable memories of Glasgow for me. Thanks all my dear friends in China and UK. I am truly blessed to have all of you in my life.

Last, but no the least, thanks to my dearest family, my parents, my sister and my brother. Thank you for your continuous love, support and understanding. You believe in me even more than myself. I love you.

Contents

List of Tables

List of Figures

Nomenclature

a	absorption coefficient
A	pre-exponential factor
A_p	particle surface area
a_1, a_2	stoichiometric coefficients
c_1, c_2, c_3	constants
c_p	specific heat capacity
C	molar concentration of species
$C_{1\varepsilon}$, $C_{2\varepsilon}$, $C_{3\varepsilon}$	constants
C_D	drag coefficient
C_S	pollutant concentration
C_l	linear-anisotropic phase function coefficient
d	diameter
D_corr	dilution correction
D_i	diffusion coefficient of species
D_ij	binary diffusion coefficient for the i-j species pair
$D_{T,i}$	thermal diffusion coefficient for the i^{th} species
e	specific internal energy
E	entropy generation rate
E_a	active energy
E_h	rate of entropy generation due to heat transfer
E_m	rate of entropy generation due to mass transfer
E_r	rate of entropy generation due to chemical reactions
E'	average entropy generation rate
f_h	fraction of heat absorbed by the particle
$\vec{f}_i$	body force per unit mass
F_d	drag force
F_od	oxygen-based dry factor
g_x	acceleration gravity
G	incident radiation
G_b	turbulent kinetic energy generation due to buoyancy gradients

G_k	turbulent kinetic energy generation due to mean velocity gradients
h	specific enthalpy
h_{fg}	latent heat of devolatilization
h'	enthalpy of mixture
$H_{reac_{cr}}$	enthalpy of reaction *cr*
HHV	heating value of fuel
$J_{i,j}$	molecular mass flux
k_a	rate of constant of char combustion reactions
k	turbulence kinetic energy
k_c	thermal conductivity
k_{cr}	rate constant of reaction *cr*
k_d	kinetic rate of devolatilization reaction
K	reaction rate
Le	Lewis number
m	mass
M	molecular weight
MP	weight percentage of species
n_{cr}	number of chemical reactions
N	number of chemical species
Nu	Nusselt number
p	pressure
p^0	reference pressure
q_j	energy flux
$\vec{q}$	heat-flux vector
$\vec{q}_R$	radiant heat-flux vector
Q_i	internal production rate for thermal energy
Q_r	radiation flux
Re	Reynolds number
R_i	net rate of production of species *i* due to chemical reactions
$R_{i,cr}$	chemical production rate for species *i*
R_u	universal gas constant
s	specific entropy
s_b	Stefan-Boltzmann constant
$\vec{s}$	entropy flux vector
S_E	effective area of entropy generation
t	time
t_{pl}	particle life time
T	temperature

T^0	reference temperature
u	velocity
$\vec{u}$	velocity vector
$\vec{V}_i$	diffusion velocity of the i_{th} species
$\vec{V}'_{i,cr}$	stoichiometric coefficients of the reactants of the i_{th} species in reaction cr
$\vec{V}''_{i,cr}$	stoichiometric coefficients of the products of the i_{th} species in reaction cr
X	mole fraction
Y	mass fraction
Y_M	dissipation rate due to fluctuating dilatation

Greek Symbols

α	distribution coefficient of volatile in sold fuels
μ	viscosity
μ_c	specific chemical potential
μ_m	molecular viscosity
λ	thermal conductivity
ρ	density
ω_i	mass production rate of the i_{th} species per unit volume
ε	dissipation rate
ε_p	particle emissivity
θ_R	radiation temperature
σ	rate of entropy generation per unit volume
Φ	viscous dissipation
Γ	radiation parameter

Superscripts

$a_{i,cr}$	reaction order of the i_{th} species in reaction cr
b	temperature exponent
d	reaction order of gaseous reactants
e	reaction order of oxygen

Subscripts

cr	chemical reaction number
i	the i_{th} species
j	indices: 1,2,...,N
g	gas
p	particle
rg	gaseous reactants
m	composition of chemical element H
n	composition of chemical element O
x,r	coordinates

Chapter 1

Introduction

1.1 Background

Global primary energy consumption has been constantly increasing in recent decades and nearly doubles since 1970, yet the ways that energy is generated have not changed much [1]. Fossil fuels such as coal, oil and natural gas are the main supplier of the world's energy as fossil fuels are cheap, efficient and reliable sources of energy. Currently, over 80% of energy across the world is supplied by fossil fuels and it is considered to maintain this dominance in the foreseeable future [2]. Data revealed in British Petroleum (BP) report (Figure 1.1) provides a comprehensive view of the proportion of different fuels in the world's primary energy consumption. It clearly indicates that coal is still a major source of energy.

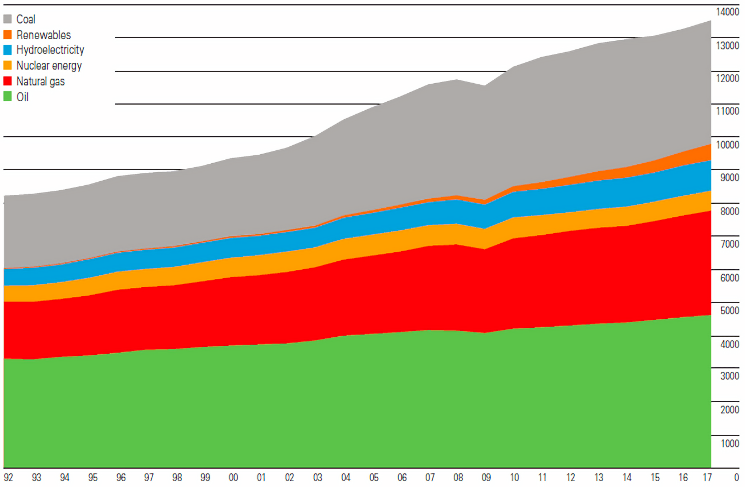

Figure 1.1: World primary energy consumption [1].

Based on its wide distribution in all continents, coal has last for a long time, which can be up to 115 years and longer than the conventional oil and gas reserves. Coal has been the biggest contributor to power generation in the past few decades [1]. Moreover, coal is expected to continue to account for a big factor in power generation due to the development of mining technologies.

Currently, the proven coal reserves reach 1035012 million tonnes [1], which has increased by 5.3% since 2007. Meanwhile, with increasing in both global consumption and production, the coal market had a mini-revival [1]. Global coal consumption raised by 1% with nearly 5% of that being in India. It is reported that the annual world production of coal in 2017 increased significantly by 3.2% including markable increases in both Chinese (3.5%) and United State (6.9%) [1]. All these indicate that coal still has broad application prospects and hence deserves paying attention to.

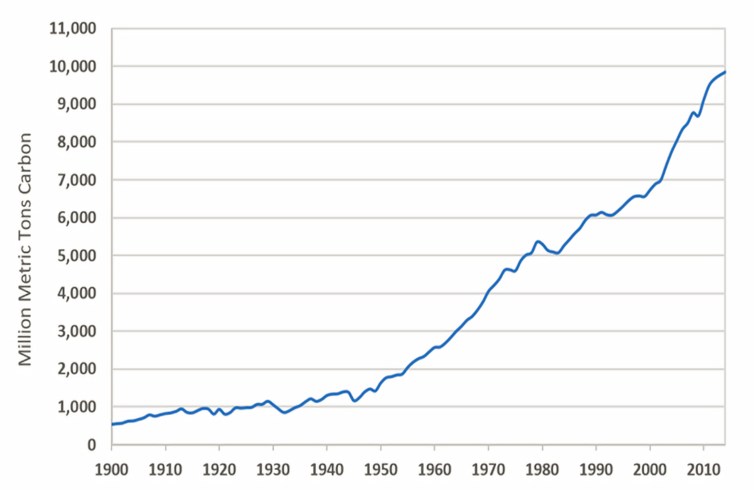

Figure 1.2: Global carbon emissions from fossil fuels (1900-2014) [3].

Unfortunately, the heavy use of fossil fuel has resulted in an alarming increase in greenhouse gas emissions, which has been a matter of serious concerns recently [4]. At present, fossil fuel combustion for heat and electricity generation, public, domestic and transport sectors, and industrial application produces about 78% of CO_2 emissions [5]. Figure 1.2 shows the changing trend of CO_2 emissions from fossil fuel since 1900. Climate Change Report of Intergovernmental Panel on Climate Change (IPCC) [5] states that the increase in growth rate of atmospheric concentration of CO_2 is about 2ppm/year observed over the last 60 years in line with increasing global energy consumption, which is the evidence showing that the increase in atmospheric CO_2 is the primary contributor with the global warming.

It is clear that efforts must be made to reduce CO_2 emissions to avoid or minimise the adverse influences of climate change. As electricity and heat production which has a great consumption of fossil fuels account for the largest proportion in global CO_2 emissions, the elimination of CO_2 emissions from this sector is of primary importance. Approaches for cutting CO_2 emissions from energy related fields can be summarized below [5].

- Increasing use of sustainable biomass from forestry and agricultural waste instead of fossil fuel.
- Improving the efficiency of the power generation process and the transmission system.

- Widening the application of renewable energy technologies for power generation such as wind energy, solar energy.
- Improving the energy efficiency to reduce the demand of electricity and heat generation.
- Developing technologies for carbon capture and storage (CCS).

Referring to a global renewable energy report for 2040 published by the European Renewable Energy Council (EREC) [6], the renewable energy aims at accounting for 23.6% of the world's energy field till 2020 and 47.7% till 2040. Among all the sources of renewable energy, biomass is regarded to be a very promising one for electricity generation and transportation biofuels in the future. The biomass usage is anticipated to have a continuous increasing in the following decades [6] (Fig. 1.3).

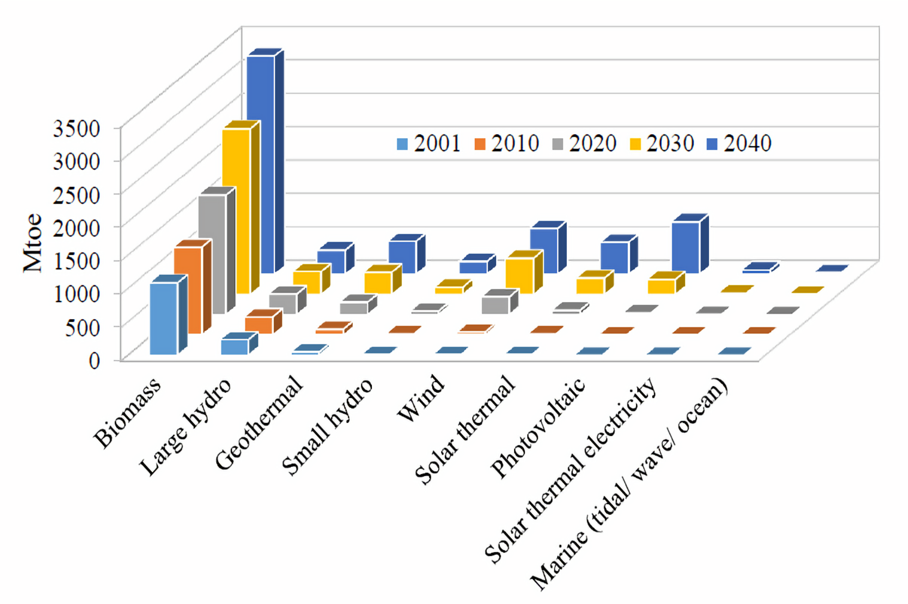

Figure 1.3: Renewable energy sources till 2040 [6].

The term "biomass" is associated with a broad range of fuels. The National Energy Foundation (NEF) classifies biomass into four categories [7]: Woodfuels, Energy crops, Agricultural waste and Municipal and industrial waste. The sources include naturally grown forests, energy plantations, herbaceous plants, by products from different industries such as food, wood processing, manures, and paper industries or municipal solid waste [8]. Biomass is regarded as an renewable energy because of absorbing CO_2 through photosynthesis during its growth process.

Different from other renewable sources, biomass especially agricultural waste and woodfuels is quite common and widespread across the world. Electricity generated by biomass is considered to be a key role in providing secure and clean electricity to 2020 and beyond in UK [9].

The use of biomass fuel for sustainable and environmentally friendly fuel goes beyond energy provision. Biomass is an important renewable energy that can be chosen at present. The increase in generation from biomass has been driven by the need to replace unabated coal combustion with a reliable, renewable, sustainable technology. Biomass although a renewable fuel still has carbon emissions associated with cultivation, fuel processing, transport, any direct (and indirect) land use changes and the reduction in conversion efficiency of the plant.

Carbon capture and storage (CCS) has been identified as a potential emissions reduction technology. CCS is the process of capturing CO_2 emissions from large scale emitters such as power generation, oil, cement, chemical or steel production, transporting it via pipelines or ships and storing it to prevent emissions to atmosphere. The CCS technology includes three steps: capture, transport and storage with many different individual technology options available in each step. There are three leading technologies for carbon capture, known as pre-combustion capture, post-combustion capture and oxy-fuel combustion technology.

- Pre-combustion capture: Pre-combustion capture aims at removing CO_2 prior to combustion by converting fossil fuels into synthesis gas which mainly includes a mixture of hydrogen, carbon monoxide, carbon dioxide. It is typically applied synonymously with Integrated Gasification Combined Cycle (IGCC). Low electric efficiency in the carbon capture process is a major obstacle against this technology [10].

- Post-combustion capture: Post-combustion capture means separating and capturing carbon dioxide from the flue gas of conventional coal or biomass fired power stations. Separating carbon dioxide from the flue gas including large amounts of nitrogen is the biggest challenge faced by the post-combustion capture technology [11].

- Oxy-fuel combustion: Oxy-fuel combustion refers to the combustion of pulverised fuel including coal and biomass in oxygen rich gas atmosphere instead of air [12]. By applying this, a CO_2 rich flue gas is generated which requires minimal treatment to purify. Therefore, oxy-fuel combustion technology is one of the main methods being considered for carbon capture from large coal and biomass fired power stations [13].

Here, we focus on introducing pulverised fuel combustion in oxy-fuel technology in CO_2 capture application. This technology is achieved by removing nitrogen contents from air to the combustion system through air separation in advance and generates flue gas with high concentration of CO_2 which is easy for carbon dioxide capture. The flue gases are then recycled back into the furnace to maintain the gas and temperature required for the combustion [14]. The recent studies of oxy-fuel combustion prove that it is effective for CO_2 emissions reduction in laboratory [15] [16]. In addition, research about varying oxygen concentration gas conditions are being conducting [17] [18].

Apart from CO_2 emissions, pollutants including soot, nitrogen oxides (NO_x) and sulphur oxides (SO_x) from fossil fuel combustion are a serious concern as well. Their severe effects on corrosion of combustion equipment, photochemical smog and acid rain cannot be neglected [19].

Nitrogen oxides, including nitric oxide (NO), nitrogen dioxide (NO_2), nitrous oxide (N_2O), is one of the most important pollutants generated during the combustion of solid fuels. Thermal-NO_x, prompt-NO_x and fuel-NO_x are considered to be the main mechanisms of NO_x emissions formation during solid fuels combustion [20].

- Thermal-NO_x is formed through the oxidation of the molecular nitrogen in gas flow under high temperature conditions. Therefore, it is highly temperature-dependent [21].
- Prompt-NO_x refers to the NO_x formed from molecular nitrogen and hydrocarbon fragments resulting from the devolatilization process near the reaction zone of flame [22]. Prompt-NO_x accounts for less than 5% of the total NO_x emissions, and is normally ignored in the combustion of solid fuels [23].
- Fuel-NO_x is the NO_x generated from fuel containing nitrogen. It is the main source of NO_x emissions in the combustion of solid fuels [24].

The SO_x emissions are generated because of the oxidation of fuel containing sulfur, which is oxidized to SO_2 and SO_3 during the combustion process of solid fuels. Sulfuric acid will be formed when the gaseous SO_x condenses on the particles and then attaches water. SO_x emissions are the major cause of acid rain , and also lead to the corrosion of combustion equipment. It is shown that over half of total SO_x emissions are produced from coal and biomass fired boilers [25].

In conclusion, the rising worldwide awareness about environmental constraints has led to legislative actions in most industrialised countries [26]. It calls for developing new combustion technologies for clean conversion of conventional and renewable fuels to heat. To address these issues, biomass and oxy-fuel combustion technology are regarded as a promising renewable energy source and a effective technology to reduce CO_2 emission. However, due to the variation of gas contents and oxygen concentration in the furnace gas environment, the combustion process of pulverised fuel is greatly influenced by oxy-fuel conditions, and the related processes such as heat and mass transfer is affected as well. Therefore, the fundamental investigation about single coal and biomass particle under varying oxy-fuel conditions is desirable.

1.2 Aims and objectives of the work

The overall objectives of this thesis are two-fold. First, it aims to provide further understanding on what happens to single coal or biomass particle during the combustion process with varying oxygen concentrations, especially under carbon dioxide background gas environment. The evolutions of temperature, major chemical species, formation of pollutants and entropy generation during the transient combustion process should be investigated in detail. Second, smouldering combustion of biomass is investigated with the aim of obtaining an insight into the behaviour of the reactive front. In particular, the influences of the operating parameters upon the front speed are examined carefully. The specific objectives of this work are as follows.

- To develop a numerical combustion model including both homogeneous and heterogeneous reactions occurring in coal and biomass combustion based on the existing experimental data.
- To compare the numerical results of the computational modelling with the existing experimental data to validate the combustion model.
- To analyse the spatio-temporal evolution trends in temperature, species and pollutants to evaluate the parameters that dominate the combustion behaviour under different gas conditions.
- To evaluate the spatio-temporal evolutions and the overall irreversibilities associated with combustion of biomass and coal particles in different atmospheres.
- To conduct experimental work to investigate the propagation of reaction fronts and instabilities during biomass smouldering combustion.

1.3 Contributions of the thesis

As oxy-fuel combustion technology of pulverised coal and biomass is very much under development, particularly in the high oxygen concentration (over 50%) conditions, the numerical simulations of single coal and biomass particle combustion with oxygen concentration varying from 20% to 100% under quiescent or active low conditions are conducted. Due to the measurement limitations of single particle combustion in experiments, the numerical simulations are conducted to investigate the transfer of heat and mass and thermodynamic characteristics during single particle combustion under various gaseous atmospheres. The unsteady temperature and species concentration fields during the single particle combustion process are revealed.

The present studies show that there are conflicting results about the effects of CO_2 atmosphere and oxygen concentration on NO_x and SO_x emissions. Some studies indicate that the combustion media do not affect the formation of pollutant emissions, while some other studies report the differences in O_2/N_2 and O_2/CO_2 conditions. As a result, more investigation on NO_x and SO_x emissions under different gas conditions are necessary before establishing solid conclusions. This study supports that more NO_x is emitted in O_2/N_2 atmospheres than in O_2/CO_2

due to the strong formation of thermal NO_x. However, there are less SO_2 emissions produced in nitrogen containing atmosphere compared to those in carbon dioxide containing atmospheres.

Entropy is defined as a measurement of the amount of energy which is unavailable to do work and of the disorder of a system. It is, therefore, an essential thermodynamic property in the irreversible processes such as combustion. Entropy generation in an irreversible process leads to process efficiency. Although capturing of carbon dioxide from coal fired power stations substantially reduces their greenhouse gas emissions, it adversely affects their thermal efficiency and the influences of oxy-coal combustion upon destruction of exergy are still largely unknown. This work presents the entropy generation due to heat and mass transfer and chemical reactions during the single coal and biomass particle combustion process. It is the first study on unsteady entropy generation in oxy-fuel combustion of a single solid particle.

In addition to the direct and fast combustion applied in power stations, smouldering combustion is another kind of combustion phenomenon that can not be neglected in the field of biomass combustion. Smouldering combustion is quite complicated and difficult to understand as it includes both homogeneous and heterogeneous reactions taking place in a porous fuel beds. The experiments conducted in this work presents the influence of ignition temperature and air flow rate on the smouldering combustion characteristics and front propagation properties.

1.4 Published work

1.4.1 Journal publications

- L. Wang, N. Karimi*, M.C. Paul, T. Sutardi. *Numerical modelling about combustion characteristics and pollutant emissions from a single biomass particle in oxy-fuel combustion*. Energy & Fuels. 2019, 33(2): 1556-1569.

- L. Wang, N. Karimi*, T. Sutardi, M.C. Paul. *Numerical modelling of unsteady entropy generation in oxy-combustion of single coal particles with varying flow velocities and oxygen concentrations*. Applied Thermal Engineering. 2018, 144: 147-164.

- T. Sutardi, L. Wang, M.C. Paul*, N. Karimi. *Numerical Simulation Approaches for Modelling a Single Coal Particle Combustion and Gasification*. Engineering Letters. 2018, 26(2): 257-266.

- L. Wang, N. Karimi*, M.C. Paul. *Gas-phase transport and entropy generation during transient combustion of single biomass particle in varying oxygen and nitrogen atmospheres*. International Journal of Hydrogen Energy. 2018, 43(17): 8506-8523.

- L. Govone, M. Torabi, L. Wang, N. Karimi*. *Effects of nanofluid and radiative heat transfer on the double diffusive forced convection in microreactors*. Journal of Thermal Analysis and Calorimetry. doi:10.1007/s10973-018-7027-z.

1.4.2 Conference presentations

- L. Wang*, N. Karimi, M.C. Paul. *Numerical study of single coal particle combustion in* O_2/N_2 *and* O_2/CO_2 *atmospheres*. 12th International Conference on Heat TransferâĂİ, Fluid Mechanics and Thermodynamics, Costa del Sol, Spain, 2016.
- L. Wang*, N. Karimi, M.C. Paul. *NO Emission from a single coal particle combustion in* O_2/N_2 *and* O_2/CO_2 *atmospheres*. 5th UK-Japan Engineering Education League Workshop, Glasgow, UK, 2017. (Poster Presentation)
- L. Wang*, N. Karimi, M.C. Paul. *Numerical modelling of single coal particle combustion in different gas atmospheres*. 29th Scottish Fluid Mechanics Meeting, Edinburgh, UK, 2016. (Poster Presentation)
- L. Wang*, N. Karimi, M.C. Paul. *Numerical simulation of coal combustion using Euler-Lagrange Model*. IOP Combustion Physics Group One-day meeting on Current Research in Combustion, Loughborough, UK, 2015. (Poster Presentation)

1.5 Thesis structure

This thesis has been constructed as follows.

- Chapter 1: An introduction to the world's energy situation, renewable biomass, carbon capture and storage (CCS) technology and pollutant emissions during coal and biomass combustion is presented.
- Chapter 2: A comprehensive review of coal and biomass combustion, entropy generation and NO_x and SO_x emissions during the combustion process and smouldering combustion is given.
- Chapter 3: Theoretical and numerical methodologies used for simulations of single particle combusiton and post-processing, and experimental methods of biomass packed bed smouldering combustion are introduced.
- Chapter 4: Eular-Lagrange simulations of single coal and biomass particles combustion are conducted using conmercial software ANSYS Fluent. The numerical results are compared with the existing experimental data to validate the model. Details of combustion

process including particle mass loss and evolutions of gas-phase temperature and major gaseous species are investigated through the numerical simulations.

- Chapter 5: NO_x and SO_x emission predictions during single biomass combustion under both O_2/N_2 and O_2/CO_2 gas atmospheres with oxygen concentration changing from 20% to 100% are conducted. The overall NO_x and SO_x PPM and their emission rates are used to compare the emission performance of biomass particle in different gaseous atmospheres.

- Chapter 6: Based on the validated numerical combustion model, a post-processing of gas-phase entropy generation is conducted. The gas-phase entropy caused by heat transfer, mass transfer and chemical reactions during combustion process under varying oxygen concentration conditions in O_2/CO_2 environment is calculated. The irreversibilities during a single coal and biomass transient combustion process is further examined.

- Chapter 7: An experimental study on smouldering combustion of biomass packed bed is presented. Different ignition temperatures and air flow rates are used to investigate the characteristics of smouldering combustion of two kinds of biomass fuel. Pattern and speed of the smouldering front, smouldering temperature and heating rate under different conditions are investigated to analyse the combustion and propagation characteristics of biomass packed bed smouldering combustion.

- Chapter 8: The conclusion and summary of each chapter are presented together here. Some recommendations for future work are put forward.

The thesis structure is represented by flow chart shown in Fig. 1.4.

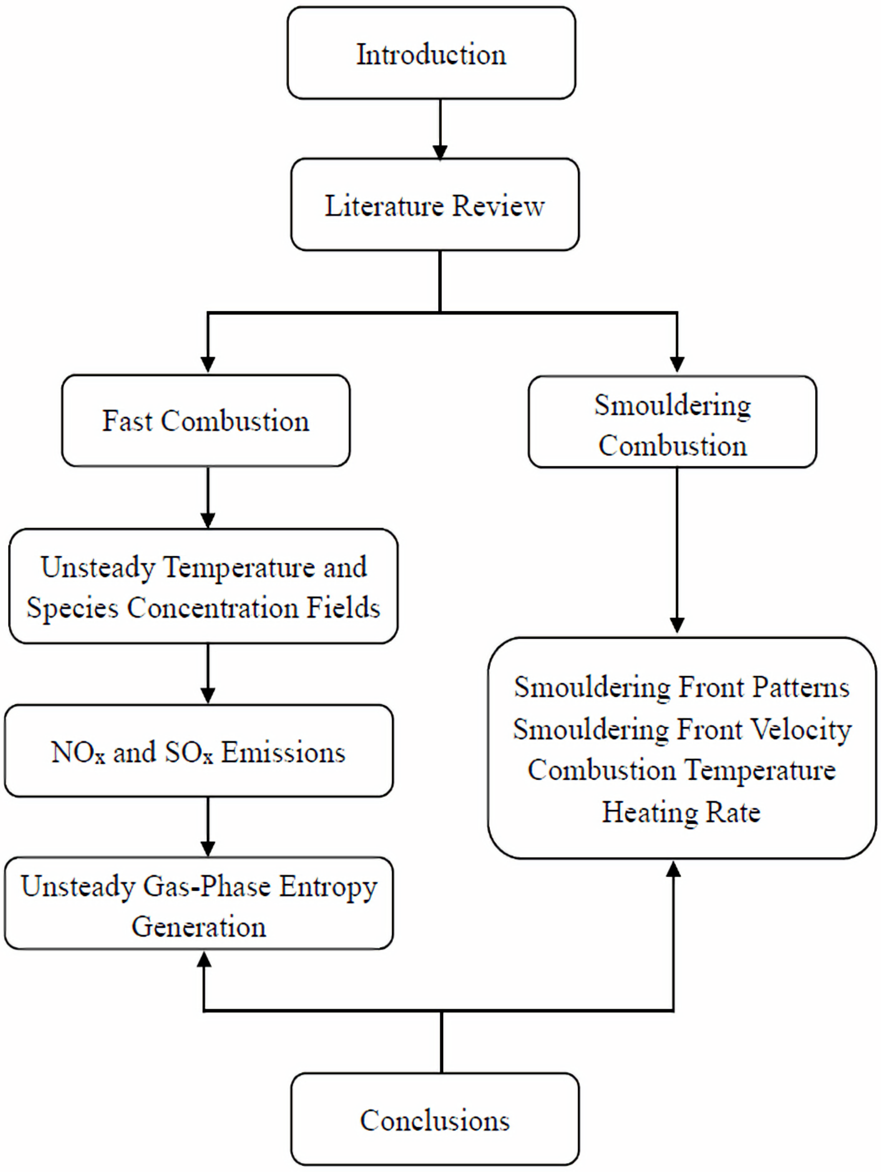

Figure 1.4: Flow chart of thesis structure.

Chapter 2

Literature review

In this chapter, a general review of the combustion of coal and biomass is given. First, an overview of coal and biomass particles direct combustion under varying is to be presented. Then, the NO_x and SO_x emissions during the combustion process is reviewed. An overview on the entropy generation in the combustion system is given after that. Finally, the smouldering combustion phenomena, especially the instabilities of the reaction front is discussed.

2.1 Coal and biomass combustion

Pulverised combustion is perhaps the most common technology for utilising biomass and coal energy, which is still and, most probably, will continue to be amongst the main resources for power and heat generation [27]. The compositions and molecular structures found in the carbonaceous fuel such as coal and biomass are very complex. The main chemical elements of coal and biomass is carbon (C), hydrogen (H), oxygen (O), nitrogen (N), sulphur (S) and some additional varying quantities constituents like sodium (Na), chlorine (Cl) etc. The combustion characteristics of solid fuels are greatly affected by the variation of shares of the above mentioned elements in the solid fuels.

Direct combustion of solid fuels is a conversion process where heat is generated. There are several major chemical and physical phenomena occurring during this combustion process [28] (Fig. 2.1). Generally, the principal combustion process involves three stages: (1) devolatilization stage the volatiles released from the solid fuels, (2) homogeneous stage the combustion of the released volatiles and (3) char oxidation the burning of the solid carbon [29]. It can be seen that the solid fuels combustion is a multi-phase, multi-scale and multi-components process which is quite complicated. Studies about solid fuel particles combustion have been done and the results show that the process is dependent on the fuel type, the particle size, the particle size distribution, the operating pressure and temperature, the gaseous environment etc. [30].

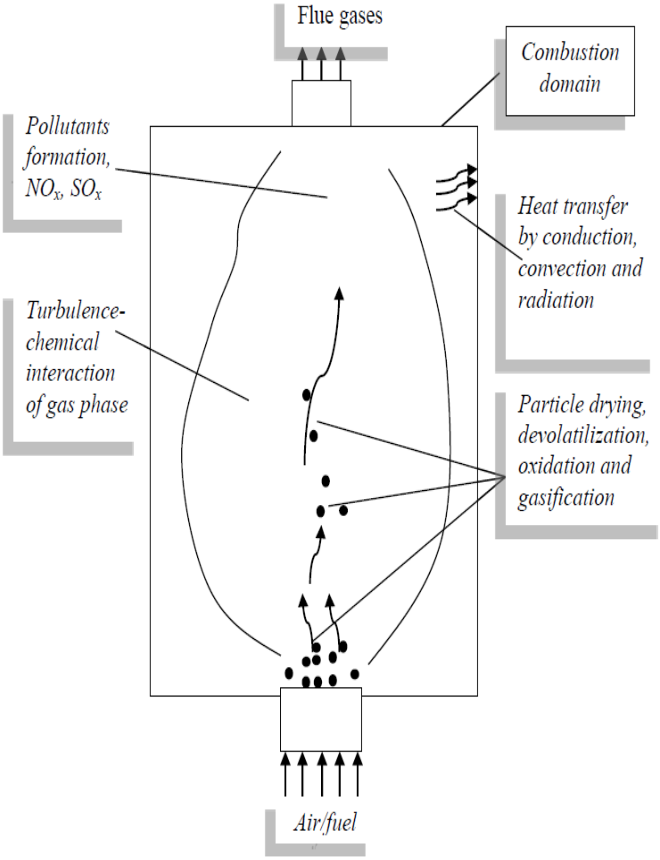

Figure 2.1: Various chemical and physical mechanisms during solid fules combustion [28]

Recently, oxy-fuel combustion is developed to be a well-demonstrated technology capable of facilitating carbon capture and storage which aims at reducing [31]. However, capturing of carbon dioxide from coal and biomass fired power stations substantially reduces the high level of CO_2 emission from their conventional combustion, but the combustion process of pulverised fuels and the thermal efficiency is greatly influenced by oxy-fuel combustion due to the variation of gas contents and oxygen concentration in the reactor [32]. High complexity of pulverised and fluidised bed coal combustion has led to an interest in analysing transient combustion of single coal particles [33]. Such studies allow for the development of fundamental understanding of the underlying physicochemical processes in single coal or biomass particle combustion.

Bu et al. [34] examined ignition behaviour of single bituminous coal particle under O_2/N_2 and O_2/CO_2 atmosphere with O_2 concentration up to 40%. They found that, compared with O_2/N_2 environments the ignition delay time is much longer than in O_2/CO_2 atmosphere, and the effect of atmosphere on the devolatilization process is almost negligible under the same O_2 concentration. They also concluded that the devolatilization process of a fuel particle is mostly controlled by the thermal properties such as thermal capacity, thermal conductivity and the convective heat transfer coefficient rather than N_2 or CO_2 atmospheres at the same oxygen concentration [35].

Further, the experimental study of single char particle under oxy-fuel combustion conditions [36] revealed that it takes longer time for the particle to reach the peak temperature under O_2/CO_2 gas atmospheres. The apparent average combustion rate of the particle drops when replacing N_2 by CO_2, and the effect is more notable in higher oxygen concentration environment [36].

Khatami et al. [37] [38]conducted experiments to investigate the combustion behaviour of single coal and biomass particles under oxy-fuel conditions. They found that the ignition delay of coal particles was drastically prolonged in the slow-heating O_2/CO_2 environments compared with fast-heating ones [37]. When replacing the background gas N_2 by CO_2, the combustion intensity of all fuels was distinctly decreased and increasing the oxygen concentrations under O_2/CO_2 increased the likelihood of particle combustion [38].

Experiments with single char particle combustion from lignite and bituminous coals in a laboratory scale fixed bed reactor under various O_2/N_2 and O_2/CO_2 gas conditions were conducted by Brix et al. [39]. They found that for the two kinds of char particles, the particle surface temperature are higher in O_2/N_2 than in O_2/CO_2 environments, and it increases along with enhancing oxygen concentration [39]. Yet, there is no clear link between the particle surface temperature and the particle mass for both of the investigated fuels [39].

Zhou et al. [40] studied the ignition properties and combustion characteristics of single coal particle under O_2/N_2 gas conditions with various coflow temperature, gas flow rate and oxygen concentration. The results showed that, the particle temperature increases along with the coflow temperature or gas flow rate increasing. Further, enhancing oxygen concentration shortens the particle ignition delay time and decreases the ignition temperature, and the influence is more obvious under high gas flow rate.

Riaza et al. [41] investigated the combustion characteristics of four kinds of biomass particles in both air and oxy-fuel conditions. The results showed that, for a single particle, the volatile combustion and char combustion happen sequentially for all the four types of biomass. Under the same oxygen concentration (21%), the burnout times of the volatile and char are longer when changing the background gas from N_2 to CO_2, while the combustion temperatures and combustion intensity are reduced. When increasing the oxygen concentration up to 21% under CO_2 atmospheres, the time of volatile and char combustion decreases successively and the combustion temperature raised.

Tolvanen et al. [42] studied experimentally and numerically the combustion behaviour of two coal chars under both O_2/N_2 and O_2/CO_2 environments with oxygen molar concentration varying from 2% to 12%. The experimental results showed that, when substituting CO_2 for N_2, the surface temperature and mass loss rate of char particles becomes lower, and the effect is more obvious on particle surface temperature. Timothy et al. [43] observed the entire combustion process of single coal particles. They got the data of devolatilization durations and overall burnout times of bituminous and lignite coals with particle size in 90-105 μm. They found that the average particle surface temperatures of the lignite coal (2000K) is lower than that of the bituminous coal (2300K).

Lee et al. [44] observed the motion of pulverized coal particles during the transient combustion process in a hot gas flow field. They found that, the vertical velocity of the coal particles increased faster while the horizontal velocity dropped more quickly at higher oxygen concentrations. Further, all the chemical processes such as devolatilization and the combustion of volatile and char are greatly affected by the oxygen concentration. Moreover, they concluded that, the shape of volatile flames is influenced by the oxygen concentration as well. It is more spherical under higher mole fraction of oxygen than lower mole fraction of oxygen [45].

Shen et al. [46] found that the particle burnout properties of superfine pulverized coal is dependent on the operating conditions in multi staged combustion ratio. Joutsenoja et al. [47] reported 2280-2300K as the average particle temperatures of lignite and bituminous coals by conducting related combustion experiments. Murphy et al. [48] found that the average char particle temperature of a sub-bituminous coal was 2200K and that of a bituminous coal was around 2050K when the oxygen concentration is 24%.

None of these, however, provides any information on the scalar fields in the gaseous environment surrounding the particle. Exceptions to this are a few recent works that applied high speed, planar laser diagnostics to the problem of transient coal combustion. Koeser et al. [49] [50] visualized the volatile and char combustion zone for single coal particles through OH-radicals images taken by high-speed laser−induced fluorescence. They found that, the ignition of coal particles is dependent on the particle size but the larger particles have a longer ignition delay time [49], and the distance between the volatile combustion zone and coal particles is determined by the oxygen concentration [50].

In the absence of experimental studies, numerical simulations are the effective way to predict the transient scaler fields in the single particle combustion. Oxy-combustion of pulverised coal has been already subject to extensive numerical simulations. Zou et al. [51] successfully simulated the ignition process of pulverized coal combustion under oxy-fuel conditions by using ANSYS Fluent. The interaction between the char combustion and volatiles combustion and their rates are obtained during the numerical simulations [51]. The effect of gas and solid particle radiation on the oxy-fuel combustion of coal particles was investigated by Johansson et al. [52] with a

Statistical-Narrow-Band (SNB) model. Richter et al. [53] conducted the numerical simulations to get the species concentration fields in both solid particles and the gas atmosphere under steady condition.

Through direct numerical simulations, Chabane et al. [54] examined the unsteady, multicomponent gaseous flow in the vicinity of a carbonaceous reactive surface. These authors considered several homogeneous and heterogeneous reactions and analysed the interactions between these two groups. They also identified the transitions from oxidation to gasification regimes [54]. The work of Chabane et al. further explored the contribution of Soret and Dufour effects upon the transfer of heat and mass in the investigated configuration [54].

A detailed numerical simulation of single coal particle devolatilisation and ignition was conducted by Tufano et al. [55]. An extensive set of homogenous chemical reactions in a laminar flow were considered in this study. The influences of enhanced oxygen levels mixed with either nitrogen or carbon dioxide on the particle ignition and flame development were investigated [55]. They highlighted the importance of particle preheating and Reynolds number in determining the value of ignition delay [55]. They revealed through modelling that, the particle ignition delay time is determined by the potential particle preheating, particle Reynolds number and the criterion employed for extraction of ignition delay [55].

Biomass are generally used for co-firing with coal as pulverized fuels [56]. Many efforts have been devoted to co-combustion of different coal with biomass and studies have been conducted to identify the special effects of co-combustion on ignition [57], the flame characteristics [58], species emission [59] and the performance of the furnace [60]. Little research focuses on understanding the transient combustion process of pulverized biomass particles.

Lu et al. [61] successfully established a one-dimensional model to simulate the biomass particle combustion process under spherical and cylindrical and flat plate shapes. They revealed that the composition and temperature gradients in biomass particles have a greater influence the predicted and measured rates of temperature rise, especially for large particles. Wang et al. [62] conducted numerical simulations of transient combustion of single biomass particle when oxygen molar concentration varying from 21% to 100%. The influence of enriched oxygen concentration on heat and mass transfer in the transient burning process is investigated by constructing a spatio-temporal model.

The present review of literature (Table 2.1)shows that, the analyses of pure biomass particles combustion especially under oxy-fuel combustion is rare. Moreover, the unsteady temperature and species concentration fields has remained unachievable during the biomass and coal com-

Table 2.1: Summary of studies on single particle combustion

Researchers	Fuel Type	Remarks
Bu et al. [34]	Coal Particle	Ignition delay time, devolatilization process.
Bu et al. [36]	Char Particle	Particle temperature, combustion rate.
Khatami et al. [37] [38]	Coal/Biomass Particle	Ignition delay time, particle life time, particle temperature.
Riaza et al. [41]	Biomass Particles	Volatiles and char combustion rates.
Lee et al. [44] [45]	Coal Particles	Particle velocity, volatiles flame.
Koeser et al. [49] [50]	Coal Particles	Visualized ombustion zone through OH-radicals images.
Zou et al. [51]	Coal Particles	Interactions between volatiles and char combustion.
Johansson et al. [52]	Coal Particles	Radiation effects on oxy-fuel combustion.
Richter et al. [53]	Coal Particles	Species concentration fields under steady condtions.
Lu et al. [61]	Biomass Particle	One-dimensional model, different assumptions of particle shape.

bustion process. The significance of such data stems from the fact that the spatio-temporal evolutions of the temperature and concentration fields dominate the unsteady rate of entropy generation [63] and also influence formation of the air pollutants [64]. Therefore, studies on single coal and biomass particle combustion, particularly oxy-fuel combustion of these particles are called for deeper understanding.

2.2 NO_x and SO_x emissions

The weighted contents of nitrogen and sulphur in coal and biomass are normally ranged 0.5%-2% and 0.5%-3%, respectively [65] [66]. Although concentrations of N and S in biomass are rather low, the emissions of pollutants, (e.g. NO, NO_2, SO_2, SO_3). produced during direct combustion for heat and power generation has attracted considerable attention [67] due to the serious environmental effects [68]. Studies have been conducted to further understand the pollutant formation and develop methods to minimize them.

The factors influencing the pollutant emissions include the combustion temperature [69], operating pressure [70], fuel size [71], limestone [72], air staging [73] etc.. Valentim et al. [69] found that more NO_x emissions is generated during the coal fluidised bed combustion process when the temperature increases from 700°C to 1000°C. Svoboda et al [70] concluded that the NO_x emissions decrease with increasing operating pressure and the effect of oxygen molar fraction is more pronounced at lower pressure conditions.

Shen et al. [46] conducted the experimental work of superfine pulverized anthracite coal under both single and multi air staging conditions in a drop tube furnace to study the NO_x emissions. The results indicate that, in single air staged combustion, superfine pulverized coal has better reduction efficiency of NO_x emissions than regular particle size. Moreover, the reduction efficiency is higher in multi air staged combustion compared with single air staged combustion.

Tarelho et al. [74] experimentally investigated the effects of excess air and air staging on NO formation in fluidized bed coal combustion. Increasing the excess air resulted in an increase in NO emissions, while NO emissions decreased with increasing the scale of the air staging. However, Wang et al. [75] reported that air staging does not play an important role in reducing NO emissions for biomass combustion for the co-firing experiments of coal and biomass in a drop tube furnace. In Zhao et al.'s work [76], the results showed that temperature increases result in both higher NO_x and SO_2 emissions in algae biomass combustion. Further, they reported that the higher content of sulphur in the fuel promotes the SO_x emissions and its conversion rate while the NO_x emissions are not regularly depended on the nitrogen content [76].

Zhou et al. [77] investigated the behaviours of fuel-N, volatile-N and char-N of single bituminous and anthracite coal particles converting to NO_x emissions within various flow temperatures. The experimental work revealed that, most of the NO_x pollutants are generated from Char-N and only 20%-30% are from volatile-N for both bituminous and anthracite coal particles, while over 50% of N_2O are from volatile-N instead. The conversation ratios of fuel-N, char-N and volatile-N nearly keep stable when the flow temperature changes for anthracite coal particles, while the ratios increase for bituminous. Moreover, the conversion to N_2O decreased when increasing the flow temperature. Zhou et al. [78] reported that the temperature produced little influence on the conversion of fuel-N, volatile-N and char-N to NO_x for anthracite when burning a single coal particle. While for a single biomass particle, they found that the conversion ratios of fuel-N to NO are at peaks when temperature is 1100K as it varies from 1000-1200K, and at oxygen concentration 30% when it increases from 20% to 50% [78].

Courtemanche et al. [79] conducted research on NO_x and SO_2 emissions with different equivalence ratios and temperatures. They found that higher equivalence ratios strongly decrease NO_x emissions in air combustion, while increase with increasing temperature. SO_2 emissions nearly does not change with fuel-lean mixtures but are higher in the nitrogen-free gas than in air combustion. The work of Tian et al. [80] showed that, H_2S and COS emissions are higher in CO_2 atmosphere than in N_2 atmosphere, while SO_2 was lower. Under CO_2 atmosphere, the main peaks of SO_2, COS and H_2S become more evident with the peak values increase while O_2 concentration increases.

The effects of O_2/N_2 and O_2/CO_2 gas atmosphere on NO_x and SO_x emissions have been investigated. In the experiments done by Brix et al. [39] about single lignite and bituminous char particle combustion in O_2/N_2 and O_2/CO_2 atmospheres with varying oxygen concentration, it was concluded that, the NO formation is similar in O_2/N_2 and O_2/CO_2 for lignite char, while more NO is produced for bituminous char when changing N_2 to CO_2. Further, the higher oxygen concentration or the bigger particle size is, the smaller ratio of char-N is converted to NO.

Li et al. [81], Duan et al. [82], Daood et al. [83] and their co-workers all reported that NO emissions were much lower in oxy-fuel combustion than in air combustion experimentally as there is no formation of thermal-NO_x caused due to the absence of nitrogen in the flow. Shao et al. [84] found that the average NO_x concentration increases along with increasing oxygen concentration, and the maximum value and peak shape of the NO_x concentration curve changed with temperature. Specifically, the average NO_x concentration increases when the temperature varying from 823K to 923K and declines when the temperature varying from 923K to 1223K. Duan et al. [85] reported that CO_2 atmosphere suppresses/diminishes NH_3 yield and enhances/increases HCN yield and the HCN/NH_3 ratio is elevated in CO_2 atmosphere compared with that in Ar atmosphere.

Croiset et al. [86] found that SO_2 yield is a bit higher while replacing N_2 by CO_2, and SO_2 emissions are similar under 28% O_2/CO_2 and 35% O_2/CO_2 but increases when oxygen concentration was up to 42% for coal combustion. Moron et al. [87] presented that CO_2 atmosphere decreased the conversion ratio of sulphur in the single staged combustion of coal and biomass. Duan et al. [88] reported that, for bituminous coal, the SO_x concentration is higher under O_2/CO_2 conditions compared to O_2/N_2 ones. Moreover, as the O_2 concentration increases in O_2/CO_2 mixture, SO_2 yield increases first and then decreases with a maximum at 30% O_2 concentration [88].

However, still different findings of nitrogen and sulfur emissions were obtained. Permchart et al. [89] suggested that, NO_x emissions from biomass combustion highly depend on the fuel-nitrogen content in the fuel and are slightly influenced by the operating conditions. Liu et al. [90] also found that SO_2 emission is not affected by the combustion media. Zheng et al. [91] concluded that SO_x emissions are governed by oxygen concentration rather than CO_2 atmosphere. Hu et al. [92] presented that SO_x emissions were similar in N_2 and CO_2 gas atmospheres and the influence of temperature on SO_2 emissions is quite small for coal combustion. Ren et al. [93] reported that there are no clear links between SO_2 emission and sulphur fractions in biomass fuel when it burns in the drop-tube furnace operating at 1400K.

The preceding review of literature (Table 2.2) indicates that, so far, most investigations have been focused on coal or char combustion under oxy-fuel conditions, and there are only few studies regarding single coal or biomass particle combustion under oxy-fuel conditions. More importantly, the existence of inconsistent, and sometimes conflicting results on NO_x and SO_x emissions highly necessitates conduction of further investigations.

Table 2.2: Summary of studies on NO_x and SO_x emissions

Researchers	Fuel Type	Remarks
Valentim et al. [69]	Coal Particles	NO_x emissions increase in higher temperatures conditions.
Svoboda et al. [70]	Coal Particles	NO_x emissions decrease in higher pressure conditions.
Shen et al. [46]	Coal Particles	NO_x emissions decrease when burning superfine coal particles.
Wang et al. [75]	Coal/Biomass Particles	Air staging does little to NO_x reduction in the co-firing of coal and biomass particles.
Zhao et al. [76]	Biomass Particles	Higher NO_x and SO_x emissions in higher temperature conditions. Higher content of sulphur in the fuel, higher SO_x emissions.
Tian et al. [80]	Coal Particles	Lower SO_2 emissions in O_2/CO_2 conditions compared to O_2/N_2 conditions.
Shao et al. [84]	Biomass Particles	Higher NO_x emissions in higher oxygen concentration conditions.
Croiset et al. [86]	Coal Particles	Higher SO_2 emissions in O_2/CO_2 conditions compared to O_2/N_2 conditions.
Duan et al. [88]	Coal Particles	SO_2 yield increases first and then decreases when O_2 concentration increases in O_2/CO_2 mixtures.
Permchart et al. [89]	Biomass Particles	NO_x emissions depend on the nitrogen content in the fuel rather than operating conditions.
Liu et al. [90]	Coal Particles	SO_2 emission is not influenced by combustion media.
Zheng et al. [91]	Coal particles	SO_x emissions are highly affected by oxygen concentration.

2.3 Entropy generation

It is well-established that combustion is, by far, the most irreversible process taking place in thermal power stations [94]. Recent studies of coal fired power stations showed that the exergy efficiency of circulating fluidised bed boiler can be lower than 30% [95]. This figure clearly reflects the significant role of combustion process in exergetic losses of thermal power generation. Thus, future improvements in power stations are subject to obtaining a thorough understanding of the irreversibilities of combustion technologies [96]. The recent emphases on low carbon power generation have led to the development of oxy-combustion [97] and a fast growing interest in combustion of biomass [98]. Combination of these two technologies along with carbon capture and storage introduces a potential method of negative carbon emissions in power generation [99].

Practical optimisation of oxy-fuel combustion of biomass requires examining the thermodynamic irreversibilities associated with burning of biomass particles in oxygen enriched atmospheres. This, in turn, calls for accurate simulation of coal and biomass combustion in atmospheres with varying concentration of oxygen. Given the high complexities of pulverised biomass combustion, analysing combustion of a single biomass particle is expected to better reveal the fundamentals of thermodynamic irreversibilities. Such analysis will be inevitably transient and therefore rather distinctive to the conventional second law studies of reactive flows [100].

The general field of entropy generation in the combustion process has already received a considerable attention from the scientific community [101]. A vast majority of the literature in this area has focused on entropy generation in combustion of gaseous fuels under premixed or diffusion modes. In a series of numerical studies, Chen et al. investigated entropy generation on opposing jet combustion of hydrogen and blends of hydrogen and methane in premixed [102] [103] and non-premixed [104] modes. Through Lattice-Boltzmann simulations, these authors performed extensive parametric studies and showed that the jet Reynolds number is a key parameter characterising the generation of entropy. In particular, Chen et al. [105] asserted that for low Reynolds number the irreversibility associated with chemical reactions is the dominating source of entropy generation. However, at high Reynolds number the hydrodynamic irreversibilities become more significant.

Emadi et al. [106] analysed the local generation of entropy in a hydrogen-enriched, turbulent non-premixed flame. Their results revealed that, in general, thermal conduction is the most significant source of entropy generation and is followed by that of chemical and mass diffusion processes [106]. However, preheating of air resulted in the reduction of thermal irreversibility and maintained the chemical and mass transfer irreversibilities unchanged. Hence for combustion with preheated air (at above 750K) chemical irreversibilities were reported as the dominant source of entropy generation [106]. On this basis, Emadi et al. [106] recommended preheating as a means of improving the exergetic efficiency of combustion. More recently, Safer et al. [107] simulated non-premixed combustion of syngas in a counter flow configurations. These authors [107] calculated the rate of entropy generation for different hydrogen contents in the syngas and showed that hydrogen enrichment reduces the irreversibility of the process. Their results also revealed that chemical irreversibilities are the most significant source of entropy generation in the investigated flame configuration [107].

Data collected from direct numerical simulations (DNS) were used by Farran and Chakraborty to evaluate entropy generation in turbulent premixed flames [108]. These authors argued that decreasing the global Lewis number results in increasing thermal, chemical and mass diffusion irreversibilities. Yet, the regime of turbulent premixed combustion was judged insignificant in entropy generation process. Another DNS study of entropy generation in premixed flames revealed that increasing the combustor pressure and the extent of exhaust gas recirculation intensify the rates of irreversibility [109]. It was also shown that for the low Reynolds numbers the chemical irreversibilities dominate the generation of entropy [109]. Safari et al. [110] conducted a large eddy simulation of entropy generation in turbulent non-premixed jet flames. They found that increases in the turbulence intensity of the jet leads to higher chemical and thermal irreversibilities in the flame [110].

Entropy generation minimisation has been also applied to the design of practical combustors. In a recent study, Arjmandi et al. [111] simulated the generation of entropy and the second law performance of a swirling bluff-body stabilised flame in a gas turbine combustor. In a parametric study they investigated the influences of equivalence ratio, fuel-inlet flow rate, bluff-body aspect ratio, swirl number, and air-inlet velocity upon the entropy generation and accordingly suggested an optimised design of the combustor [111].

Entropy generation in single phase combustion has been also extended to microsystems through analysing combustion of mixtures of H_2 and CH_4 [112] in microchannel and micro-planar configurations. Multiple step chemical kinetics was employed in these studies, which revealed that the total entropy generation within the system increases by augmenting the inlet velocity of the reactants. Jiang et al. [113] showed that concentration of CO and H_2 can significantly affect the share of chemical irreversibility in the total entropy generation.

The problem of entropy generation in premixed combustion of hydrogen air mixtures in micro-combustors was investigated by Jejurkar et al. [114]. This study showed that chemical reactions, heat conduction and mass diffusion are respectively the most important sources of irreversibilities in premixed, micro combustion [114]. It was also demonstrated that combustion irreversibility deceases as the thermal conductivity of the micro-combustor walls increase [114]. In addition to classical premixed and non-premixed combustion modes, entropy generation calculations have been further performed for catalytic partial oxidation of methane [115]. It was shown that chemical irreversibilities dominate the rate of entropy generation in catalytic partial oxidation of methane in a Swiss-roll reactor [115].

Compared to those of single phase, investigations of the second law performance of multiphase combusting flows are much less frequent. In an early theoretical study, Puri calculated theoretically the entropy generation during combustion of a droplet [116]. In this work, the optimised size of the droplet and the velocity of gaseous atmosphere were found [116]. In another pioneering work, Dash et al. examined the transient combustion of a single liquid droplet in a convective atmosphere [117]. They numerically solved the unsteady governing equations together with a single step chemical reaction [117]. The results revealed the temperature distribution and convection coefficients around the droplet and also predicted the time trace of entropy generation in the course of transient burning process [117]. This study was later extended to droplet burning in quiescent atmospheres [118]. It was demonstrated that the initial temperature ratio of the droplet and the atmosphere and also the initial Damk*ö*hler number are the key parameters in determining the rate of exergy destruction in droplet combustion [118]. In a more recent numerical investigation, entropy generation was evaluated in quasi-steady combustion of a droplet [119]. It was shown that entropy generation by thermal and chemical mechanism are quite similar [119]. Further, the authors indicated that entropy generation rate decreases with increasing ambient temperature and increases with the particle diameter [119].

Gas-phase entropy generation in transient combustion of methanol droplets were examined theoretically and numerically by Pope et al. [120]. In this work, stationary droplet combustion in a low temperature, nearly quiescent environment and also moving droplet in preheated atmospheres were examined [120]. The results indicated that by increasing the initial Reynolds number generation of entropy by transfer of heat and mass decreases. However, irreversibilities generated by chemical reactions are intensified [120]. Similar to that shown in single-phase reactive flows, Pope et al. [120] demonstrated that the chemical and thermal irreversibilities dominate the generation of entropy, while the contribution of mass transfer is negligible.

Although combustion characteristics of coal and biomass particles in oxygenated media have been investigated to some extent, the thermodynamics of the solid fuels combustion have received little attention. As a matter of fact, the thermodynamic irreversibilities associated with the more general problems of particle and droplet combustion are still largely unexplored. This shortage of studies is expected to be mainly due to the multiphase and transient nature of particle and droplet combustion, which makes the transport and thermodynamic analyses complicated. The limited literature in this area is reviewed in the followings.

Calculation of entropy generation in solid fuel combustion is restricted to a few investigations on coal and biomass combustion. On the basis of the numerical analyses of a pulverised coal combustor, Som et al. [121] developed an exergy balance for the reactive system under steady state. Mondal et al. [122] constructed a model of transport phenomena and entropy generation for combustion of a single coal particle in quiescent, hot atmosphere. Because of the stationarity of the particle, spherico-symmetric governing equations were solved in this work. The influences of coal particle diameter and chemical composition and also those of the free stream temperature on the temporal evolution of the irreversibilities were further analysed in Ref. [122]. Baloyi et al. [123] examined the steady, exergetic behaviour of a small-scale wood-fired fluidised bed combustor. This study was primarily concerned with the effects of air fuel ratio upon the rate of entropy generation of an adiabatic burner. It was shown that there is an optimal value of air fuel ratio for which the entropy generation is minimal [123].

The preceding survey of literature (Table 2.3) clearly shows that already there exist in-depth investigations of thermodynamic irreversibilities in single-phase, gaseous combustion. Important conclusions have been made about these systems. For instance, chemical reactions heat conduction and mass diffusion are respectively regarded as the major contributors to entropy generation in premixed flames, while the order of significance is different in non-premixed flames. Further, multiple studies have clarified the effects of preheating and equivalence ratios in gaseous steady combustion. Nevertheless, the equivalent studies in multiphase combustion are currently lacking. This is, particularly, the case for transient combustion of solid fuels, which is perhaps due to the complexity of unsteady combustion in burning of solid particles.

Further to the significant role of direct coal and biomass combustion in the current and future energy systems, thermochemical conversion of biomass through gasification is becoming a key technology for syngas and hydrogen production [124]. In recent years, there has been a rapidly increasing interest in optimising biomass gasifiers [125]. Amongst other techniques, exergy and entropy generation minimisation have been employed to improve the design of biomass gasification systems [126]. Central to achieving improved modelling of the second law performance of biomass gasifiers, is obtaining an in-depth understanding of transport and entropy generation during gasification of single particles.

To achieve these goals, the studies for irreversibilities generation during the transient combustion of single coal and biomass particles in both O_2/N_2 and O_2/CO_2 atmospheres with varying concentration of oxygen should be conducted.

Table 2.3: Summary of studies on entropy generation

Researchers	Phase	Remarks
Chen et al. [102] [103]	Gaseous Phase	Entropy generation in H_2 and CH_4 combustion under premixed mode.
Chen et al. [104] [105]	Gaseous Phase	Entropy generation in H_2 and CH_4 combustion under non-premixed mode.
Emadi et al. [106]	Gaseous Phase	Entropy generation in a turbulent non-premixed H_2 enriched CH_4 air flame.
Safer et al. [107]	Gaseous Phase	Entropy generation in turbulent syngas diffusion flame.
Farran et al. [108]	Gaseous Phase	Entropy generation in turbulent premixed flames
Borghesi et al. [109]	Gaseous Phase	Entropy generation in high-pressure turbulent reactive flow.
Safari et al. [110]	Gaseous Phase	Entropy generation in a turbulent non-premixed flame.
Wang et al. [112]	Gaseous Phase	Entropy generation in CH_4-H_2-air flames.
Jejurkar et al. [114]	Gaseous Phase	Entropy generation in H_2-air premixed flames.
Chen et al. [115]	Gaseous Phase	Entropy generation in catalytic partial oxidation of CH_4.
Puri et al. [116]	Gaseous-liquid Phase	Entropy generation during a droplet combustion.
Dash et al. [117]	Gaseous-liquid Phase	Entropy generation during a droplet combustion under convective condition.
Raghavan et al. [119]	Gaseous-liquid Phase	Entropy generation during the quasi-steady combustion of spherical liquid particles.
Pope et al. [120]	Gaseous-liquid Phase	Unsteady gas-phase entropy during a droplet combustion.
Baloyi. [123]	Gaseous-Solid Phase	Entropy generation in wood-fired combustor.
Mondal et al. [122]	Gaseous-Solid Phase	Entropy generation during a coal particle combustion.

2.4 Smouldering combustion

Smouldering is a slow, correspondingly low-temperature, and flameless combustion mode, which is supported by the heat generated when oxygen directly reacts with the surface of porous fuels [127]. Wildfires, smoking cigarettes, burning incense and in-situ combustion are the most common examples of smouldering combution [128]. The major difference between smouldering combustion and flaming combustion is the fuel, where homogeneous reactions occurring between a gaseous fuel and a gaseous oxidiser in the former and heterogeneous reactions taking place between a gaseous oxidiser and a solid fuel in the latter [129].

Smouldering combustion can happen when the porous media which contains a solid carbonaceous char is heated [130]. This is determined by the characteristics of porous media structure: a high surface area to volume ratio allowing diffusion of oxygen and combustion products [130]. A high level of thermal insulation is achieved due to the high air content of these fuels, which reduces heat losses and sustains combustion under low heat release rates conditions. Smouldering combustion taking place inside a porous fuel bed is a form of filtration combustion [131]. Filtration combustion refers to the propagation of an exothermic reaction wave in a porous medium involving fluid oxidiser filtration [131]. It includes the cases in which the gaseous reactant is present within the pores of a medium or the porous medium itself is the reactant. The latter is a form of smouldering combustion. Unlike most forms of smouldering combustion where free air outside the medium provides the oxidiser for the reaction, in filtration combustion it is the air flowing through the pores which provides oxygen to the reaction site. Thus, filtration combustion has a number of practical applications, such as ores treatment, regeneration of coked catalysts and in-situ combustion in hydrocarbon reservoirs [131].

Filtration combustion can be classified into two combustion modes: forward smouldering and reverse smouldering [132]. In forward smouldering, the combustion wave moves in the same direction of air flow while it moves against with the flow in reverse smouldering. Therefore, all the conduction, convection and radiation heat transfer move towards the unburned fuel in forward smouldering. Preheating of unburned fuel help the combustion reach super-adiabatic temperatures. While under reserve smouldering, the heat is transported upstream by conduction and radiation mechanisms and convection transports heat in the opposite direction. They act to balance each other out as the opposing transport direction. Due to this difference, the propagation of forward smouldering combustion front is usually unsteady, while the reserve propagation is normally steady [133]. Inhaling through a cigarette is a good example of forward smouldering where both the oxygen and the reaction front move towards the smoker. On the contrary, the combustion mode of exhaling through a cigarette is reserve smouldering [134].

Aldushin et al. [135] found that hydrodynamic perturbations are the major cause of instabilities. For both forward and reverse combustion, the reduction of resistance to air flow due to the increasing porosity in the burnt region is the basic mechanism which leads to unstable waves. In forward combustion the generation of gaseous products during combustion is another unstable effect, while it is a stabilized effect in reverse combustion. They [135] showed that the finger instabilities of smouldering combustion fronts could be characterized as a solution of a Saffman-Taylor problem. The Saffman-Taylor problem is originally formulated to describe the displacement of one fluid by another having a smaller viscosity, in a porous medium or in a Hele-Shaw configuration [136].

Zik et al. [137] conducted experimental work to consider the structure characteristics of fingers by burning filter paper between two parallel plates with a narrow gap, which was similar to a Hele-Shaw cell. They found that in the absence of convection, the Peclet number determined the spacing between fingers and heat loss determined the finger width [137]. If regardless of heat loss, the finger width was linearly dependent on the gap between plates [138]. The experimental results were well explained by the theory of Aldushin [135].

Aldushin et al. successfully observed a finger-like filtration combustion front by burning dried sawdust in a slit-like rectangular channel [139] and asymmetric fingers propagated along one of the channel walls [140]. They pointed out that in filtration combustion problem, there were asymmetrical fingers since the interface was a chemical reaction front with zero surface tension, while for Saffman-Taylor problem, there were no asymmetrical solutions due to the effect of surface tension at the interface. Aldushin et al. [141] established a 2D mathematical model of unsteady filtration combustion when the air flow was in the same direction of the combustion front to investigate the filtration combustion front propagation modes. The results of numerical simulations showed that, the front lost its stability at the ratio between the permeability of gas product and fuel powder (K) closed to 1. When $K>1$, the time of the breakup of the quasi-steady front initiated at the ignition stage decreased and the self-organization of the nonuniform structure of the combustion front occurred more rapidly with increasing K. With the changes in channel width and filtration coefficient, there were other structures of the front. In another work [142], they conducted the simulations of a 2D model of coflow filtration combustion in a slit-like reactor. These authors [142] observed the manifestation of hydrodynamic and thermal instability simultaneously upon a decrease in the ratio of heat capacity of gas to fuel or an increase in ratio of permeability of product to fuel and the reactor width.

Pojman et al. [143] found that in autocatalytic chemical reactions, when thermal and solutal effects on density changes were cooperative, the up going fronts were stable. However, when the two effects were in competition, both up and down going fronts had possible instabilities [143].

Kalliadasis et al. [144] considered the solutal and thermal effects on fingering instabilities of exothermic reaction-diffusion fronts in porous media. The stabilities of both ascending and descending fronts were influenced by the interplay between chemical reaction and solutal-thermal effects, and when Lewis number was above unity, the double-diffusive phenomena played an important role as well.

Moreover, the ascending front stabilized while descending front destabilized with Lewis number increasing. Hejazi et al. [145] examined the viscous fingering of reactive miscible flow displacements in a homogeneous porous media and used a pseudo-spectral method to solve the continuity equation, Darcy's law and volume-averaged forms of convection-diffusion-reaction equations. The development and growth of the instability in terms of the amount of chemical products predicted based on the mobility ratio at the initial front between two reactants and effective mobility ratios between chemical products and either one of the two reactants. Redapangu et al. [146] used a two-phase lattice Boltzmann method to study the effects of viscosity differential on buoyancy-induced interpenetration of two immiscible fluids in a tilted channel. They observed relatively stable fingers under high viscosity ratios and the intensity of the front instabilities and the transverse interpenetration of fluids increased with a decrease in viscosity differences on fluids.

Schult et al. [147] consider porous cylindrical samples closed to the surrounding environment except at the ends, with gas forced into the sample through one of the ends. A smoulder wave was initiated at that end and propagates in the same direction as the flow of the gas. They found the smoulder wave solutions of the front velocity, temperature and oxygen concentration using asymptotic methods with both reaction leading and reaction trailing structures. Based on the theory of Schult [147], Akkutlu et al. [148] studied the properties of forward combustion fronts propagating at a constant velocity in the presence of heat losses. They obtained the explicit expression of front velocity, temperature and oxygen concentration under adiabatic, convective and conductive modes. The structure and stability properties of forward smoulder waves were numerically studied by Lu et al. using a simplified thermal-diffusive model [149]. They found that forward smoulder fronts were linearly stable for any incoming air flow rate in adiabatic condition, while considering convective heat loss, fingering instabilities occurred when the incoming flow rate was within a narrow range near 1-D extinction limit.

Kuwana et al. [150] presented a model to describe the unstable smouldering front of a thin solid burning in a narrow gap and defined Lewis number as the ratio of the solid thermal diffusivity to the oxygen diffusivity. Their study [150] showed that when Lewis number varied from 0.1 to 1, there was weaker instabilities with larger Lewis number, and the speed of smouldering front was close to 1-D propagation and increased with Lewis number increasing. A detailed parametric study was conducted by Rostami et al. [151] based on a transient two-dimensional model for the forward and natural smouldering of a porous biomass fuel. The results showed that, the lateral mass transfer boundary condition for oxygen and the heat transfer coefficient for natural smouldering case were the most significant parameters, and the main influencing parameters for forward smouldering were the airflow rate in the porous medium and the porosity of the medium. Saidi et al. [152] developed a three-dimensional model to numerically simulate the process of a burning cigarette reasonably. Results including velocity profiles, gas and temperatures, coal shape and burn rates. were obtained. Dodd et al. [153] established a two-dimensional numerical transport model with an eight-step reduced reaction mechanism to study the spontaneous transition from smouldering to flaming combustion in polyurethane foam. Reaction rates, species profiles and phase temperatures were examined.

Table 2.4: Summary of studies on smouldering combustion

Researchers	Method	Remarks
Zik et al. [137]	Experimental	Fingers structure.
Aldushin et al. [139] [140]	Experimental	Figures structure, front propagation.
Aldushin et al. [141]	Numerical	Front propagation.
Pojman et al. [143]	Numerical	Front instabilities.
Kalliadasis et al. [144]	Numerical	Front instabilities.
Redapangu et al. [146]	Numerical	Fingers structure.
Hejzi et al. [145]	Numerical	Front instabilities.
Akkutlu et al. [148]	Numerical	Front instabilities.
Kuwana et al. [150]	Numerical	Front propagation.
Saidi et al. [152]	Numerical	Front velocity, fuel burn rate.
Dodd et al. [153]	Experimental Numerical	Transition from smouldering to flaming combusion.

In conclusion, smouldering is a fundamental combustion problem. It involves heterogeneous combustion between gas and solid phases and heat and mass transport phenomena. Most studies focus on the characteristics of fingers and instabilities of the reactive front during smouldering combustion process. However, the existing studies are not enough to obtain a comprehensive view about smouldering combustion. Investigations about ignition and extinction, the front speed, the transition to instabilities or flaming and combustion emissions are lacked, and more experimental and theoretical research are required.

Chapter 3

Theoretical, numerical and experimental methods

This chapter is to introduce the methodology used to conduct the single coal and biomass particle combustion simulations and post-processing of gas-phase entropy generation during the transient combustion process. The first part describes the instantaneous equations for multiphase reactive flow, with the addition of a discrete particle injection accounted. Then, the combustion model and chemical kinetics considered for the single fuel particle combustion are introduced. The devolatilization process, char combustion reactions and homogeneous reactions are discussed. The third part is concerned with the modelling of NO_x and SO_x emissions. The formation mechanisms of main pollutant species such as NO, SO_2, SO_3 and some intermediates like NH_3, HCN, H_2S are described in detail. The derivation of gas-phase entropy generation rate based on the Gibbs equation is presented later. Lastly, the experimental apparatus for biomass smouldering combustion is introduced.

3.1 Governing equations

Regarding a multiphase reactive flow, the changes of pressure, temperature, flow velocity and species in both gas and discrete phase are the results of fluid flow, heat and mass transport and chemical reactions. There are conservation laws for the quantities such as mass, momentum and energy. Therefore, the numerical modelling is established on a set of governing equations. The detailed governing equations used in this work are described in this section.

3.1.1 Conservation of mass

The mass continuity equation representing the law of mass conservation in cylindrical coordinate is described below (Eq. 3.1) [154],

$$\frac{\partial \rho}{\partial t}+\frac{\partial}{\partial x}(\rho u_x)+\frac{\partial}{\partial r}(\rho u_r)+\frac{\rho u_r}{r}=0 \tag{3.1}$$

Here, x, r are the axial and radial coordinates respectively, and the variations in θ direction have been ignored. t is the time coordinate, ρ is the mixture density, u_x and u_r are the components of the velocity vector $\vec{u}$.

3.1.2 Conservation of momentum

For 2D axisymmetric geometries, the axial and radial momentum conservation equations are given by Eq. 3.2 and 3.3 [154],

$$\begin{aligned}\frac{\partial(\rho u_x)}{\partial t}&+\frac{1}{r}\frac{\partial}{\partial x}(r\rho u_x u_r)+\frac{1}{r}\frac{\partial}{\partial r}(r\rho u_x u_r)\\ =-\frac{\partial p}{\partial x}&+\frac{1}{r}\frac{\partial}{\partial x}\left[r\mu_m\left(2\frac{\partial u_x}{\partial x}-\frac{2}{3}(\bigtriangledown\cdot\vec{u})\right)\right]\\ &+\frac{1}{r}\frac{\partial}{\partial r}\left[r\mu_m\left(\frac{\partial u_x}{\partial r}+\frac{\partial u_r}{\partial x}\right)\right]+\rho g_x\end{aligned} \tag{3.2}$$

$$\begin{aligned}\frac{\partial(\rho u_r)}{\partial t}&+\frac{1}{r}\frac{\partial}{\partial x}(r\rho u_x u_r)+\frac{1}{r}\frac{\partial}{\partial r}(r\rho u_r u_r)\\ =-\frac{\partial p}{\partial r}&+\frac{1}{r}\frac{\partial}{\partial r}\left[r\mu_m\left(2\frac{\partial u_r}{\partial r}-\frac{2}{3}(\bigtriangledown\cdot\vec{u})\right)\right]\\ +\frac{1}{r}\frac{\partial}{\partial x}&\left[r\mu_m\left(\frac{\partial u_x}{\partial r}+\frac{\partial u_r}{\partial x}\right)\right]-2\mu_m\frac{2}{3}\frac{\mu_m}{r}(\bigtriangledown\cdot\vec{u})\end{aligned} \tag{3.3}$$

where, p is the static pressure, μ_m is the molecular viscosity, g_x is the acceleration gravity.

3.1.3 Balance of energy

Temperature T is required to evaluate the density and chemical reaction rate in the combustion system. It can be obtained by solving the energy equation which is shown below [154],

$$\frac{\partial(\rho h')}{\partial t}+\frac{\partial(\rho h' u_r)}{\partial r}+\frac{\partial(\rho h' u_x)}{\partial x}=\frac{\partial p}{\partial t}-\frac{\partial q_j}{\partial(x,r)}+Q_i \tag{3.4}$$

where:

$$h'=\textstyle\sum_{r=1}^{N}Y_i h_i \tag{3.5}$$

$$q_j=-\frac{\lambda}{c_p}\frac{\partial h'}{\partial(x,r)} \tag{3.6}$$

In the Eq. 3.4, h' is the enthalpy of the mixture, q_j is the energy flux, Q_i is the internal production rate for thermal energy. The calculation of h' and q_j are provided by Eq.3.5 and Eq.3.6. There, h_i is the absolute internal enthalpy of species i, Y_i is the mass fraction of species i in the mixture, N is the number of species in the gas phase, λ is the thermal conductivity of the mixture, c_p is the specific heat for the mixture.

3.1.4 Conservation of species

In addition to the governing equations mentioned above, the conservation equation of mass of species is also needed to describe the reactive flow [154].

$$\frac{\partial\left(\rho Y_i\right)}{\partial t}+\frac{\partial\left(\rho Y_i u_r\right)}{\partial r}+\frac{\partial\left(\rho Y_i u_x\right)}{\partial x}=\frac{\partial\left(J_{i,j}\right)}{\partial\left(x,r\right)}+R_i \tag{3.7}$$

where, $J_{i,j}$ is the molecular mass flux of species i, R_i is the net production rate of species i due to chemical reactions.

In this equation, the first term on the left represents the rate of mass change of species i, and the second and third term on the left express the net rate of mass decrease of species i due to convection. The terms on the right hand describe the net rate of mass increase of species i due to diffusion and the net rate of mass increase of species i due to source respectively.

The molecular mass flux of species normally includes mass diffusion, pressure diffusion and thermal diffusion [155]. In most combustion systems, only mass diffusion is considered [156]. Thus, the diffusion flux can be written using the Fick's law as:

$$J_{i,j}=-\rho D_i\frac{\partial Y_i}{\partial\left(x,r\right)} \tag{3.8}$$

where D_i is the diffusion coefficient of species i.

$$R_i=M_i\sum\nolimits_{r=1}^{n}R_{i,cr} \tag{3.9}$$

$$R_{i,cr}=K_{cr}\left(V''_{i,cr}-V'_{i,cr}\right)\prod\nolimits_{i=1}^{N}c_i^{a_{i,cr}} \tag{3.10}$$

$$K_{cr}=A_{cr}T^{b}exp\left(-E_{a,cr}/R_uT\right) \tag{3.11}$$

3.1.5 Equation of state

The gaseous mixture including reactants and products is assumed to be ideal gas. Therefore, the state equation can be expressed in the following form [157]:

$$p = \rho R_u T \sum_i^N \frac{Y_i}{M_i} \tag{3.12}$$

In this equation, T is the mixture temperature, M_i is the molecular weight of species i and R_u is the universal gas constant $(R_u = 8.1314\ KJ/Kmol \cdot K)$.

3.1.6 Equations of particles

Except for modelling the chemically reacting flow in the gas phase, the changing of solid fuel particles should also be included in pulverized fuel combustion. In the Euler-Lagrange approach, the particle phase is solved under the Discrete Phase Model (DPM).

The Newton's second law is the theoretical basis of the motion equation of discrete phase particle which is used to calculate its trajectory. It is given by [154]:

$$m_p \frac{du_p}{dt} = F_d \left(u_g - u_p\right) + g_x \left(\rho_p - \rho\right) \tag{3.13}$$

where m_p is the mass of the particle, u_p and u_g are the instantaneous velocity of the particle and gas respectively, ρ_p is the density of the particle, F_d represents the drag force and can be calculated as Eq. 3.14:

$$F_d = \frac{3\mu}{\rho_p d_p^2} \frac{C_D Re_p}{4} \tag{3.14}$$

$$C_D = c_1 + \frac{c_2}{Re_p} + \frac{c_3}{Re_p^2} \tag{3.15}$$

$$Re_p = \frac{\rho d_p \left|u_p - u_g\right|}{\mu_g} \tag{3.16}$$

where μ is the viscosity, μ_g is the gas viscosity, d_p is the diameter of the particle, C_D is the drag coefficient, Re_p is the relative Reynolds number, c_1, c_2 and c_3 are constants and the values are given by Morsi and Alexander [158].

The energy balance of the particle can be described as [159] [160]

$$\begin{aligned} m_p C_{p,p} \frac{dT_p}{dt} = \pi d_p \lambda Nu \left(T_g - T_p\right) + A_p \varepsilon_p S_b \left(\theta_R^4 - T_p^4\right) \\ + \frac{dm_p}{dt} h_{fg} - f_h \sum_i^N \frac{dm_p}{dt} H_{reac_{cr}} \end{aligned} \tag{3.17}$$

where, $C_{p,p}$ is the heat capacity of the particle, T_p and T_g are the particle temperature and gas phase temperature respectively, λ is the thermal conductivity of gas phase, Nu is the Nusselt number, A_p is the surface area of the particle, ε_p is the particle emissivity, S_b is the Stefan-Boltzmann constant $\left(5.67032 \cdot 10^{-8}\ W/m^2 \cdot K^4\right)$, θ_R is the radiation temperature, f_h is the fraction of heat absorbed by the particle, $H_{reac_{cr}}$ is the enthalpy of reaction cr, h_{fg} is the latent heat of devolatilizaiton. And the Nusselt number is calculated by [160]:

$$Nu = 2.0 + 0.6 \cdot Re_p^{1/2} \cdot \left(C_p \mu_g / \lambda\right)^{1/3} \tag{3.18}$$

In Eq. 3.17, the term on the left hand side represents the temporal rate of change in the sensible enthalpy of the particle. Further, the first and second terms on the right hand side show the heat transfer from the particle by the mechanisms of heat convection and radiation. The third term on the right hand side denotes the energy change during particle devolatilisation process. The last term on the right hand side represents the fraction of the enthalpy of heterogeneous reactions that is absorbed by the particle.

3.1.7 Turbulence model

The standard $k-\varepsilon$ model is the applied turbulence model in this work. It is proposed by Launder and Spalding and is a model based on the transport equations for the turbulence kinetic energy (k) and its dissipation rate (ε). The model transport equation for k is derived from the exact equation, while the model transport equation for ε was obtained using physical reasoning and bears little resemblance to its mathematically exact counterpart. The model transport equations for k and ε are given by ANSYS Fluent [154] and shown below.

$$\frac{\partial (\rho k)}{\partial t} + \frac{\rho k u}{\partial (x,r)} = \frac{\partial}{\partial (x,r)} \left[\left(\mu + \frac{\mu_t}{\sigma_k} \right) \frac{\partial k}{\partial (x,r)} \right] + G_k + G_b - \rho \varepsilon - Y_M \tag{3.19}$$

$$\frac{\partial (\rho \varepsilon)}{\partial t} + \frac{\rho \varepsilon u}{\partial (x,r)} = \frac{\partial}{\partial (x,r)} \left[\left(\mu + \frac{\mu_t}{\sigma_\varepsilon} \right) \frac{\partial \varepsilon}{\partial (x,r)} \right] + C_{1\varepsilon} \frac{\varepsilon}{k} \left(G_k + C_{3\varepsilon} G_b \right) - C_{2\varepsilon} \frac{\varepsilon^2}{k} \tag{3.20}$$

where σ_k and σ_ε are the turbulent Prandtl numbers for k and ε respectively, G_k is the generation of turbulent kinetic energy due to the mean velocity gradients, G_b is the generation of turbulence kinetic energy due to buoyancy, Y_M is the dissipation rate due to fluctuating dilatation in compressible flow. $C_{1\varepsilon}$, $C_{2\varepsilon}$ and $C_{3\varepsilon}$ are model constants. The default values for the constants are given by FLUENT [154].

3.1.8 Thermal radiation

In high-temperature combustion systems, heat transfer trough thermal radiation affects the combustion process largely and can not be negligible. It allows heat to be transferred from the gas mixture in high temperature to the surroundings which is cooler. This leads to changing in the combustion environment.

P-1 radiation model is based on spherical harmonic method and is a first order approximation to the radiative transport equation and is based on the expansion of radiation intensity I into an orthogonal series of spherical harmonics. This model has been widely used in particle combustion [159] [160]. In P-1 radiation model, the radiation flux Q_r is calculated using the following equation [154]:

$$Q_r = -\frac{1}{3\left(a+\sigma_s\right) - C\sigma_s} \bigtriangledown G \tag{3.21}$$

Here, a is the absorption coefficient, σ_s is the scattering coefficient, C_l is the linear-anisotropic phase function coefficient, and G is the incident radiation.
By introducing the parameter $\mathit{\Gamma} = 1/\left(3\left(a+\sigma_s\right) - C\sigma_s\right)$, Equation 3.21 can be simplified to [154]:

$$Q_r = -\mathit{\Gamma} \bigtriangledown G \tag{3.22}$$

And the transport equatin for G is:

$$\bigtriangledown \cdot \left(\mathit{\Gamma} \bigtriangledown G\right) = aG - 4aS_bT^4 \tag{3.23}$$

where S_b is the Stefan-Boltzmann constant $\left(5.67032 \cdot 10^{-8}\ W/m^2 \cdot K^4\right)$.
The weighted-sum-of-gray-gases model (WSGGM) is employed for determing the absorption coefficient of the gas phase. The WSGGM-cell based method, which calculates the mean beam length based on a characteristic cell size from the Computational Fluid Dynamics (CFD) model has been used.

3.2 Combustion model

The combustion of solid fuels is a multi-phase, multi-scale and multi-components process which includes complex chemical and physical phenomena. Normally, four physicochemical processes were considered during combustion of solid fuel particles [161]. These include devolatilisation of the particle, volatile (represented by CH_mO_n) combustion, char (represented by C(s)) oxidation and other gas phase reactions [161]. The combustion phenomena need to be considerably simplified for numerical simulations, the detailed combustion mechanism used in this work is described below.

3.2.1 Devolatilization

Firstly, the particles are heated by the hot surrounding gases and also thermal radiation from the walls and consequently they first release their moisture content (drying process). Then volatiles are released rapidly (devolatilisation process). In this study, the release of volatiles is described by the single rate model [162]. It is assumed that the rate of devolatilisation is first-order and depends on the amount of volatiles remaining in the particle and employs global kinetics [159]. The reaction and its kinetic rate are:

$$R_1 : coal, biomass \rightarrow \alpha\, volatile + (1-\alpha)\, char \tag{3.24}$$

$$k_d = Aexp\left(-E_a/RT\right) \tag{3.25}$$

where α is the distribution coefficient of volatile in coal or biomass.

3.2.2 Char combustion

Char is produced through the devolatilisation process and reacts with oxygen through the heterogeneous process of combustion and gasification. The combustion products are carbon dioxide CO_2 and carbon monoxide CO. The heterogeneous reactions are defined as [154] [163] [164]:

$$R_2 : C(s) + O_2 \rightarrow CO_2 \tag{3.26}$$

$$R_3 : C(s) + 0.5\, O_2 \rightarrow CO \tag{3.27}$$

$$R_4 : C(s) + CO_2 \rightarrow 2CO \tag{3.28}$$

The reactions of char oxidation to CO_2 (R_2) and CO (R_3) are exothermic and occur very rapidly, but the reduction reaction of CO_2 to CO (R_4) is endothermic. Another char-H_2O reaction is considered during the char combustion process where H_2O comes from the oxidation of volatile matter (R_6).

$$R_5 : C(s) + H_2O \rightarrow CO + H_2 \tag{3.29}$$

Then, the reaction rate K is defined as:

$$K = k_a C_{C_s} C_{rg} \tag{3.30}$$

where, C_{rg} is the concentration of the gaseous reactant, which is O_2 for R_2 and R_3, and CO_2 and H_2O for R_4 and R_5, respectively. k_a is the reaction rate constant given by the Arrhenius type relation:

$$k_a = AT^b exp\left(-E_a/R_u T\right) \tag{3.31}$$

The kinetic parameters of the chemical reactions are given in Table 3.1.

3.2.3 Homogeneous reactions

The combustion of volatile matter (vol) is an important homogeneous reaction in pulverized coal and biomass combustion process. The volatile matter is released during the devolatilization stage. The detailed chemical species in the volatile matter are not completely understood due to the complex chemical structure of coal and biomass [165]. For simplicity, the volatile matter is regarded as a single species which can be represented as CH_mO_n. The ratio of carbon (C), hydrogen (H) and oxygen (O) is determined by the ultimate analysis of the solid fuel and varies from the fuel type [160]. The chemical reaction is expressed as below:

$$R_6 : CH_mO_n + a_1O_2 \rightarrow CO_2 + a_2H_2O \tag{3.32}$$

Here, m and n is the calculated composition of hydrogen (H) and oxygen (O) containing in the volatile matter based on the type of coal and biomass. Therefore, the value of the stoichiometric coefficient a is given based on the mass conservation law in chemical reactions.

$$a_1 = (1 + m/4 - n/2) \tag{3.33}$$

$$a_2 = m/2 \tag{3.34}$$

Besides the homogeneous combustion of volatile matter, the oxidation of CO and H_2 to CO_2 and H_2O respectively are involved [166] [167]. The expressions of reactions are given as:

$$R_7 : CO + 0.5\,O_2 \rightarrow CO_2 \tag{3.35}$$

$$R_8 : H_2 + 0.5\,O_2 \rightarrow H_2O \tag{3.36}$$

The reaction rates of the homogeneous reactions are defined by:

$$K = AT^b exp\left(-E_a/R_uT\right)\left[C_{rg}\right]^d\left[C_{O_2}\right]^e \tag{3.37}$$

Here C_{rg} is the concentration of CH_mO_n for R_6, CO for R_7 and H_2 for R_8, respectively, and C_{O_2} is the concentration of oxygen. For the composition of volatile matter (CH_mO_n), the calculation method will be reported in Chapter 3 which is based on the ultimate and proximate analysis of coal and biomass. The kinetic parameters of the chemical reactions are given in Table 3.1.

Overall, six gaseous species are defined in this study: CH_xO_y, O_2, CO_2, CO, H_2O and N_2. Further, the reaction rates of the reactions R_2-R_5 is determined by a User-defined Function (UDF) that is exported to ANSYS Fluent. The other processes such as turbulence, turbulence-chemistry interaction, thermal radiation and devolatilization of particles are modelled by applying the existing sub-models in the solver. Table 3.1 presents the kinetic parameters related to the homogeneous reactions in summary.

Table 3.1: Chemical reactions kinetics constants

Reaction NO.	Reaction	Kinetic parameters			d	e	Ref.
		A	E	β			
R_1	coal $\rightarrow$ α volatile + $(1-\alpha)$ char biomass $\rightarrow$ α volatile + $(1-\alpha)$ char	3.12E+05	7.4E+07	-	-	-	[154]
R_2	$C(s) + O_2 \rightarrow CO_2$	0.002	7.9E+07	0	-	-	[154]
R_3	$C(s) + 0.5\ O_2 \rightarrow CO$	0.052	1.33E+08	0	-	-	[163]
R_4	$C(s) + CO_2 \rightarrow 2\ CO$	4.4	1.62E+08	1	-	-	[164]
R_5	$C(s) + H_2O \rightarrow CO + H_2$	1.33	1.47E+08	1	-	-	[164]
R_6	$CH_mO_n + a_1\ O_2 \rightarrow CO_2 + a_2\ H_2O$	2.12E+11	2.21E+08	-	0.2	1.3	[154]
R_7	$CO + 0.5\ O_2 \rightarrow CO_2$	1.30E+11	1.26E+08	-	0.5	0.5	[166]
R_8	$H_2O + 0.5\ O_2 \rightarrow H_2O$	5.69E+11	1.46E+08	-	1	0.5	[167]

The nitrogen and sulphur containing in the solid fuels are converted to pollutants including various nitrogen compounds such as NO, NH_3 and HCN, and sulphur compounds such as SO_2, H_2S and SO_3. The following sections present the theoretical background of NO_x and SO_x modelling.

3.3 NO_x model

The NO_x pollutants are formed through thermal-NO_x, prompt-NO_x and fuel-NO_x mechanisms during solid fuels combustion process. As discussed in section 1.2, prompt-NO_x has a negligible contributor to total NO_x emissions and can be ignored in pulverized coal and biomass combustion [168], only thermal-NO_x and fuel-NO_x are considered in this work.

3.3.1 Thermal NO_x

The formation of thermal NO_x is determined by a set of highly temperature-dependent chemical reactions known as the extended Zeldovich mechanism [169]. The principal reactions governing the formation of thermal NO_x from molecular nitrogen are as follows: The mechanism of Thermal-NO is proposed by Zelovich [169]. During the numerical modelling, the partial equilibrium approach for radicals O and OH concentrations is applied together. The reactions involving in thermal-NO are represented as below:

$$O + N_2 \xrightarrow{k_1} N + NO \tag{3.38}$$

$$O + N_2 \xleftarrow{k_2} N + NO \tag{3.39}$$

$$N + O_2 \xrightarrow{k_3} O + NO \tag{3.40}$$

$$N + O_2 \xleftarrow{k_4} O + NO \tag{3.41}$$

$$N + OH \xrightarrow{k_5} H + NO \tag{3.42}$$

$$N + OH \xleftarrow{k_6} H + NO \tag{3.43}$$

where k_1, k_3, k_5 represent the forward rate constants of the reactions, k_2, k_4, k_6 represent the backward rate constants, and O, H, N and OH are oxygen radical, hydrogen radical, nitrogen radical and hydroxyl radical. The rate constants of the reactions are calculated by the Arrhenius equation $k = AT^{\beta}exp(-E/R_uT)$. Fluent uses the values complied by Hanson and Salimian [170] as given in Table 3.2.

Table 3.2: Rate constants for thermal NO_x chemical reactions [170]

Rate constant	A	β	E
k_1	1.8E+08	0	38370
k_2	3.8E+07	0	425
k_3	1.8E+04	1	5680
k_4	3.8E+03	1	20820
k_5	7.1E+07	0	450
k_6	1.7E+08	0	24560

3.3.2 Fuel NO_x

Regarding fuel-NO_x, the nitrogen contained in the coal and biomass particles is assumed to be distributed between the volatile matter (vol-N) and the char (char-N), and is completely devolatilized during the combustion process [171]. This assumption is indicated by most experimental studies of coal pyrolysis [159] [172]. The split of nitrogen in the fuel into volatiles and char is essential for NO_x formation. Therefore, when modelling fuel-NO_x in coal and biomass combustion system, nitrogen release during both the devolatilization and char oxidation stages need to be considered.

The nitrogen released from the fuel particles converts to NO_x pollutants through the intermediates HCN and NH_3 (shown in Fig. 3.1) [173] [174]. For the nitrogen contained in the volatile matter, it is through the intermediates HCN and NH_3 firstly and then reacts with oxygen to form NO partly. For nitrogen contained in the char, two variations of fuel-NO_x pathways [175] [176] are considered. The first mechanism assumes that the nitrogen contained in the char fully converted to the intermediates HCN and NH_3 which are then converted to NO partially (Figures 3.1(a) and 3.1(b)). The assumption of the second mechanism is that the char-N completely converts to NO directly (Figures 3.1(c) and 3.1(d).

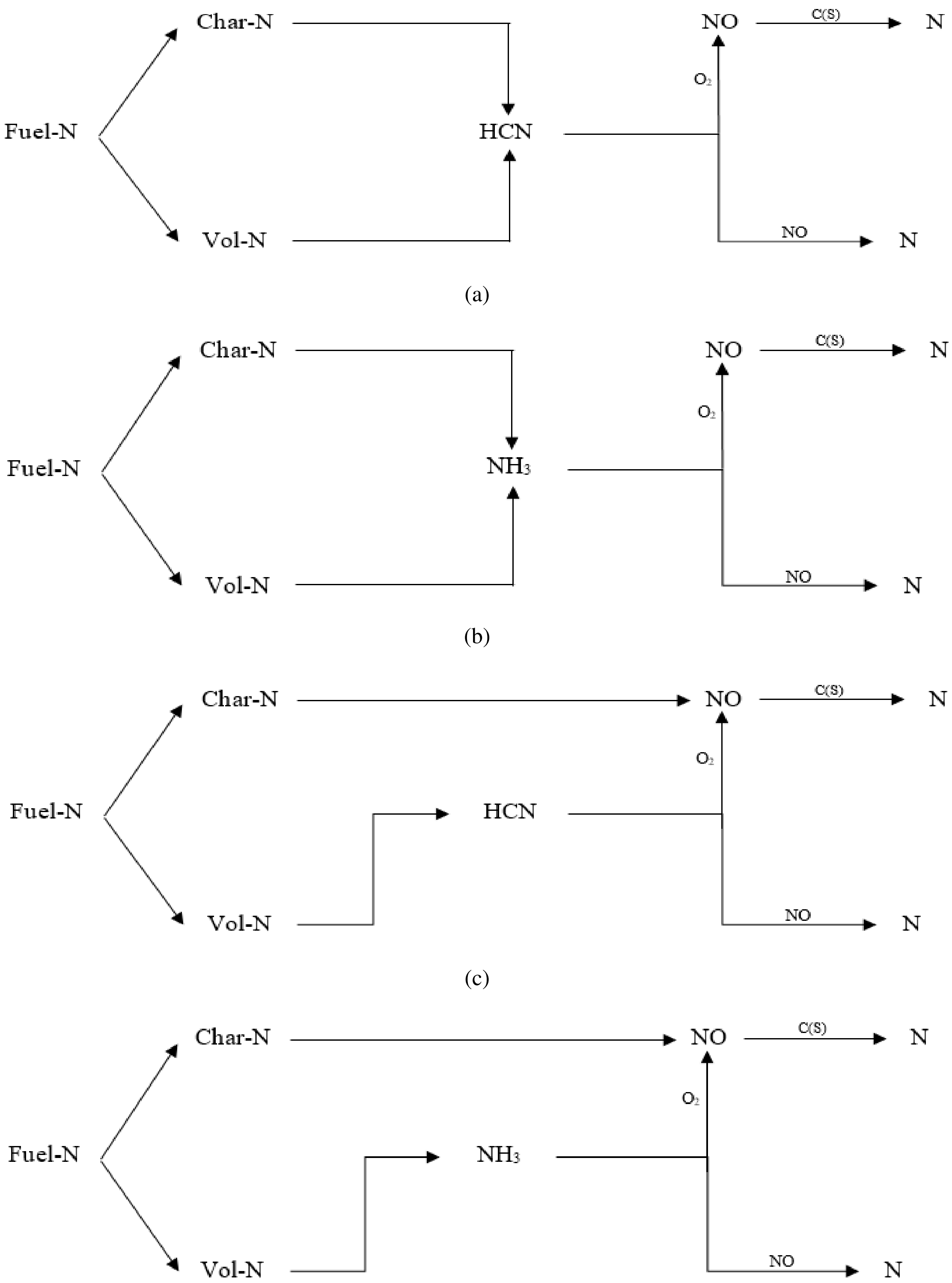

(d)

Figure 3.1: Fuel-NO pathways [175] [176]

The reactions involved in NO formation fuel-NO$_x$ are shown as follows:

$$HCN + O_2 \xrightarrow{k_7} NO + \cdots \tag{3.44}$$

$$NH_3 + O_2 \xrightarrow{k_8} NO + \cdots \tag{3.45}$$

$$HCN + NO \xrightarrow{k_9} N_2 + \cdots \tag{3.46}$$

$$NH_3 + NO \xrightarrow{k_{10}} N_2 + \cdots \tag{3.47}$$

The rate of conversion of HCN and NH$_3$ are given by De Soete [177] as described below:

$$k_7 = A_1 X_{HCN} X_{O_2}^a exp(-E_1/RT) \tag{3.48}$$

$$k_8 = A_2 X_{NH_3} X_{O_2}^a exp(-E_2/RT) \tag{3.49}$$

$$k_9 = A_3 X_{HCN} X_{NO} exp(-E_3/RT) \tag{3.50}$$

$$k_{10} = A_4 X_{NH_3} X_{NO} exp(-E_4/RT) \tag{3.51}$$

where X is the mole fraction of related species, a is the oxygen reaction order and T is the instantaneous temperature. The kinetics of these reactions are given in Table 3.3 and the oxygen reaction order is taken from Table 3.4.

Table 3.3: Reaction kinetics for fuel NO$_x$ chemical reactions [177]

Rate of reaction	A	E
k_7	1.0E+10	280451.95
k_8	4.0E+06	133947.2
k_9	3.0E+12	251151
k_{10}	1.0E+08	113017.95

Table 3.4: Oxygen reaction order for fuel NO$_x$ chemical reactions [177]

Oxygen mole fraction	a
$X_{O_2} \leq 0.0041$	1
$0.0041 \leq X_{O_2} \leq 0.0111$	-3.95 - $0.9 ln X_{O_2}$
$0.011 \leq X_{O_2} \leq 0.03$	-0.35 - $0.1 ln X_{O_2}$
$X_{O_2} \geq 0.03$	0

3.4 SO$_x$ model

The oxidation of fuel-bound sulphur is the only source of SO$_x$ emissions. During coal and biomass combustion, some of the sulfur is released as H$_2$S, COS, SO$_2$ and CS$_2$ when devolatilizaiton happens, while rest of the sulfur is retained in the char to be oxidized at a later stage. SO_2 and SO_3 are the final products of oxidization. For low sulfur fuels, the sulfur is regarded to mainly release as H_2S. An eight-step mechanism [178] together with one SO_3 formation reaction [179] are used to describe the reaction mechanisms for sulphur oxidation. Table 3.5 lists the detailed reactions with the rate constants (for a rate constant $k = AT^b exp(-E/RT)$). Here, M represents nitrogen or oxygen in the gaseous environment. For the calculations, the concentrations of [O] and [OH] have been calculated through partial equilibrium assumptions based on [O_2] and [H_2O] concentrations, respectively. The concentration of [H] is assumed to be proportional to the concentration of O radical, which can be evaluated from one of the existing methods in ANSYS Fluent [154].The species N_2 is used as the dilutant.

Table 3.5: Mechanism for SO_x formation [178] [179]

Reaction	A	b	E
$H_2S + H \rightarrow SH + H_2$	1.82E+07	0	7.48E+03
$H_2S + H \leftarrow SH + H_2$	9.37E+06	0	6.25E+04
$OH + H_2S \rightarrow H_2) + SH$	1.38E+02	0	3.74E+03
$OH + H_2S \leftarrow H_2) + SH$	3.11E+07	0	1.22E=05
$SO + OH \rightarrow H + SO_2$	1.62E+08	0	2.56E+03
$SO + OH \leftarrow H + SO_2$	7.69E+09	0	1.19E+05
$SH + O \rightarrow SO + H$	3.55E+08	0	2.69E=03
$SH + O \leftarrow SO + H$	2.99E+09	0	1.69E+05
$O + H_2S \rightarrow SH + OH$	4.36E+03	0	1.38E+04
$O + H_2S \leftarrow SH + OH$	9.88E+08	0	6.04E+04
$SO + O_2 \rightarrow SO_2 + O$	4.47E+05	0	2.70E+04
$SO + O_2 \leftarrow SO_2 + O$	1.66E+06	0	7.61E+04
$H + SH + M \rightarrow H_2S$ + M	1.10E+03	0	0
$H + SH + M \leftarrow H_2S$ + M	8.67E+14	0	3.82E+05
$SO + O \rightarrow SO_2$	4.47E+05	0	2.70E+04
$SO + O \leftarrow SO_2$	1.67E+06	0	7.61E+04
$SO + O + M \rightarrow SO_2$ + M	8.71E+09	-1.8	4.12E+03
$SO + O + M \leftarrow SO_2$ + M	1.91E+14	0	5.21E+05
$SO_2 + O \rightarrow SO_3$	3.63E+12	0	4.12E+03
$SO_2 + O \leftarrow SO_3$	7.41E+14	0	-3.46E+05

3.5 Derivation of gas-phase entropy generation

The derivation of gas-phase entropy generation is based on the ideal gases assumption. Thus, here we have the following equation regarding the specific chemical potential $\mu_{c,i}$, the specific enthalpy h_i and the partial specific entropy s_i for the ith species and its gradient form:

$$\mu_{c,i} = h_i - Ts_i \tag{3.52}$$

$$\bigtriangledown\mu_{c,i} = \bigtriangledown h_i - T\bigtriangledown s_i - s_i\bigtriangledown T \tag{3.53}$$

where

$$h_i = h_i^0 + \int_{T^0}^{T} c_{p,i}dT \tag{3.54}$$

$$s_i = s_i^0 + \int_{T^0}^{T} \frac{c_{p,i}}{T}dT - R_i\ln\frac{p}{p^0} - R_i\ln X_i \tag{3.55}$$

where h_i^0 and s_i^0 are the specific heat of formation and entropy at the referenced temperature T^0 and pressure p^0, $c_{p,i}$ is the specific heat capacity, $p_i = X_i p$ is the partial pressure, and $R_i = R_u\,W_i$ is the specific gas constant of the ith species.

Combining Eq. 3.53, Eq. 3.54, Eq. 3.55 and the equation of ideal-gas state, we can have the following equation:

$$-\bigtriangledown h_i + T\bigtriangledown s_i = -\frac{1}{\rho_i}\left(p\bigtriangledown X_i + X_i\bigtriangledown p\right) \tag{3.56}$$

The gas-phase entropy generation term is derived through the way described by Pope [120] and Hirschfelder [155]. Firstly, the vector form of the conservation equations of energy (Eq. 3.57), species (Eq. 3.58) and continuity (Eq. 3.59) presented by Williams [180] are introduced:

$$\rho\frac{Du}{Dt} = -\bigtriangledown\cdot\vec{q} - p\left(\bigtriangledown\cdot\vec{v}\right) + \Phi + \rho\sum_{i=1}^{N} Y_i\vec{f}_i\cdot\vec{V}_i \tag{3.57}$$

$$\rho\frac{DY_i}{Dt} = \omega_i - \bigtriangledown\cdot\left(\rho Y_i\vec{V}_i\right) \tag{3.58}$$

$$\frac{D\rho}{Dt} + \rho\bigtriangledown\cdot\vec{v} = 0 \tag{3.59}$$

where ρ and u is the density and internal energy of the gas mixture, $\vec{q}$ is the heat flux vector, $\vec{v}$ is the velocity vector, Φ is the viscous dissipation, Y_i is the mass fraction of the ith species, $\vec{f}_i$ is the body force per unit mass, $\vec{V}_i$ is the diffusion velocity of the ith species and ω_i is the mass production rate of the ith species per unit volume.

Hirschfelder [155] also presented the change in specific entropy as:

$$\rho\frac{Ds}{Dt} = -\bigtriangledown\cdot\vec{s} + \sigma \tag{3.60}$$

The relationship between the change of specific internal energy e and change of the specific entropy s based on the Gibbs equation is described as:

$$Tds = de + pd\left(\frac{1}{\rho}\right) - \sum_i \mu_{c,i}dY_i \tag{3.61}$$

Applying differential change in the applicable parameters, then the Gibbs equation can be written as:

$$T\frac{\partial s}{\partial t} = \frac{\partial e}{\partial t} - \frac{p}{\rho^2}\frac{\partial \rho}{\partial t} - \sum_i \mu_{c,i}\frac{\partial Y_i}{\partial t} \tag{3.62}$$

Substituting the the vector form of the conservation equations of energy (Eq. 3.57), species (Eq. 3.58) and continuity (Eq. 3.59) into Eq. 3.62, it gives:

$$T\frac{Ds}{Dt} = -\frac{1}{\rho}\triangledown\cdot\vec{q} + \frac{\Phi}{\rho} + \sum_i Y_i\vec{f_i}\vec{V_i} - \frac{1}{\rho}\sum_i \mu_{c,i}\left[\omega_i - \triangledown\cdot\left(\rho Y_i\vec{V_i}\right)\right] \tag{3.63}$$

Multiplying $\frac{\rho}{T}$ with Eq. 3.63 leads to:

$$\rho\frac{Ds}{Dt} = -\frac{1}{T}\triangledown\cdot\vec{q} + \frac{\Phi}{T} + \frac{\rho}{T}\sum_i Y_i\vec{f_i}\vec{V_i} - \frac{1}{T}\sum_i \mu_{c,i}\left[\omega_i - \triangledown\cdot\left(\rho Y_i\vec{V_i}\right)\right] \tag{3.64}$$

Here, the second term and last term in Eq. 3.64 can be rewritten in the following forms:

$$-\frac{1}{T}\triangledown\cdot\vec{q} = -\triangledown\left(\frac{\vec{q}}{T}\right) - \frac{\vec{q}}{T^2}\cdot\triangledown T \tag{3.65}$$

$$\begin{aligned} -\frac{1}{T}\sum_i \mu_{c,i}\triangledown\cdot\left(\rho Y_i\vec{V_i}\right) = \triangledown\cdot\frac{1}{T}\sum_i\left(\mu_{c,i}\rho Y_i\vec{V_i}\right) + \frac{1}{T^2}\sum_i\left(\mu_{c,i}\rho Y_i\vec{V_i}\right)\cdot\triangledown T \\ -\frac{1}{T}\sum_i \rho Y_i\vec{V_i}\cdot\triangledown\left(\mu_{c,i}\right) \end{aligned} \tag{3.66}$$

Substituting the new forms into Eq. 3.64, we can get:

$$\begin{aligned} \rho\frac{Ds}{Dt} = -\triangledown\cdot\left[\left(\frac{\vec{q}}{T}\right) - \frac{1}{T}\sum_i \mu_{c,i}\rho Y_i\vec{V_i}\right] - \frac{\vec{q}}{T^2}\cdot\triangledown T + \frac{\Phi}{T} \\ +\frac{\rho}{T}\sum_i Y_i\vec{f_i}\cdot\vec{V_i} - \frac{1}{T}\sum_i \mu_{c,i}\omega_i + \frac{1}{T^2}\sum_i\left(\mu_{c,i}\rho Y_i\vec{V_i}\right)\cdot\triangledown T \\ -\frac{1}{T}\sum_{i=1}\rho Y_i\vec{V_i}\cdot\triangledown\left(\mu_{c,i}\right) \end{aligned} \tag{3.67}$$

Comparing Eq. 3.60 and Eq. 3.67, the expressions of the entropy flux $\vec{s}$ and the entropy generation rate per unit volume σ can be described as:

$$\vec{s} = \left(\frac{\vec{q}}{T}\right) - \frac{1}{T}\sum_i \mu_{c,i}\rho Y_i\vec{V_i} \tag{3.68}$$

$$\begin{aligned} \sigma = -\frac{\vec{q}}{T^2}\cdot\triangledown T + \frac{\Phi}{T} + \frac{\rho}{T}\sum_i Y_i\vec{f_i}\cdot\vec{V_i} - \frac{1}{T}\sum_i \mu_{c,i}\omega_i \\ +\frac{1}{T^2}\sum_i\left(\mu_{c,i}\rho Y_i\vec{V_i}\right)\cdot\triangledown T - \frac{1}{T}\sum_i \rho Y_i\vec{V_i}\cdot\triangledown\left(\mu_{c,i}\right) \end{aligned} \tag{3.69}$$

Further, Eq. 3.69 can be simplified to:

$$\sigma = -\frac{\vec{q}}{T^2} \cdot \bigtriangledown T + \frac{\Phi}{T} + \frac{1}{T} \sum\nolimits_i \rho Y_i \vec{V}_i \cdot \left(\vec{f}_i + \frac{\mu_{c,i}}{T} \bigtriangledown T - \bigtriangledown \mu_{c,i} \right) - \frac{1}{T} \sum\nolimits_i \mu_{c,i} \omega_i \tag{3.70}$$

Here, we make some simplifying assumptions to continue the derivation of gas-phase entropy generation: (1) The gravity ($\vec{g}$) is the only external body force per unit mass considered in this work and other body forces are negligible: $\vec{f}_i = \vec{g}$; (2) The effect of pressure gradient is ignored; (3) The irreversibility due to Dufour and Soret effects is also negligible; (4) The radiation heat transfer is ignored.

Therefore we can define the heat flux $\vec{q}$ as:

$$\vec{q} = -\lambda \bigtriangledown T + \rho \sum\nolimits_i Y_i \vec{V}_i h_i \tag{3.71}$$

And the equation of velocity diffusion is:

$$\bigtriangledown X_i = \sum_{j=1;j\neq i}^{N} \left(\frac{X_i X_j}{D_{ij}} \right) \left(\vec{V}_j - \vec{V}_i \right) + \sum_{j=1;j\neq i}^{N} \left(\frac{X_i X_j}{D_{ij}} \right) \left(\frac{D_{T,j}}{\rho_j} - \frac{D_{T,i}}{\rho_i} \right) \left(\frac{\bigtriangledown T}{T} \right) \tag{3.72}$$

where the subscripts i and j represents the species, D_{ij} is the binary diffusion coefficient for the $i-j$ species pair, $D_{T,i}$ and $D_{T,j}$ is the thermal diffusion coefficient for the referred species.

Substituting Eq. 3.56, Eq. 3.71 and Eq. 3.72 into Eq. 3.70 and rewriting, it results in:

$$\sigma = \frac{\lambda}{T^2} (\bigtriangledown T)^2 - \frac{\rho R_u}{\overline{W}} \sum\nolimits_i V_i \cdot \bigtriangledown X_i - \frac{1}{T} \sum\nolimits_i \mu_{c,i} \omega_i \tag{3.73}$$

The three terms on the right of Eq. 3.73 represent the entropy generation rate per unit volume caused by heat transfer (σ_h), mass transfer (σ_m) and chemical reactions (σ_{cr}). And the individual terms are:

$$\sigma_h = \frac{\lambda}{T^2} (\bigtriangledown T)^2 \tag{3.74}$$

$$\sigma_m = -\frac{\rho R_u}{\overline{W}} \sum\nolimits_i V_i \cdot \bigtriangledown X_i \tag{3.75}$$

$$\sigma_r = -\frac{1}{T} \sum\nolimits_i \mu_{c,i} \omega_i \tag{3.76}$$

Using the expression of V_i mentioned in Ref. [181]: $V_i = -\frac{D_{im}}{Y_i} \bigtriangledown Y_i$, the entropy generation rate per unit volume due to mass transfer (σ_m) can be rewritten as:

$$\sigma_m = \frac{\rho R_u}{\overline{W}} \sum\nolimits_i \left(\frac{D_{im}}{Y_i} \right) \cdot \bigtriangledown X_i \tag{3.77}$$

Defining S_E as the effective area considering irreversibility changes during the transient combustion process, the gas-phase entropy generation rate for the whole system at any moment is given by:

$$E_S = \int \sigma dS_E \tag{3.78}$$

And the entropy generation rates due to heat transfer (E_h), mass transfer (E_m) and chemical reactions (E_r) can be obtained by substituting the corresponding entropy generation rates per unit volume:

$$E_h = \int \sigma_h dS_E \tag{3.79}$$

$$E_m = \int \sigma_m dS_E \tag{3.80}$$

$$E_r = \int \sigma_r dS_E \tag{3.81}$$

In this work, a single coal or biomass particle was released into a drop-tube furnace and then ignited and combust under the high temperature of around 1400K. Here, particle life time $\left(t_{pl}\right)$ accounts for the time from the release of the particle to the extinction of the particle. The average entropy generation rate over the particle life time $\left(E_S^{'}\right)$ can be calculated using the equation below:

$$E_S^{'} = \frac{1}{t_{pl}} \int_0^{t_{pl}} E_S dt \tag{3.82}$$

3.6 Experimental setup

The experimental setup showing the air flow, ignition and main body on the smouldering combustion of biomass packed bed is presented in Figure 3.2. During operation, the air flow firstly goes through the air filter regulator and the air mass flow controller. After these two devices, the filtered and regulated air is obtained and it then enters the main body. The main body is a mild steel concave box. The ignition plate which consists of honeycomb ceramic plates and resistance wires is placed in the main body and a high temperature resistance glass plate that matches the size of the concave box is placed on the top to make the system closed. The ignition plate that is consisted of several ceramic honeycomb plates and resistance wires is placed in the main body. The resistance wires are used to heat the ceramic plates when they are connected to DC power. The fuel box filling with biomass particles is closely next to the ignition plate. Thermocouples are used to measure the temperature of the ignition plate and biomass packed bed and the data is collected by a thermocouple data logger. The gaseous products of smouldering combustion can exhaust from the holes left at the bottom of the main body. In order to reduce the heat loss of the system, several layers of thermal insulation films are applied to cover the mild steel body.

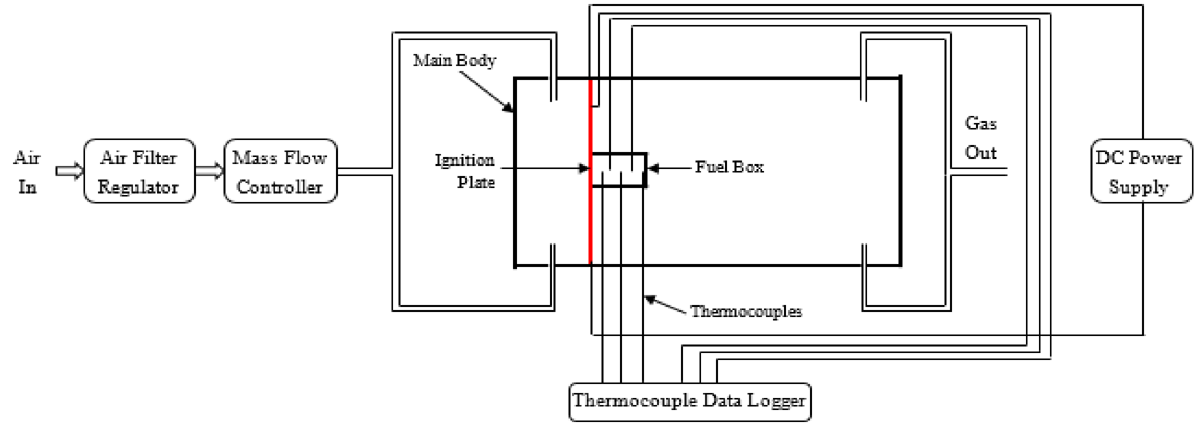

(a) Schematic view of experimental setup

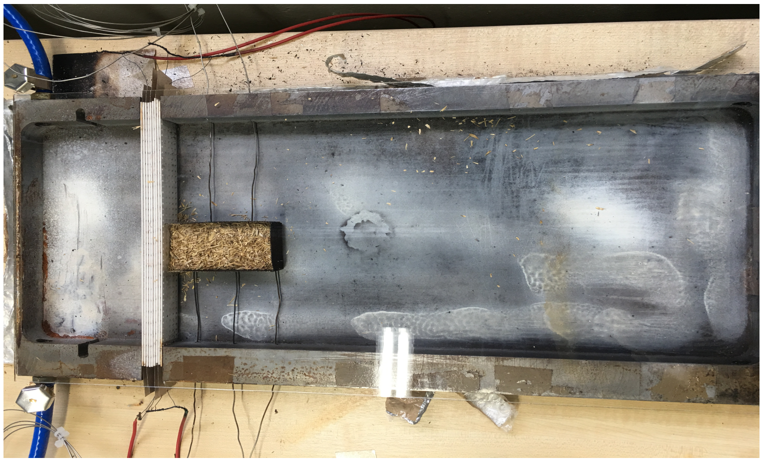

(b) Image of the real rig

Figure 3.2: The experimental setup for biomass packed bed smouldering combustion.

3.6.1 Main body

A mild steel concave box is the main body of the experimental rig. This concave box is 510mm in length, 260mm in width and 30mm in depth. Holes in suitable sizes for thermocouples and air-in and air-out tubes are left when processing. The technical drawing of the main body is shown in Figure 3.3. A fuel box with the size of 100mm in length, 60mm in width and 25mm in depth is placed close to the ignition plate and in the central line of the concave box. In order to close the system and make the smouldering combustion process visible, a high temperature resistance quartz glass plate that matches the size of the concave box is placed on the top. Clear fused quartz glass is a unique material with an unrivalled combination of purity, high temperature resistance, thermal shock resistance, high electrical insulation, optical transparency and chemical inertness.

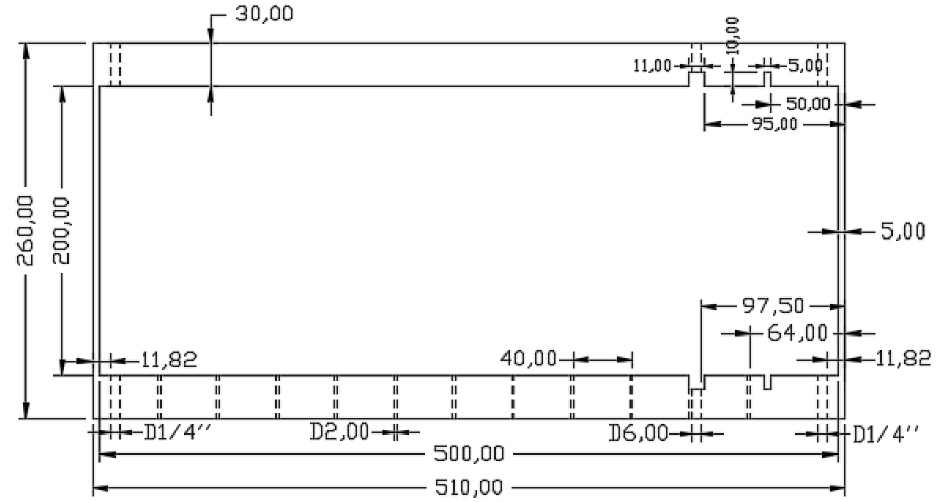

(a) Top view

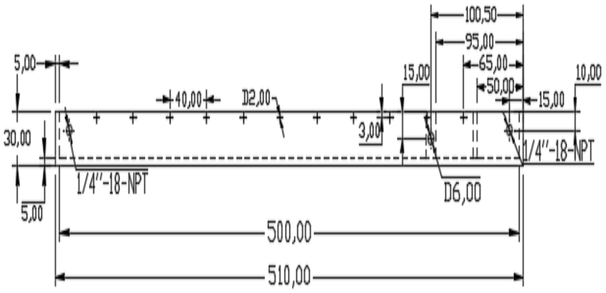

(b) Front view

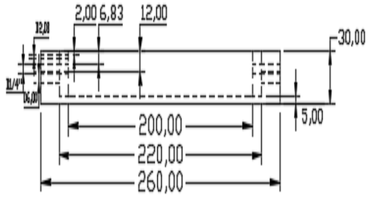

(c) Left view

Figure 3.3: The technical drawing of main body part.

3.6.2 Air flow unit

The air flow is supplied by the air supply system in the laboratory. The gas tube is first connected with an air filter regulator and followed by a mass flow controller. The air filter regulator is SMC AW20-F02 and shown in Fig. 3.4a. Air leaving a compressor is hot, dirty, and wet which can damage and shorten the life of downstream equipment. The air filter regulator is applied to remove water vapour, oil and dust from air to make it ready for use. The operating pressure and temperature of the air filter regulator is 0.3-1.0MPa and 0-60°C. The pressure of output air is between 0.05 and 0.7MPa. The air mass flow controller is a device used to measure and control the flow of fluids (liquids or gases). ALICAT MC-20SLPM-D/5M (Fig. 3.4b), which can provide responsive and stable control in 50ms is applied here. The specified air flow rate can be set in the air mass flow controller and the required amount of air during the experiment goes through the controller and enter the main body. Therefore, by applying air filter regulator and air mass flow controller, clean and quantitative air can be supplied to the system.

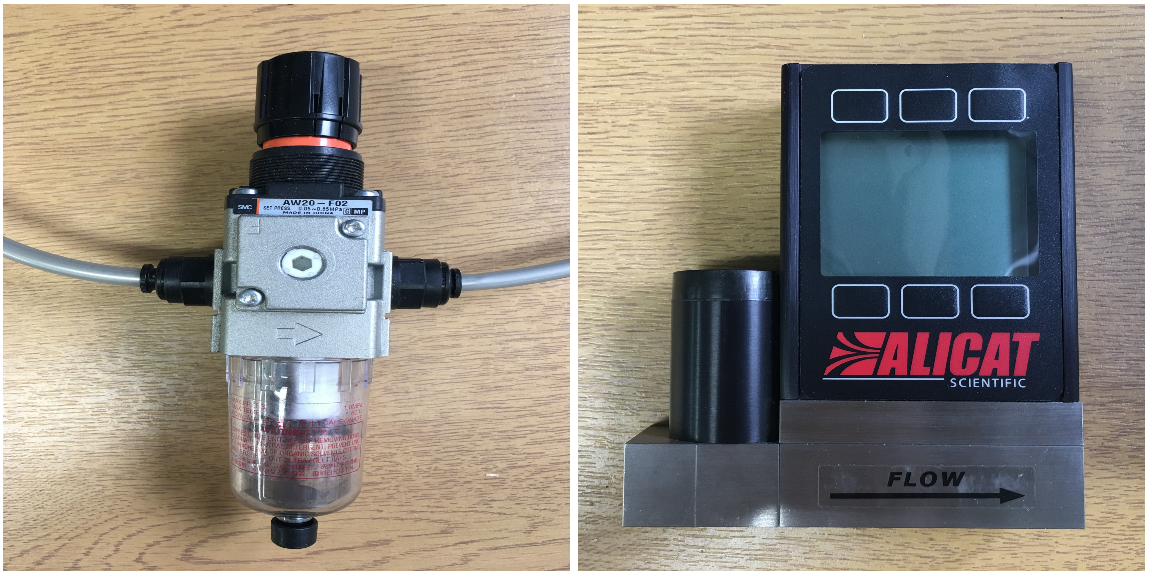

(a) Air filter regulator (b) Mass flow controller

Figure 3.4: Air flow unit.

3.6.3 Ignition unit

The required temperature of the ignition plate is 220°C-300°C for the smouldering combustion experiments. As the main body is made of mild steel, which is electrically conductive, materials with high properties of electrical insulativity and thermal conductivity are needed for the ignition unit to reduce the output of DC power supply. A combination of several honeycomb ceramic plates and resistance wires are selected to compose the ignition plate. The ceramic plate is made of Aluminium Nitride (AlN) ceramic. The AlN ceramic has reliable insulation and excellent thermal conductivity. The AlN ceramic plates are processed to honeycomb shaped plates (Fig. 3.5a). The honeycomb structure aims at letting the air go through and becoming uniform when getting to the fuel. The ceramic plate is 232mm in length, 24mm in width and 1mm in thickness. The diameter of the holes in the ceramic plates is 2mm.

Resistance wires and DC power are other two important components of the ignition unit. The resistance wires are inserted across the holes in the honeycomb plates and then are connected to DC power supply. Thus, a pure resistor element circuit is formed and the resistance wires can be

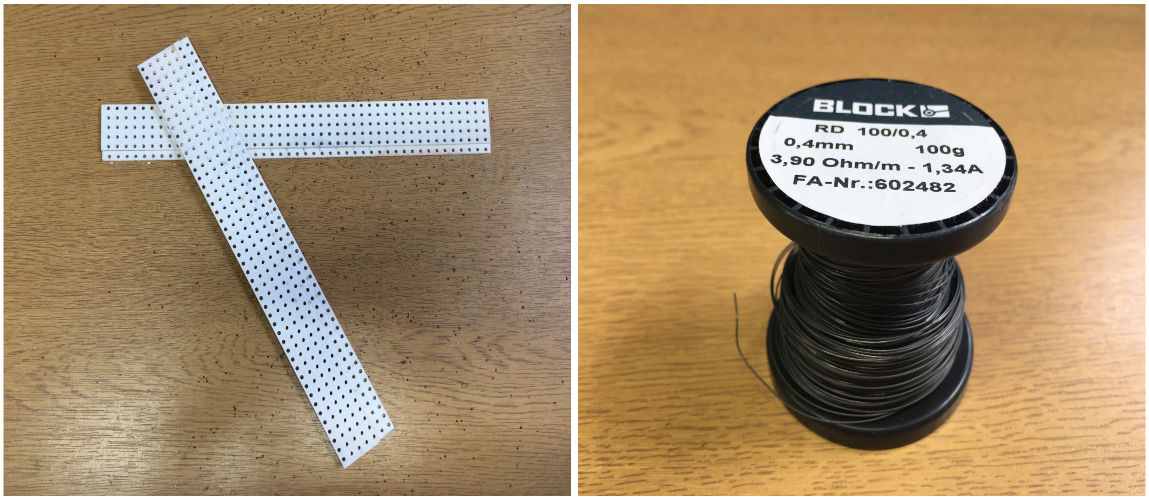

(a) Ceramic plates (b) Resistance wire

(c) DC power

Figure 3.5: Ignition unit.

regarded as heating wires. Therefore, the ceramic plates can achieve the required temperature with specified voltage and current supply and can be used to ignite the biomass packed bed. The resistance wire used in this work is Block RD 100/0.4 (Fig. 3.5b). The diameter of the resistance wire is 0.4mm and the resistance is $3.9\Omega/m$. The DC power supply applied here is Rapid NP-9625-209G with output voltage 0-30V and output current 0-10A (Fig. 3.5c).

3.6.4 Temperature measurement unit

The experiments of smouldering combustion of biomass packed bed are conducted under the ignition temperature 220°C, 250°C and 280°C. In order to track the temperature of the ignition plate and the biomass packed bed, mineral insulated thermocouples in Type K-310 Stainless Steel are used. When measuring the temperature of the biomass packed bed during smouldering combustion process, five thermocouples are used. The first one is placed 15mm away from the ignition plate and the distance between the thermocouples is 15mm as well (Fig. 3.2b). A

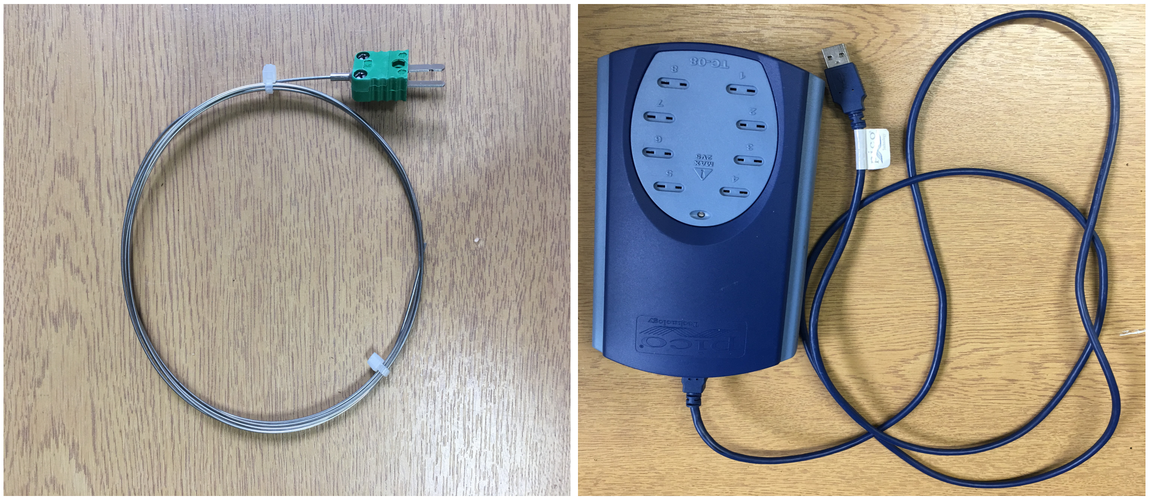

(a) Thermocouple (b) Data logger

Figure 3.6: Temperature measurement unit.

Pico TC-08 Thermocouple Data Logger (Fig. 3.6b) is used to collect the real time data. The temperatures at measured points are recorded every second during the smouldering combustion process.

Chapter 4

Evolution of the transient process of single particle combustion

This chapter presents the numerical modelling work of the combustion process of single coal and biomass particle in a drop-tube furnace under various gas conditions. A lignite coal (DECS-11) and a kind of biomass (Bagasse) are used in this work. Both active flow and non-active flow are applied to the single particle combustion. The oxygen concentrations vary from 20% to 100% in nitrogen (N_2) or carbon dioxide (CO_2) environments. The numerical results are compared against with existing experimental data to validate the numerical model. The particle mass loss and position during the combustion process are tracked to investigate the particle combustion process under different gas conditions. The evolution of gaseous species is obtained to look into the unsteady heat and mass transfer phenomena.

4.1 Fuel Properties

The coal sample was from the Pittsburgh Coal bank and the biomass sample are from a production plant Sugarcane in Brazil. The proximate and ultimate analysis of the coal DECS-11 and the biomass Bagasse in the work are given in Table 4.1 [37]. In order to simplify the numerical modelling, the molecular formulas of the two kinds of fuels have been simplified into a form with dry ash free (DAF) basis. The contents of Nitrogen (N), Sulphur (S) and Sodium (Na) are ignored. For lignite coal DECS-11 on DAF basis, there is 62% volatile matter and 38% fixed carbon (char) with the proximate analysis. The elemental composition of the coal DECS-11 on DAF basis is 74.55% Carbon (C), 4.5% Hydrogen (H) and 20.95% Oxygen (O), respectively. The relative proportion composition of the volatile is determined by assuming that its mass is 62% of 1 kg of the DAF composition. Thus: $0.62 = (x/100)\ C + (4.5/100)\ H + (20.95/100)\ O$, then $x = 36.55\%$. The elemental composition of volatile matter is $C_{36.55/12}H_{4.5/1}O_{20.95/16}$ and it can be written as $CH_{1.48}O_{0.43}$. The molecular weight of the volatile matter is 20.36 $kg/kmol$.

Table 4.1: Proximate and ultimate analysis of the fuel [37]

Fuel Type	DECS-11 Lignite	Bagasse Sugarcane residue
Proximate analysis as received		
Moisture (%)	33.4	4.4
Volatile Matter (%)	37.4	83.9
Fixed Carbon (%)	22.9	7.7
Ash (%)	6.4	4.0
Ultimate analysis (Dry basis)		
Carbon (%)	66.2	44.3
Hydrogen (%)	4.0	5.7
Oxygen (%)	18.6	45.5
Nitrogen (%)	0.9	0.2
Sulfur (%)	0.7	0.07
Sodium (%)	0.66	-
Ash (%)	9.6	4.2
Lower Heating Value (MJ/kg)	25.7	16.3

The lower heating value of volatile matter (LHV_{vol}) is calculated with the following equation:

$$LHV_{vol} = \frac{LHV_{coal} - F_C * LHV_C}{F_{vol}} \tag{4.1}$$

Here, F_C and F_{vol} represent the mass fraction of char and volatile matter in the coal, and LHV_{coal} and LHV_C are the lower heating value of the coal and the char, respectively. And LHV_C is regarded to be equal to the value of fixed carbon (32900KJ/kg). Thus, we have: $LHV_{vol} = (25700\ -\ 0.38 \times 32900)/0.62 = 21287.1\ KJ/kg$. Then $LHV_{vol} = 21287.1 \times 20.36 = 433405.2903\ KJ/kmol$.

Therefore, the oxidation of volatile matter of the coal DECS-11 particle can be represented by $CH_{1.48}O_{0.43}\ +\ 1.55\ O_2\ \rightarrow\ CO_2\ +\ 0.74\ H_2O$. The enthalpy of the volatile can be calculated by the enthalpy change between the products and reactants. This is represented as:

$$H_{reac} = \sum h_{products} - \sum h_{reactants}, \tag{4.2}$$

where H_{reac} is the heat of reaction and is equal to the lower heating value of the volatile matter (LHV_{vol}), $h_{products}$ and $h_{reactants}$ are the enthalpy of formation of products and reactants, respectively. The value of enthalpy of the species O_2, CO_2 and H_2O are obtained from Fluent Database and they are 0, $3.935*10^5$ $KJ/kmol$ and $2.418*10^5$ $KJ/kmol$, respectively [154]. Thus, the value of enthalpy of the volatile matter is: $h_{vol} = LHV_{vol} - [1 \times h_{CO_2} + 0.74 \times h_{H_2O}]$, then $h_{vol} = -1.3909 \times 10^5$ $KJ/kmol$.

The molecular formula, molecular weight and enthalpy of the biomass Bagasse particle are obtained by following the above steps. The volatile matter of Bagasse can be represented as $CH_{1.89}O_{0.94}$, and the molecular weight is 28.93 $Kg/kmol$. The value of enthalpy is -1.9455×10^5 KJ/kmol which is based on the following volatile oxidation reaction: $CH_{1.89}O_{0.94} + 1.0025\, O_2 \rightarrow CO_2 + 0.945\, H_2O$.

4.2 Model geometry and operating conditions

The basic configuration of the reactor used in this work was taken from the Ref. [37] (see Fig. 4.1). The single coal and biomass particles were released at the top of the furnace and free-falling into the radiation zone where the particles were ignited and combust. The drop-tube reactor is represented by a 2D axisymmetric shape geometry as reported in Fig. 4.1b with the inlet diameter of 70mm and the hot wall length of 250mm. The operating conditions are shown in Table 4.2.

Some assumptions are made in order to simplify the modelling: (1) the gas phase is treated as an ideal-gas mixture, (2) the coal and biomass particles are assumed to be spherical in shape, (3) the interactions between the particles are neglected.

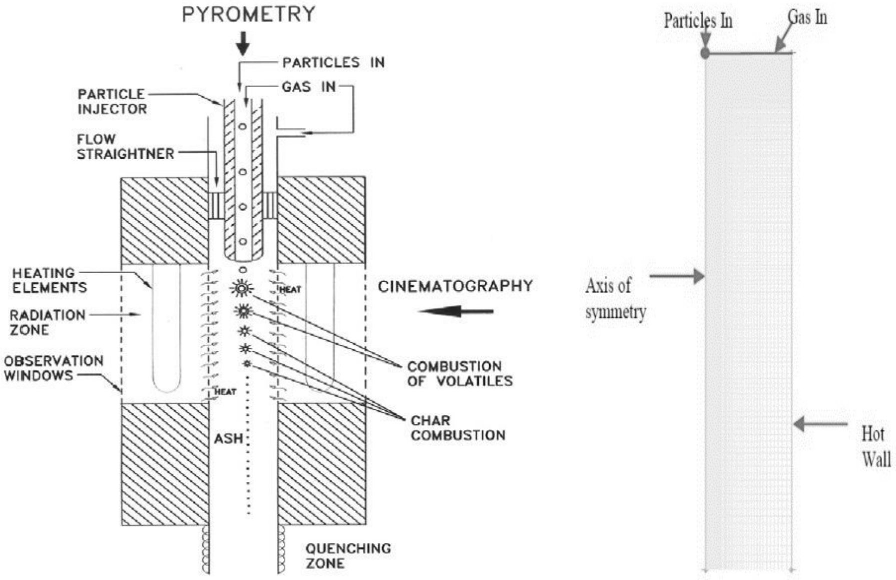

(a) Experimental setup [37] (b) Computational domain

Figure 4.1: Schematic view of experimental setup [37] and computational domain.

Table 4.2: Operating Conditions [37]

Parameters	Values	
	Quiescent Flow	Active Flow
Wall temperature	1400K	1400K
Temperature of injecting gas	1200K	1200K
Velocity of gas	0	4.55cm/s
Diameter of particles	80μm	80μm
Initial temperature of particles	750K	1050K
Velocity of particles	15cm/s	15cm/s
Oxygen concentrations	20%, 40%, 60% 80%, 100%	21%, 27%, 37% 68%, 77%, 100%

4.3 Mesh independency study

The mesh for the geometry shown in Fig. 4.1b is generated using ICEM for the numerical simulations. A steady-state computation was initially carried out with a grid resolution having a total of 29,925 control volumes, which is shown in Fig. 4.1b. In order to prove that the solution is independent of the mesh used in the simulations, it is important to carry out a grid-independency study. Therefore, the grid density was slightly reduced to 18,950, and then symmetrically increased to 37,710 and 52,680 control volumes to check their sensitivity on simulated results.

Figure 4.2 shows the temperature inside the reactor along the axisymmetric line for the four grids and the predicted results show reasonably good agreement with small variation at the upstream of the reactor. Moreover, Figure 4.3 and 4.4 show the mass-averaged mole fraction of

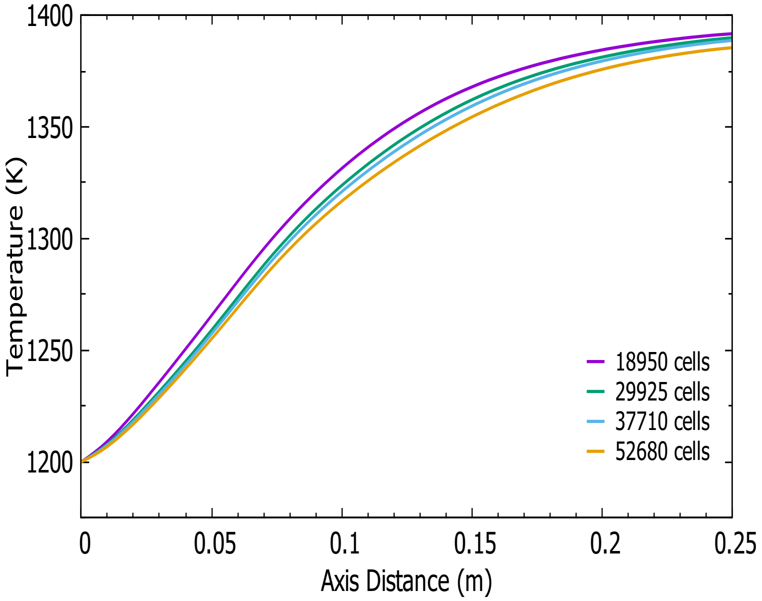

Figure 4.2: The variation of temperature predicted along the axisymmetric line of the reactor with different grids (DECS-11, Active flow, 37%O_2 & 63%N_2).

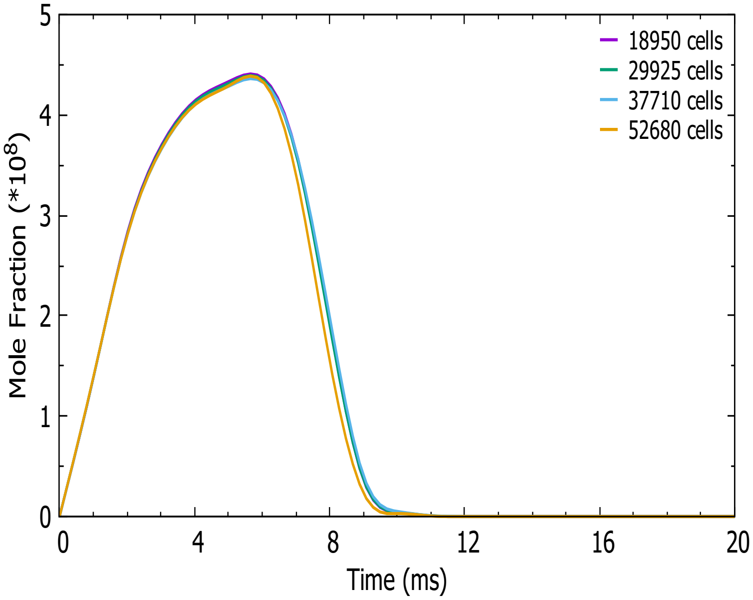

Figure 4.3: The variation of mole fraction of volatiles predicted in the reactor with different grids (DECS-11, Active flow, 37%O_2 & 63%N_2).

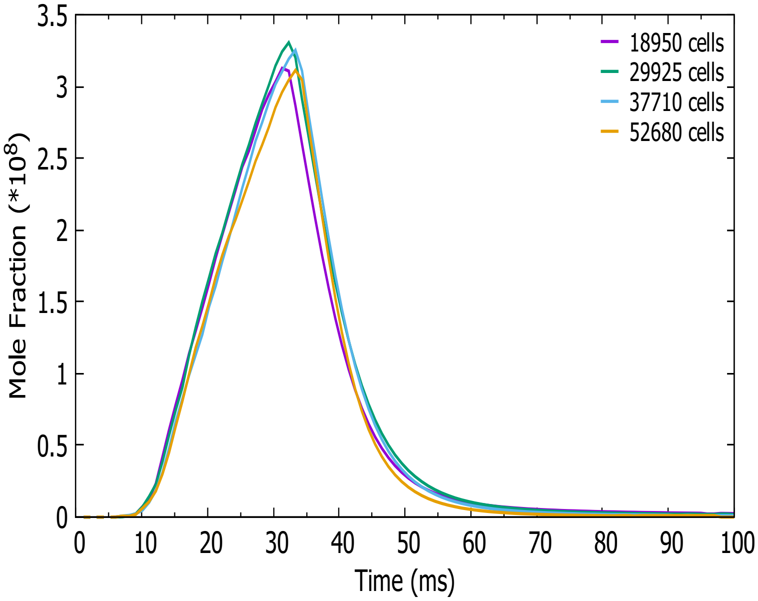

Figure 4.4: The variation of mole fraction of CO in the reactor with different grids (DECS-11, Active flow, 37%O_2 & 63%N_2).

volatiles (Vol) and carbon monoxide CO in the reactor. It is shown that, the simulation results based on the four meshes are very close to each other except for the small discrepancies in the upstream region. Therefore, the grid that has a total number of cells of 299,25 was sufficient for obtaining a grid-independent CFD solution and used for carrying out the reported simulations.

4.4 Validation of numerical model

Ignition delay time, the particle life time and the maximum temperature encountered during the transient combustion of Bagasse and DECS-11 particles were used to validate the numerical model by comparing with the experimental data reported in Refs. [37] [38]. It should be noted that following the experiments, the ignition delay time accounts for the duration that was commenced with the biomass particle releasing into the drop furnace and terminated at the ignition moment. Particle life time shows the time taken from the biomass particle releasing to the extinction of the particle. Further, particle maximum temperature is the highest temperature of the particle encountered during the course of the transient combustion process.

Table 4.3: Summary cases and compared results of Bagasse (Active Flow)

Gas	Ignition Delay Time(ms)		Particle Life Time (ms)		Maximum Temperature(K)		
Conditions	Exp.	Num.	Exp.	Num.	Exp.	Num.	Error(%)
21% O_2/N_2	3	3.2	18	18.3	1900	1891.72	0.44
27% O_2/N_2	9	8.8	18	18.3	2150	2100.44	2.31
37% O_2/N_2	4	3.9	10	10.4	2370	2386.66	0.70
77% O_2/N_2	5	5.1	11	11.8	2700	2702.92	0.11
100% O_2	3	3.2	8	8.1	2950	2926.13	0.81
27% O_2/CO_2	9	9.4	40	39.6	1630	1635.71	0.35
37% O_2/CO_2	4	4.3	19	18.0	2280	2266.18	0.61
77% O_2/CO_2	5	5.4	12	11.3	2650	2652.38	0.09

Table 4.4: Summary cases and compared results of DECS-11 (Active Flow)

Gas	Ignition Delay Time(ms)		Particle Life Time (ms)		Maximum Temperature(K)		
Conditions	Exp.	Num.	Exp.	Num.	Exp.	Num.	Error(%)
21% O_2/N_2	5	5.1	42	41.9	2000	1972.85	1.36
27% O_2/N_2	5	5.2	38	38.6	2420	2431.01	0.45
37% O_2/N_2	6	6.5	32	32.7	2400	2385.15	0.62
68% O_2/N_2	6	5.1	18	17.1	2950	2919.96	1.02
100% O_2	6	5.9	19	19.2	2900	2889.13	0.37
27% O_2/CO_2	5	5.4	52	50.9	1980	1981.82	0.09
37% O_2/CO_2	6	5.4	32	33.0	2300	2268.49	1.37
68% O_2/CO_2	6	5.1	18	17.1	2950	2991.13	1.39

Table 4.5: Summary cases and compared results of DECS-11 (Quiescent Flow)

Gas Conditions	Ignition Delay Time(ms)		Particle Life Time (ms)		Maximum Temperature(K)		
	Exp.	Num.	Exp.	Num.	Exp.	Num.	Error(%)
20% O_2/N_2	16	16.2	75	77.3	2300	2096.39	8.85
30% O_2/N_2	17	17.6	58	57.4	2406	2367.11	1.64
40% O_2/N_2	17	16.8	50	47.8	2612	2578.17	1.31
60% O_2/N_2	14	14.4	37	38.5	2780	2699.93	2.93
80% O_2/N_2	13	13.6	30	33.6	3050	3033.65	0.54
100% O_2	11	10.6	27	28.2	3094	3070.95	0.74
20% O_2/CO_2	21	21.2	113	107.9	2125	2125.62	0.03
30% O_2/CO_2	19	19.3	70	72.1	2250	2217.89	1.43
40% O_2/CO_2	17	17.1	57	56.4	2406	2364.95	1.73
60% O_2/CO_2	13	12.9	40	40.6	2650	2635.34	0.55
80% O_2/CO_2	12	11.7	32	32.3	2968	2954.36	0.49

In the experimental studies, spectral measurement was used to monitor the whole combustion process. The start and end points of the particle combustion were deduced from the onset and termination of the recorded highest-intensity signal from the reactive particle, and the temperature was obtained through signal post-processing [182] [183]. In accordance with this methodology, in the simulations the ignition and extinction moments of the particle were deduced by the start and end points of char combustion reactions (R_2-R_5). Further, the temperature of the particle was tracked under the discrete phase modelling (DPM).

Tables 4.3, 4.4 and 4.5 illustrate comparisons between the current numerical simulations and the experimental measurements [37] [38] of coal and biomass particles combustion under varying gas conditions. In total, 81 data points were used for comparison. The existence of a close agreement between the simulated and measured data is evident and the error of particle maximum temperature is within 2.5% for all cases. Given these, we can conclude that the numerical model is validated.

4.5 Particle mass loss and particle position

The single biomass or coal particle mass and position were tracked and recorded under DPM model during the numerical simulations. The calculated history of particle mass loss under different concentrations of oxygen and for both active and quiescent flow conditions is shown in Fig. 4.5. The temporal location during the transient combustion process is given in Fig. 4.6.

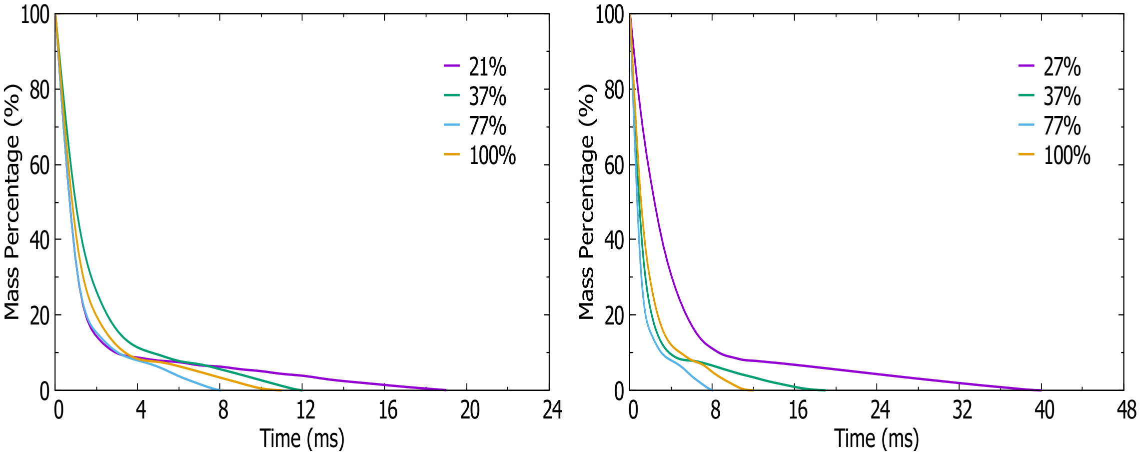

(a) Bagasse, Active flow, O_2/N_2 (b) Bagasse, Active flow, O_2/CO_2

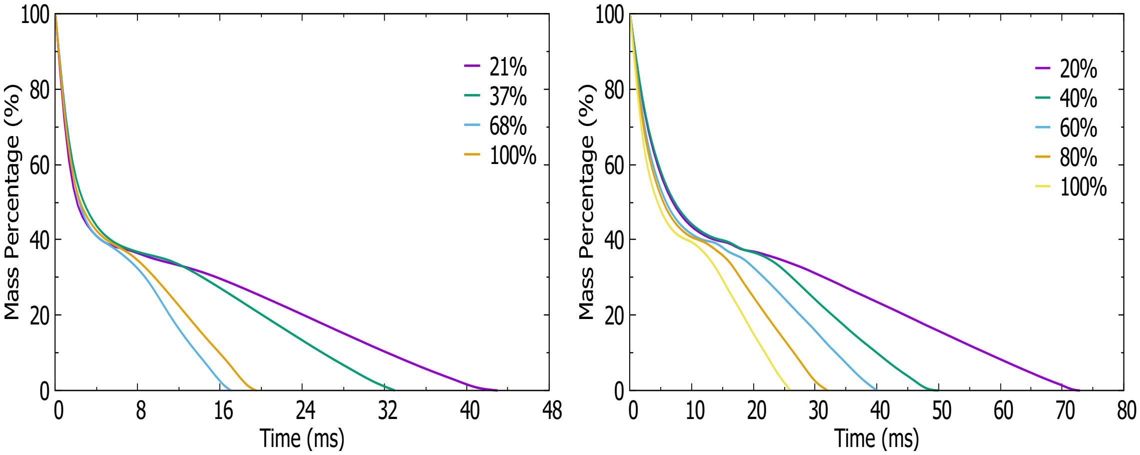

(c) DECS-11, Active flow, O_2/N_2 (d) DECS-11, Quiescent flow, O_2/N_2

Figure 4.5: Illustration of single particle mass loss under various gas conditions.

Figure 4.5a and 4.5b show the particle mass loss during a single biomass particle combustion under O_2/N_2 and O_2/CO_2, respectively. The similar trend is observed in the figures. It is clear that the inflection points of the curves divide the whole process of particle combustion into two stages: devolatilisation stage and char combustion stage. The mass loss of the particle within the first few milliseconds is quite significant, which corresponds to devolatilisation stage prior to the particle ignition. Over this stage large molecules are decomposed to lighter gas phase matter and are released to the surrounding atmosphere. Figures 4.5a and 4.5b further show that ignition of the particle majorly impedes the rate of mass loss and for all investigated oxygen concentrations the char burning stage lose mass much slower than the devolatilisation stage. Increasing the concentration of oxygen accelerates the combustion process and hence the rate of mass loss. However, regardless of the composition of the surrounding atmosphere, most the particle mass is lost during the devolatilisation. This is to be anticipated as the proximate analysis (dry ash free basis), shown in the section 3.1, indicates that more than 80% of the biomass particle mass consists of volatiles.

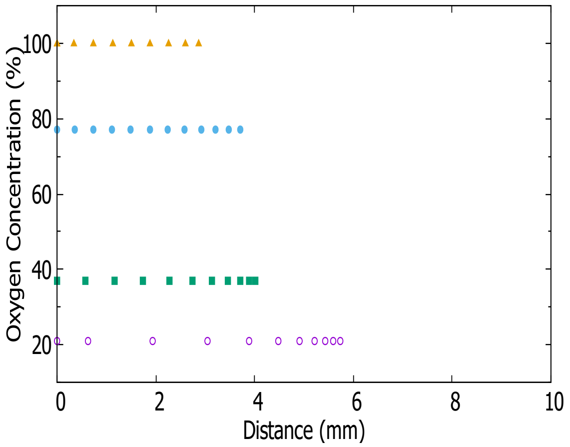

(a) Bagasse, Active flow, O_2/N_2

(b) Bagasse, Active flow, O_2/CO_2

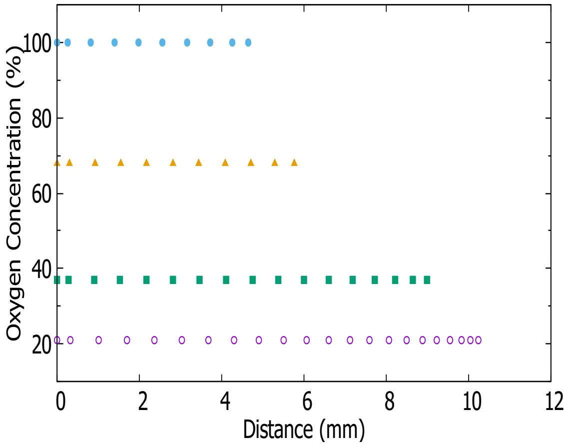

(c) DECS-11, Active flow, O_2/N_2

(d) DECS-11, Quiescent flow, O_2/N_2

Figure 4.6: Illustration of single particle position under various gas conditions.

The results of a single coal particle combustion under active and quiescent flow conditions with varying oxygen concentrations are reported in Fig. 4.5c and 4.5d. Same to biomass combustion, the devolatilisation stage and char combustion stage are distinguished clearly in the particle mass loss curves. There are no significant differences of the process devolatilisation at various gas conditions. However, the depletion rate of char particle is accelerated by the increased oxygen concentration under both active and quiescent flow conditions.

Figure 4.6 presents the temporal position of the fuel particle for every one millisecond during the transient combustion process. The time interval between points is 1.5 ms. Figure 4.6a and 4.6b refer to biomass particles under active O_2/N_2 and O_2/CO_2 environments, respectively, and Fig. 4.6c and 4.6d are for coal particles under active and quiescent O_2/N_2 environments respectively. The figures indicate that the particle kinematics, are highly affected by the mass loss. As expected, over the early stage of the particle release it accelerates downward. Yet, Figure 4.6 shows that the acceleration decreases significantly towards the end of the particle life time with the time interval of 2ms. This is due to the mass loss of the particle, which has progressively increased the relative significance of aerodynamic drag forces in comparison with the gravitational forces. Thus, the particle motion has become quite slow just before the completion of transient combustion process.

4.6 Spatio-temporal dynamics of gas-phase temperature

The temperature field within the near particle region for different moments after release of the single biomass or coal particle under various gas conditions is depicts in Figs. 4.7 and 4.8. As expected, the fluid flow, for almost the entire domain, is isothermal and at 1200K. An exception to this is a small area very close to the particle. Figures 4.7a and 4.7b show the results of single biomass particle combustion under active O_2/N_2 atmospheres.

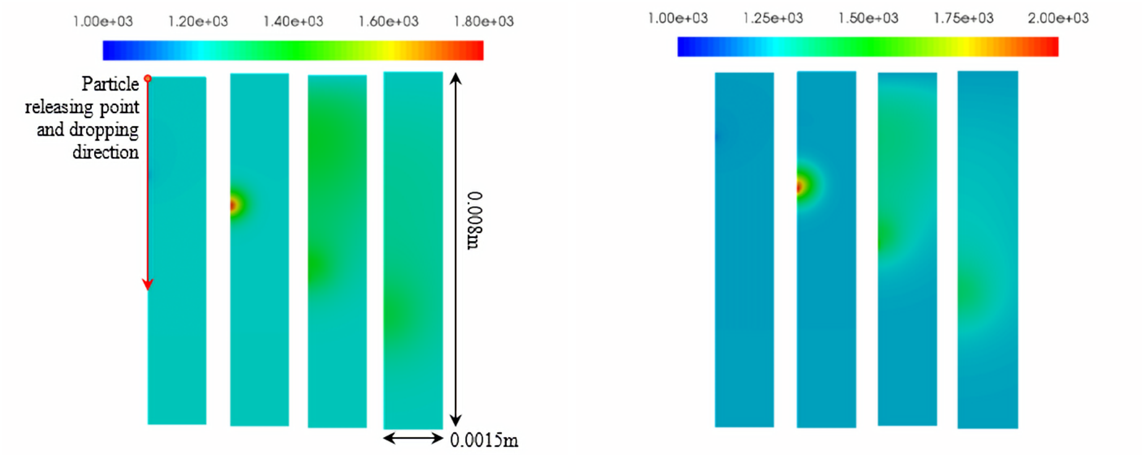

(a) AF: 37%O_2 & 63%N_2 (3-4-7-11ms) (b) AF: 77%O_2 & 23%N_2 (3-6-8-12ms)

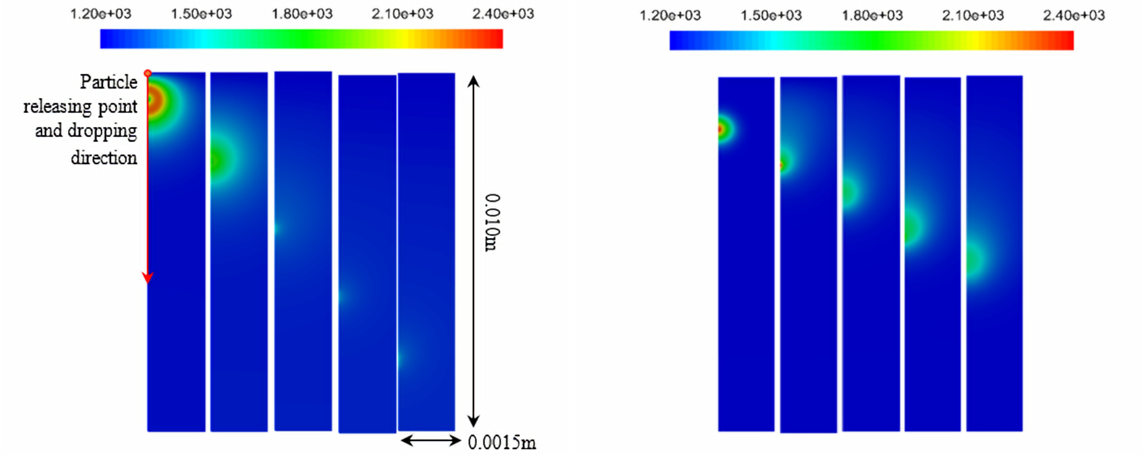

(c) AF: 37%O_2 & 63%CO_2 (2-6-10-14-18ms) (d) AF: 100% O_2 (3-5-7-9-11ms)

Figure 4.7: Spatio-temporal distribution of gas-phase temperature during Bagasse particle combustion. AF: Active Flow.

In Fig. 4.7a, the mole fraction of oxygen is 37%. The first part of this figure (the left most subfigure) corresponds to 3ms after the release of the particle, which is prior to ignition. Due to the endothermic devolatilisation process, the temperature has dropped to around 1100K in the vicinity of the particle. After 5ms the particle has already ignited and passed its peak temperature, the location of the particle and the reactive gas around it are completely clear in the second subfigure of Fig. 4.7a.

The subsequent two subfigures correspond to the final stage of combustion in which the particle becomes exceedingly small and the temperature of the reactive region has decreased. The same qualitative behaviour is observed in Fig. 4.7b for oxygen mole fraction of 77%. In this figure, the temperature of the burning particle after 6ms is 2000K. This is subsequent to the ignition and occurrence of the peak temperature. The particle and flow temperature drop significantly towards the end of the particle life time. Figure 4.7b also shows the temperature of the domain after the completion of the transient burning process. Importantly, the none-reactive flow at this stage still features significant temperature gradients. As will be discussed later, this has major influences upon the transient irreversibilities of the process.

The temperature field within the near particle region when the Bagasse particle combustion happened in active O_2/CO_2 gas conditions is given in Fig. 4.7c and 4.7d. Figure 4.7c corresponds to an atmosphere consisting of 37% O_2 and 63% CO_2 on molar basis. The left most subfigure refers to 2ms after the release of the particle, which is prior to particle ignition. However, the oxidisation of volatiles (R_6), which can happen almost simultaneously with the devolatilisation process (R_1), has led to the formation of hot cloud of reactive gases around the particle. It is important to note that gas temperature significantly drops as the surface of the particle is approached. This is because volatiles oxidation reactions can only occur in gas-phase and the devolatilisation process is endothermic and thus cools the gas in the immediate surroundings of the particle. As the particle combustion process progresses, the temperature difference disappears but the gas around the particle still has a higher temperature than the domain. In the late combustion stage, the particle becomes exceedingly small due to the depletion of char combustion (R_2-R_5), and both the temperature and size of the reactive region decrease.

Figure 4.7d shows the transient combustion behaviour when the particle burns in pure oxygen, which is markedly different with that under 37% O_2 and 63% CO_2 conditions (Fig. 4.7c). In this figure, the temperature of the burning particle at 3ms is almost 2400K. The volatiles and char combust at the same time, thus the peak temperature appears in the middle of the reactive region, and the particle and flow temperature drop significantly towards the end of the particle life time. It should be noted that as the first figure accounts for 2ms and 3ms in case c and case d, respectively and combustion is more intense at higher oxygen concentrations, the temperature difference becomes more noticeable in case c than case d. As discussed later, the temperature evolution is heavily dependent upon the oxygen concentration and type of the atmosphere.

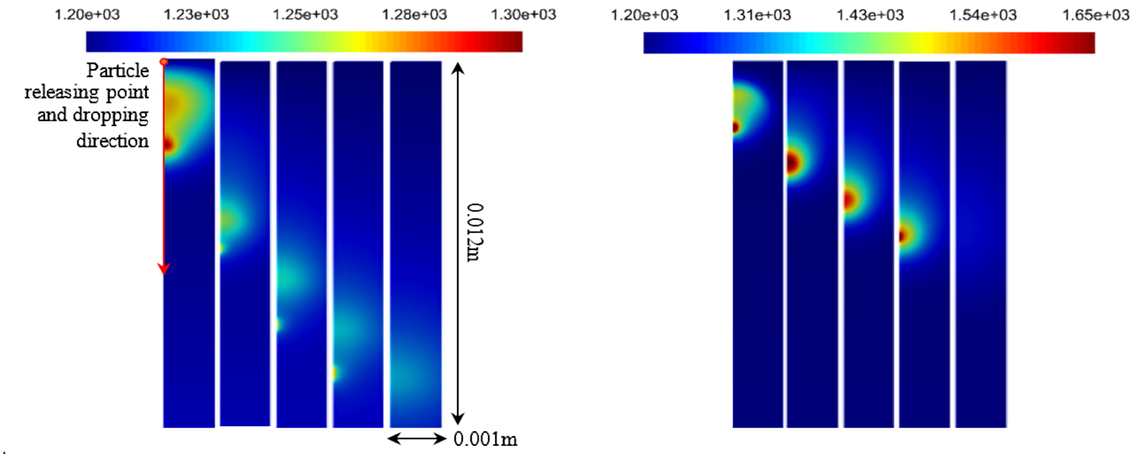

(a) AF: 21%O_2 & 79%N_2 (9-19-29-39-49ms) (b) AF: 100%O_2 (7-11-15-19-23ms)

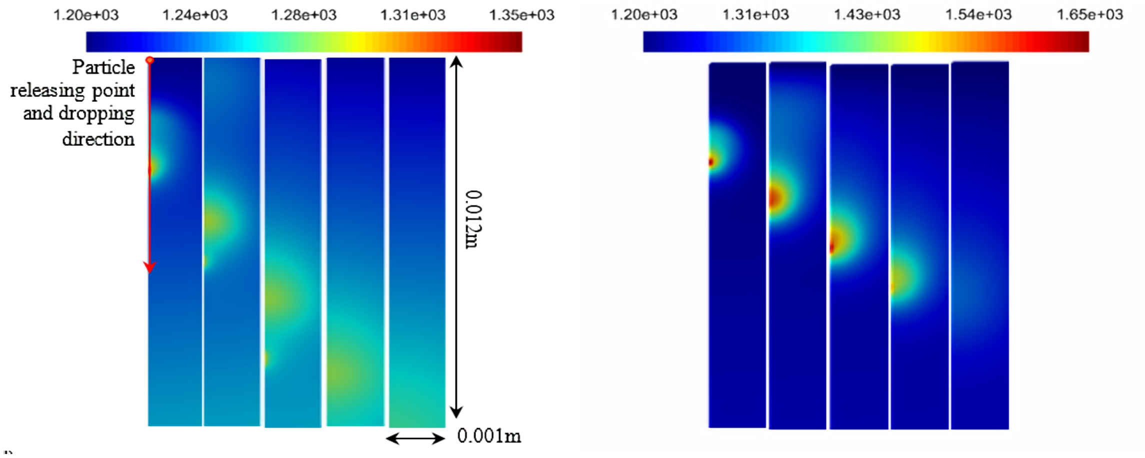

(c) QF, 40%O_2&60%N_2 (20-30-40-50-60ms) (d) QF: 80%O_2&20%N_2 (14-20-26-32-38ms)

Figure 4.8: Spatio-temporal distribution of gas-phase temperature during DECS-11 particle combustion. AF: Active Flow, QF: Quiescent Flow.

Two different oxygen concentrations have been shown for the cases with active and quiescent flow of single particle combustion (see Fig. 4.8). The time intervals between the snapshots have been maintained constant. The investigated periods start from a moment after the ignition and extend for a period longer than the particle life time (Tables 4.4 and 4.5). As a result, the last parts of each subfigure correspond to non-reactive media. Figure 4.8 clearly shows that in the course of the burning process, rise of the gas temperature occurs around the particle and also in a region shortly downstream of the dropping particle. As will be discussed later, the increase of temperature around the particle is due to the homogenous combustion of volatiles and heterogeneous combustion of char. However, the downstream hot gas is formed by the volatiles combustion. Figure 4.8 indicates that although changes in oxygen concentration alters duration of the burning process and gas temperature, the qualitative temperature field remains more and less independent of the mole fraction of oxygen.

It should be noticed that, under O_2/CO_2 gas atmosphere, the devolatilisated gas was ignited once it was released from the biomass particle, which was much prior to the ignition of char particle. While under O_2/N_2 gas atmosphere the volatiles and char particle were ignited at the same time. Actually, the question of whether the volatiles and chars combust sequentially was studied by Howard et al. [166]. The problem appeared to be complicated and had a relationship with several factors including the particle size, oxygen concentration, particle density, ignition temperature of the fuel in a given gas condition, the volatile matter evolved from the fuel.

4.7 Evolution of gaseous species during transient combustion process

4.7.1 The history of mole fraction of gaseous species

The time trace of mole fraction of the major gaseous species for different atmospheres and with and without advection, during the single particle combustion process are shown in Fig. 4.9 (Bagasse) and Fig. 4.10 (DECS-11). Here, it should be noted that, the mole fraction of CO_2 is not shown in the cases of CO_2-based gas atmospheres due to the little influence caused by the combustion of single coal or biomass particle.

An air like atmosphere and pure oxygen when a single biomass particle combust under active flow conditions have been analysed in Figs. 4.9a and 4.9b. The very fast release of volatile matters within the first few milliseconds of the process is clear in both figures. Ignition is marked by the onset of CO_2 and H_2O formation, which expectedly coincides with the peak point in the volatile formation curve. Immediately after ignition, the concentration of volatiles drops sharply, while those of CO_2 and H_2O increase quickly. Figures 4.9a and 4.9b show that in both cases the rate of formation of water vapour and carbon dioxide are almost exactly the same for the post ignition period. Nonetheless, for pure oxygen atmosphere, shown in Fig. 4.9b, the rate of CO_2 formation exceeds that of H_2O after about 1ms, which is contributed by reaction R_2. In both Figs. 4.9a and 4.9b formation of CO_2 and H_2O occurs most rapidly, while the products of volatilisation are burning and hence the mole fraction of volatiles is non-zero. As soon as the volatiles are totally consumed and the chemical system becomes largely heterogeneous, the rate of CO_2 formation decreases noticeably. Further, the concentration of H_2O starts to decrease, which is due to the consumption of H_2O by reaction R_5. It should be noted that as Fig. 4.9 depicts, concentration of H_2 remains negligibly small during the entire burning process and therefore the water generation by oxidation of hydrogen is a minor contributor to the total H_2O mole fraction. Formation of carbon monoxide starts just before the end of volatile burning process and increases towards a maximum value and reduces to zero at the end of the particle life time. The reduction of CO life span in pure oxygen (Fig. 4.9b) in comparison with air (Fig. 4.9a)

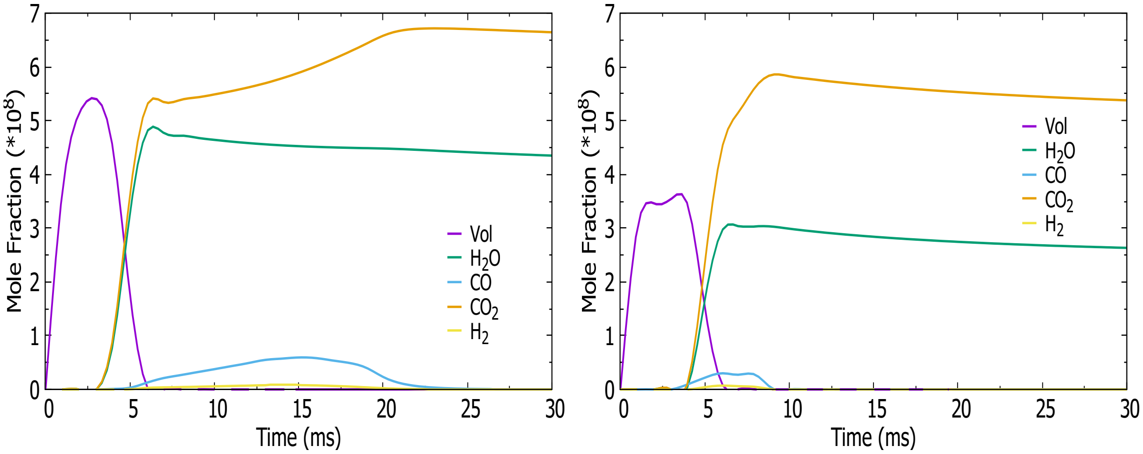

(a) Active flow, 21%O_2 & 79%N_2 (b) Active flow, 100%O_2

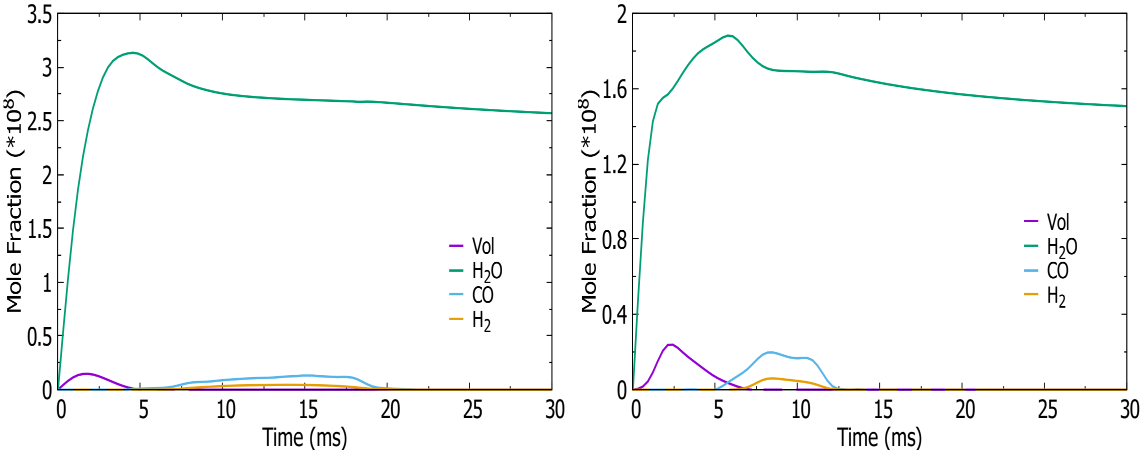

(c) Active flow, 37%O_2 & 63%CO_2 (d) Active flow, 77%O_2 & 23%CO_2

Figure 4.9: History of mass-averaged mole fraction of major chemical species during Bagasse particle combustion.

is completely clear in this figure.

The results of single Bagasse particle burnt in different oxygen concentration of O_2/CO_2 gas atmospheres are shown in Fig. 4.9c and 4.9d. It is noted that under O_2/CO_2 conditions (Figs. 4.9c and 4.9d), the peak values of the volatile matters formation curve are much smaller than that under O_2/N_2 conditions. This is because, when CO_2 is the background gas, the volatiles is ignited and starts combusting as being released from the biomass particle to the surroundings. Thus, there is no accumulation stage for the volatile matters to achieve a high peak value like in O2/N2 atmosphere where the volatiles is ignited much later. The difference of volatiles combustion in different background gas conditions leads to the different appearing time of CO_2 and H_2O that are mostly generated through reaction R_6. Further, the concentration of H_2O starts to decrease as it reacts with char particle to form H_2 and CO (R_5). The concentration of H_2 remains negligibly small during the entire burning process due to the consumption of H2 by reaction R_8.

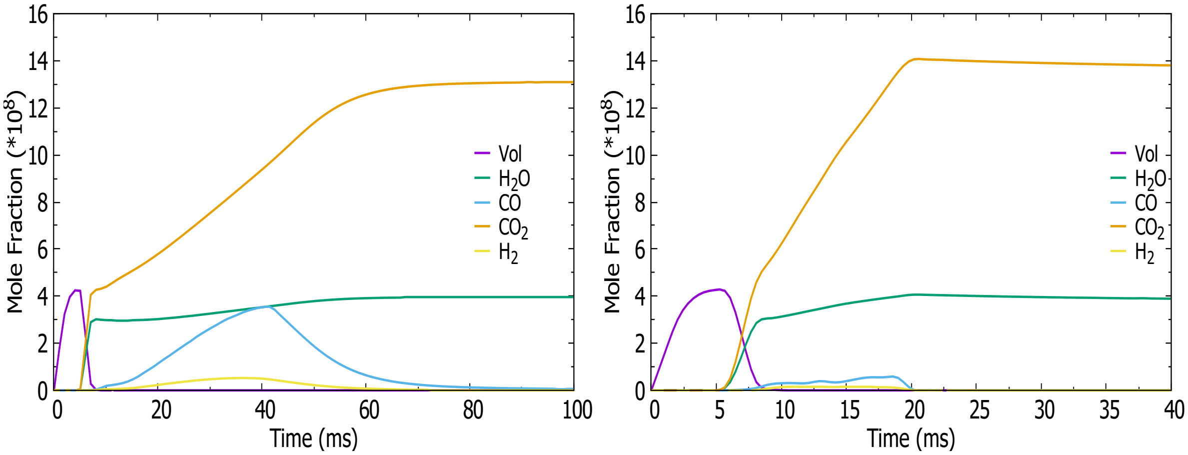

(a) Active flow, 21%O_2 & 79%N_2 (b) Active flow, 100%O_2

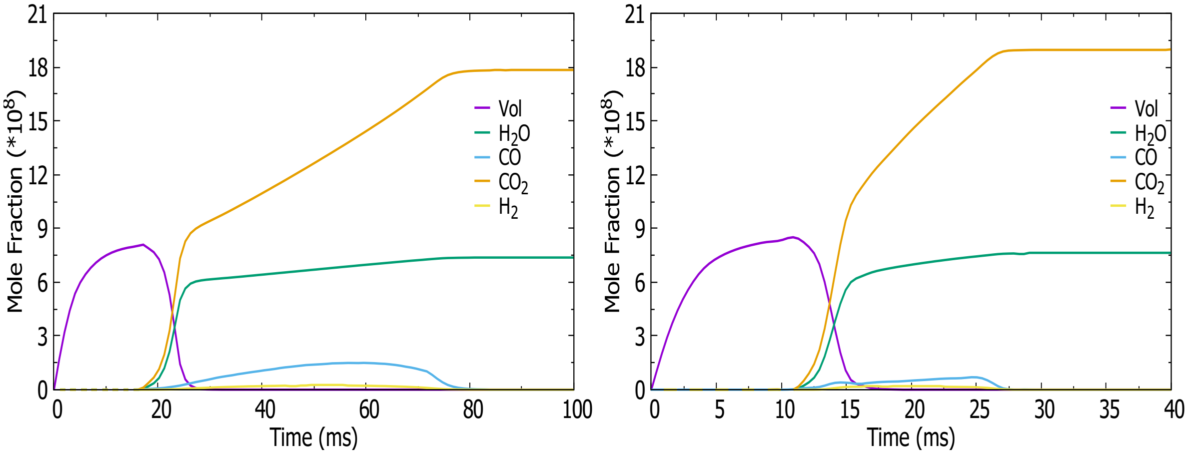

(c) Quiescent flow, 20%O_2 & 80%N_2 (d) Quiescent flow, 100%O_2

Figure 4.10: History of mass-averaged mole fraction of major chemical species during DECS-11 particle combustion.

It should be noted that, the concentration of CO increases towards a maximum value and reduces to zero at the end of the particle life time. Further, the reduction of CO life span is accelerated by the increased oxygen concentration. In conclusion, Fig. 4.9 confirms that, the combustion behaviour is quite different under O_2/N_2 and O_2/CO_2 conditions. This is particularly the case when the formation and consumption of volatile matters are considered.

Figure 4.10 shows the the history of mole fraction of the major gaseous species in four selected cases of single DECS-11 particle combustion. Similar to single biomass particle combustion process, the release of volatiles immediately after dropping the particle (at t=0) is evident. The mole fraction of volatiles increases at the beginning of the devolatilisation process till it reaches a maximum value at the moment of ignition. It then drops quickly, indicating the fast combustion rate of the volatiles. It should be clarified that as Fig. 4.10 and Table 4.3 show, ignition happens quicker in the active flow compared to the quiescent flow. This is due to the difference in the initial temperatures of the coal particle in these two cases (see Table 4.2). Ignition and oxidation of volatiles results in very fast production of CO_2 and H_2O through the homogenous reaction R_6. By termination of the combustion of volatiles, the rate of CO_2 and H_2O production decreases significantly. At the char combustion phase, these species are predominantly generated by reactions R_2 and R_8. Further, production of a relatively small amount of carbon monoxide and hydrogen by reactions R_3, R_4 and R_5 can be readily seen in Fig. 4.10. CO and H_2 are eventually converted to carbon dioxide and water vapour through reactions R_7 and R_8. According to Fig. 4.10, the chemical and advection characteristics of the atmosphere have strong effects upon the formation and consumption of the species. A comparison between Figs. 4.10a and 4.10b shows that by replacing air with pure oxygen, the concentrations of CO and H_2 have majorly dropped. The same trend can be seen for the cases under quiescent flow shown in Figs 4.10c and 4.10d. This is because of the fast progress of reactions R_7 and R_8 in oxygen, which deplete CO and H_2 quickly and hence maintain their concentrations at low levels.

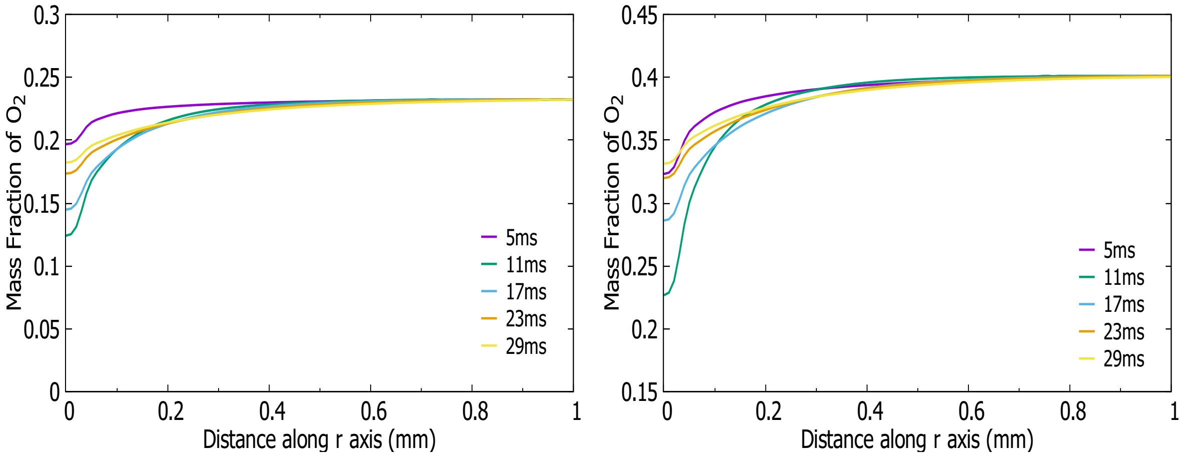

(a) Active flow, 21%O_2 & 79%N_2 (b) Active flow, 37%O_2 & 73%N_2

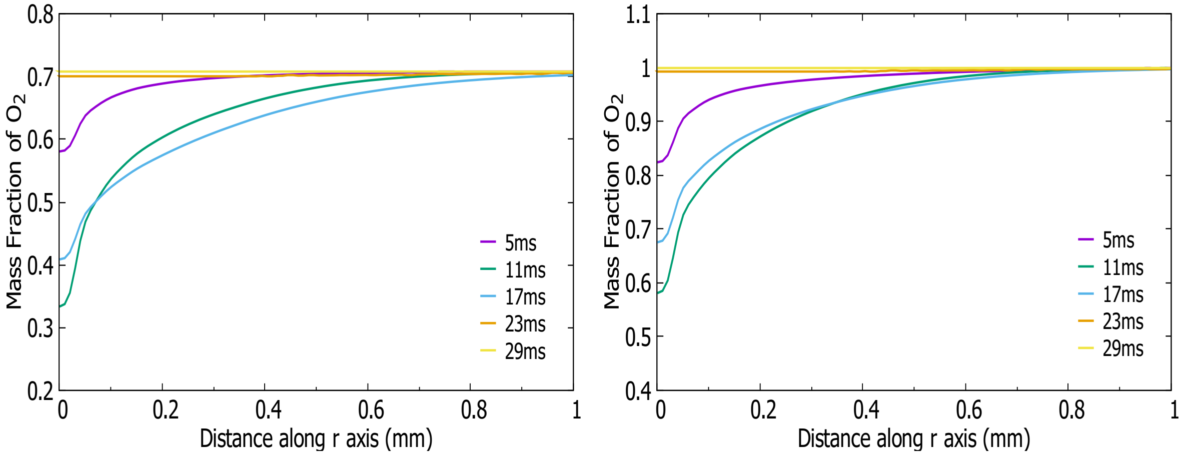

(c) Active flow, 68%O_2 & 32%N_2 (d) Active flow, 100%O_2

Figure 4.11: Distribution of oxygen mass fraction along a horizontal line initiating at the particle centre during DECS-11 particle combustion.

4.7.2 Radial distribution of oxygen concentration during combustion process

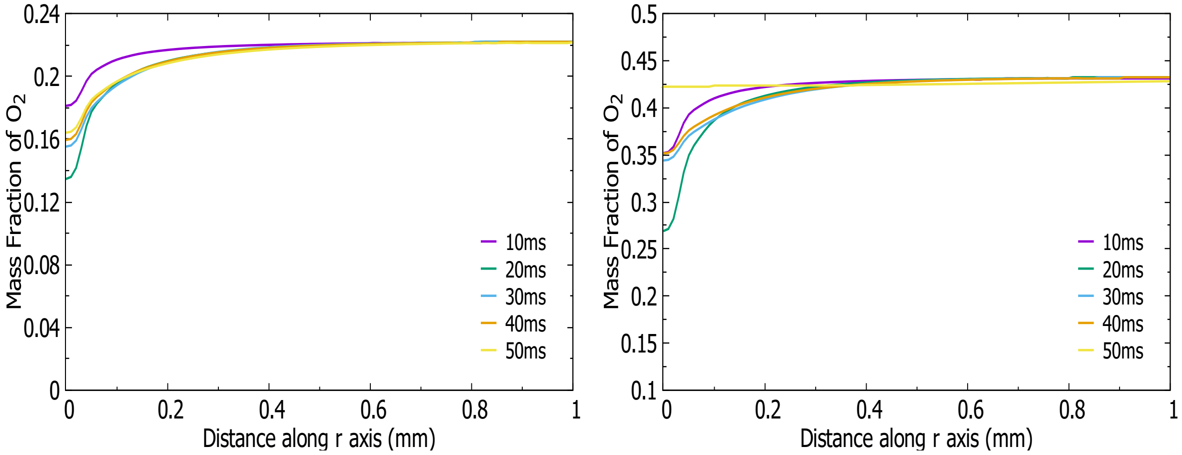

(a) Quiescent flow, 20%O_2 & 80%N_2 (b) Quiescent flow, 40%O_2 & 60%N_2

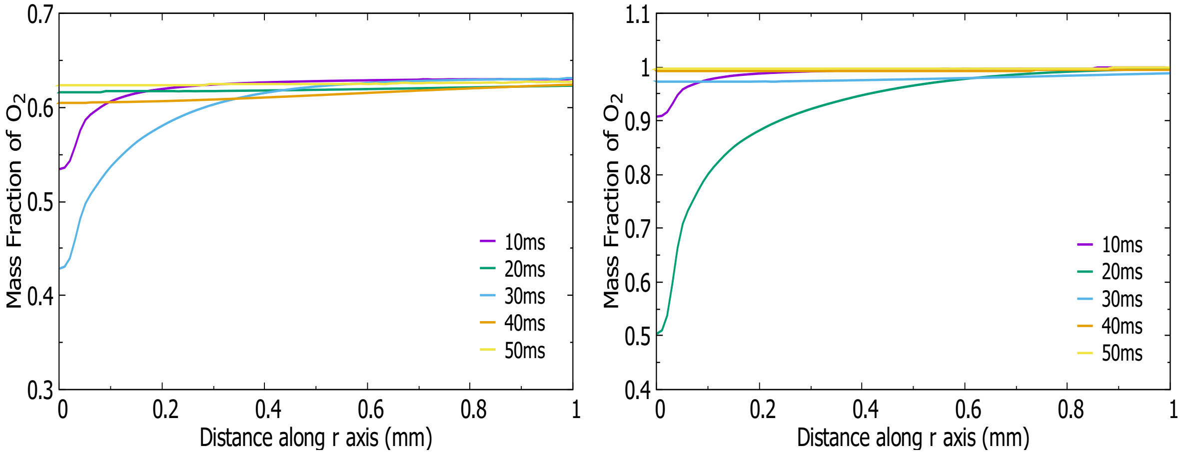

(c) Quiescent flow, 60%O_2 & 40%N_2 (d) Quiescent flow, 100%O_2

Figure 4.12: Distribution of oxygen mass fraction along a horizontal line initiating at the particle centre during DECS-11 particle combustion.

Consumption of oxygen is an important parameter governing the combustion process and thus the evolution of oxygen boundary layer is of high significance. Figures 4.13-4.12 show the radial distribution of the mass fraction of oxygen for selected instances of time after releasing the single coal or biomass particle. Each graph shows the variations in the mass fraction of oxygen along a radius that initiates from the external surface of the particle and penetrates for 1mm into the surrounding gases.

All four different concentrations of oxygen when the Bagasse particle burnt in O_2/N_2 atmosphere have been investigated in Fig. 4.13. For the lowest concentration of oxygen in Fig. 4.13a, oxygen mass fraction in the vicinity of the particle drops at the moment of ignition (3ms) and continues to decrease for the first 6ms before it rises again in the rest of the burning process. This

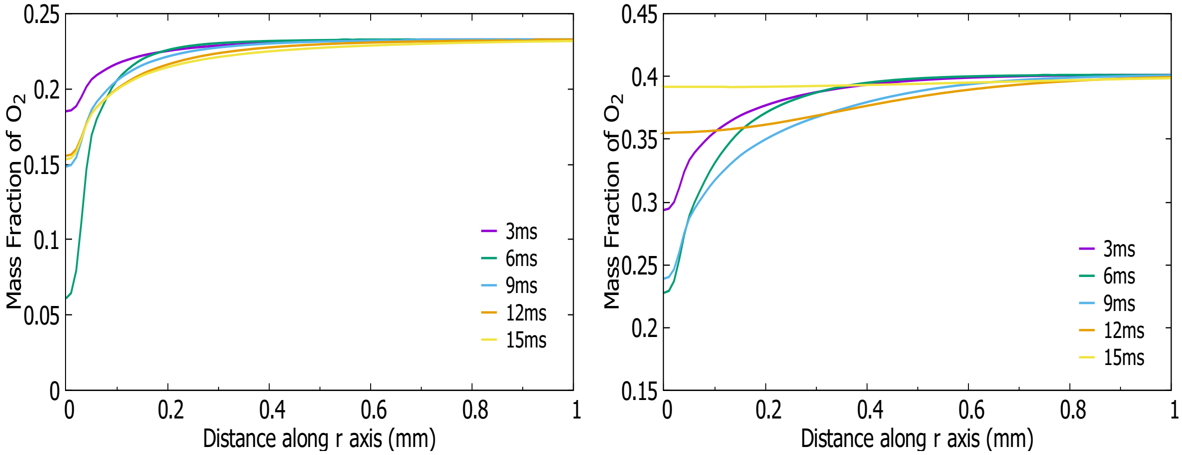

(a) Active flow, 21%O_2&79%N_2 (b) Active flow, 37%O_2 & 73%N_2

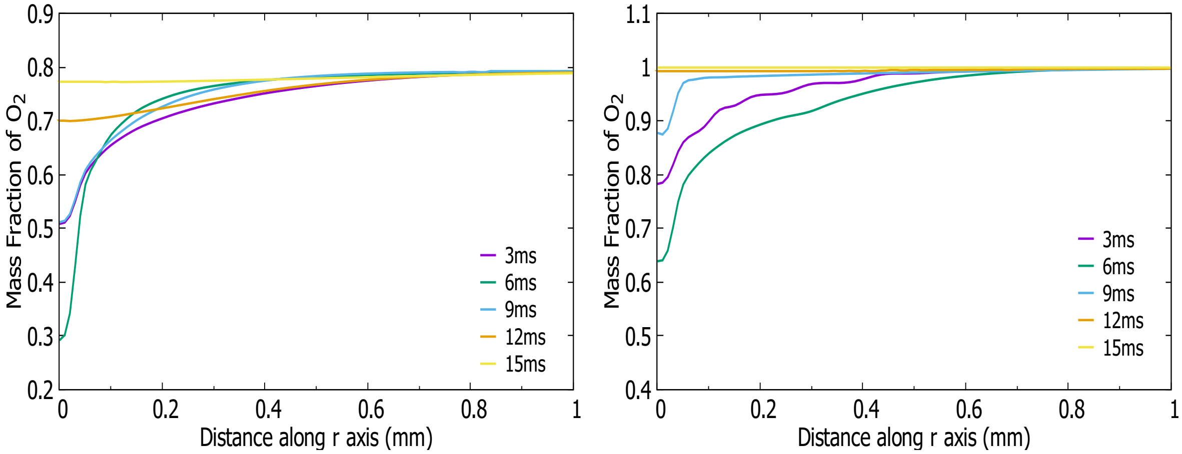

(c) Active flow, 77%O_2 & 23%N_2 (d) Active flow, 100%O_2

Figure 4.13: Distribution of oxygen mass fraction along a horizontal line initiating at the particle centre during Bagasse partile combustion.

figure shows that particle combustion can affect oxygen concentration of the surrounding gas for a maximum radial distance of about 400μm from the external surface of the particle. Increasing the concentration of oxygen in Figs. 4.13b, 4.13c and 4.13d results in the following changes. First, the radial extent of oxygen depletion extends significantly. For instance, Fig. 4.13b shows that under 37% mole fraction of oxygen burning can influence the concentration of oxygen up to 800μm away from the surface. Second, the decrease in the mass fraction of oxygen becomes a lot more pronounced. Figure 4.13c, for instance, shows that mass fraction of oxygen drops from nearly 0.8 far from the particle to almost 0.3 on the surface of the particle. However, this value is considerably smaller in Fig. 4.13a. Given that the mass of particle and hence the total amount of fuel is fixed in all investigated cases, this result may seem counterintuitive. However, it should be recalled that combustion duration becomes significantly faster under oxygen enriched atmospheres (see Table 4.3). Hence, although the total amount of oxygen for complete oxidation of the fuel particle is unchanged, the rate of oxygen consumption in Figs. 4.13b, 4.13c and 4.13d is generally higher than that in Fig. 4.13a. The difference when the single biomass

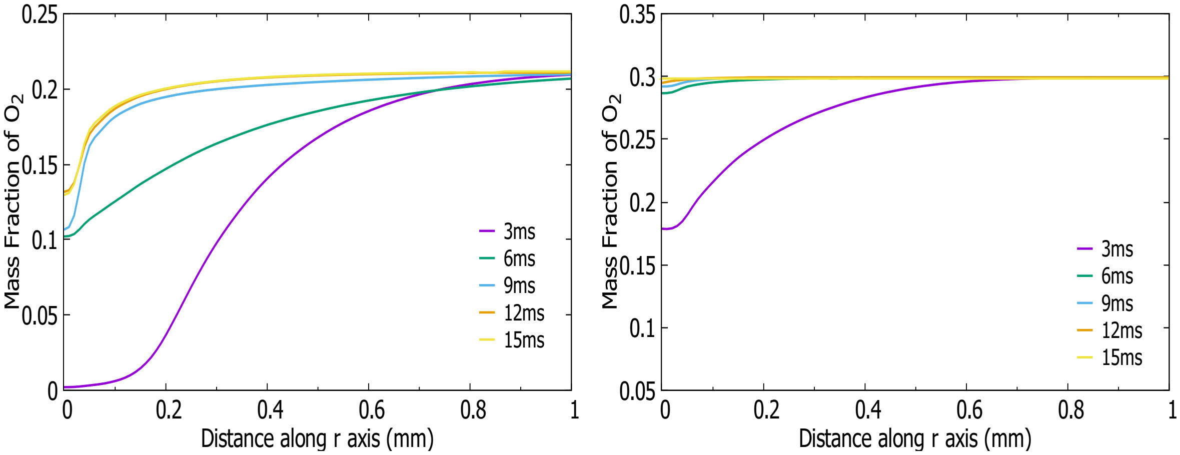

(a) Active flow, 27%O_2 & 73%CO_2 (b) Active flow, 37%O_2 & 73%CO_2

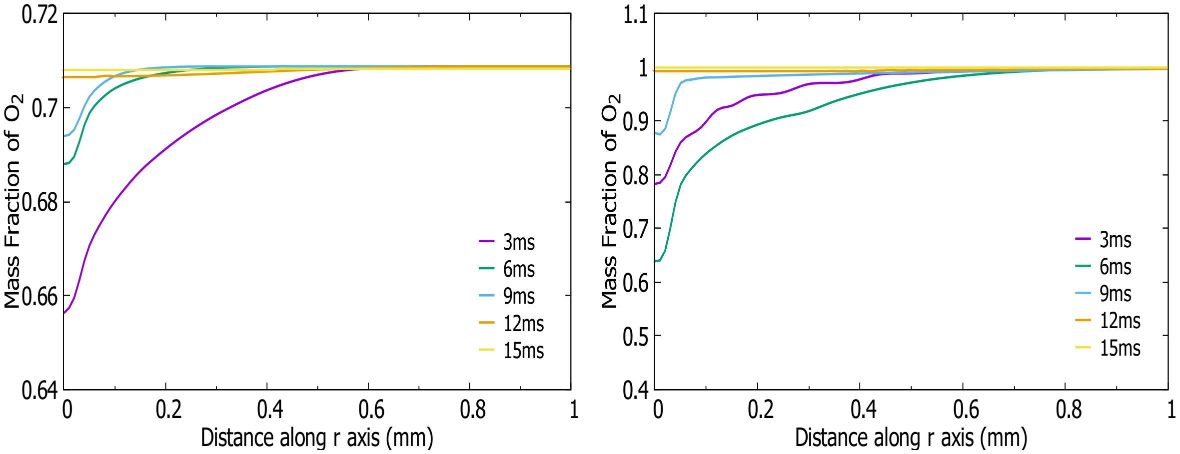

(c) Active flow, 77%O_2 & 23%CO_2 (d) Active flow, 100%O_2

Figure 4.14: Distribution of oxygen mass fraction along a horizontal line initiating at the particle centre during Bagasse particle combustion.

particle burnt in O_2/CO_2 gas conditions is the oxygen consumption at the beginning stage after releasing the particle. It is clearly shown in Fig. 4.14a-4.14c that the mass fraction of oxygen is much lower at the time t=3ms. The consumption of oxygen is caused by the oxidation reaction of the devolatilizated gases (R_6) where it happened along with the appearance of the volatile matters.

Figures 4.11 and 4.12 show the radial distribution of oxygen mass fraction at different times during the single coal particle burning process. Both active (Fig. 4.11) and quiescent (Fig. 4.12) flows with varying concentration of oxygen have been investigated. Reduction of oxygen concentration near the particle is evident in all subfigures. At early times this is due to the homogenous oxidation of volatiles (R_6), whereas during the char combustion the heterogeneous reactions R_2 and R_3 as well as the homogeneous oxidation of CO (R_7) and H_2 (R_8) consume oxygen. Figure 4.11 provides a clear indication about the thickness of the concentration boundary layer formed by the oxygen deficit. This is where, for a given instance of time, the oxygen concentration profile asymptotically approaches that of the longest duration of time (29ms for the active flow and 50ms for quiescent flow). Figure 4.11 show that, under active flow, increasing the mole fraction of oxygen results in the growth of the thickness of the concentration boundary layer. Further, the amount of oxygen deficit within the boundary layer increases significantly as the mole fraction of the oxygen increases. It is important to note that as the initial mass of the particle has been maintained constant throughout all experiments, the total amount of oxygen consumed in the course of the burning process is fixed. The faster combustion in oxygenated atmospheres causes consumption of the required oxygen in a short time, rendering smaller concentrations of oxygen in the vicinity of the coal particle. This behaviour is equally observable in cases under active flow (Fig. 4.11) and also for those under the quiescent flow (Fig. 4.12).

4.7.3 Spatio-temporal distributions of gaseous species

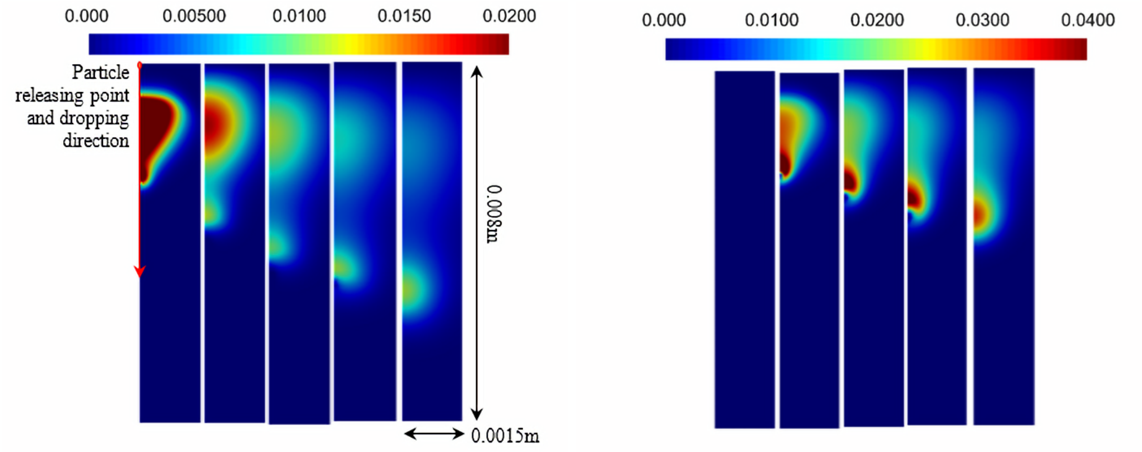

(a) AF: 21%O_2 & 79%N_2 (5-9-13-17-21ms)

(b) AF: 77%O_2 & 23%N_2 (5-7-9-11-13ms)

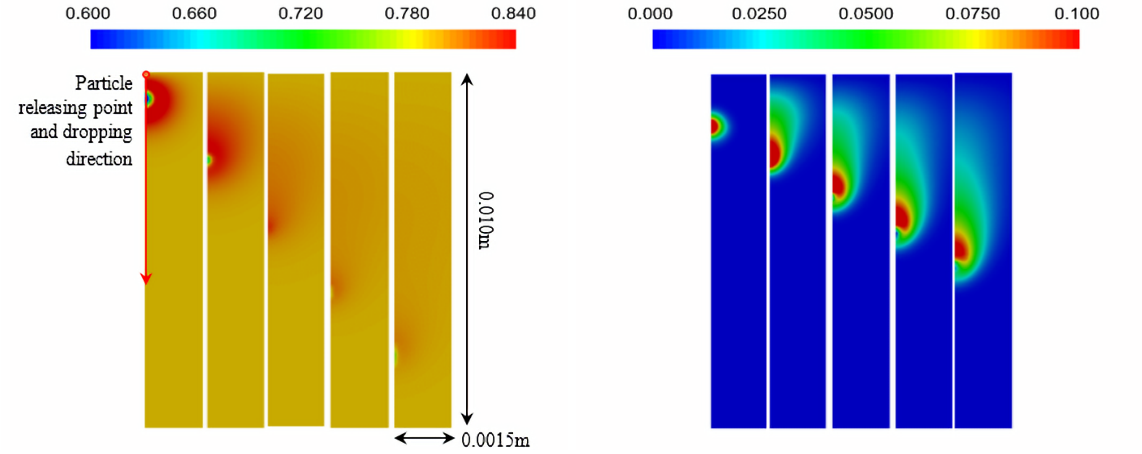

(c) AF: 37%O_2 & 63%CO_2 (2-6-10-14-18ms)

(d) AF: 100%O_2 (3-5-7-9-11ms)

Figure 4.15: Spatio-temporal distribution of mass fraction of CO_2 during Bagasse particle combustion. AF: Active Flow.

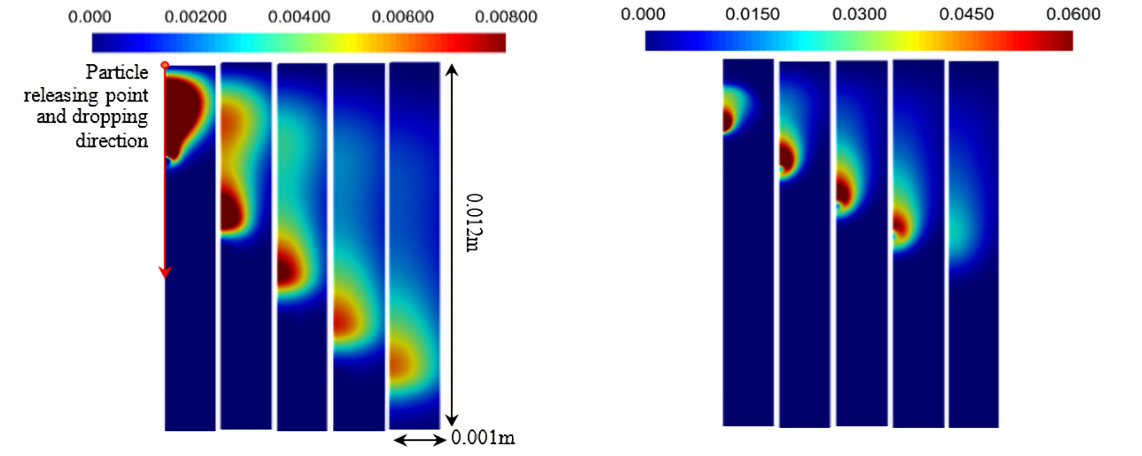

(a) AF: 21%O_2 & 79%N_2 (9-19-29-39-49ms) (b) AF: 100%O_2 (7-11-15-19-23ms)

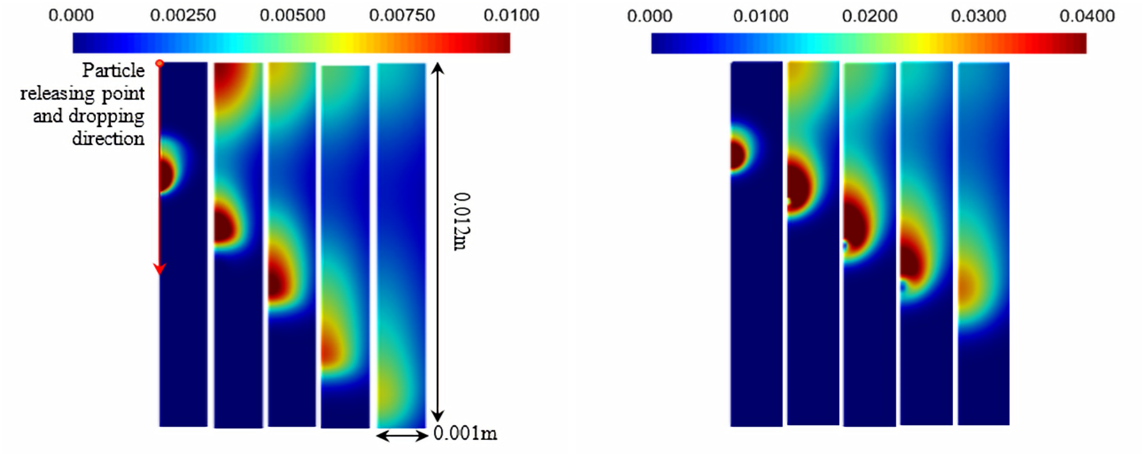

(c) QF: 40%O_2 & 60%N_2 (20-30-40-50-60ms) (d) QF: 80%O_2 & 20%N_2 (14-20-26-32-38ms)

Figure 4.16: Spatio-temporal distribution of mass fraction of CO_2 during DECS-11 particle combustion. AF: Active Flow, QF: Quiescent Flow.

Spatio-temporal distributions of different chemical species CO_2, CO, H_2O and H_2 are investigated to give a deeper insight to the mass transfer during the transient coal and biomass particle combustion process.

Figures 4.15a-d show the spatio-temporal distribution of CO_2 for the four considered gas conditions. They are active 21% O_2/N_2 (Fig. 4.15a), 77% O_2/N_2 (Fig. 4.15b), 37% O_2/CO_2 (Fig. 4.15c) and 100% O_2 (Fig. 4.15d), respectively. Formation of a large amount of CO_2 shortly after the ignition is evident in Fig. 4.15a. This is due to the oxidisation of the volatiles, as denoted by the homogenous reaction R_6. The subsequent production of carbon dioxide in the vicinity of the particle by reactions R_2 and R_7 is clear in other subfigures of Fig. 4.15a. These subfigures also show that the initial cloud of CO_2 diffuses out and is partially advected downstream. Notably, it is inferred from Fig. 4.15a that the production of carbon dioxide occurs chiefly by homogenous reactions almost immediately after ignition. This finding can be found when tracing the formation history of mole fraction of CO_2 (Fig. 4.9a). At higher mole frac-

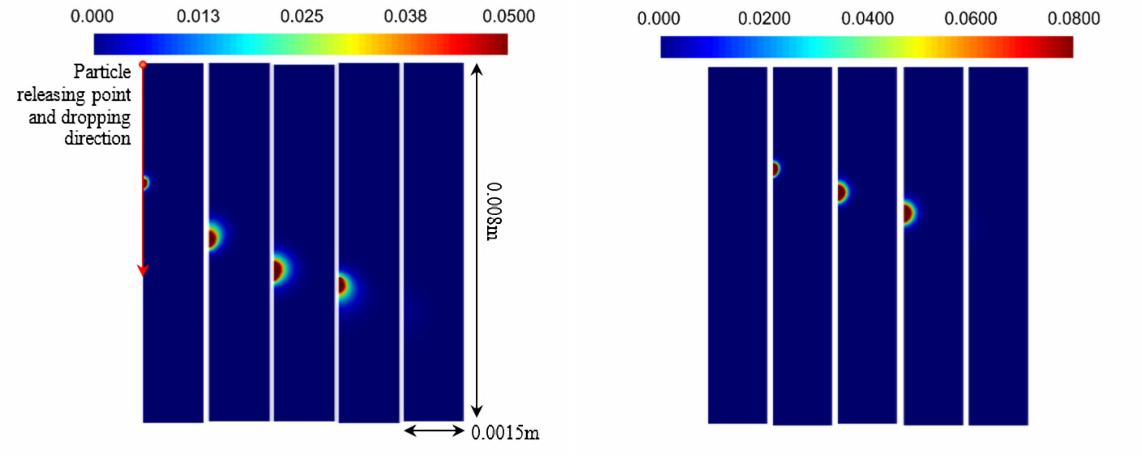

(a) AF: 21%O_2 & 79%N_2 (5-9-13-17-21ms) (b) AF: 77%O_2 & 23%N_2 (5-7-9-11-13ms)

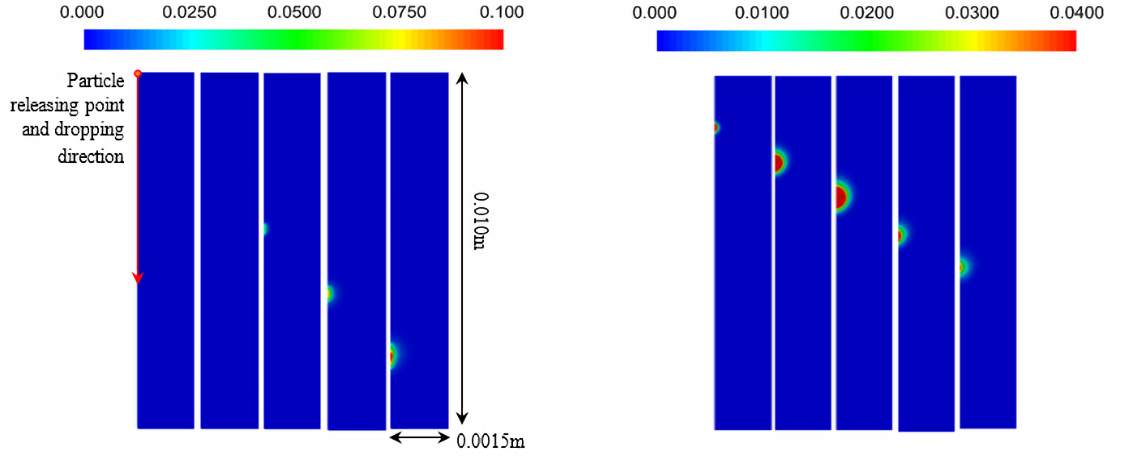

(c) AF: 37%O_2 & 63%CO_2 (2-6-10-14-18ms) (d) AF: 100%O_2 (3-5-7-9-11ms)

Figure 4.17: Spatio-temporal distribution of mass fraction of CO during Bagasse particle combustion. AF: Active Flow.

tion of oxygen, shown in Fig. 4.15b, the qualitative trend of carbon dioxide generation remains largely unchanged. No CO_2 is observed prior to the ignition and the post-ignition plume of CO_2 is advected and diffuses during the transient burning process. However, a comparison between Figs. 4.15a and 4.15b reveals that under 77% oxygen mole fraction and for the entire combustion process, the highest concentration of CO_2 within the reactor is situated close to the particle. This is clearly not the case in Fig. 4.15a in which the CO_2 concentration around the burning particle is considerably smaller than that produced by combustion of devolatilisation gases. The disparity can be attributed to the intensification of reaction R_2 and also R_3+R_7 due to higher oxygen concentration.

Figure 4.15c and 4.15d show the spatio-temporal distribution of CO_2 for the two specified oxygen concentrations in O_2/CO_2 gas environment. Due to the homogeneous reaction (R_6), a large amount of CO_2 is formed immediately after the combustion of the volatiles. Yet, the CO_2 cloud diffuses quickly into the background atmosphere, which leaves the high concentration of CO_2 to

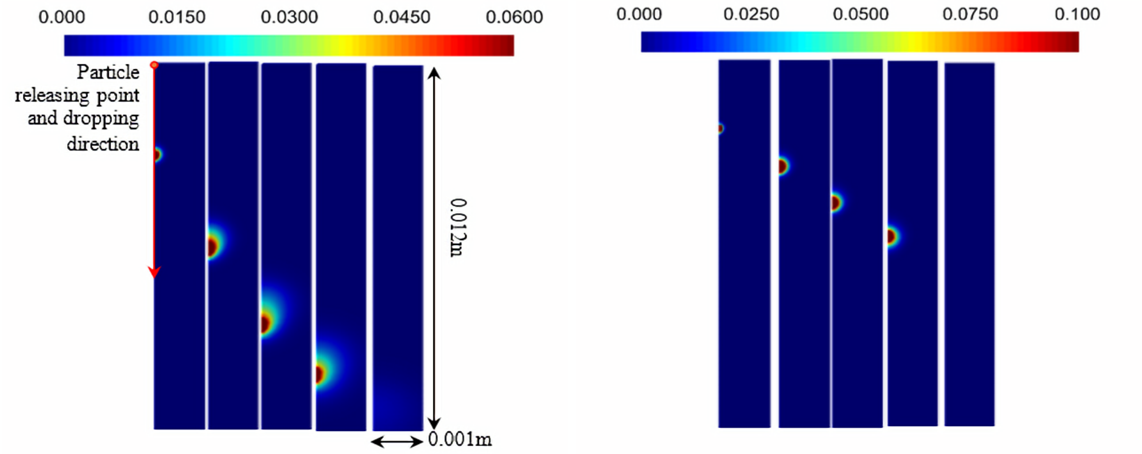

(a) AF: 21%O_2 & 79%N_2 (9-19-29-39-49ms) (b) AF: 100%O_2 (7-11-15-19-23ms)

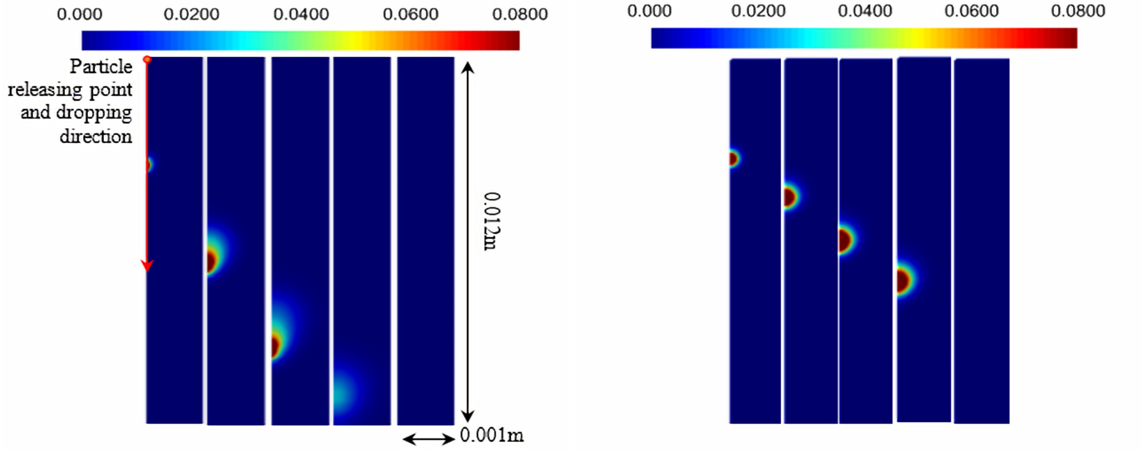

(c) QF: 40%O_2 & 60%N_2 (20-30-40-50-60ms) (d) QF: 80%O_2 & 20%N_2 (14-20-26-32-38ms)

Figure 4.18: Spatio-temporal distribution of mass fraction of CO during DECS-11 particle combustion. AF: Active Flow, QF: Quiescent Flow.

the vicinity of the particle. The results of pure oxygen concentration are reported in Fig. 4.15d. Due to the simultaneous combustion of volatiles and char in this case, there is no concentration gradient at the centre of the CO_2 cloud. Further, in the absence of the CO_2 background gas, the cloud of CO_2 formed during the combustion process appears clearer in this figure.

Similar to the biomass particle combustion in O_2/N_2 atmosphere, when the coal particle burning in air (Fig. 4.16a), a large amount of CO_2 is generated shortly after the ignition. Combustion of volatiles described by reaction R_6, combustion of CO (R_7) and also heterogeneous char combustion (R_2) contribute with the generation of carbon dioxide. Amongst these, oxidation of volatiles happens immediately after the ignition and progresses quickly. As a result, there is a large of amount of CO_2 production in the early stage of the burning process (Fig. 4.16a). As time elapses, the CO_2 cloud formed by combustion of volatiles diffuses into the atmosphere, while being advected downstream by the motion of the atmosphere. Since the products of the homogeneous combustion of volatiles are at high temperature (see Fig. 4.8), the buoyancy forces

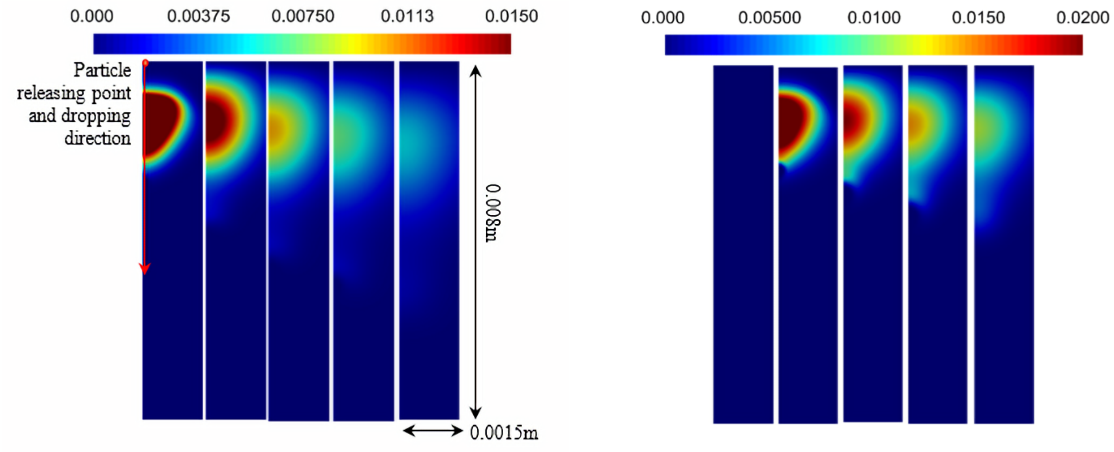

(a) AF: 21%O_2 & 79%N_2 (5-9-13-17-21ms) (b) AF: 77%O_2 & 23%N_2 (5-7-9-11-13ms)

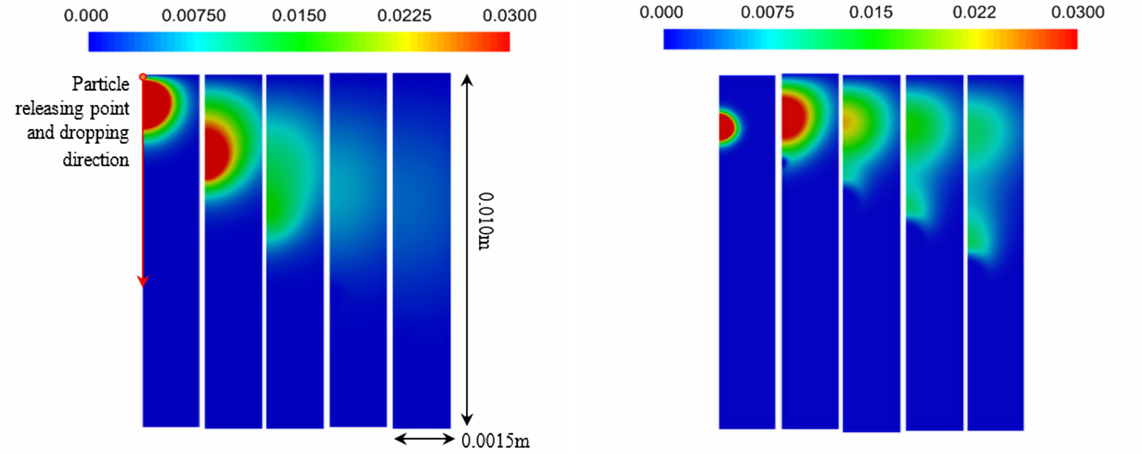

(c) AF: 37%O_2 & 63%CO_2 (2-6-10-14-18ms) (d) AF: 100%O_2 (3-5-7-9-11ms)

Figure 4.19: Spatio-temporal distribution of mass fraction of H_2O during Bagasse particle combustion. AF: Active Flow.

slow down the downstream motion of the CO_2 cloud. Hence, in Fig. 4.16a, there appears to be two distinctive regions with high CO_2 concentration. This is less pronounced under combustion in pure oxygen shown in Fig. 4.16b in which the short duration of combustion does not allow for the buoyancy forces to develop two distinctive regions of high CO_2 concentration.

Figures 4.17 and 4.18 show the spatio-temporal variations of carbon monoxide concentration during combustion of the biomass and coal particle in various conditions. Figure 4.17a depicts the evolution of CO in single Bagasse particle combustion under active 21% O_2/N_2 atmosphere, a small cloud of CO appears around the particle shortly after the ignition. As the process continues, the amount of CO increases as a result of the progress in R_3 and R_4 reactions. This is represented by the growth of the cloud of CO around the particle. However, at the end of the particle life time (t=21ms), the concentration of CO drops to zero. This is due to the conversion of CO to CO_2 by reaction R_7 and is an indication of the completion of the combustion process. For 77% O_2/N_2 molar concentration, Fig. 4.17b shows that no CO is generated prior to ignition

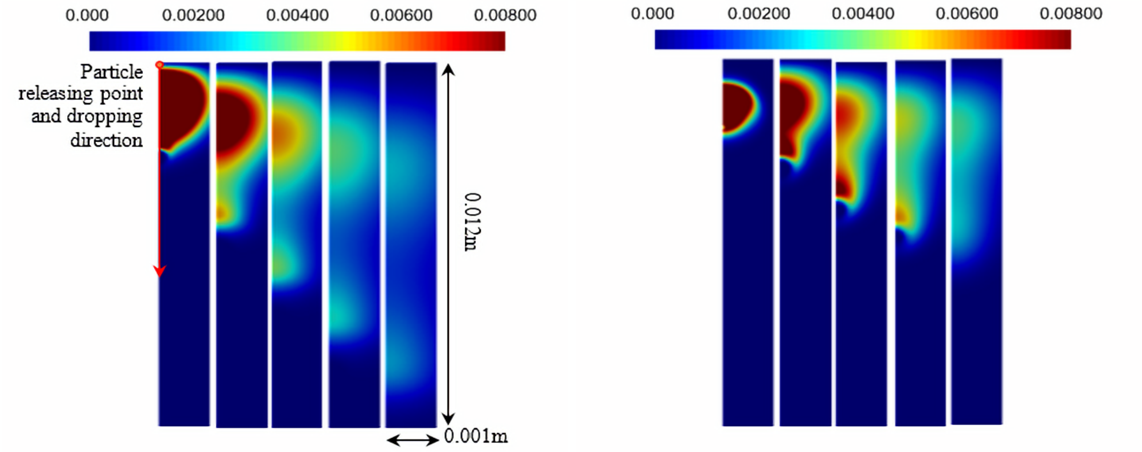

(a) AF: 21%O_2 & 79%N_2 (9-19-29-39-49ms) (b) AF: 100%O_2 (7-11-15-19-23ms)

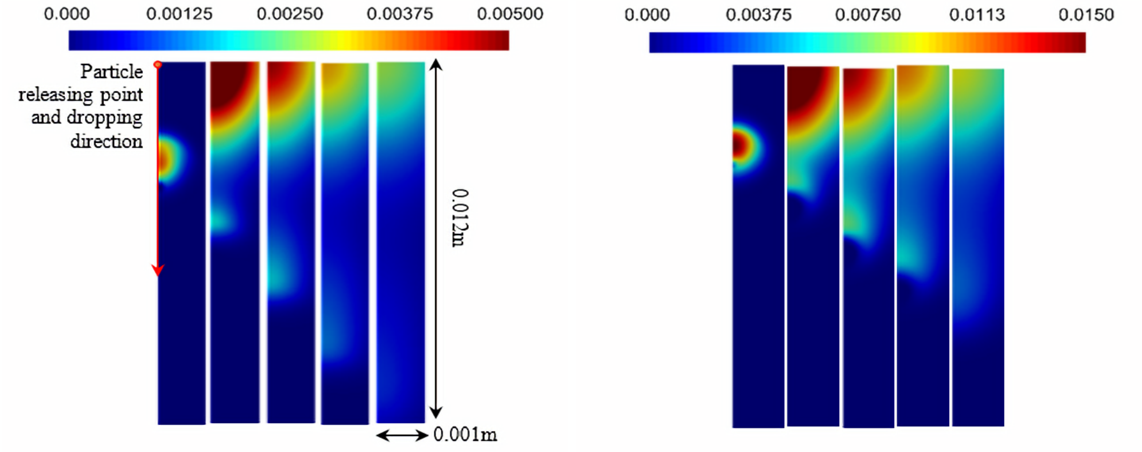

(c) QF: 40%O_2 & 60%N_2 (20-30-40-50-60ms) (d) QF: 80%O_2 & 20%N_2 (14-20-26-32-38ms)

Figure 4.20: Spatio-temporal distribution of mass fraction of H_2O during DECS-11 particle combustion. AF: Active Flow, QF: Quiescent Flow.

of the biomass particle and similar to that observed in Fig. 4.17a, after the transient burning there is no CO left in the gas atmosphere. It should be noted that as the legend of Fig. 4.17b indicates the concentration of CO in oxygen enriched atmosphere is higher compared to that with 21% of oxygen mole fraction.

The production process of CO when the biomass particle burnt in O_2/CO_2 atmosphere is shown in Fig. 4.17c and 4.17d. When the reactions R_3 and R_4 starts with the ignition of the particle, a small amount of CO is generated in the vicinity of the particle for both investigated gas conditions. Figure 4.17c shows that in the case of 37% molar fraction of oxygen, the CO cloud keeps growing as the combustion process progresses. This is driven by the high concentration of CO_2 as the background gas. The higher concentration of CO_2 leads to more CO generation through reaction R_4 during the char combustion process and inhibition of oxidation of CO by reaction R_7. However, under 100% O_2, the consumption rate of CO is quicker and it is converted to CO_2 after 7ms (R_7).

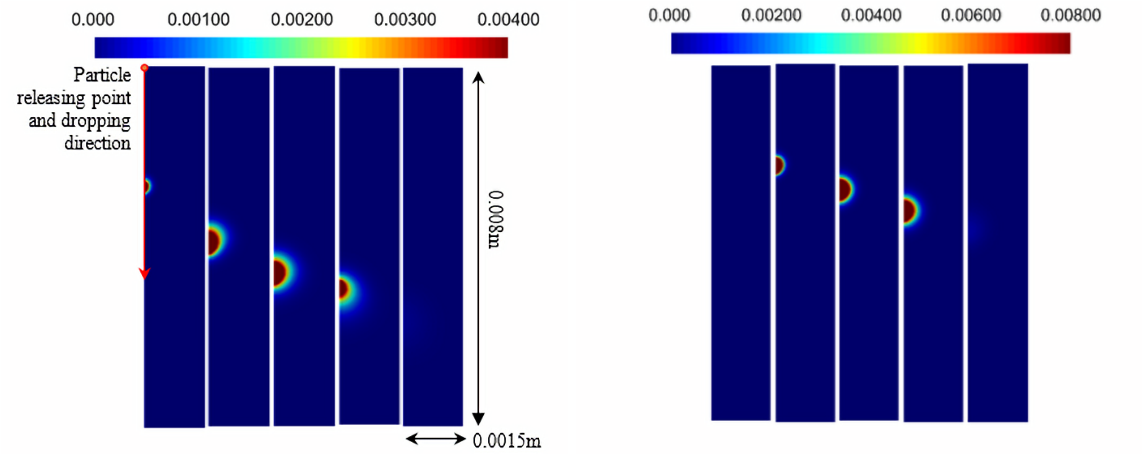

(a) AF: 21%O_2 & 79%N_2 (5-9-13-17-21ms)

(b) AF: 77%O_2 & 23%N_2 (5-7-9-11-13ms)

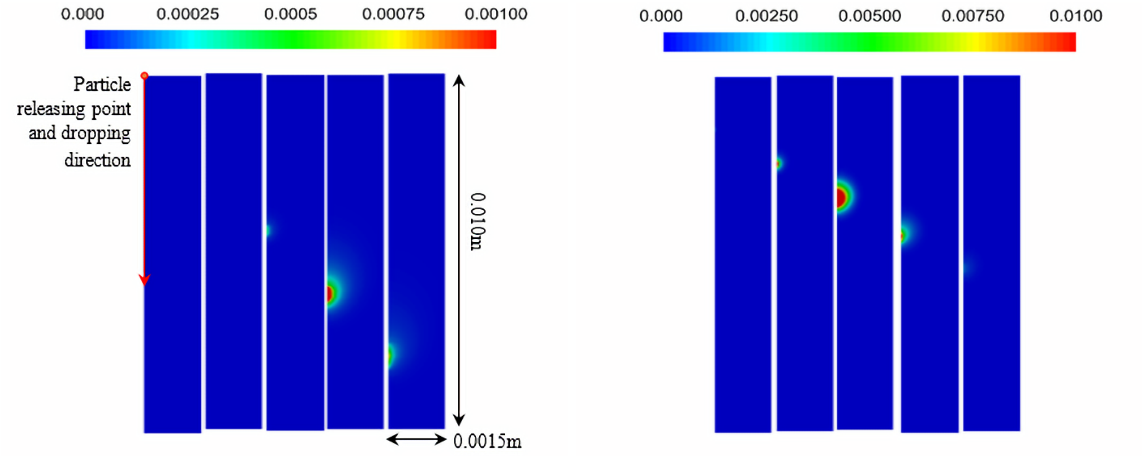

(c) AF: 37%O_2 & 63%CO_2 (2-6-10-14-18ms)

(d) AF: 100%O_2 (3-5-7-9-11ms)

Figure 4.21: Spatio-temporal distribution of mass fraction of H_2 during Bagasse particle combustion. AF: Active Flow.

The temporal variation of CO distribution during single coal particle combustion has been depicted in Fig. 4.18. In both parts of this figure, the existence of CO is limited to a small region around the particle. This is due to the fact that the production of CO is through reactions $R_3 - R_5$, which are all heterogeneous. Figure 4.18a indicates that the thickness of CO concentration boundary layer is larger than that in Fig. 4.18b. This can be explained by noting that shorter duration of the process in Fig. 4.18b, which corresponds to an oxygenated atmosphere, reduces the time available for the diffusion of carbon monoxide into the surrounding atmosphere. Since CO is an intermediate species and by the end of the combustion process it is totally consumed, the right most snapshots in Fig. 4.18b show almost no carbon monoxide. The little amount of CO observed in the last snapshot of Fig. 4.18a is because of the slow kinetics of carbon monoxide oxidation and will eventually disappear due to the oxidation of CO and conversion to CO_2 (R_7).

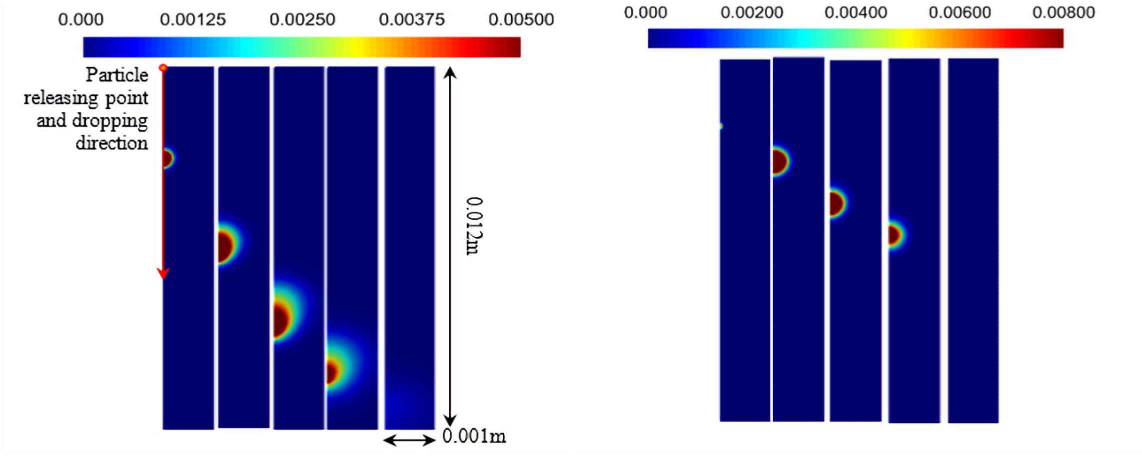

(a) AF: 21%O_2 & 79%N_2 (9-19-29-39-49ms)

(b) AF: 100%O_2 (7-11-15-19-23ms)

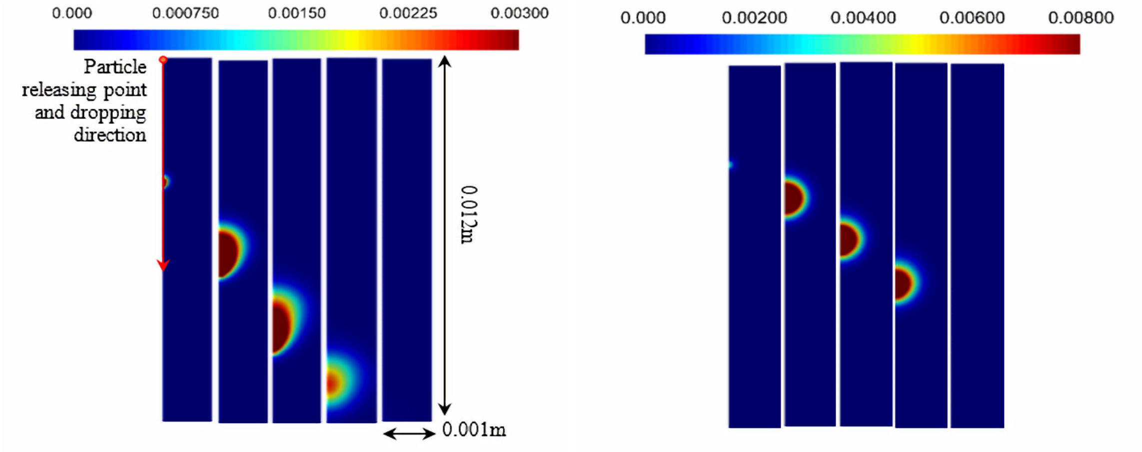

(c) QF: 40%O_2 & 60%N_2 (20-30-40-50-60ms)

(d) QF: 80%O_2 & 20%N_2 (14-20-26-32-38ms)

Figure 4.22: Spatio-temporal distribution of mass fraction of H_2 during DECS-11 particle combustion. AF: Active Flow, QF: Quiescent Flow.

Production of water vapour has been investigated in further details in Fig. 4.19 and Fig. 4.20.The water vapour is a gas phase product as a consequence of the combustion of volatile matters (R_6) and the oxidation of hydrogen (R_8). There is still some water vapour reacting with char to form hydrogen and carbon monoxide by reaction R_5. As a consequence of reaction R_6, gas phase combustion of volatile matters results in the generation of a large amount of water vapour in the early stages of the transient combustion. This can be clearly seen in Fig. 4.19a (for 21% O_2/N_2). Further, at the higher oxygen concentration case, shown in Fig. 4.19b (for 77% O_2/N_2), there is no water vapour prior to ignition, while ignition of the particle generates a dense cloud of water vapour. In both low and high oxygen cases, the water vapour cloud diffuses towards the surrounding gases and at the same time is advected downstream. This behaviour can be clearly seen in Fig. 4.19a. Nonetheless, the downstream motion of the water vapour cloud is less noticeable in Fig. 4.19b. This could be related to buoyancy effects, water molecules are lighter than the average molecular weight of the atmosphere in both investigated cases. However, by increasing the concentration of oxygen the molecular weight of the gaseous atmosphere increases and hence the buoyancy forces acting on the water vapour cloud is magnified. This effect tends to maintain most of the generated water vapour at the top section of the reactor in Fig. 4.19b.

Figures 4.19c and 4.19d report the spatio-temporal distribution of H_2O for 37% O_2 & 63% CO_2 and 100% O_2, respectively. It can be clearly seen that under 37% O_2 and 63% CO_2 environment, a large cloud of water vapour appears once the volatiles combust and it diffuses into the surrounding gases, while being advected downstream. The highest concentration of water vapour cloud appears at the first milliseconds and it becomes much slighter at the last stage of particle combustion due to the continuous diffusion. Under pure oxygen environment, water vapour through the combustion of volatile matter and hydrogen reaction with oxygen is formed after the ignition of particle. It should be noted that the downstream motion of the water vapour cloud is less noticeable at higher oxygen concentration conditions. This could be related to the buoyance effects, which hinder the downstream motion of H_2O cloud in pure oxygen environment. The shorter particle life (Table 4.3) at higher oxygen concentration conditions also results in different positions of biomass particle and changes in H_2O cloud.

Figure 4.20 illustrates the temporal evolution of water vapour during the coal particle burning process. It is clear that a large amount of H_2O is produced after the ignition through oxidation of volatiles (R_6). Water vapour is also produced by the oxidation of hydrogen (R_8), which in turn is produced in a heterogeneous reaction of steam gasification of coal (R_5). As a result, there are two local sources of H_2O. One is located within the flame produced by the combustion of volatiles and the other is around the burning particle. The progressive diffusion of the H_2O cloud into the surrounding atmosphere is apparent in Figs. 4.20a and 4.20b. Similar to that explained with regard to CO_2 in Fig. 4.16, the buoyancy forces hinder the downstream motion of H_2O cloud and thus as time goes on there are two distinctive regions in the reactor with significant H_2O concentration.

Unsteady production and the subsequent consumption of hydrogen during the combustion process is depicted in Fig. 4.21 and Fig. 4.22. Hydrogen is produced by water gas reaction (R_5) and is then consumed by hydrogen oxidation reaction (R_8). The second reaction supports the first one through production of water vapour. Nonetheless, the hydrogen is totally consumed by the end of the particle life time.

In Figure 4.21a indicating single Bagasse particle burning in active 21% O_2/N_2 conditions, the formation of hydrogen continues for the first three demonstrated snapshots. However, after 17ms the amount of hydrogen has decreased and it has completely disappeared by the end of the particle life time. This is because of the oxidation of hydrogen to water vapour by reactions R_8. A similar trend is observed in Fig. 4.21b and below 77% mole fraction of oxygen, wherein hydrogen is produced throughout most of the burning process but is ultimately totally converted to water. Yet, the transient concentrations of hydrogen in Fig. 4.21b are significantly higher than those of Fig. 4.21a. This increase could be attributed to two factors of higher temperature of the gas and water vapour concentration in the vicinity of the burning biomass particle. Hotter gas favours the progress of endothermic water gas reaction and boosts hydrogen production through reaction R_5. At the same time, the added hydrogen results in generation of more water vapour by reaction R_8, which in turn intensifies reactions R_5 and results in depletion of hydrogen. Another contributor to hydrogen production at higher oxygen concentrations is reaction R_6 in which high oxygen concentration leads to fast generation of water vapour and hence accelerates reaction R_5.

The similar trend is observed in Fig. 4.21c for 37% O_2 and 63% CO_2 and Fig. 4.21d for 100% O_2. There is no hydrogen generation prior to ignition in Figs. 4.21c and 4.21d after 8.7ms and 3.7ms, respectively. This is to be expected as devolatilisation does not produce any hydrogen. Hydrogen has a short accumulation period after ignition but has decreased and completely disappeared at the end of the combustion process. This is because of the oxidation of hydrogen to water vapour by reaction R_8. Further, a higher transient concentration of hydrogen is found in Fig. 4.21d. There are two factors that could lead to this increase. First, the higher gas phase temperature of the reactive region and second the higher water vapour concentration surrounding the particle, which could boost reaction R_5.

Figure 4.22 indicates that the oxygen concentration has a strong effect upon H_2 concentration boundary layer during single coal particle combustion. Combustion in air (Fig. 4.22a) generally results in a thicker boundary layer compared to that in pure oxygen (Fig. 4.22b). This is due to the wide diffusion of hydrogen into the surrounding atmosphere in air, which does not happen in pure oxygen. Given that the binary diffusion coefficient of hydrogen in air is not very different to that in oxygen, the disparity can be attributed to the longer process time of combustion in air. This is also clear by comparing the distance that hydrogen plume travels in each case.

4.8 Summary and Conclusions

Transient combustion of single biomass and coal particle burning inside a drop-tube furnace and within an oxygen/nitrogen or oxygen/carbon dioxide atmosphere and for active and quiescent flows was investigated numerically. The process of devolatilisation, combustion of volatiles and char and also post-combustion diffusion of heat and mass into the atmosphere were analysed in detail. The numerical simulations were compared favourably against the existing experimental results for the particle ignition delay time, particle life time and the maximum particle temperature. The results were then used to calculate the spatio-temporal evolutions of the temperature and major gaseous species for the duration of combustion and beyond. The main findings of this chapter can be summarised as follows.

1. Homogeneous combustion of devolatilised gases tends to dominate the temperature and chemical species concentration when the single particle burning at lower concentrations of oxygen.

2. For higher oxygen concentrations, the post combustion homogenous and heterogeneous reactions become increasingly more influential upon the temperature and species concentration fields.

3. For all investigated cases, the highest rate of chemical reactions occurs during combustion of volatiles. The initation of char combustion is always associated with slowing down the reactions.

4. The combustion behaviour of single biomass particle is significantly different in O_2/N_2 and O_2/CO_2 atmospheres. The volatile matters combust prior to the ignition of the particle in O_2/CO_2, while the volatiles and chars combust sequentially in O_2/N_2 conditions.

Chapter 5

Prediction of NO_x and SO_x emissions from a single biomass particle

As the nitrogen and sulphur in a single biomass particle is quite low, the NO_x and SO_x formations can be computed by post-processing. Therefore, based on the validated numerical combustion model, the NO_x and SO_x modelling are conducted to investigate the pollutants emission characteristics under varying oxygen concentrations and different background gas environments. This chapter presents the calculated NO and SO_2 PPM and their emission rates when a single biomass particle burning under O_2/N_2 and O_2/CO_2 gas conditions with oxygen concentration varying from 21% to 100%. Further, the formation process of N species (NO, NH_3, H_2S) and S species (SO_2, H_2S, SO_3) are tracked under various gas conditions to analyse the effects of oxygen concentration and CO_2 background gas.

5.1 Validation of partition assumption

As mentioned in section 2.3, the nitrogen and sulphur contained in biomass particle are assumed to be distributed evenly between the volatile matters and the char. The mass fraction of nitrogen and sulphur in Bagasse particle which was used in this work are given in Table 4.1, but the distribution of N and S in the volatile and char are unknown. The specific distribution varies in different kinds of biomass fuel and it needs to be measured for each kinds of fuel. The total amounts of the NO_x and SO_x emissions are influenced by the distribution of N and S in the volatile and char, and the partition fraction of intermediates. However, the trends under different runs of fraction assumptions are nearly the same, as confirmed by Blaid et al. [159] who ran five cases with different partition assumptions to match with the experimental results. In order to conduct the qualitative analysis of NO_x and SO_x emissions under various gas conditions, five kinds of partition assumptions of nitrogen in the volatile and char are used to validate that the changing trends of NO_x emission are the same under different chemical composition of the surrounding atmospheres. The partition assumptions are shown in Table 5.1.

Table 5.1: Partition assumptions of Nitrogen

	Case 1	Case 2	Case 3	Case 4	Case 5
Partition of Volatile-N	50%	30%	70%	50%	50%
Partition of Char-N	50%	70%	30%	50%	50%
Partition of HCN	50%	50%	50%	60%	30%
Partition of NH_3	10%	10%	10%	20%	30%
Partition of NO	40%	40%	40%	20%	40%

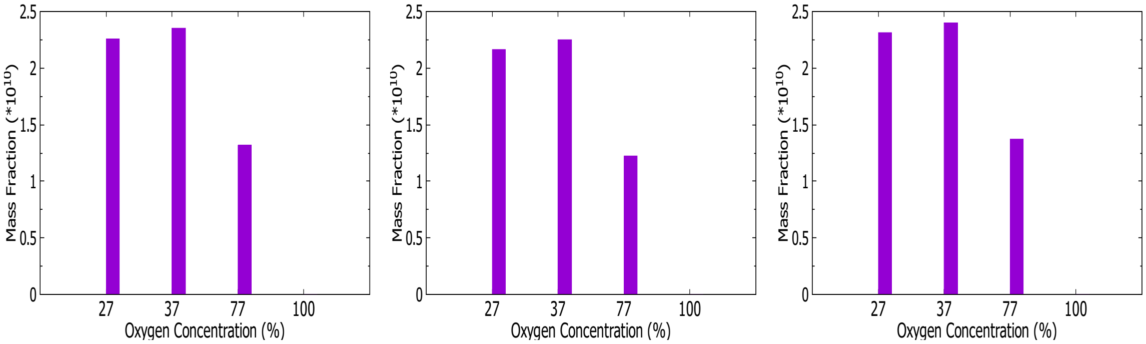

(a) Case 1 (b) Case 2 (c) Case 3

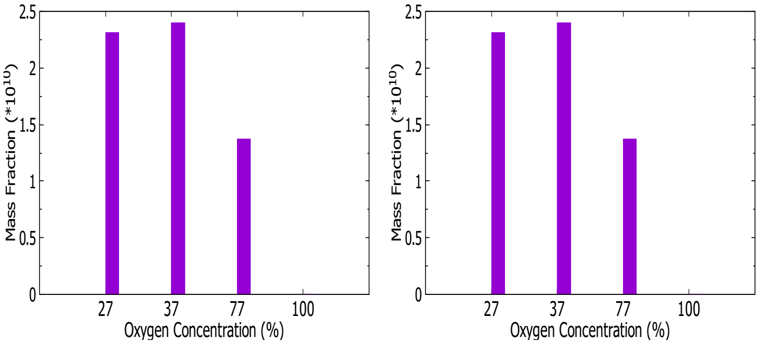

(d) Case 4 (e) Case 5

Figure 5.1: Mass fraction of NO in O_2/N_2 environments with partition assumptions (t=100ms).

The changing trend of total mass fraction of NO and NH_3 and the formation process of NO and NH_3 during combustion under different gas conditions are used to validate the partition assumption. When presenting the formation process, the percentage of species is in terms of the peak value. The compared results are shown in Figs 5.1-5.6. It is clear from these figures that, although the total amounts vary, the changing trends under varying gas conditions for different partition assumptions are the same in general. This indicates that changes in distribution of nitrogen in the volatile and char does not influence the qualitative analysis in any considerable way. The validation are done for sulphur particle assumption and the conclusion is the same. The results are given in Appendix C in detail. Given this, the qualitative analysis to investigate the effects of oxygen concentration and CO_2 background gas on NO_x and SO_x emissions can be

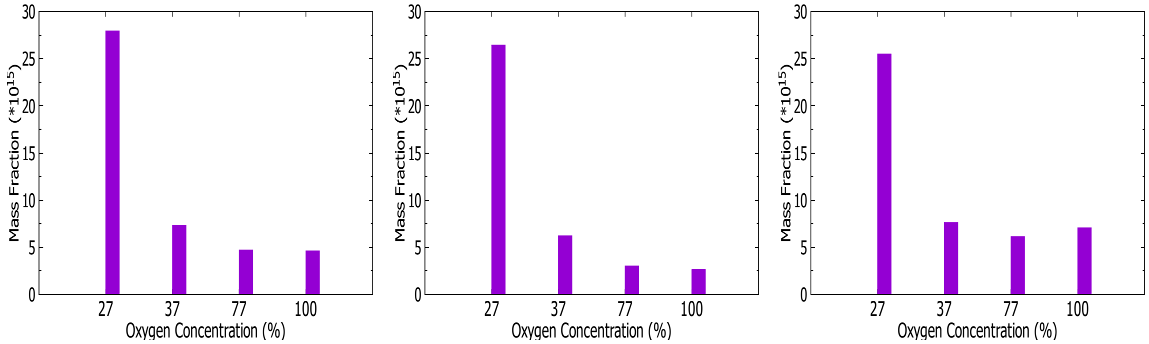

(a) Case 1 (b) Case 2 (c) Case 3

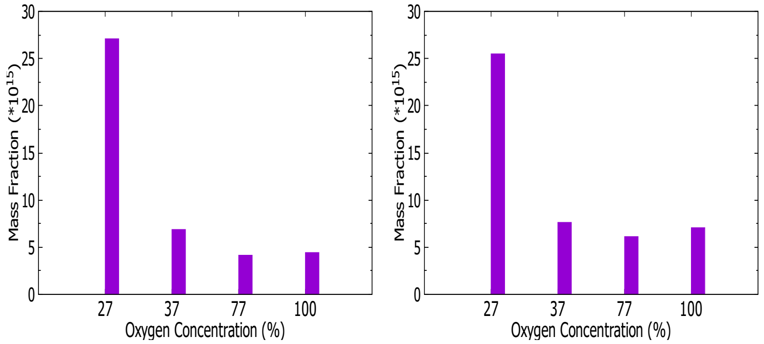

(d) Case 4 (e) Case 5

Figure 5.2: Mass fraction of NO in O_2/CO_2 environments with partition assumptions (t=100ms).

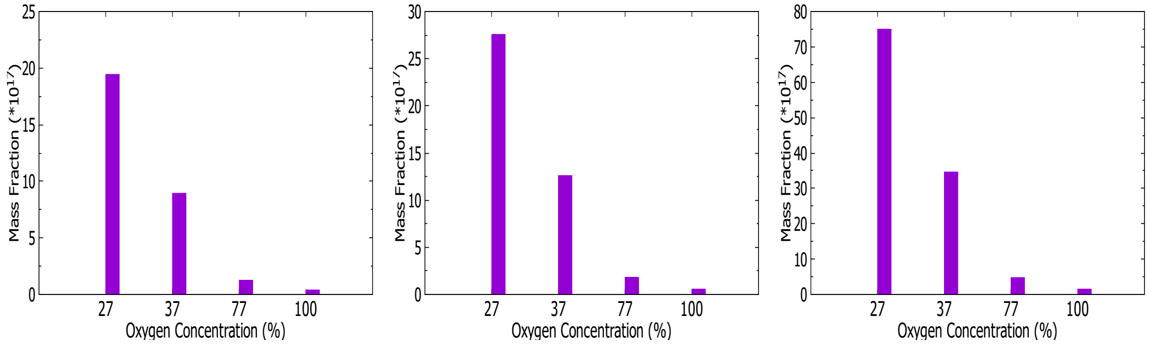

(a) Case 1 (b) Case 2 (c) Case 3

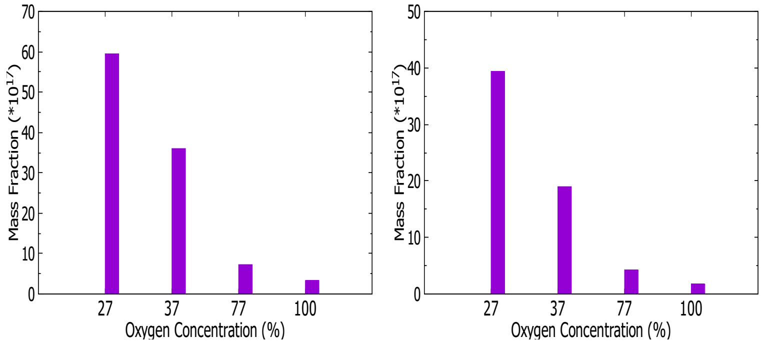

(d) Case 4 (e) Case 5

Figure 5.3: Mass fraction of NH_3 in O_2/N_2 environments with partition assumptions (t=100ms).

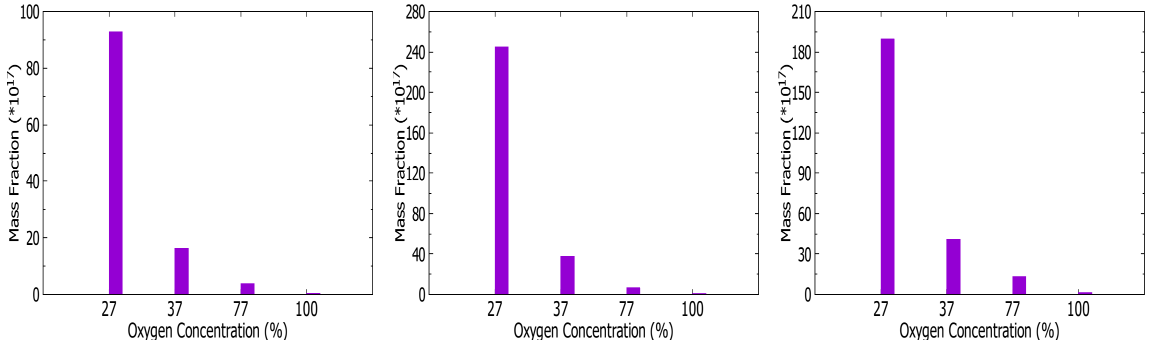

(a) Case 1 (b) Case 2 (c) Case 3

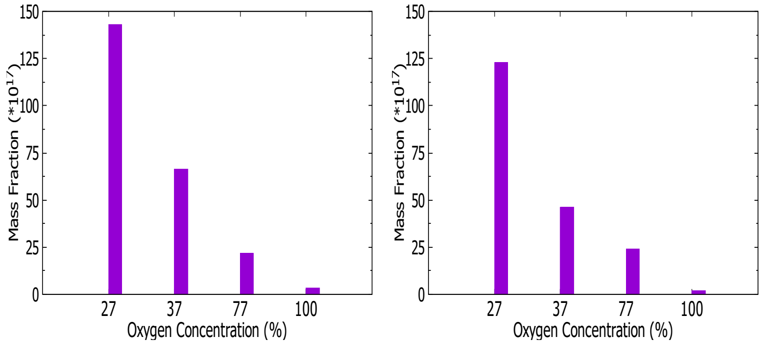

(d) Case 4 (e) Case 5

Figure 5.4: Mass fraction of NH_3 in O_2/CO_2 environments with partition assumptions (t=100ms).

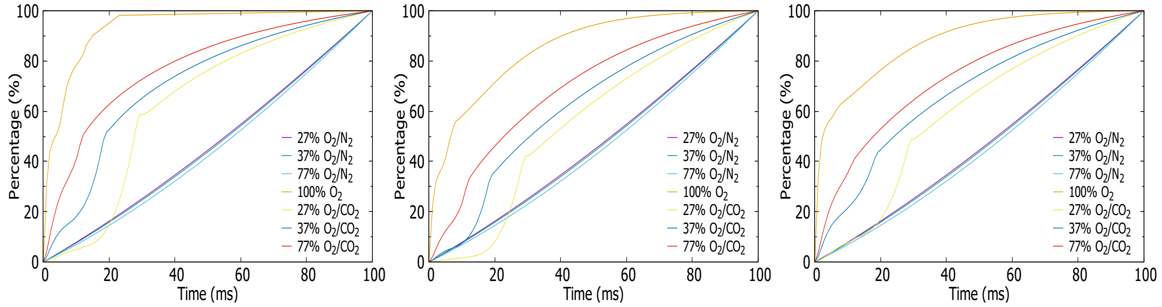

(a) Case 1 (b) Case 2 (c) Case 3

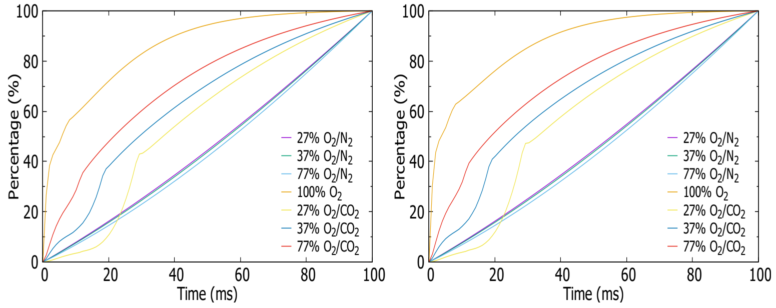

(d) Case 4 (e) Case 5

Figure 5.5: NO formation during combustion process under varying gas conditions with partition assumptions.

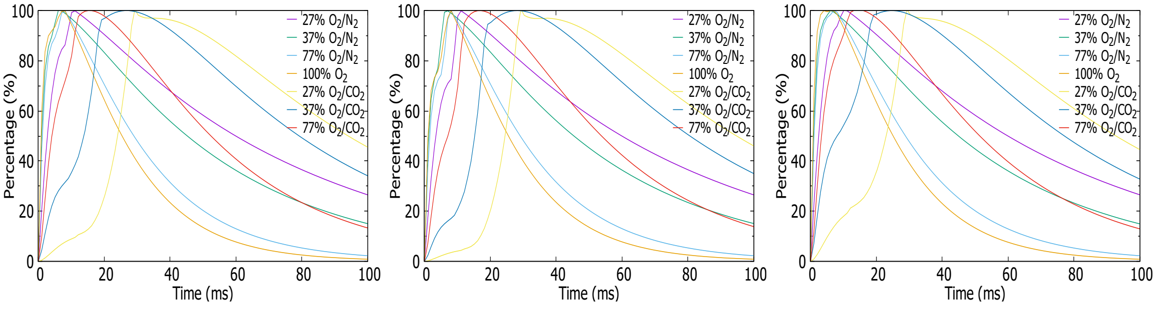

(a) Case 1 (b) Case 2 (c) Case 3

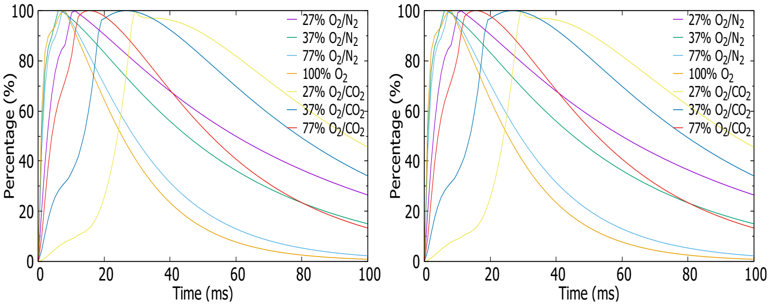

(d) Case 4 (e) Case 5

Figure 5.6: NH_3 formation during combustion process under varying gas conditions with partition assumptions.

conducted based on a specified partition assumption. In this work, case 1 of Table 5.1is selected.

5.2 Overall NO and SO_2 PPM

The overall NO and SO_2 PPM under varying O_2/N_2 and O_2/CO_2 conditions in the late stage (t=100ms) of single biomass particle combustion are presented in Fig. 5.7 and 5.8. Referring to NO PPM (Fig. 5.7), it is clearly seen that when replacing the background gas from N_2 to CO_2, the overall NO PPM is sharply reduced, and is about five orders of magnitude lower in all oxygen concentrations. This is because compared with O_2/N_2 environments, there is no formation of thermal-NO_x and only fuel-NO_x is generated under O_2/CO_2 gas atmospheres during biomass particle combustion process. This comparison also confirms that thermal-NO_x accounts for most of NO emissions in high temperature O_2/N_2 based combustion mode and cannot be ignored. Further, Fig. 5.7 shows that, under either N_2 or CO_2 based gas conditions, the higher the oxygen concentration correlates with the lower NO PPM emissions. There is a significant decrease in NO PPM under O_2/N_2 atmospheres when increasing oxygen concentration, and the NO emissions generated in pure oxygen condition is negligible compared with the other cases. Under O_2/CO_2 gas conditions, the NO PPM drops sharply when oxygen concentration increases from 27% to 37%, but it decreases slightly when oxygen concentration increased up to 77% and 100%. This is because the yield of HCN and NH_3 decreased due to less CO formation and higher combustion temperature at higher oxygen concentrations [85] [174].

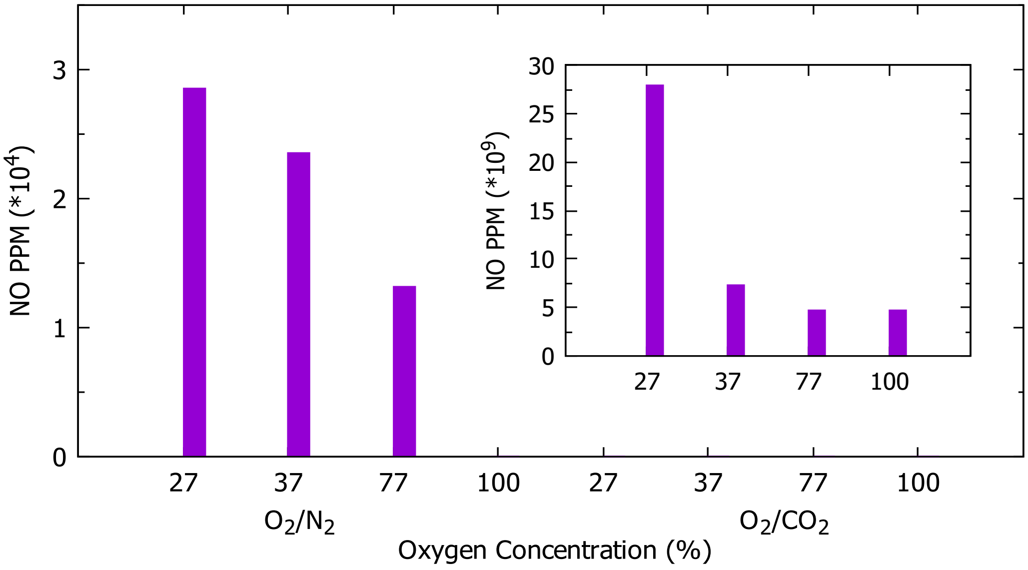

Figure 5.7: Overall NO PPM under various gas conditions

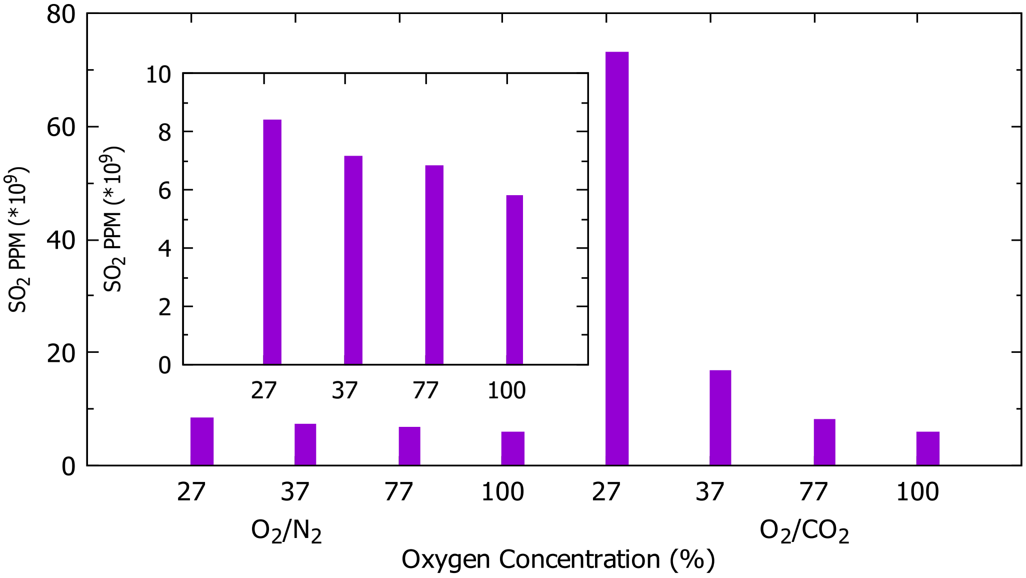

Figure 5.8: Overall SO$_2$ PPM under various gas conditions.

A comparison of SO$_2$ PPM generations is displayed in Fig. 5.8. It should be noted that, there is more SO$_2$ generated in CO$_2$ based atmospheres than that in N$_2$ based cases, and the difference is about two orders of magnitude. In particular, under O$_2$/N$_2$ gas atmospheres, the amount of SO$_2$ formed during the combustion process decreased rather moderately with increases in oxygen concentration. The case with 27% mole fraction of oxygen generated the maximum SO$_2$ in all investigated cases, but the difference in SO$_2$ generation is small when oxygen concentration raises to 37%, 77% and 100%. However, under CO$_2$ based gas conditions, the oxygen concentration has a much greater impact on SO$_2$ PPM. This is particularly the case at lower O$_2$

concentrations, as SO_2 PPM dropped markedly when oxygen concentration increased from 27% to 77%. Yet, there is only a small difference between SO_2 generation under 77% and 100% mole fraction of oxygen.

5.3 Emission rates of NO and SO_2

Pollutant emission rate referring to the mass of pollutant emitted per unit heat produced by the fuel is introduced to compare pollutant emissions between different combustion conditions. The pollutant emission rate P_E (ngJ) is calculated by the empirical formula provided in Ref. [86].

$$P_E = C_p \cdot F_{od} \cdot D_{corr} \tag{5.1}$$

Here, C_p (ng/m^3) is the concentration of pollutant, F_{od} is the oxygen-based dry factor, and D_{corr} is the dilution correction factor. These are calculated by the following equations:

$$C_p(NO) = 1.880 \cdot 10^6 \cdot [NOPPM] \tag{5.2}$$

$$C_p(SO_2) = 2.619 \cdot 10^6 \cdot [SO_2PPM] \tag{5.3}$$

$$\begin{aligned} F_d = \frac{R \cdot T}{P \cdot LHV} \cdot [\frac{MP_C}{M_C \cdot C_{O_2feed}} + \frac{\left[100/C_{O_2feed} - 1\right] \cdot MP_H}{400 \cdot M_H} + \frac{MP_S}{M_S \cdot C_{O_2feed}} \\ + \frac{MP_N}{200 \cdot M_N} + \frac{\left[100/C_{O_2feed} - 1\right] \cdot MP_O}{200 \cdot M_O}] \end{aligned} \tag{5.4}$$

$$D_{corr} = [C_{O_2feed} - C_{O_2flue}]/C_{O_2feed} \tag{5.5}$$

where, R is the ideal gas constant, P is the pressure, T is the temperature, LHV is the heating value of fuel, MP_j is the weight percentage of species j in fuel, M_j is the molecular weight of species j, and C_{O_2feed} and C_{O_2flue} are the oxygen concentration in the feed and flue gas, respectively.

The results of NO and SO_2 emission rates under varying O_2/N_2 and O_2/CO_2 atmospheres during single biomass particle combustion are presented in Figs. 5.9 and 5.10, respectively. It can be seen that, in both O_2/N_2 and O_2/CO_2 gas atmospheres, the emission rate of NO and SO_2 diminishes when oxygen concentration increases from 27% to 100%. The NO emission rate differed greatly under O_2/N_2 and O_2/CO_2 gas conditions and it was much smaller when there was no N_2 in the flow. For the emission rate of SO_2, it is about ten times larger in O_2/CO_2 than O_2/N_2 gas conditions. In general, the behaviour of NO and SO_2 emission rates are consistent with the overall emissions PPM which are discussed in the above section.

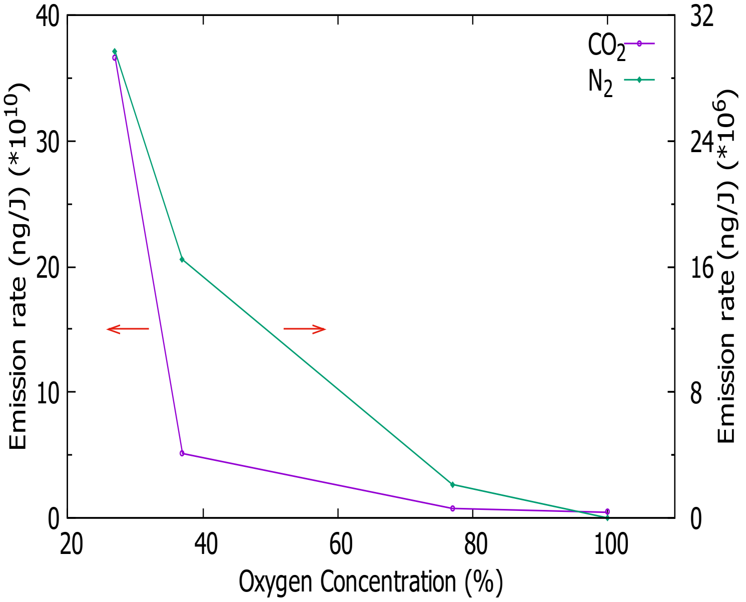

Figure 5.9: Emission Rate of NO under various gas conditions.

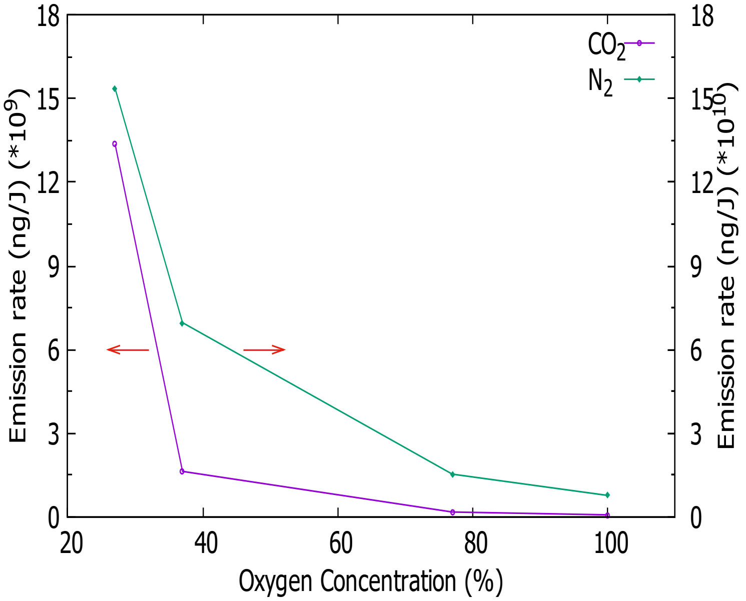

Figure 5.10: Emission Rate of SO$_2$ under various gas conditions.

5.4 Generation of N and S species during combustion process

The formation process of N species (NO, NH_3, H_2S) and S species (SO_2, H_2S, SO_3) is investigated in detail by comparing with particle mass reduction during single biomass particle combustion. The time traces of pollutants formation compared with biomass particle mass loss are presented in Figs. 5.11-5.14. The compared pollutants formation percentage in devolatilization and char combustion stages under varying oxygen concentration conditions are shown in Figs. 5.15-5.18.

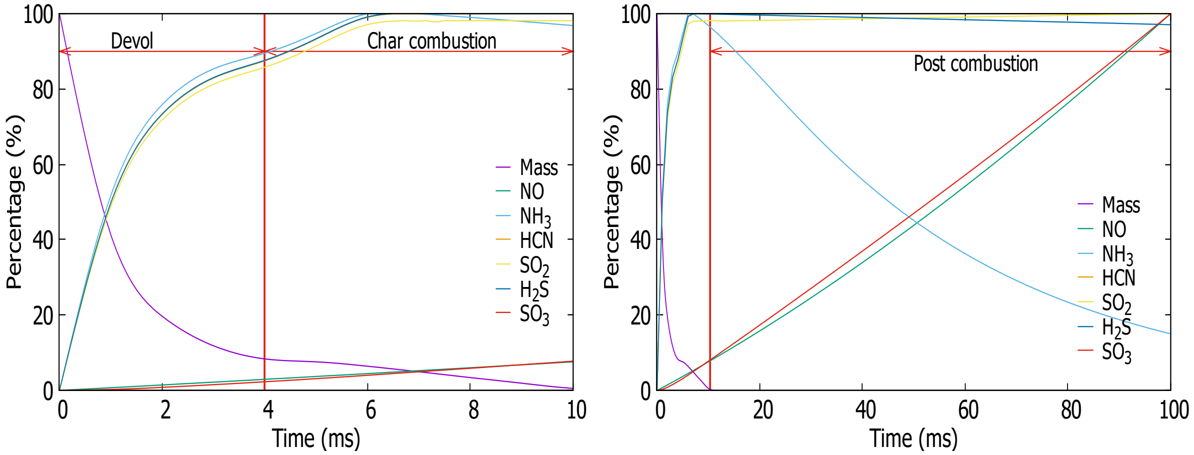

(a) (b)

Figure 5.11: Species VS particle mass reduction during single Bagasse particle combustion in 37% O_2 & 63% N_2.

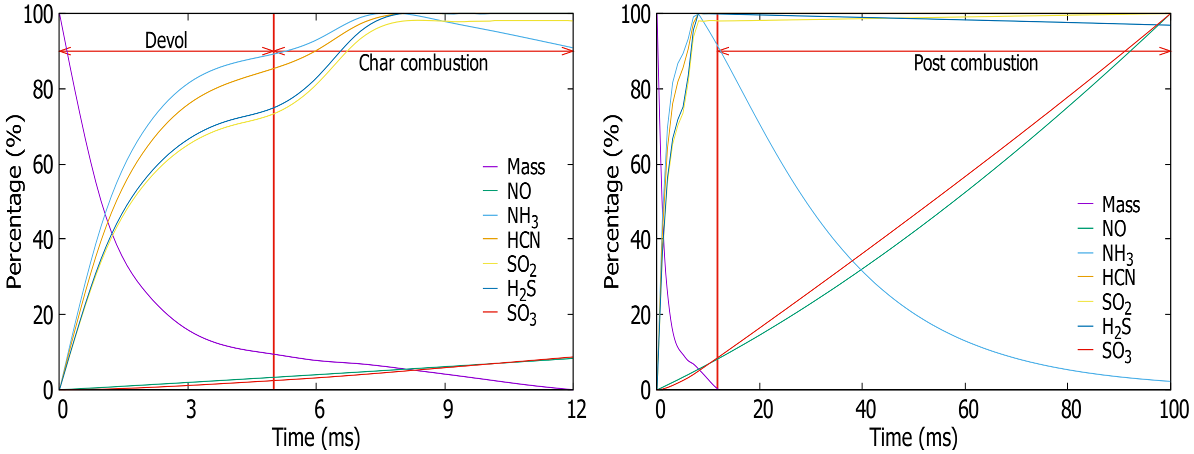

(a) (b)

Figure 5.12: Species VS particle mass reduction during single Bagasse particle combustion in 77% O_2 & 23% N_2.

Figure 5.11 shows the evolution processes of particle mass reduction and N and S species formation when single biomass particle burning in 37% O_2/N_2 gas condition. The biomass particle mass reduces rapidly when devolatilization happens and about 85% of the initial mass is lost during this stage. The char combustion accounts for the remaining 15% of total mass reduction. The two proportions are quite similar to the proximate analysis of the fuel. Due to the different reaction rates of devolatilization and char combustion, the changing of particle mass has two different slopes in the two stages, and different amounts of N and S are released at different stages of combustion. Therefore, the formation of N and S species differs as well. It can be clearly seen from Fig. 5.11 that, nearly all NH_3, H_2S, SO_2 and H_2S are formed during the period of particle combustion which includes the devolatilization and char combustion stages, and the post-combustion stage where the particle is extinct contributes little. However, the amounts

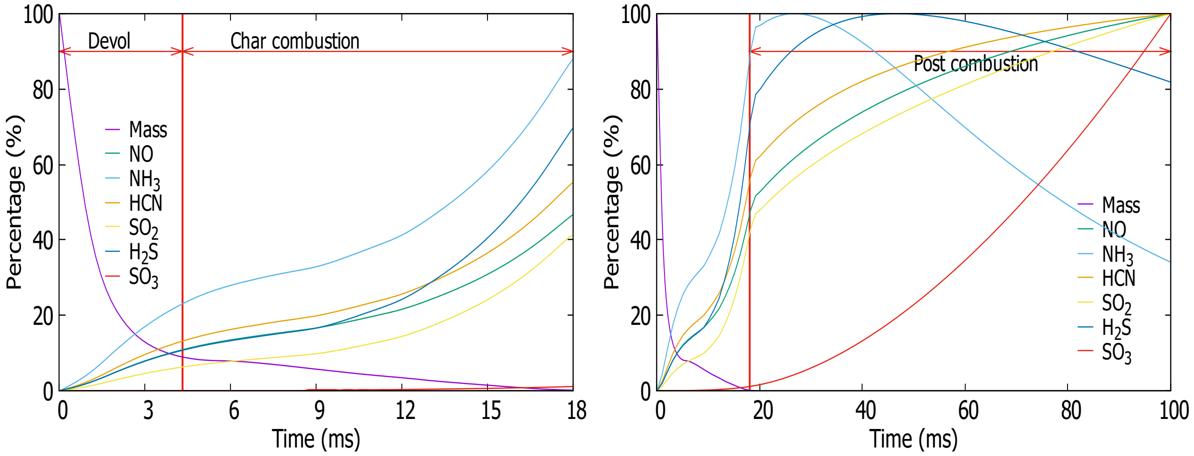

(a) (b)

Figure 5.13: Species VS Particle mass reduction during single Bagasse particle combustion in 37% O_2 & 63% CO_2.

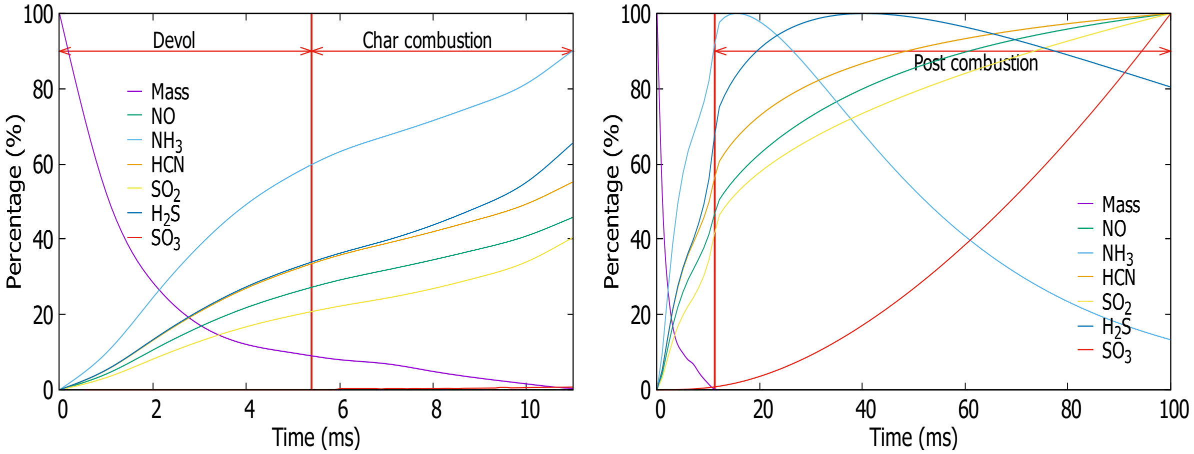

(a) (b)

Figure 5.14: Species VS Particle mass reduction during single Bagasse particle combustion in 77% O_2 & 23% CO_2.

of NO and SO_3 keep increasing in both particle combustion and post-combustion stages.

In particular, about 90% of NH_3, H_2S, SO_2 and H_2S are produced in the first 4ms and the rest 10% are formed in the later 6ms. These two instants-4ms and 10ms, are correspond to the particle ignition delay time and particle life time when the particle burning in 37% O_2/N_2 atmosphere. This indicates that about 90% of these species are formed during devolatilization process and the rest (10%) during char combustion process. These species reach the peak amount in the late stage of char combustion. Further, for the species of NH_3 and SO_2, there is no decrease after the particle vanished completely. This indicates that all the reactions related to the generation and consumption of the species are competitively same during the post-combustion stage. However, a little amounts of NH_3 continues to be consumed to generate more NO in the post-combustion stage and little H_2S is transferred to SO_2 which is converted to SO_3 finally. It should be noted that only 10% of NO and SO_3 are formed during particle combustion process, and most (about 90%) of these pollutants are generated in the post-combustion stage. This is because N_2 existing in the flow is transferred to NO through thermal-NO_x all the time and thus the amount of NO rises, and SO_3 is formed when SO_2 reacts with O_2 until it is completely depleted.

The formation processes occurring in 77% O_2/N_2 gas condition are shown in Figure 5.12. A comparison between Fig. 5.11 and 5.12 indicates that, when the oxygen concentration increases from 37% to 77%, the overall variant trend of NO_x and SO_x species are similar. However, the accumulation rate of NH_3 and SO_2 are much slower than that of HCN and H_2S in 77% O_2/N_2 gas atmosphere, while they are quite close in 37% O_2/N_2 condition. Further, the consumption rate of NH_3 during the post-combustion stage is much faster in higher oxygen concentration condition. This is because the higher oxygen concentration accelerates the conversion rates of NH_3 to NO and SO_2 to SO_3. Moreover, the inflection points, which indicates different slopes and stages are correspond to biomass particle combustion in 77% O_2/N_2 gas condition. The first inflection point is around 5ms and the time for HCN and SO_2 reaching peak value is around 11ms.

Figure 5.13 presents the mass and emissions species evolution processes under 37% O_2/CO_2 atmosphere. Evidently, replacing N_2 by O_2 influences the formation process of the pollutants significantly. NO, HCN, SO_2 continue to increase monotonically, while they have three different stages. The first stage corresponds to 0-4ms, which is the particle ignition delay time. At this stage, about 10% NO, HCN and SO_2 are formed. The second stage is 4-18ms, which is related to the char combustion process. The generation rates of NO, HCN and SO_2 become larger at this stage and eventually 50% of NO, 60% of HCN and 50% of SO_2 are produced. After the extinction of the biomass particle, the amount of NO, HCN and SO_2 keep increasing in a slow rate and the formation process of these species continues. For the species of NH_3 and H_2S, the amounts accumulate at the beginning with three different increasing rate, and they decrease later. In addition, compared with 37% O_2/N_2 gas condition, less NH_3 but more H_2S are consumed in the post-combustion stage in 37% O_2/CO_2 gas condition. Considering the formation of SO_3, the partition of SO_3 formed during the particle existing stage (0-18ms) only accounts for about 2% of total SO_3 emission. Almost all SO_3 is generated after the particle burning out (post-combustion stage). Figure 5.14 gives the results of 77% O_2/CO_2 gas condition. About 25% NO and SO_2 and 30% HCN are produced during particle ignition delay time (0-5ms). Another 25% NO and SO_2 and 30% HCN are formed during particle char combustion process (5ms-11ms), while the rest are formed in post-combustion process.

By comparing figures referring to O_2/CO_2 and O_2/N_2 gas atmospheres, it can be easily found that, the emissions formation process is quite different in O_2/CO_2 gas atmosphere from O_2/N_2 gas atmospheres. As there was no N_2 in the flow, all NO was generated from fuel-N, which is the same as NH_3 and HCN. Therefore, the NO shares the same trend as HCN when particle burning in O_2/CO_2 gas atmosphere. Meanwhile, CO_2 in the flow can restrain the reaction rates of fuel-N and fuel-S, especially volatile-N and volatile-S, and then extends the time that fuel-N and fuel-S are converted to NO_x and SO_x species.

The percentages of HCN, NH_3, SO_2 and H_2S formed in different gas conditions during devolatilization and char combustion process (Devol- and Char- respectively) are compared to show the influences of oxygen concentration and CO_2 as background gas on pollutants formation. The results are shown in Tables 5.2- 5.3 and Figs. 5.15-5.18.

Table 5.2: Percentage of HCN and NH_3 formation during Bagasse particle combustion

Gas Conditions	Devol-HCN	Char-HCN	Devol-NH_3	Char-NH_3
27% O_2/N_2	89.71	12.23	89.12	5.86
37% O_2/N_2	87.51	12.44	89.49	6.15
77% O_2/N_2	85.61	14.55	89.21	10.82
100% O_2	81.67	18.29	89.93	10.23
27% O_2/CO_2	9.32	55.71	18.42	82.21
37% O_2/CO_2	12.42	48.14	21.82	74.45
77% O_2/CO_2	31.82	23.45	57.19	40.01

Table 5.3: Percentage of SO_2 and H_2S formation during Bagasse particle combustion

Gas Conditions	Devol-SO_2	Char-SO_2	Devol-H_2S	Char-H_2S
27% O_2/N_2	91.52	9.28	92.33	18.74
37% O_2/N_2	85.79	12.36	87.64	22.27
77% O_2/N_2	73.31	24.71	74.91	24.85
100% O_2	69.15	10.6	70.76	29.11
27% O_2/CO_2	3.86	53.71	5.72	78.32
37% O_2/CO_2	5.94	40.54	10.13	67.73
77% O_2/CO_2	19.73	26.32	32.25	42.35

It can be seen that, under O_2/N_2 gas atmospheres, over 80% of the N-intermediate HCN is formed during the devolatilization process and less than 20% is formed during the char combustion process. Further, the oxygen concentration does not significantly affect the formation

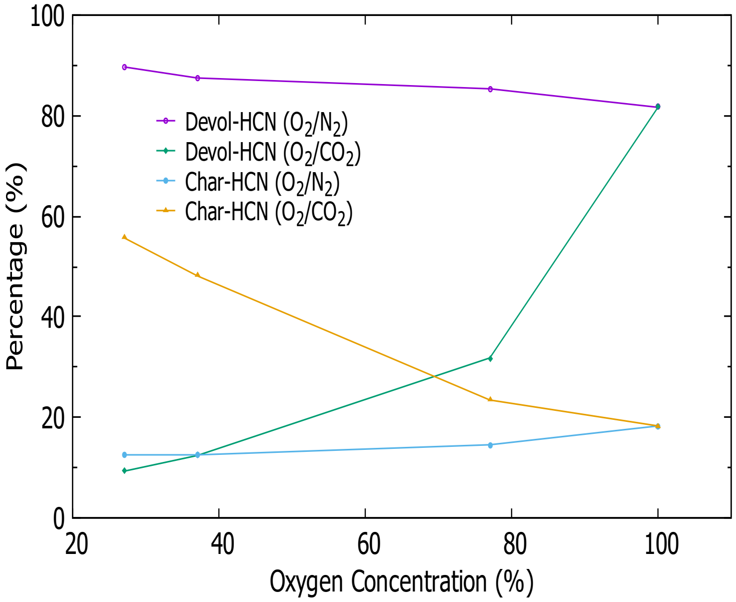

Figure 5.15: HCN formation percentage in devolatilization and char combustion stages under different gas conditions.

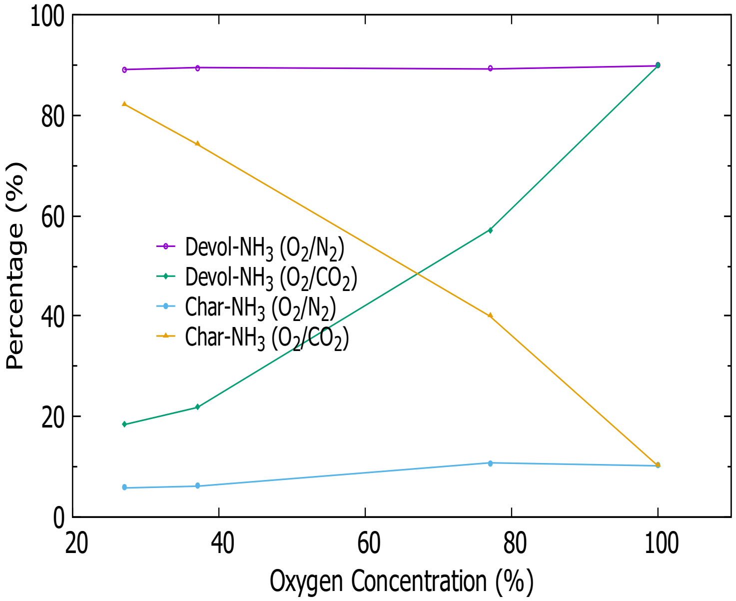

Figure 5.16: NH_3 formation percentage in devolatilization and char combustion stages under different gas conditions.

percentage. Devol-HCN slowly declines from 89.7%, 87.5%, 85.35% to 81.67% when oxygen concentration changes from 27% to 100%. Char-HCN slightly increases from 9.89%, 12.4%, 14.55% to 18.29%. Nevertheless, under O_2/CO_2 gas atmospheres, the effect of oxygen concentration is obvious. Higher concentration of oxygen greatly prompts the production of Devol-HCN and less HCN is formed along with char combustion. A similar changing trend is observed for Devol-NH_3 in O_2/CO_2 and Char-NH_3 under both O_2/N_2 and O_2/CO_2 gas atmospheres along with the changing of oxygen concentration. The formation percentage of NH_3 during the

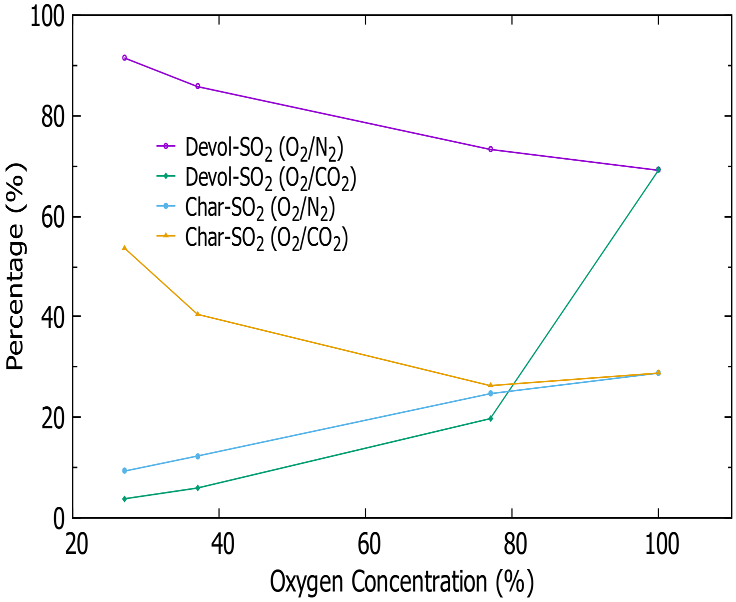

Figure 5.17: SO_2 formation percentage in devolatilization and char combustion stages under different gas conditions.

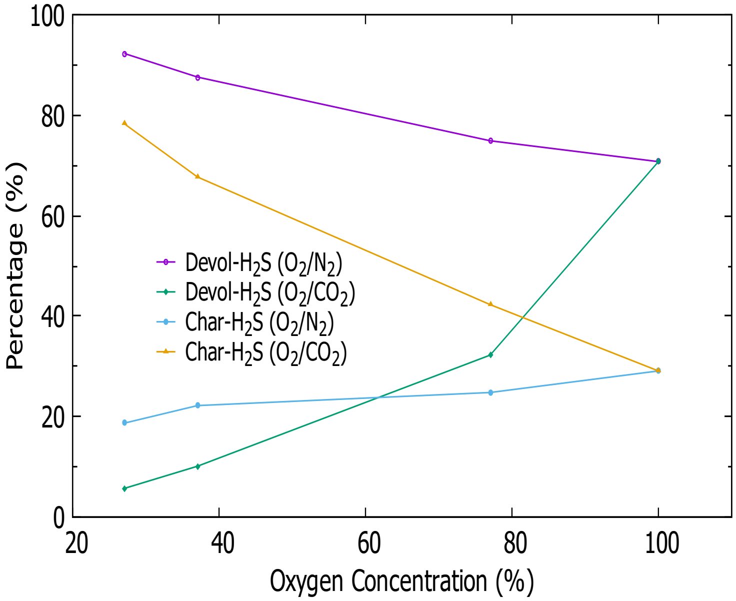

Figure 5.18: H_2S formation percentage in devolatilization and char combustion stages under different gas conditions.

stage of particle devolatilization under O_2/N_2 environment nearly keeps at 89% whent the oxygen concentration increases from 27% to 100%.

Considering the formation of SO_2, the devol-SO_2 and char-SO_2 show the opposite changing trend in O_2/N_2 and O_2/CO_2 gas atmospheres. Devol-SO_2 decreases while char-SO_2 increases when oxygen concentration becomes larger under O_2/N_2 gas conditions. While replacing N_2 with CO_2, the changing trend of devol-SO_2 and char-SO_2 is opposite when increasing oxygen concentration. Devol-SO_2 only accounts for 5.94% in 37% O_2, but it raises up to 19.74% in 77% O_2 and up to 69.15% in 100% O_2. The proportion of char-SO_2 accounts from 40.55%, 20.75% to 28.71% of the SO_2 emissions accordingly. The similar trend is found when considering the effects of oxygen concentration on the formation of H_2S during different combustion stages. Under O_2/N_2 environment, the maximum formation percentage of H_2S during the devolatilization stage appears at the lowest oxygen concentration (27%). While under O_2/CO_2 environment, char-H_2S dominates the H_2S formation in lower oxygen concentration conditions instead.

5.5 Summary and Conclusions

The NO_x and SO_x modelling were conducted based on the validated combustion model. Qualitative analysis about the influence of oxygen concentration and O_2/CO_2 environment on the pollutant emissions during single biomass particle combustion was conducted. The overall NO and SO_2 PPM and the emission rate of NO and SO_2 under O_2/N_2 and O_2/CO_2 atmosphere with varying oxygen concentration were analysed. Further, the formation process of N and S pollutant species during the transient combustion process is tracked and compared. The main findings of this work can be summarised as follows.

- It was found that more NO_x is emitted in O_2/N_2 atmospheres than in O_2/CO_2 due to the strong formation of thermal NO_x. Yet, there are is less SO_2 emission in nitrogen containing atmosphere compared to those in carbon dioxide containing atmospheres.
- NO emission rate is higher in O_2/N_2 than O_2/CO_2 atmospheres, while SO_2 emission rate has the opposite trend. When oxygen concentration increases, the emission rates of NO and SO_2 decreased under both atmospheres.
- In O_2/CO_2 atmospheres, oxygen concentration has a greater influence on the formation of NO_x. Finally, SO_x pollutants are observed to be quite sensitive to oxygen concentration in both O_2/N_2 and O_2/CO_2 environments.

Chapter 6

Gas-phase entropy generation in single particle combustion

This chapter reports the study of the gas-phase entropy generation during the coal and biomass particle transient combustion process. The irreversibilities (entropy) are generated due to the irreversible heat transfer, mass transfer and chemical reactions. Generation of entropy is a thermodynamic property of a system. As the numerical model has been rigorously validate against the experimental date, meaning that the unsteady thermodynamics of the reactive flow is simulated correctly, the entropy generation can be calculated by the spatio-temporal model developed on the basis of the earlier work [120] [181]. Therefore, it can be concluded that the approach method introducd in Chapter 2.4 is appropriate to investigate the influences of oxygen concentration on irreversibilities caused by thermal, mass and chemical reactions during the single particle combustion process.

The cases of single Bagasse and DECS-11 particle burnt under active flow with oxygen concentration varying from 21% to 100% and single DECS-11 particle burnt under quiescent flow with oxygen concentration varying from 21% to 100% are considered. The different entropy generation rates per unit volume at different stages and the history and total entropy generation of different irreversibilities during the single particle combustion are investigated in detail.

6.1 Spatio-temporal evolution of entropy generation rate per unit volume

Figures 6.1 and 6.2 demonstrate the local entropy generation during the single Bagasse particle combustion in 37%O_2 & 63%N_2 and 77%O_2 & 23%N_2 under active state, respectively. The thermodynamic irreversibilities of the process due to heat transfer, mass transfer and chemical reactions described in Eqs. 3.74, 3.77 and 3.76 were presented separately. The spatial distributions of entropy generation by each of these sources for selected instances of time and oxygen concentrations in the atmosphere are displayed in these figures. The horizontal axes of the subfigures in these two figures show the radial distance from the reactor centreline and the vertical axes represent the downward vertical distance from the particle releasing point.

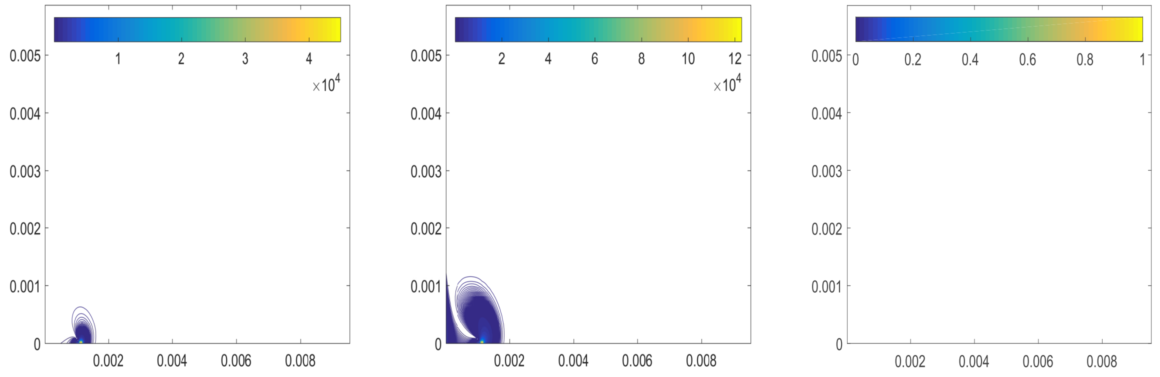

(a) $E_h, \ t = 2ms$ (b) $E_m, \ t = 2ms$ (c) $E_r, \ t = 2ms$

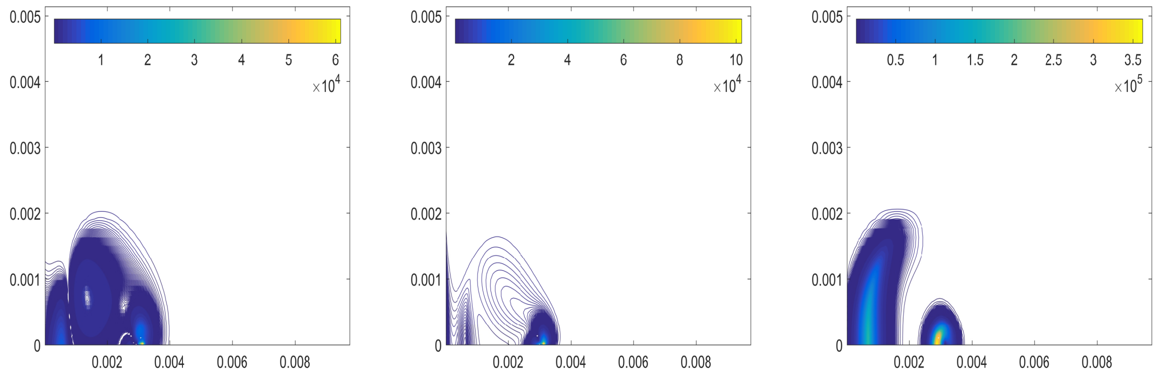

(d) $E_h, \ t = 6ms$ (e) $E_m, \ t = 6ms$ (f) $E_r, \ t = 6ms$

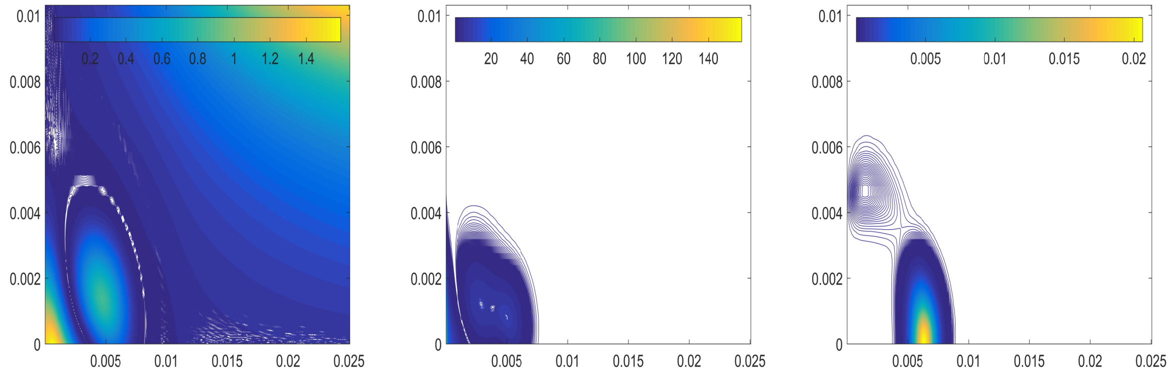

(g) $E_h, \ t = 20ms$ (h) $E_m, \ t = 20ms$ (i) $E_r, \ t = 20ms$

Figure 6.1: Spatio-temporal evolution of entropy generation rate per unit volume (W/m^2K) during Bagasse particle combustion under active flow, 37%O_2 & 63%N_2.

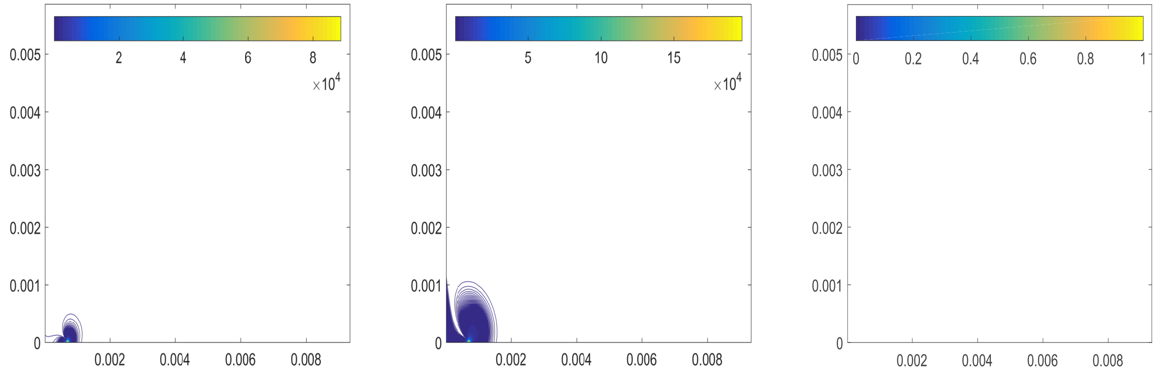

(a) $E_h, \;\; t = 2ms$ (b) $E_m, \;\; t = 2ms$ (c) $E_r, \;\; t = 2ms$

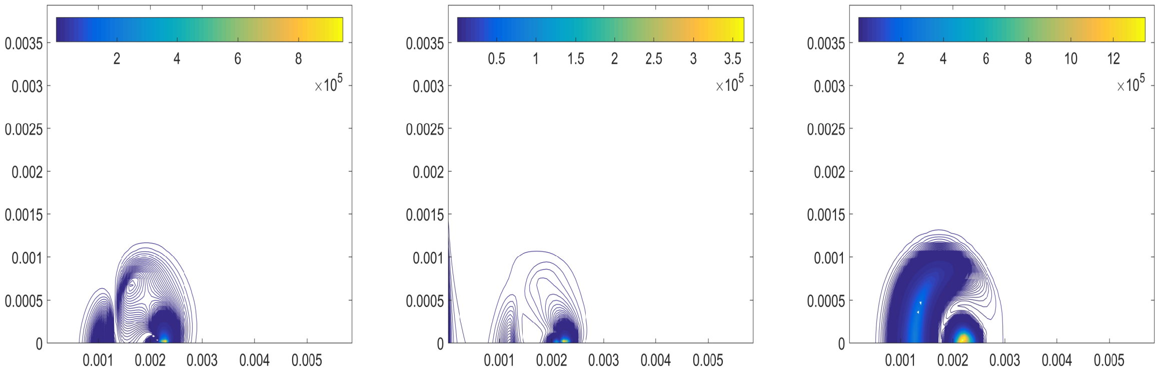

(d) $E_h, \;\; t = 6ms$ (e) $E_m, \;\; t = 6ms$ (f) $E_r, \;\; t = 6ms$

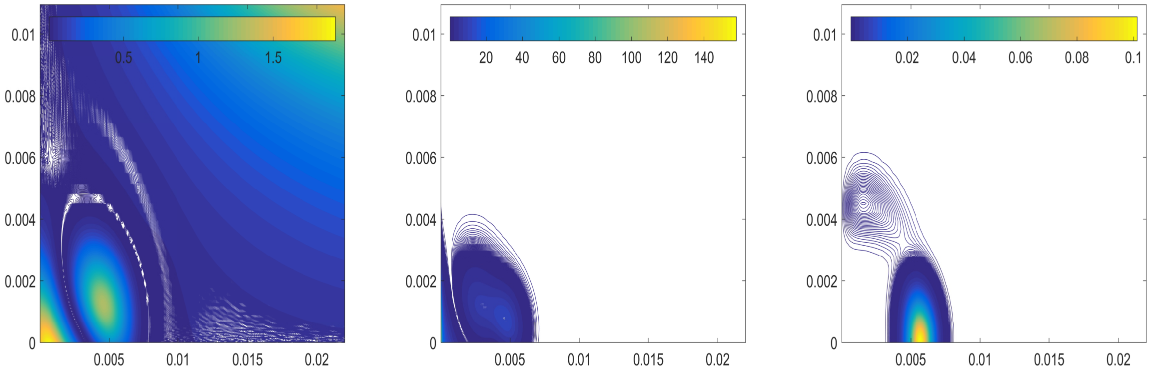

(g) $E_h, \;\; t = 20ms$ (h) $E_m, \;\; t = 20ms$ (i) $E_r, \;\; t = 20ms$

Figure 6.2: Spatio-temporal evolution of entropy generation rate per unit volume (W/m^2K) during Bagasse particle combustion under active flow, 77%O_2 & 23%N_2.

Figure 6.1 shows that for t=2ms, which corresponds to pre-ignition period, there exist some thermal entropy generation due to the endothermic devolatilisation process. Diffusion of the produced gases at this stage has resulted in mass transfer irreversibilities, while entropy generation by chemical reactions is zero. Thus, for pre-ignition stage the mass transfer irreversibility is the dominant source of entropy generation. After 6ms (the middle row in Fig. 6.1) the combustion process of the particle has progressed to some extent. It is clear that the region over which thermal entropy is generated has increased significantly, while the order of magnitude of this irreversibility has remained unchanged in comparison with the pre-ignition period. The spatial distribution of thermal irreversibility (Fig. 6.1d) further shows that there are two sources of thermal entropy generation. One situated close to the top of the reactor where volatiles have been released and reacted and the other one is around the burning particle. A comparison between Fig. 6.1b and Fig. 6.1e indicates that the reactor region affected by mass transfer has slightly decreased during the process. This is mainly due to the fact that volatile release and combustion are limited to a short time after release of the particle. Referring to Figures 4.15, 4.17, 4.19 and 4.21, it confirmed that the mass transfer of species generated after completion of volatile combustion is rather slow. This results in weakening of the mass transfer irreversibility, as depicted by Fig. 6.1e. Figure 6.1f illustrates the distribution of reaction irreversibilities at t=6ms. It is important to note that, in this figure, the entropy generation is stronger than those in Figs. 6.1e and 6.1d by an order of magnitude. Further, the regions over which chemical entropy is generated are large and comparable to those affected by thermal entropy (shown in Fig. 6.1d). Furthermore, generation of chemical entropy is clearly divided into two regions corresponding to the reaction of volatilised gases and the homogenous and heterogeneous reactions in the vicinity of the particle.

As indicated by Tables 4.4 and 4.5, the particle life time is almost 11 milliseconds for the condition shown in Fig. 6.1. Figures 6.1g-i show the distribution of irreversibilities after 20ms when the burning process has terminated but the resultant heat and species continue to diffusive and generate entropy. Compared to other subfigures, Figures 6.1g-i show a larger area of the reactor. Most notably, compared to the earlier time at t=20ms the numerical values of all sources of entropy generation have decreased massively. This is particularly the case for chemical entropy, shown in Fig. 6.1i, which is essentially zero. Figures 6.1g and 6.1h show that after completion of combustion the thermal and mass transfer irreversibilities, although smaller in value, cover a much larger area of the reactor compared to the earlier times.

Increasing the molar concentration of oxygen to 77%, the results of the different sources of entropy generation rate per unit volume are shown in Fig. 6.2. It can be clearly seen that, there are no qualitative changes in the spatio-temporal evolution of irreversibilities in this gas condition compared with 37% O_2 & 63% N_2. However, for t=6ms the magnitudes of all sources of entropy generation increased by one order of magnitude in comparison with those in the corresponding subfigures in Fig. 6.1. It also shows that at higher oxygen concentration, chemical and thermal entropy generations are stronger in the near particle region. This is distinctive to that shown in Fig. 6.1 wherein the upstream reaction of the volatilisation products and the near particle chemical activities contribute almost equally to the thermal and chemical entropy generation.

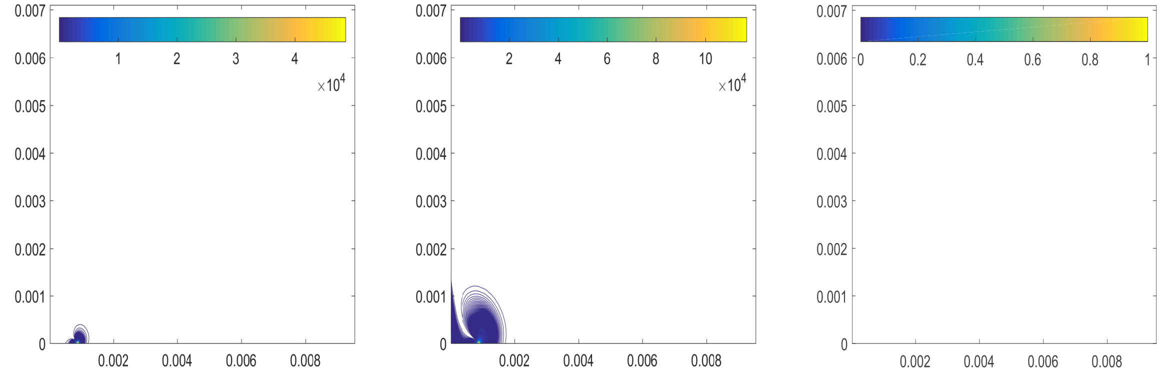

(a) $E_h, \ t = 3ms$ (b) $E_m, \ t = 3ms$ (c) $E_r, \ t = 3ms$

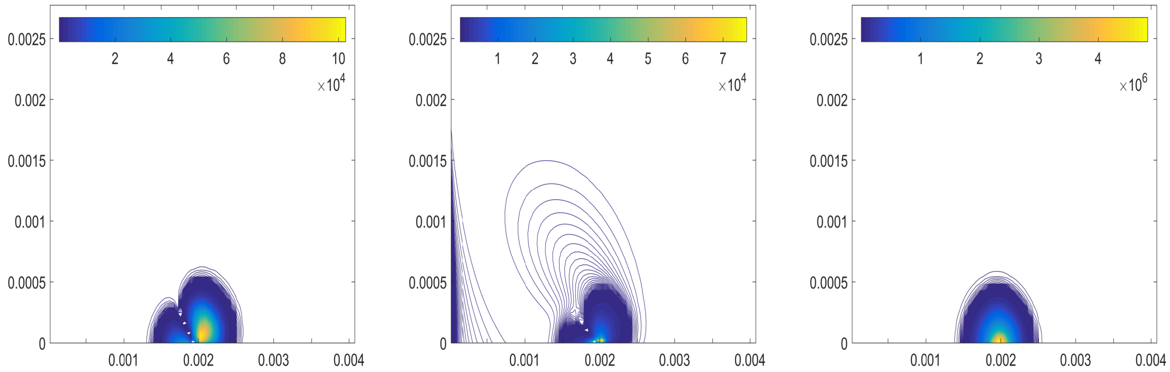

(d) $E_h, \ t = 7ms$ (e) $E_m, \ t = 7ms$ (f) $E_r, \ t = 7ms$

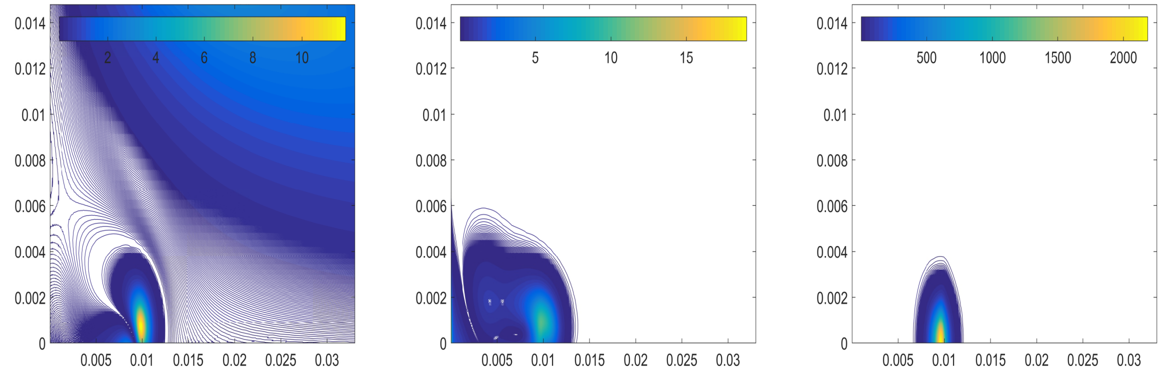

(g) $E_h, \ t = 40ms$ (h) $E_m, \ t = 40ms$ (i) $E_r, \ t = 40ms$

Figure 6.3: Spatio-temporal evolution of entropy generation rate per unit volume (W/m^2K) during DECS-11 particle combustion under active flow, 37%O_2 & 63%N_2.

The spatio-temporal evolution of entropy generation within a moving window travelling with the particle during single DECS-11 particle combustion is given in Figs 6.3-6.6. Here, Fig. 6.3 represent active 37% O_2 & 63% N_2 condition, Fig. 6.4 is for active 68% O_2 & 32% N_2 condition, Fig. 6.5 refers to quiescent 20% O_2 & 80% N_2 condition and Fig. 6.6 shows quiescent

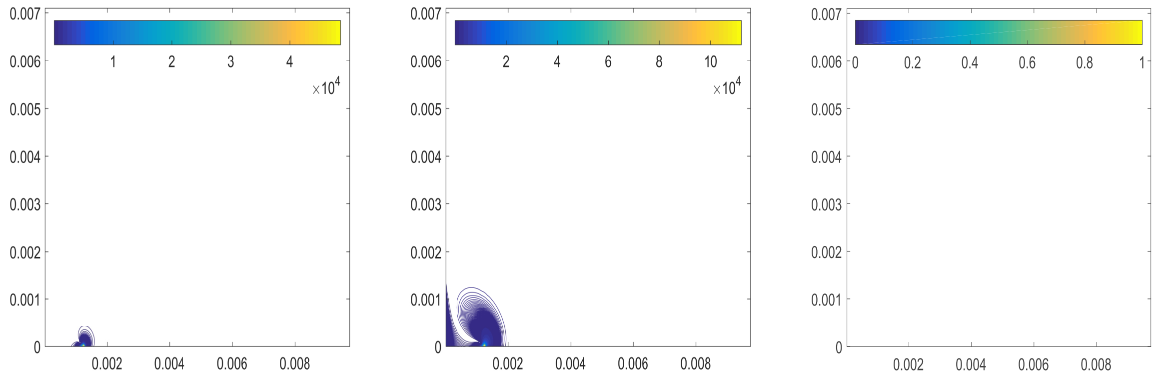

(a) $E_h, \ t = 3ms$

(b) $E_m, \ t = 3ms$

(c) $E_r, \ t = 3ms$

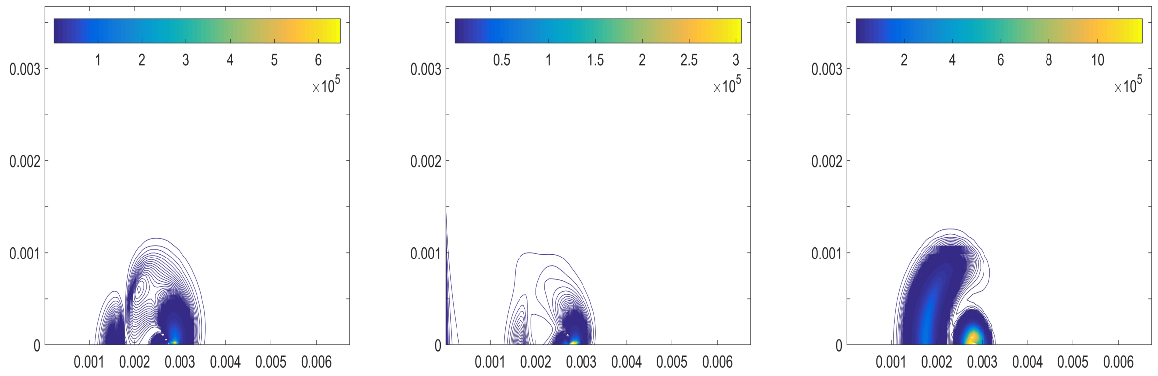

(d) $E_h, \ t = 7ms$

(e) $E_m, \ t = 7ms$

(f) $E_r, \ t = 7ms$

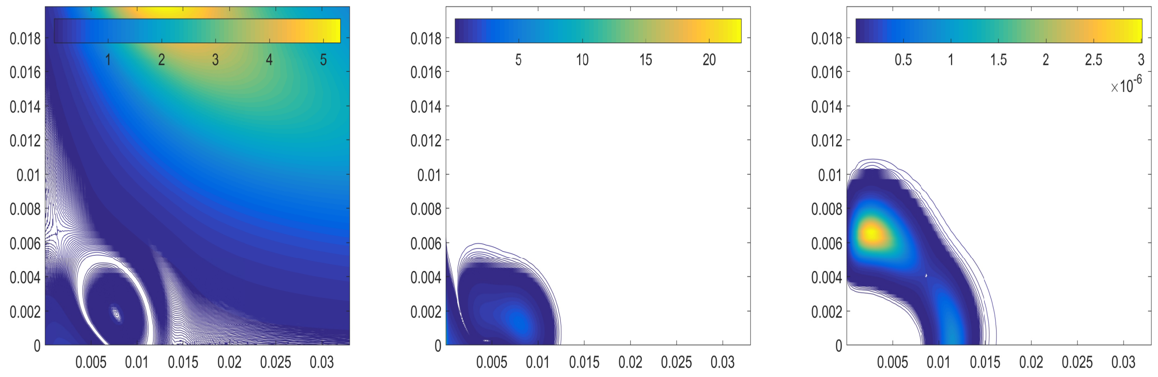

(g) $E_h, \ t = 40ms$

(h) $E_m, \ t = 40ms$

(i) $E_r, \ t = 40ms$

Figure 6.4: Spatio-temporal evolution of entropy generation rate per unit volume (W/m^2K) during DECS-11 particle combustion under active flow, 68%O_2 & 32%N_2.

100% O_2 condition. Contours of the entropy generation by thermal, chemical and mass transfer irreversibilities have been plotted for three different moments of time which is selected referring to the particle life time (Tables. 4.4).

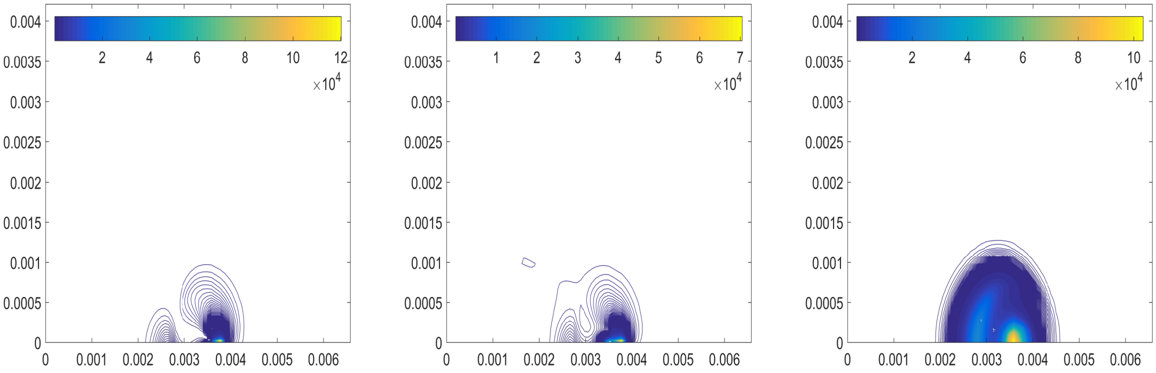

(a) $E_h, \; t = 18ms$ (b) $E_m, \; t = 18ms$ (c) $E_r, \; t = 18ms$

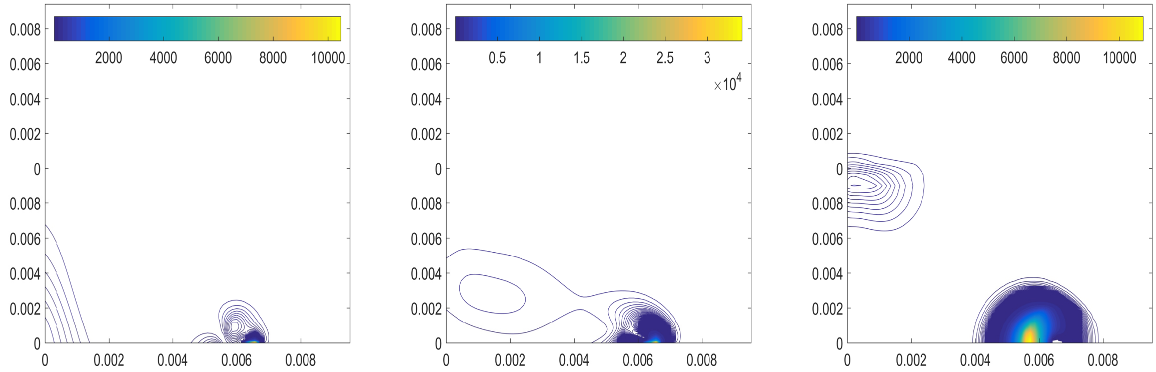

(d) $E_h, \; t = 30ms$ (e) $E_m, \; t = 30ms$ (f) $E_r, \; t = 30ms$

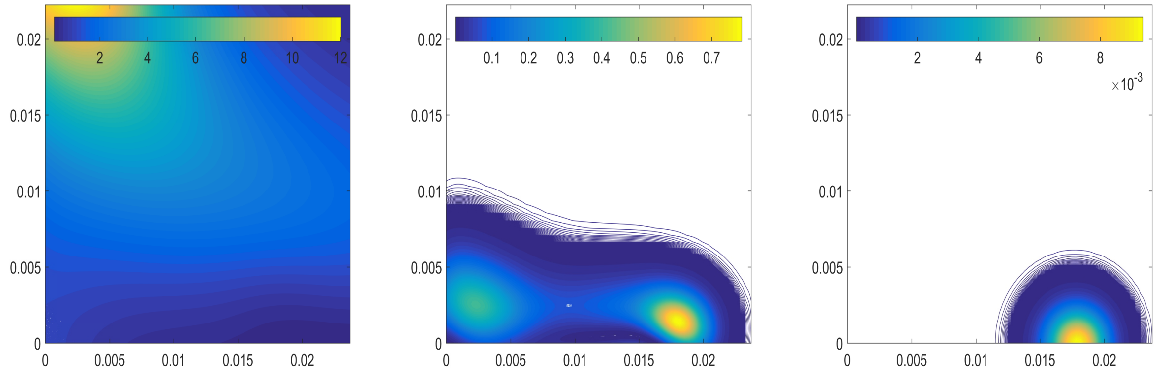

(g) $E_h, \; t = 100ms$ (h) $E_m, \; t = 100ms$ (i) $E_r, \; t = 100ms$

Figure 6.5: Spatio-temporal evolution of entropy generation rate per unit volume (W/m^2K) during DECS-11 particle combustion under quiescent flow, 20%O_2 & 80%N_2.

In Figs. 6.3 and 6.4, the first snapshots are produced at pre-ignition moment (t=3ms), which expectedly includes no chemical irreversibility but considerable mass transfer irreversibility (see Figs. 6.3b and 6.4b). Further, there are noticeable thermal entropy generations in Figs. 6.3a and 6.4a. This is due to the endothermicity of the process of volatile release, which sets a temperature gradient around the devolatising coal particle. The second snapshot at t=7ms (subfigures

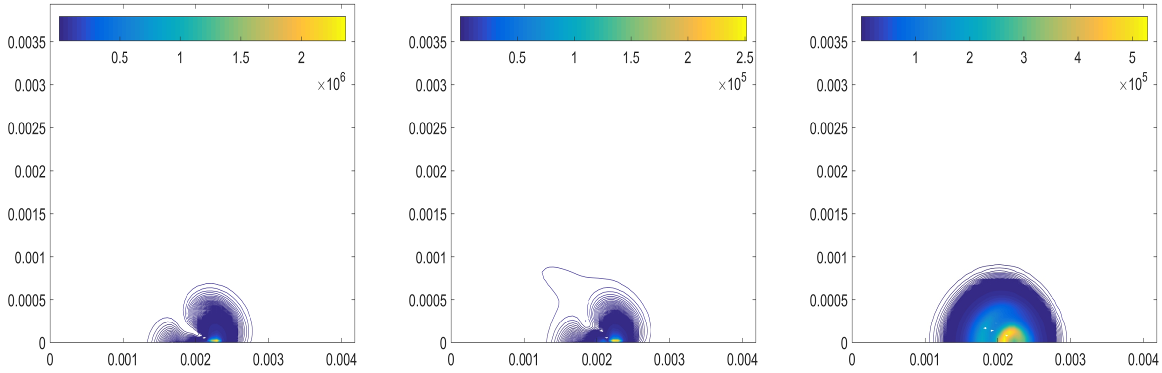

(a) $E_h, \ t = 11.5ms$ (b) $E_m, \ t = 11.5ms$ (c) $E_r, \ t = 11.5ms$

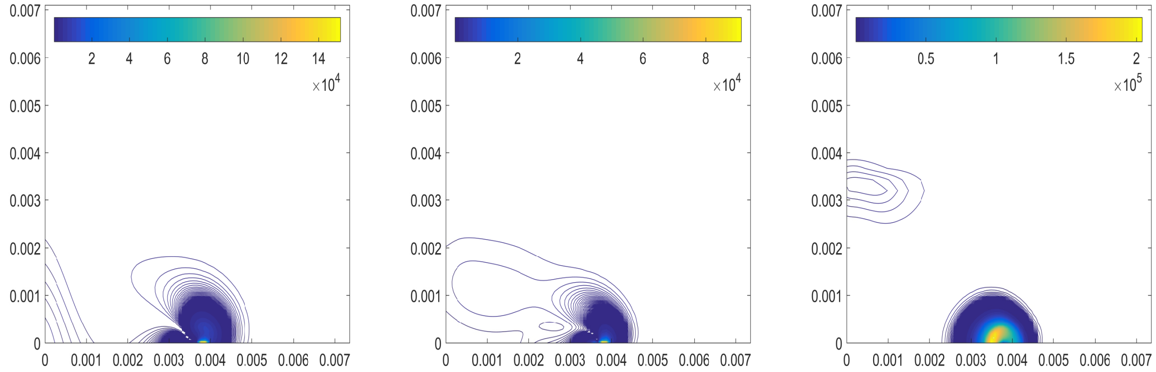

(d) $E_h, \ t = 30ms$ (e) $E_m, \ t = 30ms$ (f) $E_r, \ t = 30ms$

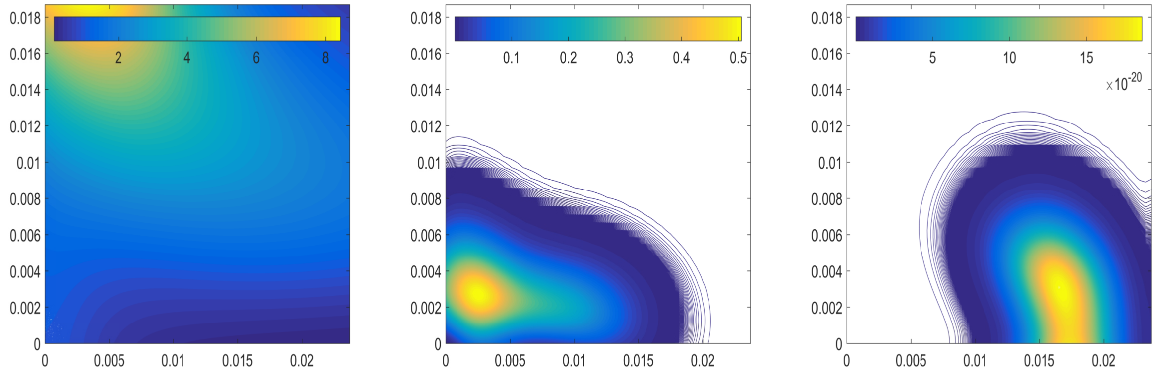

(g) $E_h, \ t = 100ms$ (h) $E_m, \ t = 100ms$ (i) $E_r, \ t = 100ms$

Figure 6.6: Spatio-temporal evolution of entropy generation rate per unit volume (W/m^2K) during DECS-11 particle combustion under quiescent flow, 100%O_2.

d, e and f of Figs. 6.3 and 6.4) captures a moment during combustion, in which all sources of irreversibility are strong. Figures 6.4d, 6.4e and 6.4f show that at t=30ms and for pure oxygen, all types of entropy generation occur in two distinctive regions, one around the particle and the other in the downstream flow. The former is because of the char combustion reactions (R_2-R_5) and the subsequent homogenous reactions (R_7 and R_8). The latter, however, is caused by the combustion of volatiles (R_6). Figures 6.3g, 6.3h and 6.3i indicate that towards the end of the particle life time (*t*=40ms), the thermal and mass transfer entropy generations are highly suppressed. However, in these figures the chemical irreversibility is still quite strong.

An air like atmosphere under quiescent flow has been investigated in Fig. 6.5. This figure shows that shortly after the ignition (*t*=18ms), there exists a large region around the particle with strong chemical irreversibility. The highest rate of chemical entropy generation happens in the vicinity of the particle, while chemical irreversibility remains strong in a region around the particle wherein the volatiles are oxidised. Figure 6.5 also indicates that thermal and mass transfer irreversibilities are limited to the areas close to the particle and their strengths are comparable to that of chemical irreversibility. In the second snapshot of this figure, at *t*=30ms the strength of the chemical irreversibility has decreases, although it still affects a relatively large area of the domain. This is due to the fact that at this stage the volatile combustion is complete and the homogenous reactions are limited to the oxidation of carbon monoxide and hydrogen (referring to Fig. 4.10(c)). The next snapshot has been produced at *t*=100ms, which corresponds to a post combustion moment. As expected, the chemical irreversibilities at this moment are almost zero. The mass transfer irreversibility has dropped to very low values. However, the thermal irreversibility remains at a noticeable value. This is because of the diffusion of the hot gases into the surrounding medium, which takes a longer time than completion of the combustion process.

Figure 6.6 depicts the same sequence, shown in Fig. 6.5, for the combustion of the coal particle in quiescent, pure oxygen atmosphere. At the first moment (*t*=11.5 ms), all the sources of irreversibility have values much greater than those in air combustion shown in Fig. 6.5. In particular, the thermal entropy has become stronger by two orders of magnitude. Further, in contrast to that in Fig. 6.5, the chemical entropy generation remains equally strong for the second snapshot at *t*=18ms. It can be verified in Fig. 4.10d that at this time the only homogenous reactions are combustion of H_2 and CO. However, it seems that the fast reactions in pure oxygen maintain the high level of chemical irreversibilities even after the termination of volatile combustion. Figure 6.6g shows that, once again, thermal entropy generation is the only form of irreversibility at post combustion stage.

6.2 History of entropy generation by different irreversibilities

The temporal variation of the integrated irreversibilities of heat transfer, mass transfer and chemical mechanisms over the effective area of the combustion zone during the single biomass and coal particle combustion under various gas conditions is shown in Figs. 6.7-6.12.

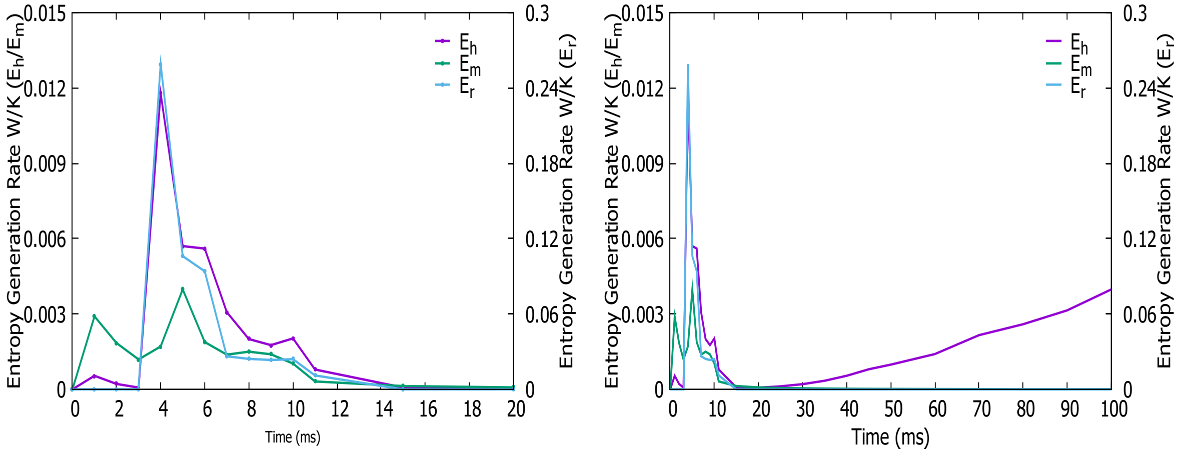

(a) (b)

Figure 6.7: History of entropy generation by different irreversibilities: Bagasse, Active flow, 37%O_2 & 63%N_2. E_H and E_M correspond to the left vertical axes and E_R to be read from the right axes.

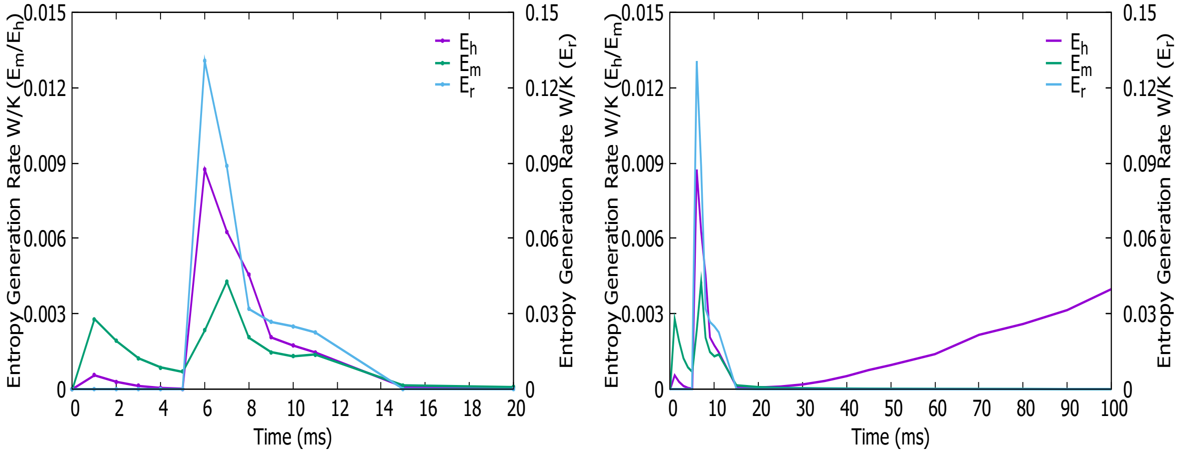

(a) (b)

Figure 6.8: History of entropy generation by different irreversibilities: Bagasse, Active flow, 77%O_2 & 23%N_2. E_H and E_M correspond to the left vertical axes and E_R to be read from the right axes.

Figure 6.7 reports the history of entropy generation for single Bagasse particle combustion in an active atmosphere with 37% mole fraction of oxygen. This figure reflects a few important points about the transient entropy generation. First, during the life time of the particle, the entropy generated by chemical reactions is at least one order of magnitude greater than that generated by the heat and mass transfer.

Second, the maximum chemical and thermal entropy generations, and hence the maximum total entropy generation, occurs at around the ignition time. Both chemical and thermal entropy generations drop sharply after the ignition. Chemical entropy vanishes after the completion of the transient burning process. However, the thermal entropy goes up and continues to grow till the end of the investigated period (100ms). This is due to the diffusion of heat of combustion into the environment after the completion of the transient combustion process. Third, the irreversibility of mass transfer includes two peaks during the particle life time. The first peak corresponds to devolatilisation period and is associated with a local peak in thermal entropy and the second peak happens shortly after the ignition. This represents the entropy generation due to the diffusion of the chemical species generated by the combustion of volatilised gases. Increasing the concentration of oxygen in Fig. 6.8 does not change the qualitative (and to a large extent the quantitative) behaviours observed in Figs. 6.7a and 6.7b.

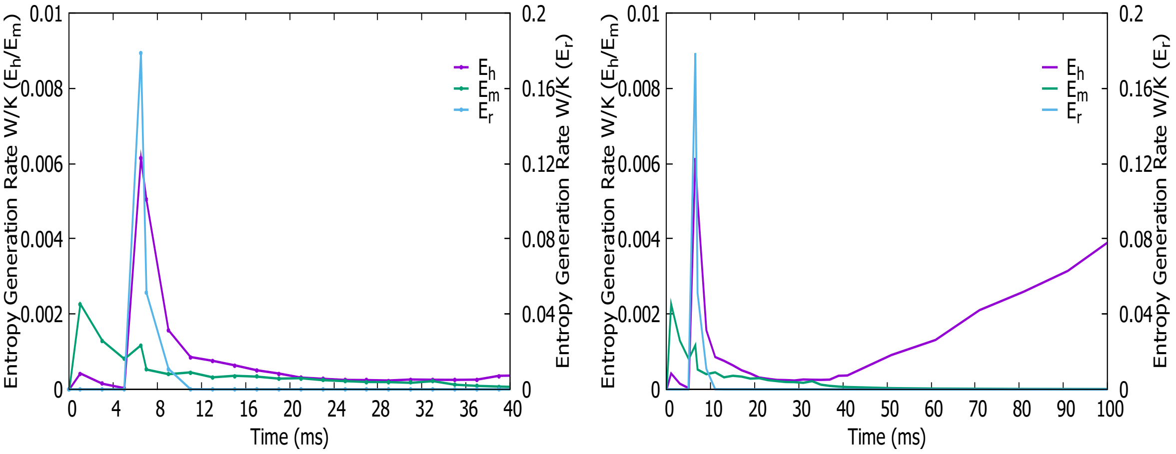

(a) (b)

Figure 6.9: History of entropy generation by different irreversibilities: DECS-11, Active flow; 37%O_2 & 63%N_2. E_H and E_M correspond to the left vertical axes and E_R to be read from the right axes.

Figures 6.9-6.12 show the history of entropy generation by different sources of irreversibility of single DECS-11 particles combustion under varying oxygen concentrations and for both active and quiescent flow conditions. Figures 6.9a and 6.9b correspond to a moderately oxygenated case (37% O_2 & 63% N_2) under active flow. This figure shows that upon the release of the particle and up to the moment of ignition, mass transfer irreversibility is the strongest source of entropy generation. Within this period, the thermal entropy generation is rather weak and there is no chemical irreversibility. The diffusion of volatiles into the surrounding environment and also the supply of heat to the endothermic devolatilisation process are the two irreversible phenomena occurring in this period. Ignition of the volatile gases results in a very sharp increase of the chemical entropy and thermal entropy generation. However, this trend is reversed after a short period and the chemical entropy generation drops down to very small values by the end of homogenous combustion phase. In general, the same qualitative behaviour is observed in the thermal entropy. However, as shown in Fig. 6.9b the thermal entropy increases towards the end

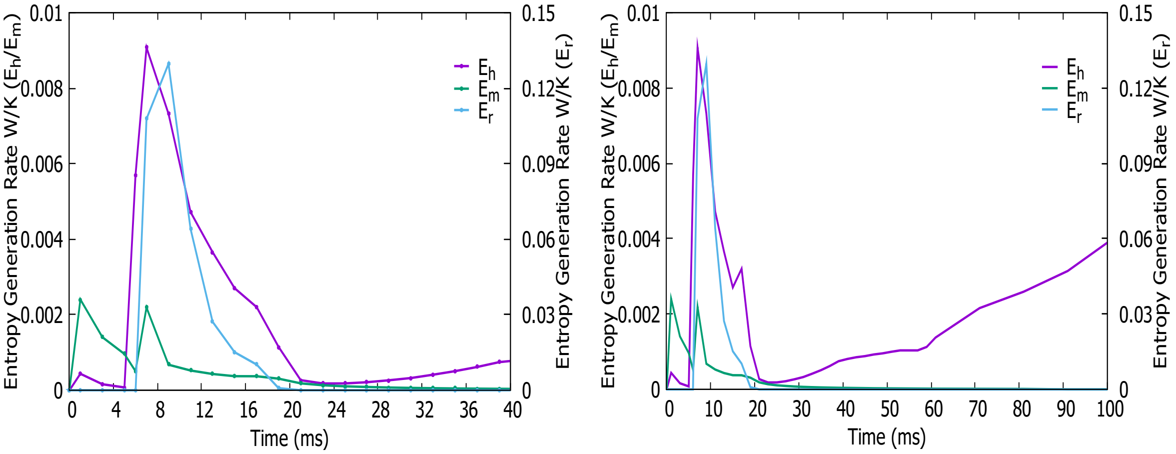

(a) (b)

Figure 6.10: History of entropy generation by different irreversibilities: DECS-11, Active flow, 68%O_2 & 32%N_2. E_H and E_M correspond to the left vertical axes and E_R to be read from the right axes.

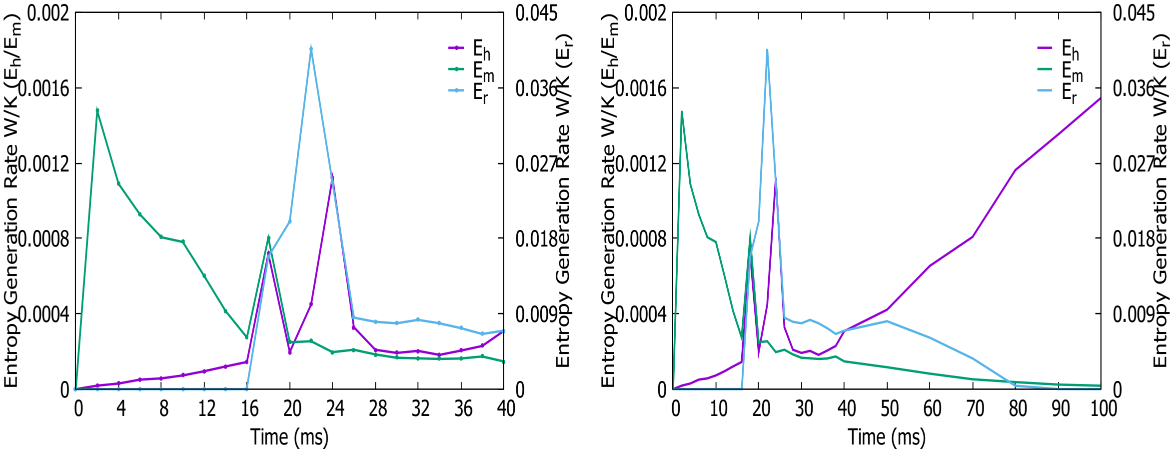

(a) (b)

Figure 6.11: History of entropy generation by different irreversibilities: DECS-11, Quiescent flow, 20%O_2 & 80%N_2. E_H and E_M correspond to the left vertical axes and E_R to be read from the right axes.

of the particle life time and keeps growing after the completion of the burning process. This is because of the diffusion of heat of combustion into the surrounding medium and is a major contributor to the thermal entropy generated during the transient combustion process.

An interesting behaviour is observed when increasing the concentration of oxygen to 68% (Fig. 6.10). Here, the rates of reduction in the chemical and thermal entropy generation after the combustion of volatiles are much less than those in Fig. 6.9. Hence, the chemical and entropy generations remain large for the entire course of particle burning. This is due to the strengthening of reactions R_2, R_3 and R_7 in the highly oxygenated atmosphere, which intensify the rate chemical reactions and heat release of char combustion.

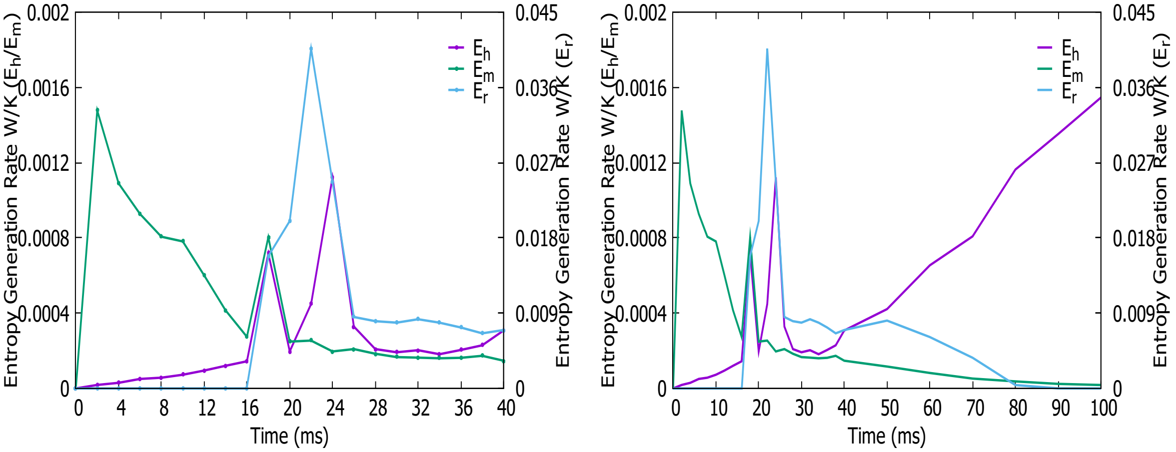

(a) (b)

Figure 6.12: History of entropy generation by different irreversibilities: DECS-11, Quiescent flow, 100%O_2. E_H and E_M correspond to the left vertical axes and E_R to be read from the right axes.

Under quiescent flow and in an atmosphere similar to air, Fig. 6.11 shows that the mass transfer irreversibility in the pre-ignition period is more significant than the thermal irreversibility during the homogenous combustion. Similar to that discussed earlier, the thermal irreversibility continues to grow within the char combustion and post-combustion periods and ultimately becomes much more significant than the mass transfer entropy generation. Compared with lower oxygen concentration case (20%O_2 & 80%N_2), major intensification of chemical entropy generation in pure oxygen atmosphere is evident in Fig. 6.12. Also these figures clearly show that during the combustion of volatiles, thermal entropy generation is much larger than that of mass transfer.

There is a general trend that can be summarized from the history of entropy generation during the single particle transient combustion process. All the time traces of mass transfer irreversibility feature two peaks. First, during the devolatilisation process, which results in the production of gas-phase volatiles, and the second peak after the ignition and during the combustion of volatiles and char.

6.3 Overall average entropy generation

The thermal, mass transfer and chemical as well as the overall entropy within the system is calculated according to Eqs. 3.78-3.81 and by time averaging the spatially integrated entropy generation discussed with regards to Table 6.1 and Figs. 6.13-6.15. Here, the time averaging was conducted for an interval of 200ms. Although not shown, this period was enough for the thermal gradients in the reactor to mostly smear out and thus the process of entropy generation to nearly come to the end.

Table 6.1: Average entropy generation of single particle combustion (W/K)

Gas Conditions	E_h	E_m	E_r	E_r
Bagasse, Active Flow				
21% O_2/N_2	0.0010	0.00006	0.0029	0.00396
37% O_2/N_2	0.0016	0.00004	0.0049	0.00654
77% O_2/N_2	0.0015	0.00003	0.0047	0.00623
100% O_2	0.0015	0.00008	0.0049	0.00648
DECS-11, Active Flow				
21% O_2/N_2	0.0024	0.00012	0.0029	0.00542
37% O_2/N_2	0.0027	0.00013	0.0041	0.00693
77% O_2/N_2	0.0024	0.00011	0.0043	0.00681
100% O_2	0.0026	0.00008	0.0044	0.00708
DECS-11, Quiescent Flow				
20% O_2/N_2	0.0013	0.00012	0.0029	0.00432
40% O_2/N_2	0.0014	0.00014	0.0034	0.00494
60% O_2/N_2	0.0014	0.00014	0.0048	0.00634
80% O_2/N_2	0.0015	0.00014	0.0052	0.00684
100% O_2	0.0015	0.00014	0.0053	0.00694

Figure 6.13 shows a comparison between the overall average entropy generation from different sources in a single biomass particle combustion under various gas atmospheres. This figure clearly shows that the chemical entropy is the most significant contributor with the irreversibility of the process. The thermal entropy has a value of the same order of magnitude as chemical entropy but roughly about three times smaller than that. The mass transfer irreversibility is much smaller than the chemical and thermal entropy generation and can be practically ignored. Figure 6.13 further shows that increasing the molar concentration of oxygen from 21% results in a considerable increase in thermal and chemical entropy generation and thus significantly intensifies the overall average entropy generation. Nonetheless, any further increase in the oxygen concentration alters the irreversibilities very slightly.

The overall average entropy generation of a single coal particle combustion at different chemical compositions of the atmosphere are presented in Fig. 6.14 for active flow conditions and Fig. 6.15 for quiescent flow conditions. Also shown in the figures is the sum of the three sources of entropy, here referred to as global entropy generation within the system. A close examination of Fig. 6.14 and 6.15 reveal a few points as follows. First, in keeping with the findings of the previous studies on steady gaseous combustion [96] and transient multiphase combustion [96] [118], mass transfer irreversibility appears to be small in comparison with that of heat transfer and chemical reactions. Second, oxygenation of the atmosphere generally results in a significant increase in the global entropy generation in comparison with combustion in air. A step change is particularly visible in the chemical entropy generation. This result is of high

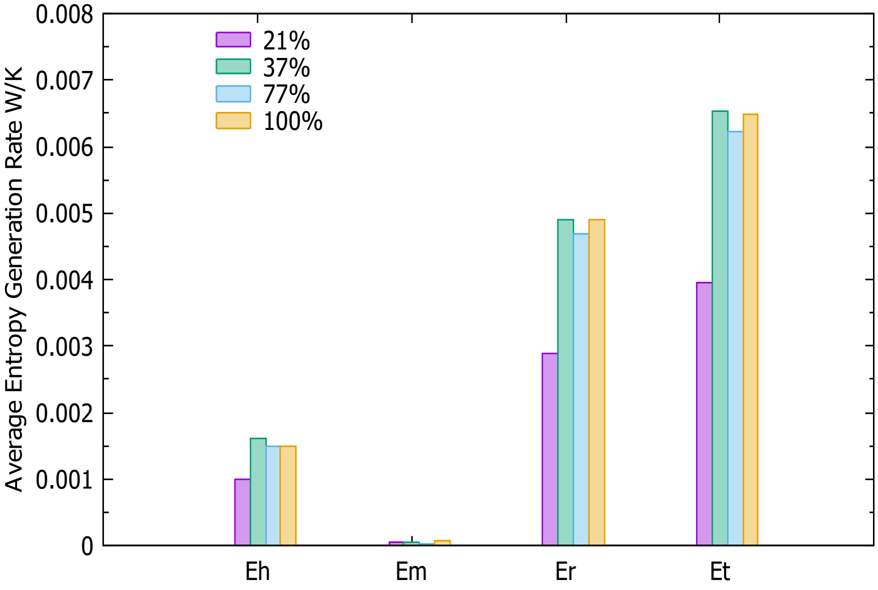

Figure 6.13: Average entropy generation for varying concentrations of oxygen: Bagasse, Active flow

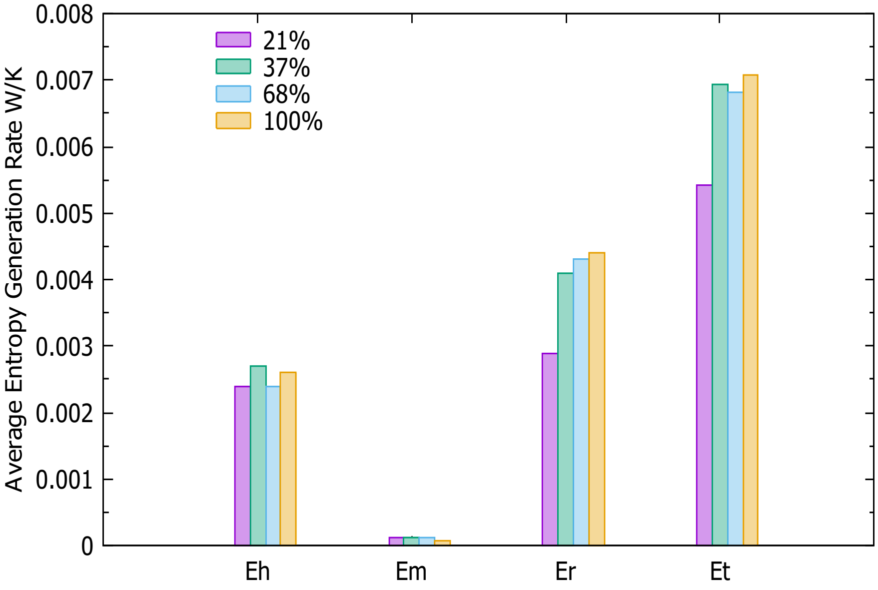

Figure 6.14: Average entropy generation for varying concentrations of oxygen: DECS-11, Active flow

practical significance, as it indicates that slight and moderate oxygenation of the combustion atmosphere can majorly boost the level of entropy generation and hence that of exergy destruction. However, once the mole fraction of oxygen reaches around 40% (37% for active flow), any further oxygenation causes only slight increases in the entropy generation. Third, under quiescent flow there appears to be a regular pattern of increasing entropy generation by increasing the concentration of oxygen. However, this pattern is less clear in active flow cases. Fourth, although the overall average entropy generations for the active and quiescent flows are nearly

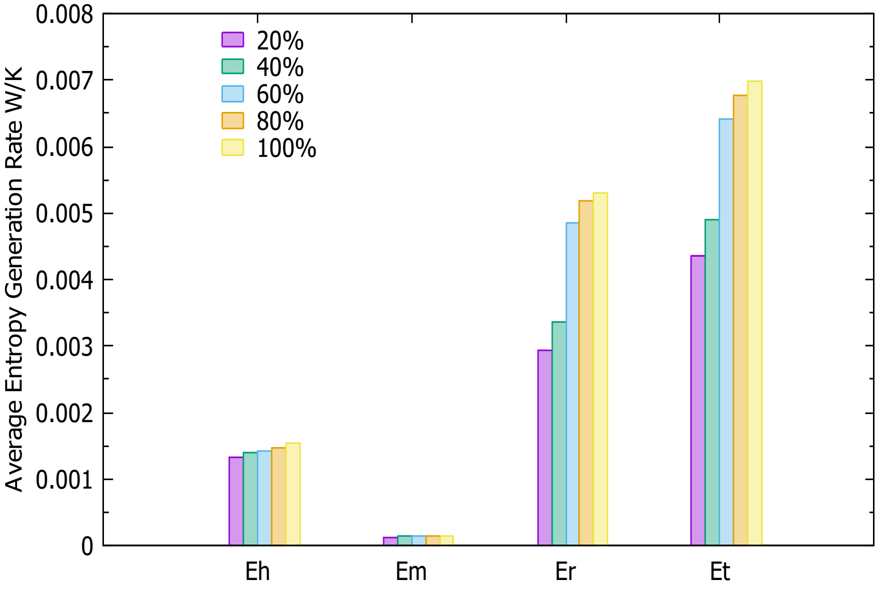

Figure 6.15: Average entropy generation for varying concentrations of oxygen: DECS-11, Quiescent flow

the same, the thermal entropy generation in quiescent flow is noticeably smaller than that of the active flow cases. The reason for this behaviour is not immediately obvious and is anticipated to be due to the modification of heat transfer by altering the flow velocity.

6.4 Summary and Conclusions

Based on the validated numerical model of single particle combustion, the unsteady local entropy fields generated by heat transfer, mass transfer and chemical reactions during the transient combustion process in O_2/N_2 atmospheres with varying oxygen concentration and for active and quiescent flow conditions were investigated. The total entropy generations were obtained by integrating this over time. The major finding of this study are summarised as follows.

1. During the pre-ignition period where only devolatilization happens, the mass transfer irreversibility is the main source of the entropy generation with some contributions from heat transfer. For the oxygenated cases, the heat transfer entropy grows substantially.

2. A very sharp increase in the irreversibility generated by chemical reactions is observed immediately after the ignition of the particle. Ignition of the devolatilised gases also generates significant thermal irreversibilities.

3. While chemical entropy generation comes to an end by the termination of the particle life time, the thermal entropy continues to be generated for a relatively long time (200ms). This is due to the diffusion of hot gases into the surroundings atmosphere.

4. The global entropy generation increases when increasing the oxygen concentrations in the atmosphere. This increase is quite significant when moderatly oxygenated atmospheres (with mole fraction of oxygen less than 40%) are compared with air. However, addition of further oxygen results in minor increases in the total entropy generation by the heat transfer and chemical reactions.

5. Overall, the chemical entropy appears to be the dominant source of irreversibility during the single biomass or coal combustion process. The thermal entropy is the second contributor with a similar order of the magnitude as that of chemical. Mass transfer irreversibility has a negligibly small contribution.

Chapter 7

Smouldering combustion of biomass packed bed

7.1 Introduction

This chapter introduces the experimental work on the smouldering combustion of biomass packed bed under varying air flow rate and ignition temperature conditions. The temperature of ceramic ignition plate is identified as the ignition temperature. Two different types of biomass particles are used to form the packed bed. Air flow rate varying from 0 to 2.4 litres per minute (LPM) and the ignition temperature changing from 220°C, 250°C to 280°C are examined. The smouldering combustion process is monitored by a camera and the temperature at different locations of the packed bed is recorded by thermocouples. Patterns of the reaction front during the smouldering combustion process are reported. The heating rate and the speed of reaction front during this process are calculated to analyse the smouldering combustion characteristics and the front propagation properties.

7.1.1 Fuel properties

There are two types of biomass fuel from Scotland farmland (Wheat straw and Wood bark) used for the experiments. The proximate and ultimate data were analysed by SGS UK Laboratories and were given in Table 7.1. Figure 7.1 gives the images of the two fuels.

7.1.2 Non-reactive test

The experimental apparatus and method were introduced in Chapter 2.5. A cold test was done to check the thermal equilibrium of the system. The operation condition with the ignition temperature at 250°C and the air flow at 1.2 LPM was chosen to conduct the test. Eleven thermocouples were placed to track the temperature at different locations of the rig (6 in the ignition plate and 5 in the central line of inner space). The locations of thermocouples and the measured results

Table 7.1: Proximate and ultimate analysis of the fuel

Fuel Type	Wheat straw	Wood bark
Proximate analysis as received		
Moisture (%)	16.2	18.4
Volatile Matter (%)	69.4	50.1
Fixed Carbon (%)	12.0	15.5
Ash (%)	2.4	16.0
Ultimate analysis (Dry basis)		
Carbon (%)	48.1	42.1
Hydrogen (%)	5.77	4.26
Oxygen (%)	42.192	34.949
Nitrogen (%)	0.62	0.49
Sulfur (%)	0.053	0.074
Chlorine (%)	0.053	0.027
Ash (%)	3.1	18.2
Lower Heating Value (MJ/kg)	14.56	12.52

(a) (b)

Figure 7.1: Images of fuel powder. (a) Wheat Straw; (b) Wood Bark.

are reported in Figs. 7.2 and 7.3.

It can be seen from Fig. 7.2 that, the temperature of the points on the ignition plate differs at the beginning, but the temperature of these points becomes nearly stable around 250°C where the highest one is 253°C and the lowest one is 247°C after about one hour. The differences among these points are negligible. Figure 7.3 reports the temperature changing trend at different points along the central line of the rig. The temperature decreases in turn against the distance away from the plate, and reaches the stable one after one hour as well. Therefore, we can conclude that the experimental rig reaches the thermal equilibrium state after being heated for about 90 minutes.

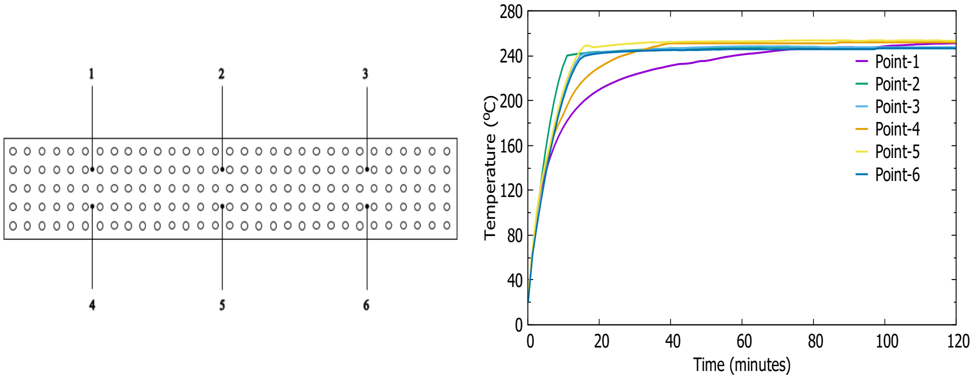

(a) (b)

Figure 7.2: Temperature profile of different points on the ignition plate in cold test.

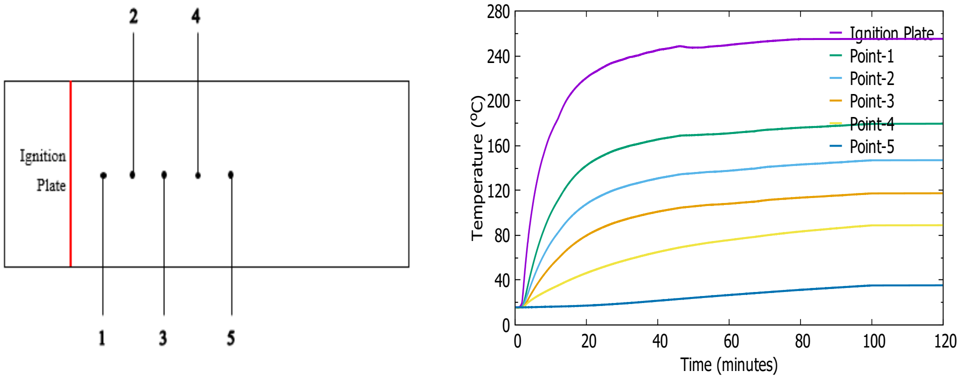

(a) (b)

Figure 7.3: Temperature profile of different points along the central line in cold test.

7.2 Shape of the smouldering combustion front

When conducting the experiments, the biomass fuel particles were put into the fuel box after the rig had been heated for two hours, which means the rig was in the thermal equilibrium state. Four air flow rates–0 LPM, 0.6 LPM, 1.2 LPM and 2.4 LPM and three ignition temperatures–220°C, 250°C and 280°C were considered in the experimental work. Thus, 12 different operating conditions were applied to the smouldering combustion of the packed bed filled with wheat straw and wood bark particles respectively. The shapes of the smouldering front for each case at a final stable state are shown below. Figure 7.4 corresponds to wheat straw packed bed under different air flow rate and ignition temperature and Fig. 7.5 for wheat straw.

It can be seen that when the ignition temperature is 220°C, the wheat straw packed bed is ignited and a reaction front appeared. Under the quiescent flow condition (0 LPM), the reaction front is close to the edge (Fig. 7.4a). Along with increased air mass flow rate, the reaction front moves forward and takes a distance away from the edge (Fig. 7.4d). But no matter under which mass flow rate, all the reaction fronts keep nearly flat and stable. There are no obvious fingers and in-

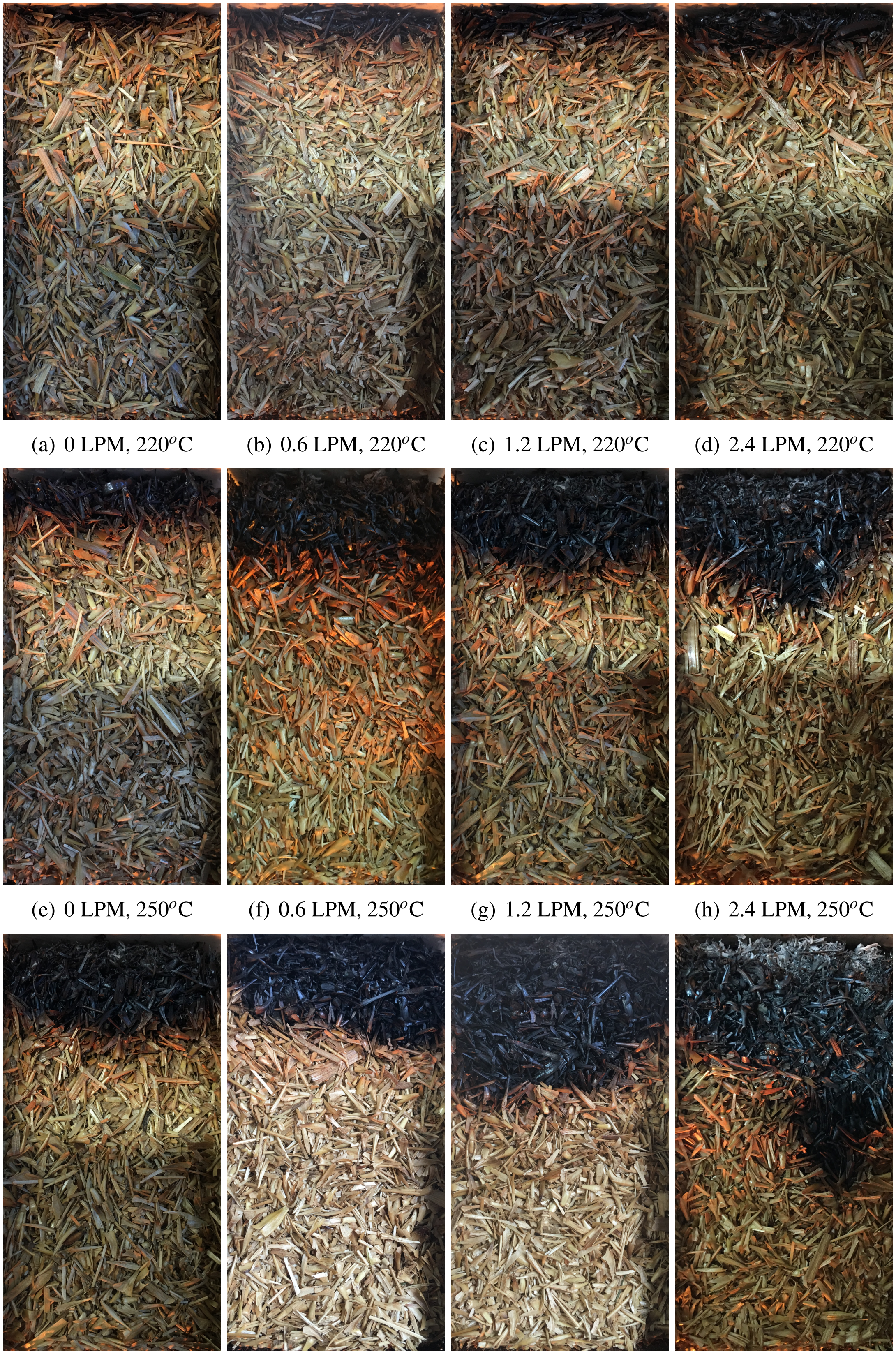

(a) 0 LPM, 220^{o}C (b) 0.6 LPM, 220^{o}C (c) 1.2 LPM, 220^{o}C (d) 2.4 LPM, 220^{o}C

(e) 0 LPM, 250^{o}C (f) 0.6 LPM, 250^{o}C (g) 1.2 LPM, 250^{o}C (h) 2.4 LPM, 250^{o}C

(i) 0 LPM, 280^{o}C (j) 0.6 LPM, 280^{o}C (k) 1.2 LPM, 280^{o}C (l) 2.4 LPM, 280^{o}C

Figure 7.4: Cinematography of wheat straw combustion.

(a) 0 LPM, 220^{o}C (b) 0.6 LPM, 220^{o}C (c) 1.2 LPM, 220^{o}C (d) 2.4 LPM, 220^{o}C

(e) 0 LPM, 250^{o}C (f) 0.6 LPM, 250^{o}C (g) 1.2 LPM, 250^{o}C (h) 2.4 LPM, 250^{o}C

(i) 0 LPM, 280^{o}C (j) 0.6 LPM, 280^{o}C (k) 1.2 LPM, 280^{o}C (l) 2.4 LPM, 280^{o}C

Figure 7.5: Cinematography of wood bark combustion.

stabilities appearing in all the four cases. When the temperature of the ignition plates increases to 250°C, the smoudlering front propagates to a farther distance when the air mass flow rate increases, where the trend is similar to the ignition temperature of 220°C. But the smouldering front is farther away from the plate for the same air mass flow rate conditions than 220°C. Moreover, it should be noticed that a finger pattern is formed visibly when the air mass flow rate reaches up to 2.4 LPM. Figure 7.4i-l reports the state of the reaction front under 280°C. It can be clearly seen that the reaction instabilities appear to all the four smouldering fronts. They do not kept flat when propagating forward and finger patterns formed in each case. It should be pointed that most of the finger patterns do not look the same in the repeated experiments. For example, in the case of ignition temperature of 280°C and air mass flow rate of 2.4 LPM, the finger pattern shown here heads to the right side (Fig. 7.4l), but in some repeated cases, it heads to the left side or the middle line. There are ash observed close to the ignition plate, which is due to strong intensity of combustion and complete combustion under the high air mass flow rate and ignition temperature conditions. In other cases, there are not such kinds of ash generated due to the limitation of combustion temperature.

The propagation characteristics of the smouldering reaction fronts during wood bark packed bed combustion are similar to the wheat straw. The smouldering fronts is flat and stable under lower temperature conditions (220°C). While the temperature increases to 280°C, the propagation distance is further and the instabilities and finger patterns appear. And at the same ignition temperature, the combustion process lasts for a longer time and a bigger area of the packed bed is burned.

7.3 Speed of the smouldering combustion front

The speed of the smouldering front demonstrates the characteristic of the reactions. It is calculated by using the distance that the smouldering combustion front propagated divided by the time taken. The compared speed of the smouldering combustion under different ignition temperatures and air mass flow rates of wheat straw and wood bark packed bed is given below.

Figure 7.6a reports the results of the wheat straw packed bed. It can be seen that, at the low ignition temperature (220°C), the speed slightly increases from 0.18 cm/min to 0.24 cm/min when the air mass flow rate changing from 0 to 2.4 LPM, which is in keeping with Figs. 7.4a-d. When the ignition temperature comes to 250°C, the speed of the smouldering reaction front shows a remarkable increase at 2.4 LPM flow rate. It features a large increase when the ignition temperature raises to 280°C and is 0.43 cm/min. At this ignition temperature, the speed of 1.2 LPM increases to 0.36 cm/min. However, under the air mass flow rate of 0 and 0.6 LPM, the speed of the reaction front did not change too much. It slightly increases from 0.18 cm/min to

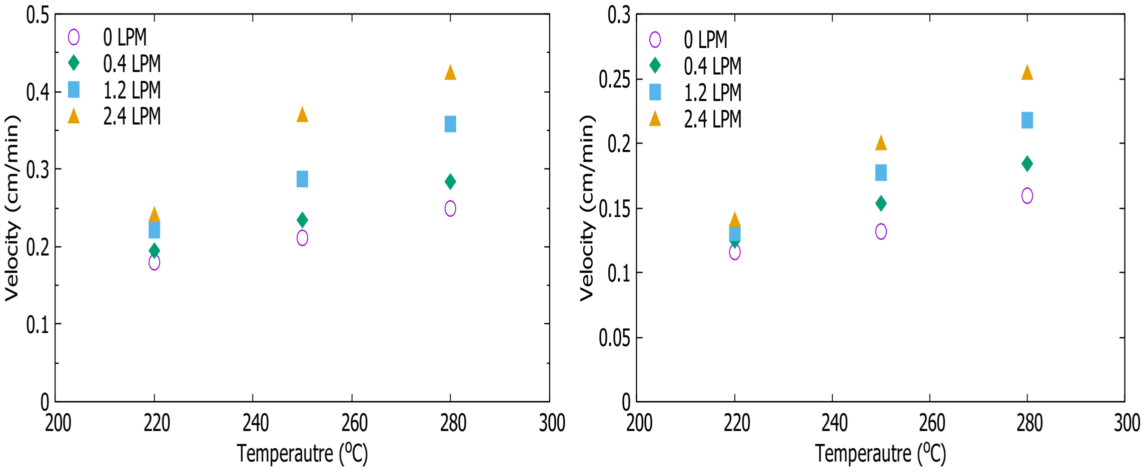

(a) Wheat straw (b) Wood bark

Figure 7.6: Speed of the smouldering front under different mass flow rate and ignition temperature.

0.24 cm/min and from 0.20 cm/min to 0.26 cm/min, respectively. The speeds of the smouldering combustion front of the wood bark packed bed under various operating conditions are presented in Fig. 7.6b. The values are pretty close to each other when the ignition temperature is 220°C. When the ignition temperature increases to 250°C and 280°C, the speed of the smouldering reaction front increases as well. In general, the higher the air mass flow rate, the larger increase in the front speed is. The speed difference between 0 and 2.4 LPM at 220°C is only 0.025 cm/min, while it is 0.1 cm/min at 280°C. Further, it should be noticed that, the front speed of wheat straw packed bed is much higher than the wood bark packed bed. It is nearly twice comparing wheat straw to wood bark. Moreover, the increase under the same air mass flow rate is more distinctive when the ignition temperature increases.

7.4 Smouldering combustion temperature

The temperature profiles of the five monitoring points along the central line of the packed bed during the smouldering combustion process under different operating conditions are given in Figs. 7.7 and 7.8. Temperature variations were recorded in 25 minutes for wheat straw and in 40 minutes for wood bark. The positions of the thermocouples were specified in Section 3.5. Firstly, on the whole, the temperature of point-1 has the greatest changes in all cases and then followed by point-2 and point-3. The temperature of point-4 and point-5 does not vary too much during the whole process.

The position of point-1 is closest to the ignition plate and combustion area. When the biomass packed bed is ignited by the ceramic plate and starts to propagate forward, the heat generated by the chemical reactions during the combustion process and from the ignition plate is firstly

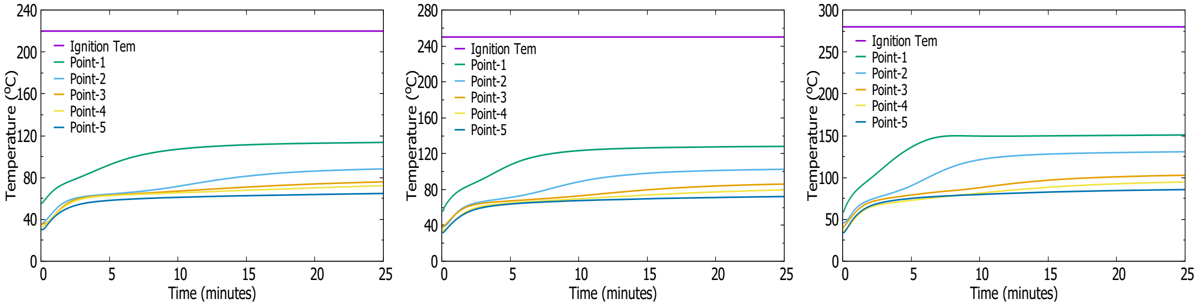

(a) 220^{o}C, 0 LPM (b) 250^{o}C, 0 LPM (c) 280^{o}C, 0 LPM

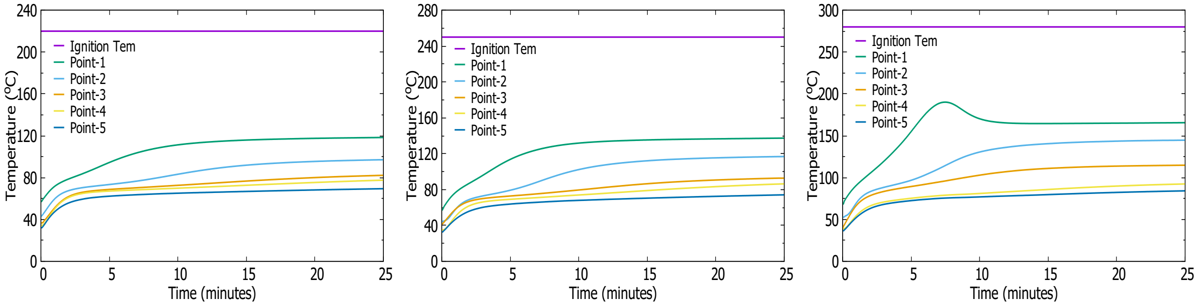

(d) 220^{o}C, 0.6 LPM (e) 250^{o}C, 0.6 LPM (f) 280^{o}C, 0.6 LPM

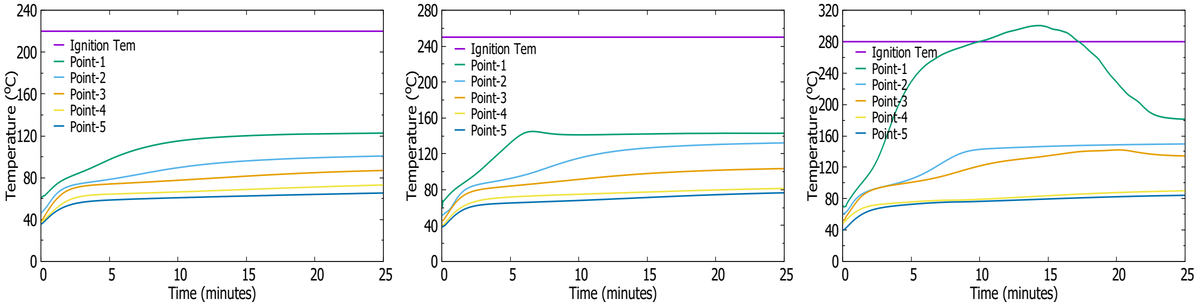

(g) 220^{o}C, 1.2 LPM (h) 250^{o}C, 1.2 LPM (i) 280^{o}C, 1.2 LPM

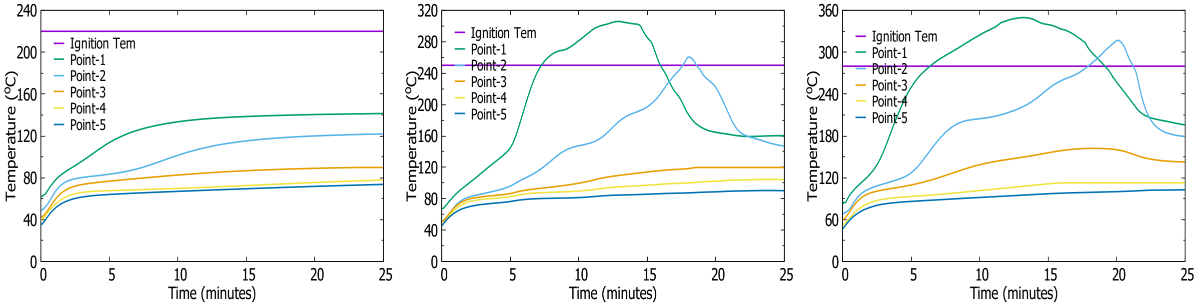

(j) 220^{o}C, 2.4 LPM (k) 250^{o}C, 2.4 LPM (l) 280^{o}C, 2.4 LPM

Figure 7.7: Wheat Straw: Temperature profile of different mass flow rate and ignition temperature.

delivered to point-1 by heat conduction between the biomass particles, heat convection through the porous structure and thermal radiation. Therefore, point-1 has the highest temperature at the final stage. It should be noticed that in higher temperature and mass flow rate cases, the temperature profile of point-1 looks like parabolas. In these cases, the temperature reaches its peak value when the reaction front moves there and the temperature drops when the reaction front

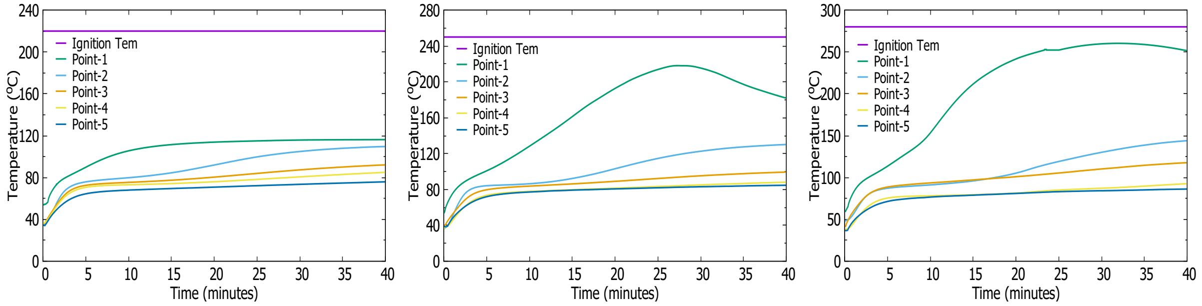

(a) 220^{o}C, 0 LPM (b) 250^{o}C, 0 LPM (c) 280^{o}C, 0 LPM

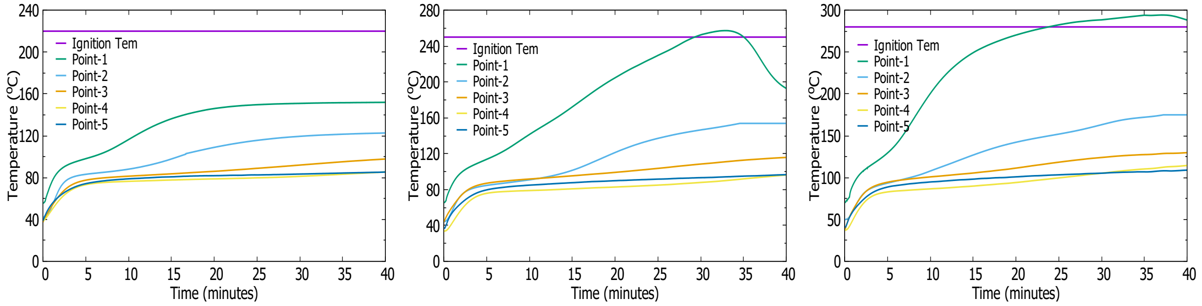

(d) 220^{o}C, 0.6 LPM (e) 250^{o}C, 0.6 LPM (f) 280^{o}C, 0.6 LPM

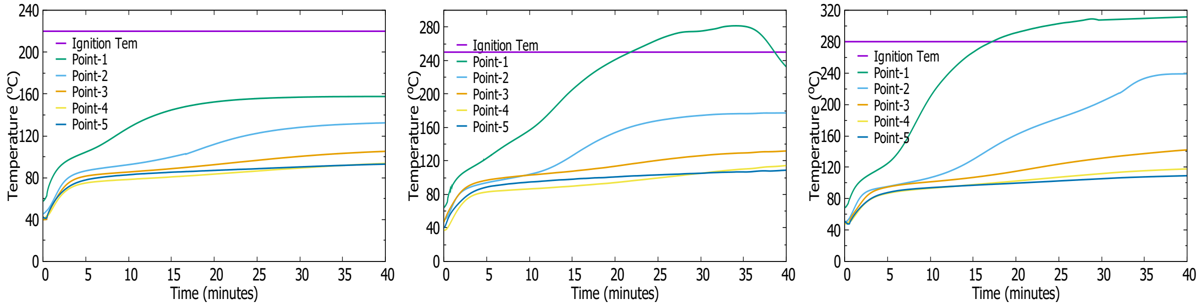

(g) 220^{o}C, 1.2 LPM (h) 250^{o}C, 1.2 LPM (i) 280^{o}C, 1.2 LPM

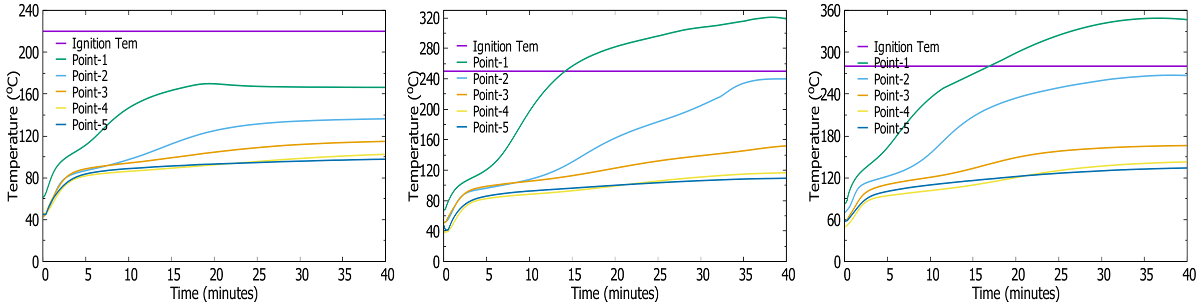

(j) 220^{o}C, 2.4 LPM (k) 250^{o}C, 2.4 LPM (l) 280^{o}C, 2.4 LPM

Figure 7.8: Wood Bark: Temperature profile of different mass flow rate and ignition temperature.

passes. Different ignition and mass flow conditions result in different peak temperatures. And under 250°C & 2.4 LPM and 280°C & 2.4 LPM operating condition, the temperature profile of point-2 has a peak (Figs. 7.7k and 7.7l). Referring to Figs. 7.4k and 7.4l, we can find that a finger pattern is formed during the smouldering combustion process and it covers the position of the point-2. Thus, like point-1, the temperature profile of point-2 has a peak value.

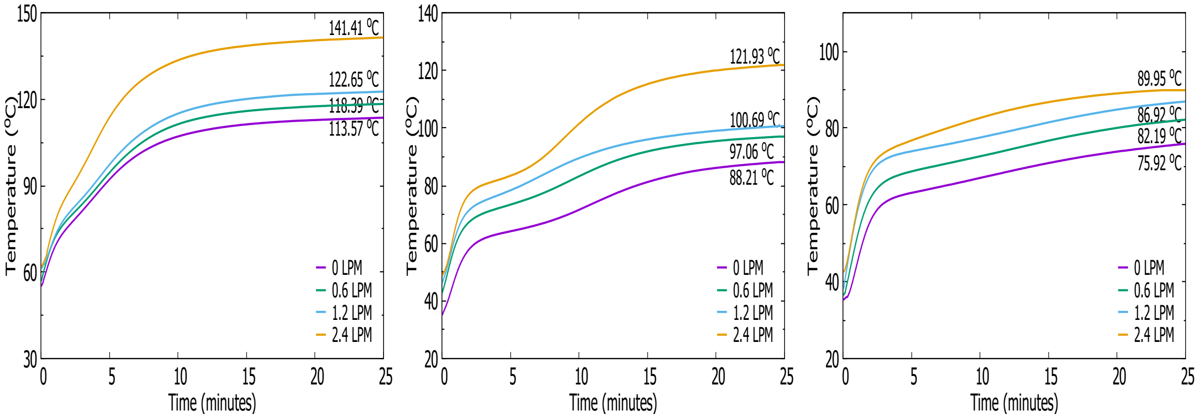

(a) Point-1, 220^{o}C (b) Point-2, 220^{o}C (c) Point-3, 220^{o}C

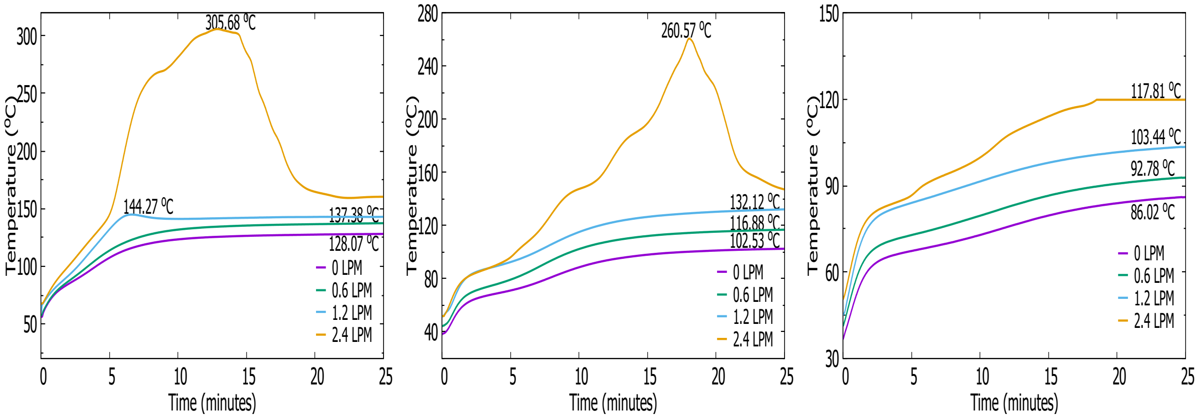

(d) Point-1, 250^{o}C (e) Point-2, 250^{o}C (f) Point-3, 250^{o}C

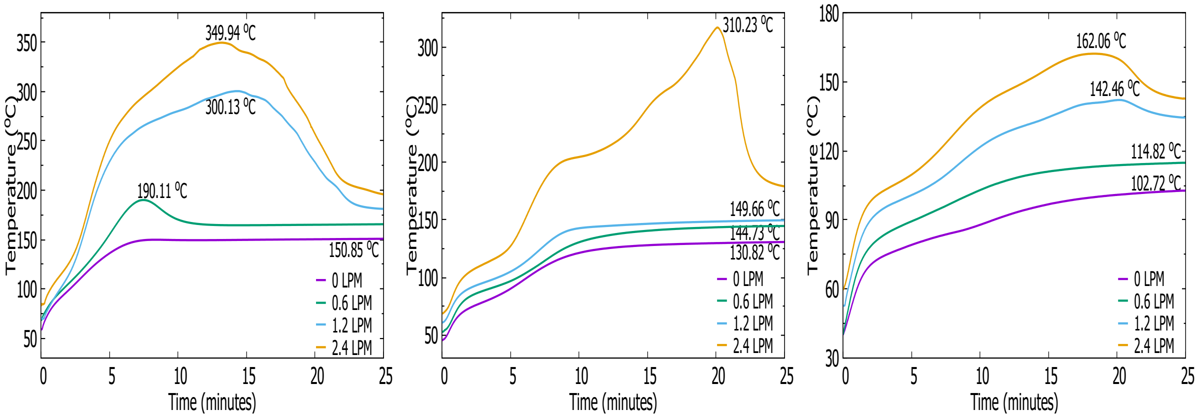

(g) Point-1, 280^{o}C (h) Point-2, 280^{o}C (i) Point-3, 280^{o}C

Figure 7.9: Wheat Straw: Temperature profile of points under different mass flow rate and ignition temperature.

The temperatures of point-4 and point-5 increase when the fuel was added into the rig for both wheat straw and wood bark packed bed. The temperature raises at the beginning is because the fuel particles is under normal temperature state and the temperature of the gas environment in the rig is much higher. After the heat exchange process ends and the fuel reaches the equilibrium state, the temperature does not vary too much and keeps nearly stable. This phenomenon

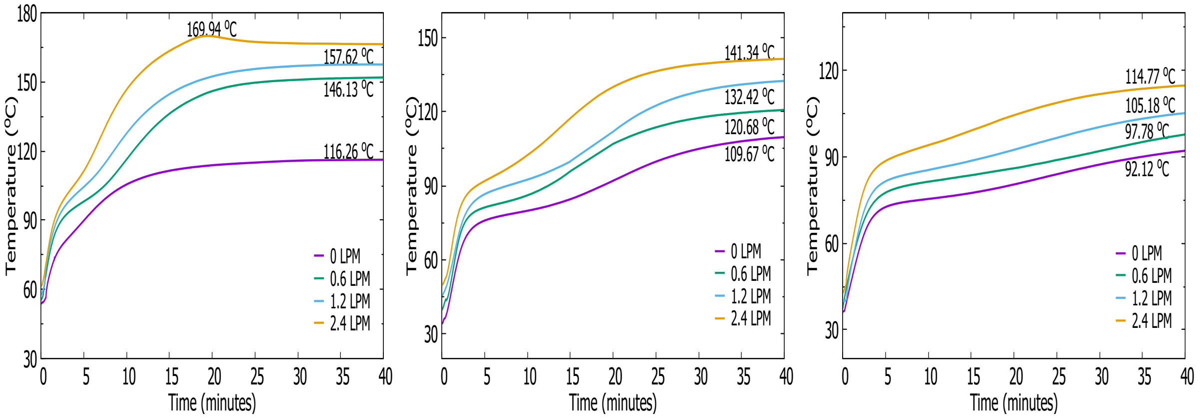

(a) Point-1, 220^{o}C (b) Point-2, 220^{o}C (c) Point-3, 220^{o}C

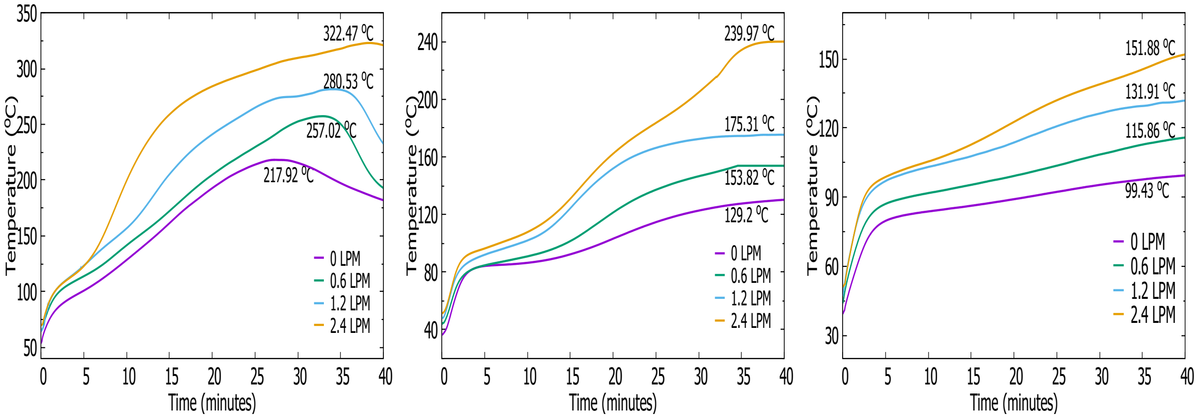

(d) Point-1, 250^{o}C (e) Point-2, 250^{o}C (f) Point-3, 250^{o}C

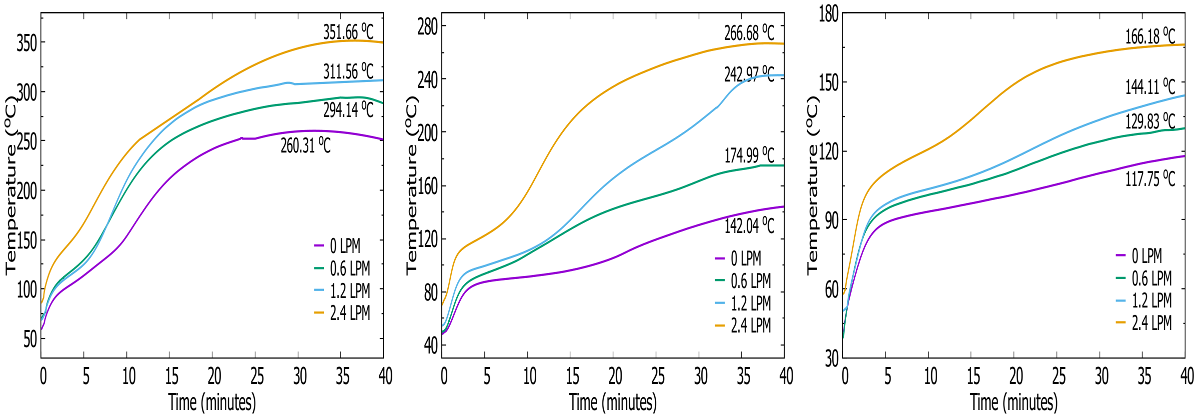

(g) Point-1, 280^{o}C (h) Point-2, 280^{o}C (i) Point-3, 280^{o}C

Figure 7.10: Wood Bark: Temperature profile of points under different mass flow rate and ignition temperature.

is consistent with the images presented in Figs. 7.4 and 7.5. The combustion areas are limited to the front part of the packed bed. Further, because of the long distance away from the ignition plate and the limitation of thermal properties, the heat from the ignition plate and that generated due to the chemical reactions is not delivered to the later part of the packed bed. Therefore, the temperature of the unburned area only changes at the early stage of the whole process, and is not influenced too much by the combustion process. However, the temperatures of point-4 and point-5 are higher when the ignition temperature and air mass flow rate increase. This is because of the enhanced heat conductive or heat convection at higher temperature conditions and faster flow conditions.

Table 7.2: Highest temperature measured during biomass packed bed smouldering combustion

Ignition Temperature (^{o}C)	Air Flow Rate (LPM)	Point-1 (^{o}C)	Point-2 (^{o}C)	Point-3 (^{o}C)
Wheat Straw				
220	0	113.57	88.21	75.92
	0.6	118.39	97.06	82.10
	1.2	122.65	100.69	86.92
	2.4	141.41	121.93	89.95
250	0	128.07	102.53	86.02
	0.6	137.30	116.88	92.78
	1.2	144.27	132.12	103.44
	2.4	305.68	260.57	117.81
280	0	150.85	130.82	102.72
	0.6	190.11	144.73	114.82
	1.2	300.13	149.66	142.66
	2.4	349.94	310.23	162.06
Wood Bark				
220	0	116.26	109.67	92.12
	0.6	146.13	120.68	97.78
	1.2	157.62	132.42	105.18
	2.4	169.94	141.34	114.77
250	0	217.92	129.2	99.43
	0.6	257.02	153.82	115.86
	1.2	280.53	175.31	131.91
	2.4	322.47	239.97	151.88
280	0	260.31	142.04	112.75
	0.6	294.14	174.99	129.83
	1.2	311.56	242.97	144.11
	2.4	351.66	266.68	166.18

From the above figures it can be seen that, the ignition temperature has a greater influence on the propagation of smouldering reaction front compared with mass flow rate of air. Further, comparing the smouldering combustion properties of the two kinds of fuel, it can be concluded that the wheat straw is more sensitive to the ignition temperature and air mass flow rate. The wood bark takes longer time to reach the peak temperature during the smouldering combustion process, and the peak temperature of point-1 is lower in the same condition. This is caused by the differences on fuel properties. Compared with wood bark, the wheat straw contains more volatile and less ash, which makes it easier to be ignited and burns. Thus, the combustion process involves more area of the packed bed.

Figures 7.9 and 7.10 compares the temperature profiles of point-1, point-2 and point-3 at the same ignition temperature, while under different air mass flow rates during the smouldering combustion process of wheat straw and wood bark packed bed, respectively. The different changing trends of temperature of these points under various operating condition are clearly demonstrated in the figures. For wheat straw, when the ignition temperature is 220°C, the temperatures of these three points under different air mass flow rate show a similar varying tendency. It raises slightly faster at the beginning and then changes to slowly increasing. The reason for the two different temperature increasing stages has been explained before. No obvious inflection or peak value appeareds in these temperature profiles. Moreover, Figs. 7.9a, b and c indicate that, all the three points have the highest temperature under the fastest flow (2.4 LPM), but the temperature differences among different air mass flow rate become smaller when the point is further from the ignition plate. When the ignition temperature increases to 250°C, the temperature of point-1 and point-2 under 2.4 LPM condition is much higher than other mass flow rate conditions due to the propagation of smouldering combustion. In other cases, the temperature of the three points raises about 20°C compared to the corresponding air mass flow rate at 220°C. When the ignition temperature reaches 280°C, the parabolic temperature profiles and peak temperatures are observed in more cases. For point-1, the temperature profiles are quite similar under 2.4 LPM and 1.2 LPM conditions with the peak temperature around 350°C and 200°C. When the air mass flow rate is 0.6 LPM, the peak temperature appears at 7 minutes but the temperature drops quickly. The high temperature does not last as long as the air flow rate is 2.4 LPM and 1.2 LPM. For point-3, the temperatures are much higher than the other two ignition temperatures, and the temperature differences amongst different mass flow conditions become larger on the contrary.

Figure 7.10 reports the related temperature profiles of wood bark packed bed. It can be easily seen that, the temperature profiles have different characteristics from wheat straw packed bed. Firstly, the temperatures of wood bark packed bed at the same position are lower than the wheat straw packed bed under the same ignition temperature and air mass flow rate. Secondly, the shape of the temperature profile is nearly the same during wood bark packed bed smouldering combustion. The temperature keeps increasing and comes to a stable stage in the cases. It does not show big differences like wheat straw packed bed smouldering combustion. Finally, it takes longer time for wood bark packed bed to reach the stable temperature. In wheat straw cases, when running the smouldering combustion experiments for 25 minutes, the smouldering combustion reactions stop and the heat exchange in the system terminates. Thus, the system reaches the equilibrium state and the temperature becomes stable. While changing the fuel to wood bark, the process takes about 40 minutes which is nearly twice of that of wheat straw. Therefore, it can be seen that, except for the operating conditions, the fuel properties have a great influence on the smouldering combustion of biomass packed bed as well.

7.5 Heating rate

The heating rate represents the temperature changing characteristic of the biomass packed bed during the smouldering combustion process. It is calculated by using the difference between the peak temperature and the initial temperature divided by the time taken to reach the peak temperature. The heating rate of point-1, point-2 and point-3 during the smouldering combustion process of the biomass packed bed under various conditions are given in Figs. 7.11 and 7.12.

Figure 7.11a reports the heating rate of point-1 during wheat straw packed bed smouldering combustion. It can be seen that, at the ignition temperature of 220°C, the heating rate is small and increased slightly from 3.41°C/min to 7.15 °C/min when the air mass flow rate increases from 0 to 2.4 LPM. The gap between the biggest one and the smallest one is about 4°C/min. When the ignition temperature increases to 250°C, the heating rate under 2.4 LPM and 1.2 LPM increases to 19.45°C/min and 12.58°C/min, respectively, while the other two raise to around 5°C/min. The differences between the heating rates under different air mass flow rates become bigger when the ignition temperature comes up to 280°C. The maximum value reaches 32.87°C/min and the minimum is 9.07°C/min. The gap between the biggest one and the smallest one has raised to about 23°C/min. For point-2 (Fig. 7.11b) and point-3 (Fig. 7.11c), the heating rate increases when increasing the ignition temperature and air mass flow rate. But the growth of heating rate decreases and the gap amongst different air mass flow rates is not as large as point-1. The heating rates of point-1, point-2 and point-3 of wood bard packed bed are reported in Fig. 7.12. The variation trend with the change of ignition temperature and air mass flow rate are similar to wheat straw packed bed. The heating rate becomes smaller from point-1 to point-3. Along with the increase of ignition temperature and air mass flow rate, the heating rate of every point increases.

It should be noticed that, the heating value of wood bark packed bed are much smaller than the wheat straw packed bed at the same position under the same operating conditions. For example, when the biomass packed bed smouldered at the ignition temperature of 280°C and air mass flow rate of 2.4 LPM, the heating rate of point-1 of wheat straw packed bed is 32.87°C/min while it is 10.67°C/min of wood bark packed bed. This is in accordance with the temperature

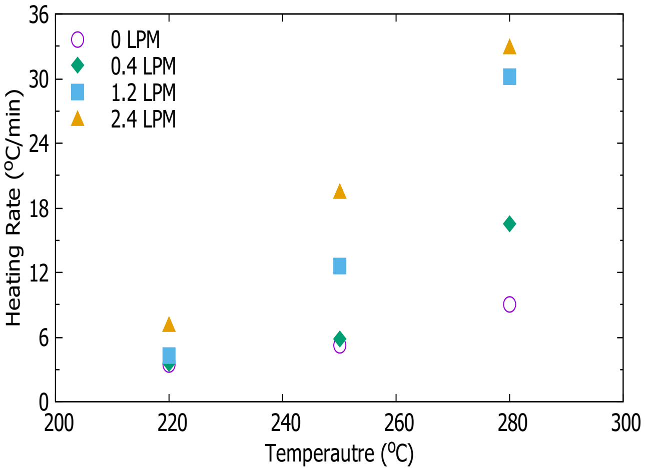

(a) Point-1

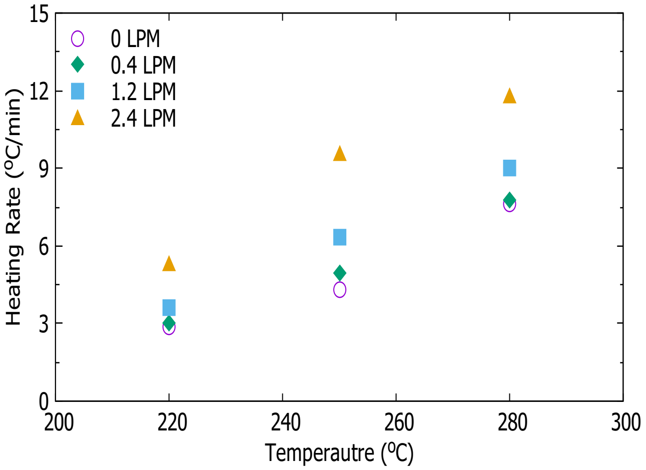

(b) Point-2

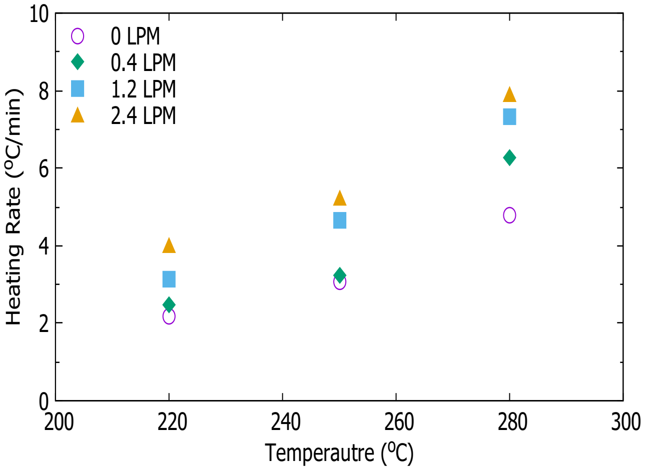

(c) Point-3

Figure 7.11: Wheat straw: Heating rates of points under different mass flow rate and ignition temperature.

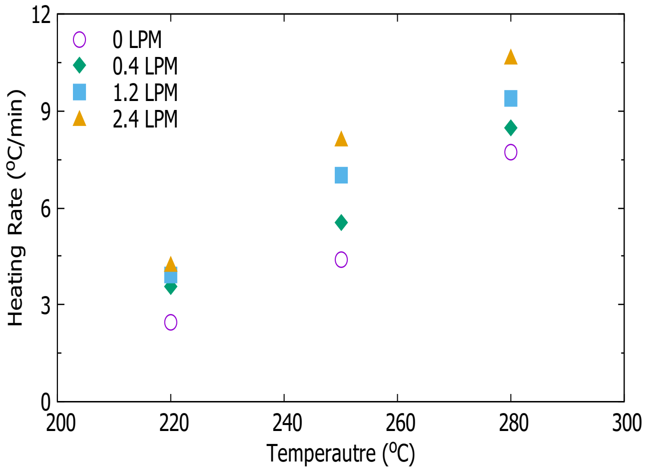

(a) Point-1

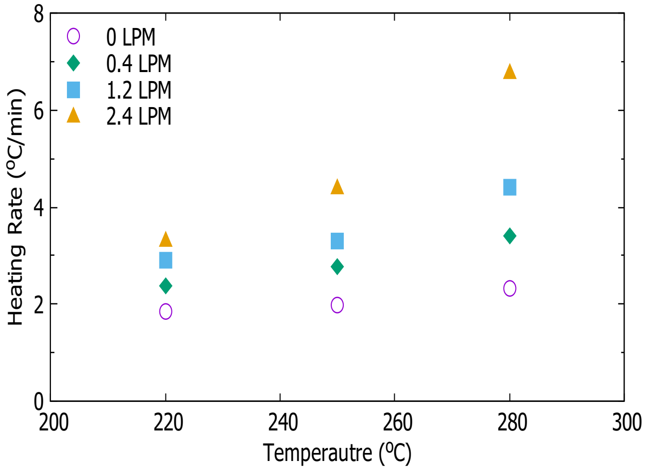

(b) Point-2

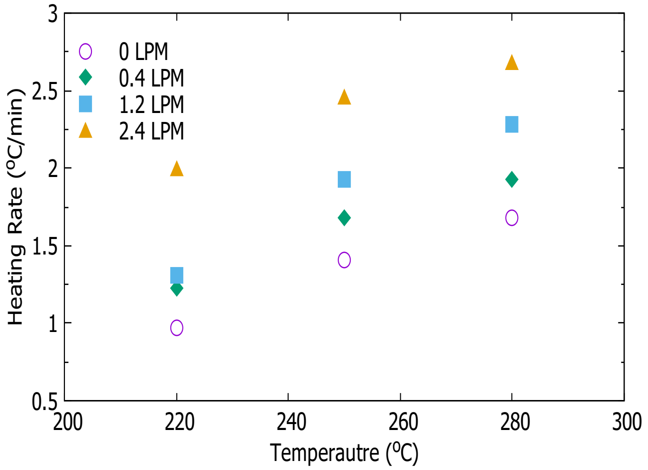

(c) Point-3

Figure 7.12: Wood bark: Heating rates of points under different mass flow rate and ignition temperature.

characteristics, and it is concluded that the properties of fuel play an important role in the smouldering combustion of biomass packed bed.

7.6 Summary and Conclusions

In this chapter, experimental work about the smouldering combustion of the wheat straw and wood bark packed bed were conducted. The shape and speed of the smouldering reaction front, the combustion temperature and the heating rate were investigated when the ignition temperature varied from 220°C to 280°C and the air mass flow rate changed from 0 to 2.4 LPM. The major findings can be summarized as follows.

1. For wheat straw packed bed, the smouldering reaction front keeps flat and propagates forward stably when the ignition temperature is 220°C. The finger pattern is firstly observed at the ignition temperature of 250°C and air mass flow rate of 2.4 LPM. When the ignition temperature increases to 280°C, the smouldering fronts have obvious instabilities for all mass flow rates. For wood bark packed bed, the front instabilities appears till the ignition temperature reaches 280°C.

2. Overall, the speeds of the smouldering reaction front among various air mass flow rate do not vary too much at lower ignition temperature. When the ignition temperature increases, the speeds under all air mass flow rates increase as well but the differences among them become larger. Moreover, the speed of the smouldering combustion front of wheat straw packed bed is faster than the wood bark packed bed.

3. The temperature of the monitoring points raises when the ignition temperature and air mass flow rate are higher. The temperature of point-1 experiences a great change when the smouldering combustion zone covers the position. And in some cases, the temperature of point-2 has the similar change. The temperatures of point-4 and point-5 do not have a great change due to the limited propagation of the smouldering combustion. Moreover, the wheat straw packed bed reaches higher temperature in a shorter combustion time at the same ignition temperature and air mass flow rate compared to wood bark.

4. Similar to the combustion temperature, the heating rate increases along with the increase of ignition temperature and air mass flow rate for both kinds of biomass fuel. And under higher ignition temperature, the differences of heating rate under various air mass flow rate becomes bigger. It proves that the ignition temperature affects the smouldering combustion more than the air mass flow rate.

5. The wheat straw packed bed and wood bark packed bed had different smouldering combustion characteristics. The combustion temperature, the heating rate and the speed of the reaction front during the smouldering combustion process are quite different in the

smouldering combustion process. The values are higher in the wheat straw packed bed smouldering combustion process and it shows a higher smouldering combustion intensity. Moreover, the lasting time of the smouldering combustion process is longer in wood bark packed bed under the same operating conditions. This indicates that the fuel properties play an important role in the biomass packed bed smouldering combustion.

Chapter 8

Conclusions and future work

The transient combustion process of a single coal and biomass particle in a drop-tube furnace in both O_2/N_2 and O_2/CO_2 gas environments with varying oxygen concentrations, and for active and quiescent flows were investigated numerically. The evolutions of gas-phase temperature, major chemical species, gas-phase entropy generation and pollutant emissions were obtained to analyse the single particle combustion characteristics. In addition, an experimental work on the smouldering combustion of biomass packed bed was conducted under different ignition temperature and air mass flow rate conditions. The major findings of these investigations are summarized in Section 7.1, and Section 7.2 presents some recommendations for future work.

8.1 Summary of the conclusions

The numerical simulations are on the basis of an existing experimental work of Ref. [37] [38] [183] in which single coal and biomass particle were reacted in a drop-tube furnace. The particle was injected at the top, and then were ignited and burned in active or quiescent O_2/N_2 and O_2/CO_2 gas conditions with oxygen concentration varying from 20% to 100%. An Eular-Lagrange numerical model coupled with Discrete Phase Model (DPM), standard $k-\varepsilon$ model, weighted-sum-of-grey-gases model (WSGGM) and P-1 radiation model (spherical harmonic method) were implemented. The SIMPLE algorithm was used for the velocity-pressure coupling and the effect of gravity was considered in the numerical simulations. Single kinetic rate devolatilization model and multiple-surface-reactions combustion model were applied for the single particle combustion process. The ignition delay time, particle life time and particle temperature were used to compare with the experimental data. The close agreement between the numerical simulations and experimental measurements confirmed the validation of the numerical model.

In general, oxygenated environments shorten the ignition delay time and particle life time and increase the particle temperature in the single particle combustion. Compared with O_2/N_2 gas conditions, the single particle has longer ignition delay time and particle life time and lower particle temperature at the same oxygen concentration in O_2/CO_2 gas conditions. The spatio-temporal evolutions of the gas-phase temperature and major chemical species for the duration of combustion and beyond are obtained and shown in Chapter 3. The results show that, the highest rate of chemical reactions appears during the combustion of volatile matters and the initation of char combustion always slows down the reactions. Further, at lower oxygen concentration conditions, the homogeneous combustion of volatile matters dominates the gas-phase temperature and chemical species concentrations. While at higher oxygen concentration atmospheres, the post combustion reactions have a greater influence on the temperature and species concentration fields. It should be noted that, there are two different kinds of combustion modes observed in the numerical simulations. When the single coal or biomass particle burning in O_2/N_2 environments, the volatile matters is ignited at the same time with the char particle. However, the devolatilisated gas is ignited once it is released from the coal and biomass particle and starts combustion prior to the ignition of char particle in O_2/CO_2 environments.

Based on the validated numerical model, NO_x and SO_x modellings are conducted. Thermal-NO_x and fuel-NO_x are considered for the NO_x formation. An eight-step mechanism together with one SO_3 formation reaction are used for the SO_x emission modelling. The overall NO, SO_2 and SO_3 PPM and emission rates are calculated to analyse the emissions characteristics. The formation process of pollutant species including NO, HCN, NH_3, SO_2, SO_3 and H_2S is tracked during the single particle combustion process. The results indicate that, more NO_x emissions are generated in O_2/N_2 atmospheres than O_2/CO_2 due to thermal-NO_x formation, while CO_2 background gas promotes the SO_2 and SO_3 emissions. Further, NO emission rate is higher in O_2/N_2 gas conditions than in O_2/CO_2 atmospheres, and SO_2 and SO_3 emission rates have the opposite trend. When oxygen concentration increases, all the emission rates decrease under both atmospheres. In addition, oxygen concentration has a bigger impact on NO_x emissions in CO_2 containing atmospheres, and SO_x pollutants are sensitive to oxygen concentration in either O_2/N_2 or O_2/CO_2 environments.

The unsteady gas-phase entropy generation due to heat transfer, mass transfer and chemical reactions during single particle transient combustion process in varying O_2/N_2 gas conditions are investigated based on the validated combustion model. The results were given in Chapter 5. The entropy generated by chemical reactions is the dominant source of irreversibility during the single particle combustion process, and it increases sharply when the particle is ignited. The entropy generated by the heat transfer is the second contributor, and it continues to be generated for a long time even after the extinction of the particle. The irreversibility due to mass transfer is the main source of the entropy generation during the pre-ignition period where only devolatilization happened, but overall it can be ignored. Moreover, the global entropy generation raises when increasing the oxygen concentration and the increase is more significant in moderately oxygenated conditions than oxygen-riched conditions.

Chapter 6 represents the experimental work of biomass packed bed smouldering combustion. In the experiments, the ignition temperature varies from 220°C to 280°C and the air mass flow rate changes from 0 to 2.4 LPM. The results show that, the ignition temperature has a greater influence on the smouldering combustion than the air mass flow rate. The smouldering reaction front keeps stable in lower temperatures and the instabilities and fingers appear when the ignition temperature and air mass flow rate increase. For wheat straw packed bed, the critical value is ignition temperature of 250°C and air mass flow rate of 2.4 LPM. For wood bark, it is 280°C and 2.4 LPM. The combustion temperature has a great increase when the ignition temperature and air mass flow rate are higher. Increasing the ignition temperature and air mass flow rate also results in higher heating rate and faster reaction front speed. Moreover, under higher ignition temperature, the differences of heat rate and reaction front speed under varying air mass flow rate become more pronounced. Further, due to the different fuel properties of wheat straw and wood bark, the smouldering combustion characteristics were different. The combustion temperature and the heating rate are lower and the speed of reaction front is much slower during the wood bark smouldering combustion process than those of wheat straw.

8.2 Recommendations for future work

In this work, the transient combustion of single Lignite coal and Bagasse biomass particle in varying gaseous environments and the smouldering combustion of biomass packed bed were investigated. Since the process of solid fuel combustion is complex, there is still a considerable amount of work that can be done for further understanding of the combustion process. Therefore, some suggestions are highlighted here for the future work.

1. The volatile matters were simplified to be treated as one species and ash content was ignored during the transient combustion modelling. A more complicated composition of volatile matters including several species can be considered during the devolatilization process to obtain more comprehensive results. Moreover, the influences of ash on the combustion process especially on the char combustion stage can be investigated.

2. The chemical reactions occurring during the transient combustion process under different gas atmospheres are quite complicated. A more detailed reaction mechanism could be used for the future numerical simulations. Attentions should be paid to the investigation of different combustion modes (whether the volatile matters and char combust sequentially) for coal and biomass under different oxygen concentration and background gas conditions.

3. This work looked into the evolution of gas-phase entropy generation when the single coal

or biomass particle combust in varying O_2/N_2 gas environments for the first time. Further work can be extended to the irreversibilities during the single particle combustion in varying O_2/CO_2 gas conditions. In addition, the NO_x and SO_x emissions during coal particles in varying O_2/CO_2 gas conditions should be explored as well.

4. For the case of smouldering combustion of biomass packed bed, the effects of the size and porosity of the packed bed and the biomass particle size on the smouldering combustion can be investigated experimentally. In addition, mathematical or numerical modelling can be done to compare with the experimental results and analyse the characteristics of the smouldering combustion front.

5. The combustion properties of a small range of coal and biomass were investigated in this work. Different types of coal particles including Bitumious and Anthracite and different kinds of biomass sources including wood-based, herbaceous and fruit biomass can be used for the numerical and experimental work. The investigations could provide better understanding of their combustion behaviours and better guidances for their further applications.

Bibliography

[1] Dubley, B. (2018). *BP statistical review of world energy June 2018*. London, UK.

[2] Hoodwink, M. M., Fail, A. P. C., Broke, R. V. D., Bends, G., Gisele, D., Turkenburg, W. C. (2003). *Exploration of the ranges of the global potential of biomass for energy*. Biomass and Bioenergy. pp: 119-133.

[3] Boden, T. A., Marland, G., Andres, R. J. (2017). *Global, regional, and national fossil fuel CO_2 emissions*. Carbon Dioxide Information Analysis Center, Oak Ridge National Laboratory, U.S. Department of Energy. U.S.A.

[4] Stocker, T. F., Qin, D., Plattner, G., Tignor, M. M., Allen, S. K., Soschung, J., Nauels, A., Xia, Y., Bex, V., Midgley, P. M. (2013). *Climate Change: The physical science basis. Contribution of working group 1 to the fifth assessment report of the Intergovernmental Panel on Climate Change*. Cambridge University Press. UK.

[5] Intergovernmental Panel on Climate Change. 2014. *Climate Change 2014: Synthesis Report. Contribution of working group I, II and III to the fifth assessment report of the Intergovernmental Panel on Climate Change*. Cambridge University Press. UK.

[6] European Renewable Energy Council (EREC). (2006). *Renewable energy scenario by 2040*. Brussels, Belgium.

[7] National Energy Foundation. *Biomass Energy*. Available online. http://wwww.nef.org.uk.

[8] Pasu, P. (2010). *Biomass gasification and pysolysis: Practical and design and theory*. Elsiever Inc.

[9] Department of Energy & Climate Change. (2012). *Government response to the consultation on proposals for the levels of banded support under the Renewable Obligation for the period 2013-2017 and the Renewable Obligation order 2012*. HM Government.

[10] Carbo, M. C., Jansen, D., Boon, D., Dihkstra, J. W., Van Den Brink, R. W., Verkooijen, A. H. M. (2009). *Staged water-gas shift configuration: Key to efficiency penalty reduction during pre-combustion decarbonisation in IGCC*. Energy Procedia. 1, pp: 661-668.

[11] Adams, R. G., Alin, J., Biede, O., Booth, N. J., Demontigny, D., Drew, R., Idem, R., Laursen, M., Peralt-solorio, D., Sanpasertparnich, T., Trunkfield, A. (2009). *CAPRICE project-Engineering study on the integration of post combustion capture technology into the power plant gas path and heat cycle*. Energy Procedia. 1, pp: 3801-3808.

[12] Buhre, B., Elliott, L. K., Sheng, C. D., Gupta, R. P., Wall, T. F. (2005). *Oxy-fuel combustion technology for coal-fired power generation*. Progress in Energy and Combustion Science. 31, pp: 283-307.

[13] Wall, T. F. (2007). Combustion proesses for carbon capture. Proceedings of the Combustion Institute. 31, pp: 31-47.

[14] Wall, T. F., Spero, Y., Elliott, C., Khare, L., Rathman, S., Zeenathal, R., Moghtaderi, F., Buhre, B., Sheng, B., Gupta, C., Yamada, R., Makino, T., Yu, J. (2009). *An overview on oxyfuel coal combustion-State of the art reserach and technology development*. Chemical Engineering Research and Design. 87, pp: 1003-1016.

[15] Toftegaard, M. B., Brix, J., Jensen, P. A., Glarborg, P., Jensen, A. D. (2010). *Oxy-fuel combustion of solid fuels*. Progress in Energy and Combustion Science. 36(5), pp: 581-625.

[16] Chen, L., Yong, S. Z., Ghoniem, A. F. (2012). *Oxy-fuel combustion of pulverized coal: Characterization, fundamentals, stabilization and CFD modeling*. Progress in Energy and Combustion Science. 38(2), pp: 156-214.

[17] Normann, F., Thunman, H., Johnsson, F. (2009). *Process analysis of an oxygen lean oxy-fuel power plant with co-production of synthesis gas*. Energy Conversion and Management. 50, pp: 279-286.

[18] Sturgeon, D. W., Cameron, E. D., Fitzgerald, F. D. (2009). *Demonstration of an oxyfuel combustion system*. Energy procedia. 1, pp: 471-478.

[19] Dong L., Gao S., Song W., Li J., Xu G. (2008). *NO reduction in decoupling combustion of biomass and biomass-coal blend*. Energy Fuels. 23(1), pp: 224-228.

[20] Bowman, C. T. (1992). *Control of combustion-generated nitrogen oxide emissions: Technology driven by regulation*. Symposium (International) on Combustion. 24(1), pp: 859-878.

[21] Pohl, J. H., Sarofim, A. F. (1977). *Devolatilization and oxidation of coal nitrogen*. Symposium (International) on Combustion. 16(1), pp: 491-501.

[22] Fenimore, C. (1971). *Formation of nitric oxide in premixed hydrocarbon flames*. Symposium (International) on Combustion. 13, pp: 373-380.

[23] Spliethoff, H. (2010). *Power generation from solid fuels*. Springer Heidelberg Dordrecht, London, New York.

[24] Visona, S. P., Stanmore, B. R. (1996). *Modelling NO_x release from a single coal particle*. Combustion and Flame. 105, pp: 92-103.

[25] Chowdhury, B. H. (1996). *Emission control alternatives for electric utility power plants*. Energy Sources. 18(4), pp: 393-406.

[26] Dooley, B. (2017). *Combustion characteristics of coal, biomass and their chars in air and oxy-fuel environments*. Ph.D. thesis. The University of Leeds.

[27] International Energy Agency. (2012). *World Energy Outlook 2012*. Paris, France.

[28] Duffy, N. (2007). *Investigation of biomass combustion in grate furnaces using CFD*. PhD thesis. national University of Ireland.

[29] Broek, R., Faajj, A., Wijk, A. (1996). *Biomass combustion for power generation*. Biomass and Bioenergy. 11, pp: 271-281.

[30] Levendis, Y. A., Joshi, K., Khatami, R., Sarofim, A. F. (2011). *Combustion behavior in air of single particle from three different coal ranks and from sugarcane bagasse*. Combustion and Flame. 158, pp: 452-465.

[31] Chen L., Yong S. Z., Ghoniem A. F. (2012). *Oxy-fuel combustion of pulverized coal: characterization, fundamentals, stabilization and CFD modeling*. Progress in Energy and Combustion Science. 38(2), pp: 156-214.

[32] Edge, P., Gharebaghi, M., Irons, R., Porter, R. T. J., Pourkashanian, M., Smith, D., Stephenson, P., Williams, A. (2011). *Combustion modelling opportunities and challenges for oxy-fuel carbon capture technology*. Chemical Engineering Research and Design. 89(9), pp: 1470-1493.

[33] Abdelmotalib, H. M., Youssef, M. A. M., Hassan, A. A., Youn, S. B., Im, I. T. (2015). *Heat transfer process in gas-solid fluidized bed combustors: a review*. International Journal of Heat and Mass Transfer. 89, pp: 567-575.

[34] Bu, C. S., Liu, D. Y., Chen, X. P., Pallares, D., Gomez−Barea A. (2014). *Ignition behavior of single coal particle in a fluidized bed under O_2/CO_2 and O_2/N_2 atmospheres: A combination of visual image and particle temperature*. Applied Energy. 115, pp: 301-308.

[35] Bu, C. S., Leckner, B., Chen, X. P., Gomez−Barea A., Liu, D. Y., Pallares, D. (2015). *Devolatilization of a single fuel particle in a fluidized bed under oxy-combustion conditions. Part B: Modeling and comparison with measurements*. Combustion and Flame. 162, pp: 809-818.

[36] Bu, C. S., Pallares, D., Chen, X. P., Gomez−Barea A., Liu, D. Y., Leckner, B., Lu, P. (2016). *Oxy−fuel combustion of a single fuel particle in a fluidized bed: char combustion characteristics, an experimental study*. Chemical Engineering Journal. 287, pp: 649-656.

[37] Khatami, R., Stivers, C., Joshi, K., Levendis, Y. A., Sarofim, A. F. (2012). *Combustion behaviour of single particles from three different coal ranks and from sugar cane bagasse in* O_2/N_2 *and* O_2/CO_2 *atmospheres*. Combustion and Flame. 159(3), pp: 1253-1271.

[38] Khatami, R., Stivers, C., Levendis, Y. A. (2012). *Ignition characteristics of single coal particles from three different ranks in* O_2/N_2 *and* O_2/CO_2 *atmospheres*. Combustion and Flame. 159(12), pp: 3554-3568.

[39] Brix, J., Navascues L. G., Nielsen J. B., Bonnek P. L., Larsen H. E., Clausen S., Glarborg P., Jensen A. D. (2013). *Oxy-fuel combustion of millimeter-sized coal char: Particle temperatures and NO formation*. Fuel. 106, pp: 72-78.

[40] Zhou K., Lin Q. Z., Hu H. W., Hu H. Q., Song L. B. (2017). *The ignition characteristics and combustion processes of the single coal slime particle under different hot-coflow conditions in* N_2/O_2 *atmosphere*. Energy. 136, pp: 173-184.

[41] Riaza J., Khatami R., Levendis Y. A., Alvarez L., Gil M. V., Pevida C., Rubiera F., Pis J. J. (2014). *Combustion of single biomass particles in air and in oxy-fuel conditions*. Biomass and Bioenergy. 64, pp: 162-174.

[42] Tolvanen H., Raiko R. (2014). *An experimental study and numerical modeling of combustion two coal chars in a drop-tube reactor: A comparison between* N_2/O_2*,* CO_2/O_2 *and* $N_2/CO_2/O_2$ *atmospheres*. Fuel. 124, pp: 190-201.

[43] Timothy, L. D,. Sarofim, A. F., Beer, J. R. (1982). *Characteristics of single particle coal combustion*. Symposium (International) on Combustion. 19, pp: 1123-1130.

[44] Lee, H., Choi S. (2015). *An observation of combustion behavior of a single coal particle entrained into hot gas flow*. Combustion and Flame. 162, pp: 2610-2620.

[45] Lee, H., Choi S. (2016). *Motion of single pulverized coal particles in a hot gas flow field*. Combustion and Flame. 169, pp: 63-71.

[46] Shen J., Liu J X., Zhang H., Jiang X. M. (2013). NO_x *emission characteristics of superfine pulverized anthracite coal in air-staged combustion*. Energy Conversion and Management. 74, pp: 454-461.

[47] Joutsenoja, T., Saastamoinen, J., Aho, M., Hernberg, R. (1999). *Effects of pressure and oxygen concentration on the combustion of different coals*. Energy and Fuels. 13, pp: 130-145.

[48] Murphy, J. J., Shaddix, C. R. (1996). *Combustion kinetics of coal chars in oxygen-enriched environments*. Combustion and Flame. 144, pp: 710-729.

[49] Koser, J., Becker L. G., Vorobiev N., Schiemann M., Scherer V., Bohm B., Dreizler A. (2015) *Characterization of single coal particle combustion within oxygen-enriched environments using high-speed OH-PLIF*. Applied Physics B: Lasers and Optics. 121, pp: 459-464.

[50] Koser, J., Becker L. G., GoBmann A., Bohm B., Dreizler A. (2017) *Investigation of ignition and volatile combustion of single coal particles within oxygen-enriched atmospheres using high-speed OH-PLIF*. Proceedings of the Combustion Institute. 36, pp: 2103-2111.

[51] Zou, C., Cai, L., Zheng, C. G. (2014). *Numerical research on the homogeneous/heterogeneous ignition process of pulverized coal in oxy-fuel combustion*. International Journal of Heat and Mass Transfer. 73, pp: 207-216.

[52] Johansson, R., Leckner, B., Andersson, K., Johnsson, F. (2013). *Influence of particle and gas radiation in oxy-fuel combustion*. International Journal of Heat and Mass Transfer. 65, pp: 143-152.

[53] Richter, A., Nikrityuk, P. A., Meyer, B. (2015). *Three-dimensional calculation of a chemically reacting porous particle moving in a hot* O_2/CO_2 *atmosphere*. International Journal of Heat and Mass Transfer. 83, pp: 244-258.

[54] Chabane, A., Truffin, K., Nicolle, A., Nicoud, F., Cabrit, O., Angelberger, C. (2015). *Direct Numerical Simulation of combustion near a carbonaceous surface in a quiescent flow*. International Journal of Heat and Mass Transfer. 84, pp: 130-148.

[55] Tufano G. L., Stein O. T., Kronenburg A., Frassoldati A., Faravelli T., Deng L., Kempf A. M., Vascellari M., Hasse C. (2016). *Resolved flow simulation of pulverized coal particle devolatilization and inigtion in air- and* O_2/CO_2-*atmospheres* Fuel. 186, pp: 285-292.

[56] Wieck-Hansen, K., Overgaard, P., Larsen, O. H. (2000). *Cofiring coal and straw in a 150 MWe power boiler experiences*. Biomass Bioenergy. 19(6), pp: 395-409.

[57] Gani, A., Morishita, K., Nishikawa, K., Naruse, I. (2005). *Characteristics of cocombustion of low-rank coal with biomass*. Energy Fuels. 19(4), pp: 1652-1659.

[58] Lu, G., Yan, Y., Cornwell, S., Whitehouse, M., Riley, G. (2008). *Impact of co-firing coal and biomass on flame characteristics and stability*. Fuel. 87(7), pp: 1133-1140.

[59] Bragato, M., Joshi, K., Carlson, J. B., Tenorio, J. A. S., Levendis, Y. A. (2012). *Combustion of coal, bagsse and blends thereof: Part I: Emissions from batch combustion of fixed beds of fuels*. Fuel. 96, pp: 43-50.

[60] Wang, X. B., Tan, H. Z., Niu, Y. Q., Pourkashanian, M., Ma, L., Chen, E. Q., Liu, Y., Liu, Z. N., Xu, T. M. (2011) *Experimental investigation on biomass co-firing in a 300 MW pulverized coal-fired utility furnace in China*. Proceedings of the Combustion Institute. 33(2), pp: 2725-2733.

[61] Lu, H., Robert, W., Peirce, G., Ripa, B., Baxter, L. (2008). *Comprehensive study of biomass particle combustion*. Energy Fuels. 22, pp: 2826-2839.

[62] Wang, L. W., Karimi, N., Paul, M. C. *Gas-phase transport and entropy generation during transient combustion of single biomass particle in varying oxygen and nitrogen atmospheres*. International Journal of Hydrogen Energy. 43(17), pp: 8506-8523.

[63] Torabi, M., Zhang, K. L., Karimi, N., Peterson, G. P. (2016). *Entropy generation in thermal systems with solid structures-a concise review*. International Journal of Heat and Mass Transfer. 97, pp: 917-931.

[64] Pedersen, L. S., Morgan, D. J., Kamp, W., Christensen, J., Jespersen, P., Dam-Johansen, K. (1997). *Effects on SO_x and NO_x emissions by co-firing straw and pulverized coal*. Energy Fuels. 11(2), pp: 439-446.

[65] Hayhurst, A. N., Vince, I.M. *Nitric oxide formation from N_2 in flames: The importance of "promt" NO*. Progress in Energy and Combustion Science. 6(1), pp: 35-51.

[66] Reddy, M. S., Venkataraman, C. (2002). *Inventory of aerosol and sulphur dioxide emissions from India. Part II-biomass combustion*. Atmospheric Environment. 36(4), pp: 699-712.

[67] Zhu C. Q., Liu S. Y., Liu H., Yang J., Liu X. Y., Xu G. W. (2015). *NO_x emission characteristics of fluidized bed combustion in atmospheres rich in oxygen and water vapor for high-nitrogen fuel*. Fuel. 139, pp: 346-355.

[68] Bueno−Lopez A., Garcia−Garcia A., Linares−Solano A. (2002). *NO_x reduction by potassium-containning coal pellets. Discussing lifetime test profiles*. Fuel Processing Technology. 77-78, pp: 301-307.

[69] Valentim B., Lemos de Sousa M. J., Abella P., Boavida D., Gulyurtlu I. (2006). *Combustion studies in a fluidised bed-The link between temperature, NO_x and N_2O formation, char morphology and coal type*. International Journal of Coal Geology. 67, pp: 191-201.

[70] Svoboda K., Pohorely M. (2014). *Influence of operating conditions and coal properties on NO_x and N_2O emissions in pressurized fluidized bed combustion of subbituminous coals*. Fuel. 83, pp: 1095-1103.

[71] Jiang, X. M., Huang, X. Y., Liu, J. X., Han, J. X. (2010). *NO_x emission of fine- and superfine- pulverized coal combustion in O_2/CO_2 atmosphere*. Energy & Fuels. 24(12), pp: 6307-6313.

[72] Tullin, C., Sarofim, A., Beer, J., Teare, J. (1995). *Effect of SO_2 and NO on the conversion of fuel nitrogen to N_2O and No in single particle combustion of coal*. Combustion Science and Technology. 106, pp: 153-166.

[73] Shen, B., Mi, T., Liu, D., Feng, B., Yao, Q., Winter, F. (2003). *N_2O emission under fluidized bed combustion condition*. Fuel Processing Technology. 84, pp: 13-21.

[74] Tarelho L. A. C., Matos M. A. A., Pereira F. J. M. A. (2006). *Influence of limestone addition on the behaviour of NO and N_2O during fluidised bed coal combustion*. Fuel. 85, pp: 967-977.

[75] Wang Y. F., Wang X. B., Hu Z. F., Li Y., Deng S. H., Niu B., Tan H. Z. (2015). *NO emissions of combustion efficiency during biomass co-firing and air-staging*. BioResources. 10(2), pp: 3987-3998.

[76] Zhao B. T., Su Y. X., Liu D. Y., Zhang H., Liu W., Cui G. M. (2016). *SO_2/NO_x emissions and ash formation from algae biomass combustion: Process characteristics and mechanisms*. Energy. 113, pp: 821-830.

[77] Zhou H., Huang Y., Mo G. Y., Liao Z. Y., Cen K. F. (2017). *Experimental investigations of the conversion of fuel-N, volatile-N and char-N to NO_x and N_2O during single coal particle fluidized bed combustion*. Journal of the Energy Institute. 90, pp: 62-72.

[78] Zhou H., Li Y., Li N., Qiu R. C., Meng S., Cen K. F. (2017). *Experimental study of the NO and N_2O emissions during devolatilization and char combustion of a single biomass particle in O_2/N_2 and O_2/H_2O under low temperature condition*. Fuel. 206, pp: 162-170.

[79] Courtemanche B., Levendis Y. A. (1998). *A laboratory study on the NO, NO_2, SO_2, CO and CO_2 emissions from the combustion of pulverized coal, municipal waste plastics and tires*. Fuel. 77(3), pp: 183-196.

[80] Tian L. N., Yang W., Chen Z. H., Wang X. H., Yang H. P. (2016). *Sulfur behaviour during coal combustion in oxy-fuel circulating fluidized bed condition by using TG-FTIR*. Journal of Energy Institute. 89, pp: 264-270.

[81] Li. W., Li S. Y., Ren Q. Q., Tan L., Li H. Y., Liu J. Z., Lu Q. G. (2014). *Study of oxy-fuel cola combustion in a 0.1 MWth circulating fluidized bed at high oxygen concentrations*. Energy Fuels. 28, pp: 1249-1254.

[82] Duan L. B., Duan Y. Q., Zhao C. S., Anthony E. J. (2015). *NO emission during co-firing coal and biomass in an oxy-fuel circulating fluidized bed combustor*. Fuel. 150, pp: 8-13.

[83] Daood S. S., Javed M. T., Gibbs B. M., Nimmo W. (2013). *NO_x control in coal combustion by combining biomass co-firing, oxygen enrichment and SNCR*. Fuel. 105, pp: 283-292.

[84] Shao L. M., Fan S. S., Zhang H., Yao Q. S., He P. J. (2013). *SO_2 and NO_x emissions from sludge combustion in a CO_2/O_2 atmohphere*. Fuel. 109, pp: 178-183.

[85] Duan L. B., Zhao C. S., Ren Q. Q., Wu Z., Chen X. P. (2011). *NO_x precursors evolution during coal heating process in CO_2 atmosphere*. Fuel. 90, pp: 1668-1673.

[86] Croiset E., Thambimuthu K. V. (2011). *NO_x and SO_2 emissions from O_2/CO_2 recycle coal combustion*. Fuel. 80, pp: 2117-2121.

[87] Moron W., Rybak W. (2015). *NO_x and SO_2 emissions of coals, biomass and their blends under different oxy-fuel atmospheres*. Atmospheric Environment. 116, pp: 65-71.

[88] Duan L. B., Zhao C. S., Zhou W., Liang C., Chen X. P. (2009). *Sulfur evolution from coal combustion in O_2/CO_2 mixture*. Journal of Analytical and Applied Pyrolysis. 86, pp: 269-273.

[89] Permchart W., Kouprianov V. I. (2004). *Emission performance and combustion efficiency of a conical fluidized-bed combustor firing various biomass fuels*. Bioresource Technology. 92, pp: 83-91.

[90] Liu H., Chaney J., Li J. X., Sun C. G. (2013). *Control of NO_x emissions of a domestic/small-scale biomass pellet boiler by air staging*. Fuel. 103, pp: 792-798.

[91] Zheng L. G., Furimsky E. (2003). *Assessment of coal combustion in $O_2 + CO_2$ by equilibrium calculations*. Fuel Processing Technology. 81, pp: 23-34.

[92] Hu Y., Naito S., Kobayashi N., Hasatani M. (2000). *CO_2, NO_x and SO_2 emissions from the combustion of coal with high oxygen concentration gases*. Fuel. 79, pp: 1925-1932.

[93] Ren X. H., Sun R., Meng X. X., Vorobiev N., Schiemann M., Levendis Y. A. (2017). *Carbon, sulphur and nitrogen oxide emissions from combustion of pulverized and torrefied biomass*. Fuel. 188, pp: 310-323.

[94] Gurturk, M., Oztop, H. F. (2016). *Exergy analysis of a circulating fluidized bed boiler cogeneration power plant*. Energy Conversion and Management. 120, pp: 346-357.

[95] Mert G., Oztop H. F. (2016). *Exergy analysis of a circulating fluidized bed boiler cogeneration power plant*. Energy Conversion and Management. 120, pp: 346-357.

[96] Som S. K., Datta A. (2008). *Thermodynamic irreversibilities and exergy balance in combustion processes*. Progress in Energy and Combustion Science. 34(3), pp: 351-376.

[97] Scheffknecht G., Al-Makhadmeh L., Schnell U., Maier J. (2011). *Oxy-fuel coal combustion - A review of the current state-of-the-art*. International Journal of Greenhouse Gas Control. 5, pp: S16-S35.

[98] Khan A. A., Jong W. D., Jansens P. J., Spliethoff H. (2009). *Biomass combustion in fluidized bed boilers: potential problems and remedies*. Fuel Processing Technology. 90(1), pp: 21-50.

[99] Riaza J., Gil M. V., ÃĄlvarez L., Pevida C., Pis J. J., Rubiera F. (2012). *Oxy-fuel combustion of coal and biomass blends*. Energy. 41(1), pp: 429-435.

[100] Arpaci V. S., Selamet A. (1988). *Entropy production in flames*. Combustion and Flame. 73(3), pp: 251-259.

[101] Nishida K., Takagi T., Kinoshita S. (2002). *Analysis of entropy generation and exergy loss during combustion*. Proceedings of the Combustion Institute. 29(1), pp: 869-874.

[102] Chen S. (2010). *Analysis of entropy generation in counter-flow premixed hydrogen-air combustion*. International Journal of Hydrogen Energy. 35(3), pp: 1401-1411.

[103] Chen S., Li J., Han H., Liu Z., Zheng C. (2010). *Effects of hydrogen addition on entropy generation in ultra-lean counter-flow methane-air premixed combustion*. International Journal of Hydrogen Energy. 35(8), pp: 3891-3902.

[104] Chen S., Liu Z., Liu J., Li J., Wang L., Zheng C. (2010). *Analysis of entropy generation in hydrogen-enriched ultra-lean counter-flow methane-air non-premixed combustion*. International Journal of Hydrogen Energy. 35(22), pp: 12491-12501.

[105] Chen S., Han H., Liu Z., Zheng C. (2010). *Analysis of entropy generation in non-premixed hydrogen versus heated air counter-flow combustion*. International Journal of Hydrogen Energy. 35(10), pp: 4736-4746.

[106] Emadi A., Emami M. D. (2013). *Analysis of entropy generation in a hydrogen-enriched turbulent non-premixed flame*. International Journal of Hydrogen Energy. 38(14), pp: 5961-5973.

[107] Safer K., Ahmed O., Fouzi T. (2017). *Entropy generation in turbulent syngas counter-flow diffusion flames*. International Journal of Hydrogen Energy. 42(49), pp: 29532-29544.

[108] Farran R., Chakraborty N. (2013). *A direct numerical simulation-based analysis of entropy generation in turbulent premixed flames*. Entropy. 15(5), pp: 1540-1566.

[109] Borghesi G., Bellan J. (2015). *Irreversible entropy production rate in high-pressure turbulent reactive flows*. Proceedings of the Combustion Institute. 35(2), pp: 1537-1547.

[110] Safari M., Sheikhi M. (2014). *Large eddy simulation-based analysis of entropy generation in a turbulent nonpremixed flame*. Energy. 78(15), pp: 451-457.

[111] Arjmandi H. R., Amani E. (2015). *A numerical investigation of the entropy generation in and thermodynamic optimization of a combustion chamber*. Energy. 81(1), pp: 706-718.

[112] Wang W., Zuo Z., Liu J., Yang W. (2016). *Entropy generation analysis of fuel premixed CH_4/H_2/air flames using multistep kinetics*. International Journal of Hydrogen Energy. 41(45), pp: 20744-20752.

[113] Jiang D., Yang W., Teng J. (2015). *Entropy generation analysis of fuel lean premixed CO/H_2/air flames*. International Journal of Hydrogen Energy. 40(15), pp: 5210-5220.

[114] Jejurkar S. Y., Mishra D. P. (2011). *Effects of wall thermal conductivity on entropy generation and exergy losses in a H_2-air premixed flame microcombustor*. International Journal of Hydrogen Energy. 36(24), pp: 15851-15859.

[115] Chen W. H., Cheng Y. C., Hung C. I. (2012). *Entropy generation from hydrogen production of catalytic partial oxidation of methane with excess enthalpy recovery*. International Journal of Hydrogen Energy. 37(19), pp: 14167-14177.

[116] Puri, I. K. (1992). *Second law analysis of convective droplet burning*. International Journal of Heat and Mass Transfer. 35(10), pp: 2571-2578.

[117] Dash, S. K., Som, S. K. (1991). *Transport processes and associated irreversibilities in droplet combustion in a convective medium*. International Journal of Energy Research. 15(7), pp: 603-619.

[118] Hiwase, S. D., Datta A., Som, S. K. (1998). *Entropy balance and exergy analysis of the process of droplet combustion*. Journal of Physics D: Applied Physics. 31, pp: 1601-1610.

[119] Raghavan V., Gogos, G., Babu, V., Sundararajan, T. (2007). *Entropy generation during the quasi-steady burning of spherical fuel particles*. International Journal of Thermal Sciences. 46(6), pp: 589-604.

[120] Pope, D. N., Raghavan, V., Gogos, G. (2010). *Gas-phase entropy generation during transient methanol droplet combustion*. International Journal of Thermal Sciences. 49, pp: 1288-1302.

[121] Som S. K., Mondal S. S., Dash S. K. (2005). *Energy and exergy balance in the process of pulverized coal combustion in a tubular combustor*. Journal of Heat Transfer. 127(12), pp: 1322-1333.

[122] Mondal S. S. (2008). *Modelling of transport processes and associated thermodynamic irreversibilities in ignition and combustion of a pulverized coal particle*. International Journal of Thermal Sciences. 47(11), pp: 1442-1453.

[123] Baloyi J., Bello-Ochende T., Meyer J. P. (2014). *Thermodynamic optimisation and computational analysis of irreversibilities in a small-scale wood-fired circulating fluidised bed adiabatic combustor*. Energy. 70, pp: 653-663.

[124] Hossain M. A., Jewaratnam J., Ganesan P. (2016). *Prospect of hydrogen production from oil palm biomass by thermochemical process - A review*. International Journal of Hydrogen Energy. 41(38), pp: 16637-16655.

[125] Ibrahim D., Acar C. (2017). *Innovation in hydrogen production*. International Journal of Hydrogen Energy. 42(22), pp: 14843-14864.

[126] Rashidi H., Khorshidi J. (2018). *Exergy analysis and multiobjective optimization of a biomass gasification based multigeneration system*. International Journal of Hydrogen Energy. 43(5), pp: 2631-2644.

[127] Rein, G. (2013). *Smouldering fires and natural fuels. In: Belcher, C. (Ed.), Fire phenomena and the earth system*. Wiley and Sons. pp: 15-33.

[128] Drysdale, D. (1998). *An introduction to fire dynamics*. Wiley.

[129] Speight, J. G. (2011). *Handbook of industrial hydrocarbon processes*. Elsevier.

[130] Ohlemiller, T. J. (1985). *Modeling of smoldering combustion propagation*. Progress in Energy and Combustion Science. 11(4), pp: 277-310.

[131] Aldushin, A. P. (1993). *New results in the theory of filtration combustion*. Combustion and Flame. 94(3), pp: 308-320.

[132] Aldushin, A. P., Matkowsky, B. J., Schult, D. A. (1997). *Upward buoyant filtration combustion*. Journal of Engineering Mathematics. 31, pp: 205-234.

[133] Ohlemiller, T. J., Lucca, D. A. (1983). *An experimental comparison of forward and reverse smoulder propagation in permeable fuel beds*. Combustion and Flame. 54(1-3), pp: 131-147.

[134] Rein, G. (2005). *Computational model of forward and opposed smouldering combustion with improved chemical kinetics*. PhD thesis. University of California.

[135] Aldushin, A. P., Matkowsky, B. J. (1998). *Instabilities, fingering, and the Saffman-Taylor problem in filtration combustion*. Combustion Science and Technology. 133, pp: 293-341.

[136] Saffman, P. G., Taylor, S. G. (1958). *The penetration of a fluid into a porous medium or Hele-Shaw cell containing a more viscous liquid*. Proceedings of the Royal Society of London Series A. 246, pp: 312-331.

[137] Zik, O., Olami, Z., Moses, E. (1998). *Fingering instabilities in combustion*. Physical Review Letters. 81(18), pp: 3868-3871.

[138] Zik, O., Moses, E. (1999). *Fingering instability in combustion: an extended view*. Physical Review E. 60(1), pp: 518-531.

[139] Aldushin, A. P., Braverman, B. Sh. (2009). *Hydrodynamic instability of filtration combustion wave*. Doklady Physical Chemistry. 427(1), pp: 125-128.

[140] Aldushin, A. P., Braverman, B. Sh. (2010). *Saffman-Taylor problem in filtration combustion*. Russia Journal of Physical Chemistry B. 4(5), pp: 788-792.

[141] Aldushin, A. P., Ivleva, T. P. (2013). *Hydrodynamic instability of the coflow filtration combustion: numerical simulation*. Doklady Physical Chemistry. 451(1), pp: 157-160.

[142] Aldushin, A. P., Ivleva, T. P. (2014). *Coflow filtration combustion in a slit-like reactor: simultaneous manifestation of fluid-dynamic and thermal instability*. International Journal of Self-Propagating High-Temperature Synthesis. 23(3), pp: 125-132.

[143] Pojman, J. A., Epstein, I.R. (1990). *Convective Effects on Chemical Waves 1: Mechanisms and Stability Criteria*. Journal of Physical Chemistry. 94, pp: 4966-4972.

[144] Kalliadasis, S., Yang, J. (2004). *Fingering instabilities of exothermic reaction-diffusion fronts in porous media*. Physics of Fluids. 16(5), pp: 1395-1409.

[145] Hejazi, S. H., Azaiez, J. (2010). *Hydrodynamic instability in the transport of miscible reactive slices through porous media*. Physical Review E, 81-056321.

[146] Redapangu, P. R., Vanka, S. P., Sahu, K. C. (2012). *Multiphase lattice Boltzmann simulations of buoyancy-induced flow of two immiscible fluids with different viscosities*. European Journal of Mechanics B/Fluids. 24, pp: 105-114.

[147] Schult, D. A., Matkowsky, B. J., Volpert, V. A., Fernandez-Pello, A. C. (1996). *Forced forward smoulder combustion*. Combustion and Flame. 104, pp: 1-26.

[148] Akkutlu, I. Y., Yortsos, Y. C. (2003). *The dynamics of in-situ combustion fronts in porous media*. Combustion and Flame. 134, pp: 229-247.

[149] Lu, Z. B., Dong, Y. (2011). *Fingering instability in forward smolder combustion*. Combustion Theory and Modelling. 15(6), pp: 795-815.

[150] Kuwana, K., Kushida, G., Uchida, Y. (2014). *Lewis number effect on smoldering combustion of a thin solid*. Combustion Science and Technology. 186, pp: 466-474.

[151] Rostami, A., Murthy, J., Hajaligol, M. (2004). *Modeling of smoldering process in a porous biomass fuel rod*. Fuel. 83, pp: 1527-1536.

[152] Saidi, M. S., Hajaligol, M. R., Mhaisekar, A., Subbiah, M. (2007). *A 3D modeling of static and forward smoldering combustion in a packed bed of materials*. Applied Mathematical Modeling. 31, pp: 1970-1996.

[153] Dobb, A. B., Lautenberger, C., Fernandez-Pello C. (2012). *Computational modeling of smolder combustion and spontaneous transition to flaming*. Combustion and Flame. 159, pp: 448-461.

[154] ANSYS, Inc. (2013) *ANSYS FLuent Theory Guide 15.0*. USA.

[155] Hirschfelder, J. O., Curtiss, C. F., Bird, R. B. (1964). *Molecular Theory of Gases and Liquids*. John Wiley & Sons, New York, 2^{nd} edition.

[156] Warnatz, J., Maas, U., Dibble, R. W. (2001). *Combustion: Physical and Chemical Fundamentals, Modeling and Simulations, Experiments, Pollutant Formation*. Springer-Verlag, Berlin Heidelberg, 3^{nd} edition.

[157] Howell, J. R., Buckius, R. O. (1992). *Fundamentals of engineering thermodynamics*. McGraw-Hill, Inc.

[158] Morsi, S. A., Alexander, A. J. (1972). *An investigation of particle trajectories in two-phase flow systems*. Journal of Fluid Mechanics. 55(2), pp: 193-198.

[159] Blaid, S., Paul, M. C., Watson, I. A. (2013). *Numerical investigation of the heterogeneous combustion processes of solid fuels*. Fuel. 141, pp: 236-249.

[160] Blaid, S. (2015). *Numerical investigation of the combustion processes of various fuels*. Ph.D. thesis. University of Glasgow.

[161] Rosendahl, L. (2013). *Biomass combustion science, technology and engineering*. Woodhead Publishing Limited, Cambridge.

[162] Badzioch, S., Hawksley, P. G. W. (1970). *Kinetics of thermal decomposition of pulverized coal particles*. Industrial & Engineering Chemistry Process Design and Development. 9(4), pp: 521-530.

[163] Chen, X., Horio, M., Kojuma, T. (2000). *Numerical simulation of entrained flow coal gasifiers. Part I: modeling of coal gasification in an entrained flow gasifier*. Chemical Energy Science. 55, pp: 3861-3874.

[164] Mayers, A. M. (1934). *The rate of reduction of carbon dioxide by graphite*. Journal of the American Chemical Society. 56: 70-76.

[165] Jenkinsa, B. M., Baxterb, L. L., Miles, T. R. (1998). *Combustion properties of biomass*. Fuel Processing Technology. 54(1-3), pp: 17-46.

[166] Howard, J. B., Williams, G. C., Fine, D. H. (1973). *Kinetics of carbon monoxide oxidation in postflame gases*. Proceedings of 14th Symposium (International) on Combustion. pp: 975-986.

[167] Serio, M. A., Hamblem, D. G., Markham, J. R., Solomon, P. R. (1987). *Kinetics of volatile product evolution in coal pyrolysis: experiment and theory*. Energy & Fuels. 1, pp: 138-152.

[168] Spliethoff, H. (2010). *Power generation from solid fuels*. Springer Heidelberg Dordrecht, London, New York.

[169] Zeldovich, Y. B. (1946). *The oxidation of nitrogen in combustion and explosions*. Acta Physicochem USSR. 21, pp: 577-628.

[170] Hanson, R. K., Salimian, S. (1984). *Survey of rate constants in H/N/O systems*. In: W.C. Gardine (editor). Combustion Chemistry. pp: 361-421.

[171] Pershing, D. W., Wendt, J. O. L. (1977). *Pulverized coal combustion: The influence of flame temperature and coal composition on thermal and fuel* $N)_x$. Symposium (International) on Combustion. 16(1), pp: 389-399.

[172] Wang, W., Brown, S. D., Hindmarsh, C. J., Thomas, K. M. (1994). NO_x *release and reactivity of chars from a wide range of coals during combustion*. Fuel. 73, pp: 1381-1388.

[173] Hill, S. C., Smoot, L. D. (2000). *Modelling of nitrogen oxides formation and destruction in combustion systems*. Progress in Energy and Combustion Science. 26(4-6), pp: 417-458.

[174] Glarborg, P., Jensen, A. D., Johnsson, J. E. (2003). *Fuel nitrogen conversion on solid fuel fired systems*. Progress in Energy and Combustion Science. 29(2), pp: 89-113.

[175] Smith, P. J., Smoot, L. D. (1985). *Coal combustion and gasification*. Plenum Press, New York.

[176] Smoot, L. D., Smith, P. L. (1985). NO_x pollutant formation in a turbulent coal system. In: Coal Combustion and Gasification. Plenum Press, New York. pp: 373-403.

[177] De Soete, G. G. (1975). *Overall reactions rate of NO and* N_2 *formation from fuel nitrogen*. In: 15^{th} Symp.(Int.) on Combustion. The Combustion Institute, Pittsburgh. pp: 1093-1102.

[178] Kramlich, J. C. (1980). *The fate and behaviour of fuel-sulfur in combustion systems*. PhD thesis. Washington State University, Washington, USA.

[179] Hunter, S. C. (1982). *Formation of* SO_3 *in gas turbines*. Transactions of the ASME. 104, pp: 44-51.

[180] Williams, F. A. (1985). *Combustion Theory* (*second ed.*). Benjamin/Cummings, Menlo Park, CA.

[181] Pope, D. N., Gogos, G. (2005). *A new multi-component diffusion formulation for the finite volume method: application to convective droplet combustion*. Numerical Heat Transfer Part B. 48, pp: 213-234.

[182] Levendis, Y. A., Estrada, K. R. (1992). *Development of multicolour pyrometers to monitor the transient response of burning carbonaceous particles*. Review of Scientific Instruments. 63, pp: 3608-3622.

[183] Khatami, R., Levendis, Y. A. (2011). *On the deduction of single coal particle combustion temperature from three-color optical pyrometry*. Combustion and Flame. 158(9), pp: 1822-1836.

Appendix A

Radiation distribution of gas-phase temperature during combustion process

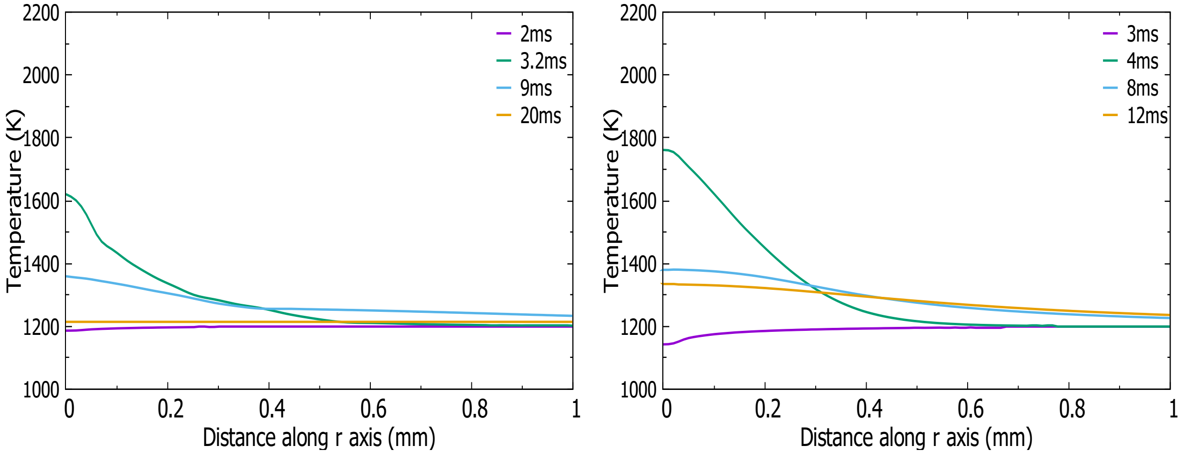

(a) Active flow, 21%O_2 & 79%N_2 (b) Active flow, 37%O_2 & 73%N_2

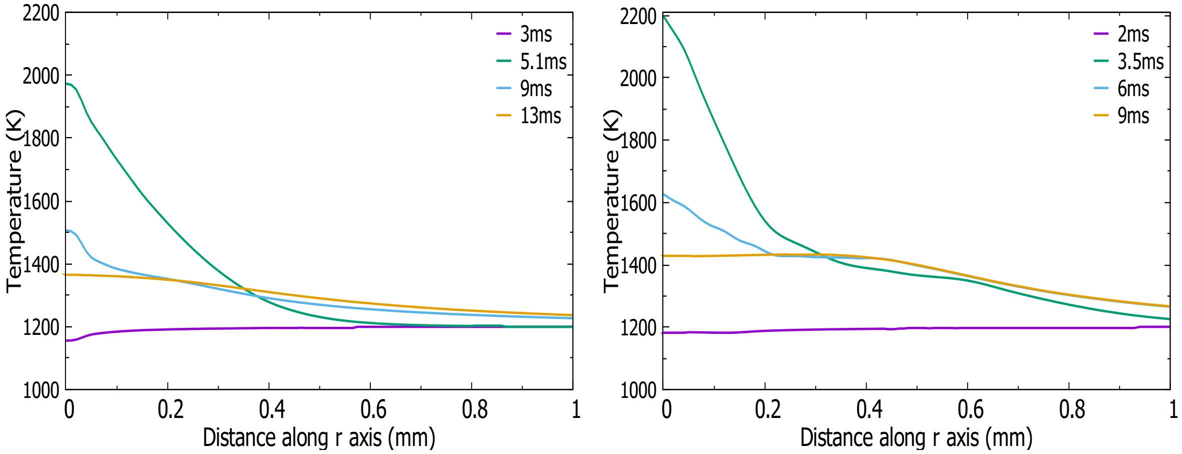

(c) Active flow, 77%O_2 & 23%N_2 (d) Active flow, 100%O_2

Figure A.1: Distribution of gaseous temperature along a horizontal line initiating at the particle centre during Bagasse particle combustion.

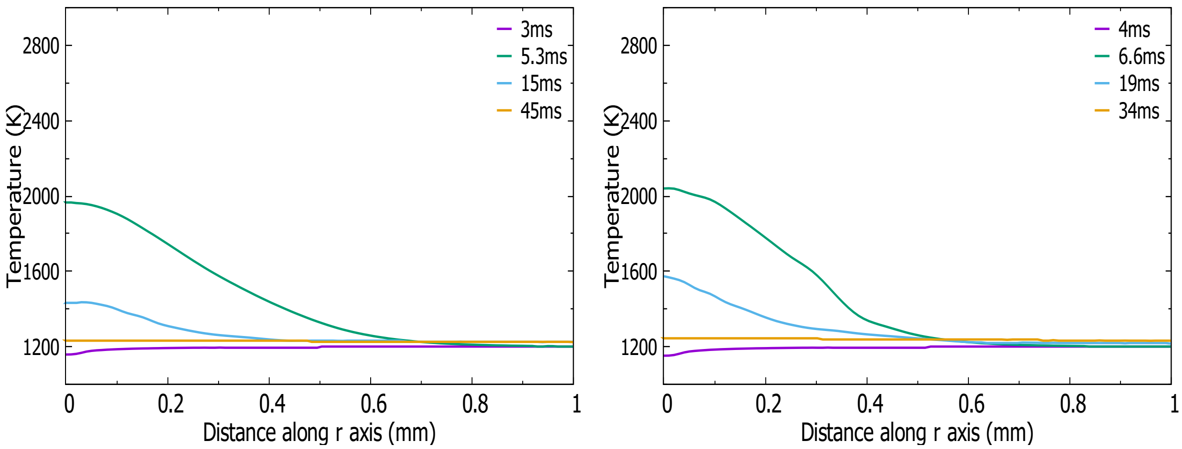

(a) Active flow, 21%O_2 & 79%N_2 (b) Active flow, 37%O_2 & 73%N_2

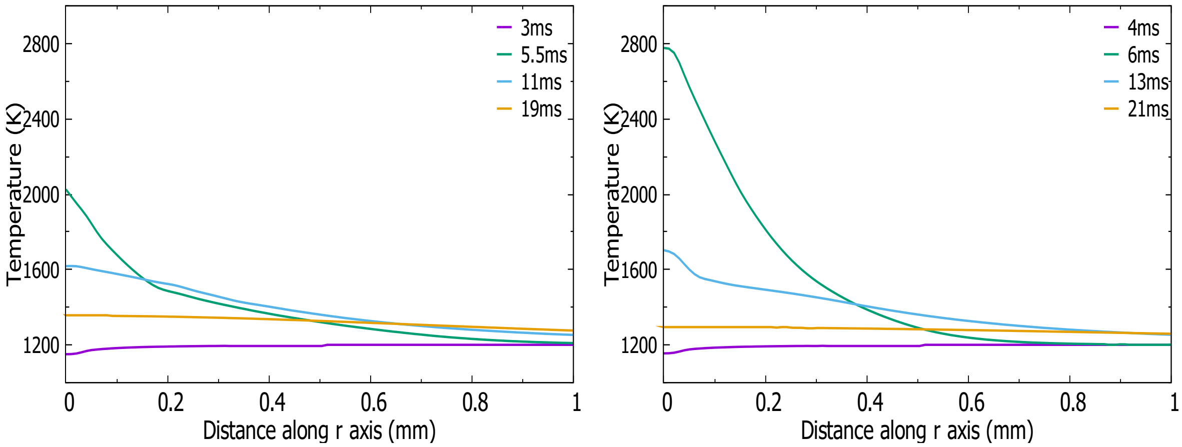

(c) Active flow, 68%O_2 & 32%N_2 (d) Active flow, 100%O_2

Figure A.2: Distribution of gaseous temperature along a horizontal line initiating at the particle centre during DECS-11 particle combustion.

Figure A.1 presents the radial distribution of gas-phase temperature along a horizontal line initiating at the particle centre during the single biomass particle combustion under varying gaseous atmospheres. The selected instances of time refer to devolatilization stage, around ignition moment, char combustion stage and near end of particle combustion. The result of single coal particle combustion is reported in Fig. A.2. The temperature profiles clearly show that the temperature drops a bit prior to ignition due to the endothermic devolatilisation process and the highest temperature appears at the moment of ignition. At the late period of particle combustion, the gas-phase temperature around the particle is much closer to the surrounding temperature due to the reduction in chemical reactions and heat transfer to surrounding environment.

Appendix B

Validation of Sulphur partition assumptions

The validation of sulphur partition assumption is conducted to confirm the changing trends of SO_x emission are the same under different chemical composition of the surrounding atmospheres. The partition assumptions are shown in Table B.1.

Table B.1: Partition assumptions of Sulphur

	Case 1	Case 2	Case 3	Case 4	Case 5
Partition of Volatile-S	33%	67%	50%	33%	33%
Partition of Char-S	67%	33%	50%	67%	67%
Partition of H_2S	40%	40%	40%	70%	50%
Partition of SO_2	60%	60%	60%	30%	50%

The changing trend of total mass fraction of SO_2 and H_2S and the percentage of SO_2 and H_2S formation during the transient combustion process under different gas conditions are used to validate the partition assumption. The compared results are shown in Figs B.1-B.6. It is clear from these figures that although the total amounts vary, the changing trends under varying gas conditions for different partition assumptions are the same in general. This indicates that changes in distribution of sulphur in the volatile and char does not influence the qualitative analysis in any considerable way.

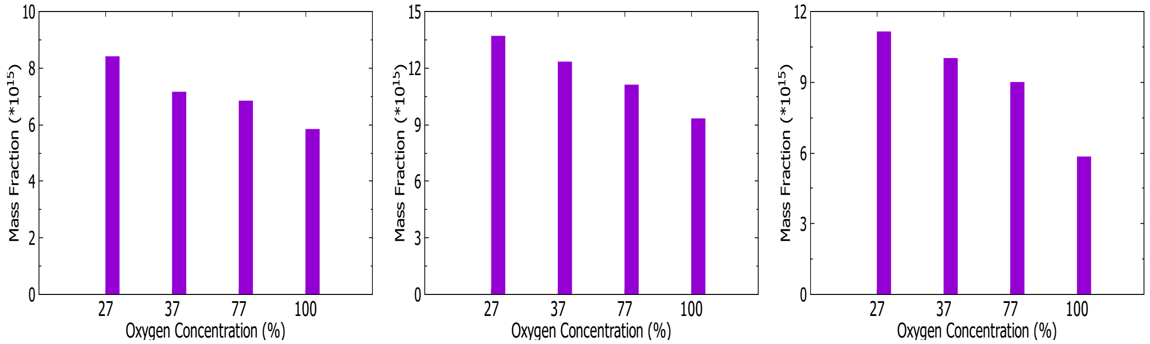

(a) Case 1 (b) Case 2 (c) Case 3

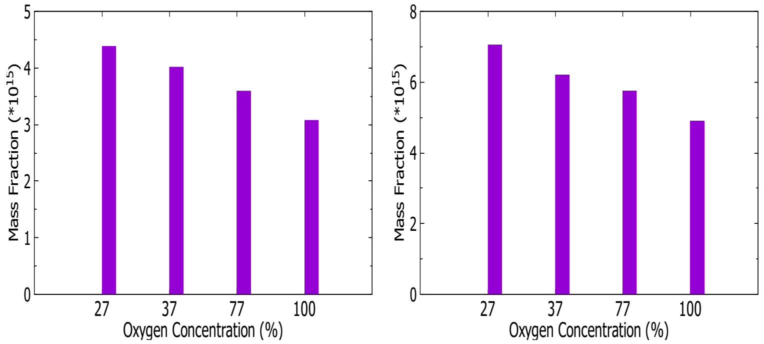

(d) Case 4 (e) Case 5

Figure B.1: Mass fraction of SO_2 in O_2/N_2 environments with partition assumptions (*t*=100ms).

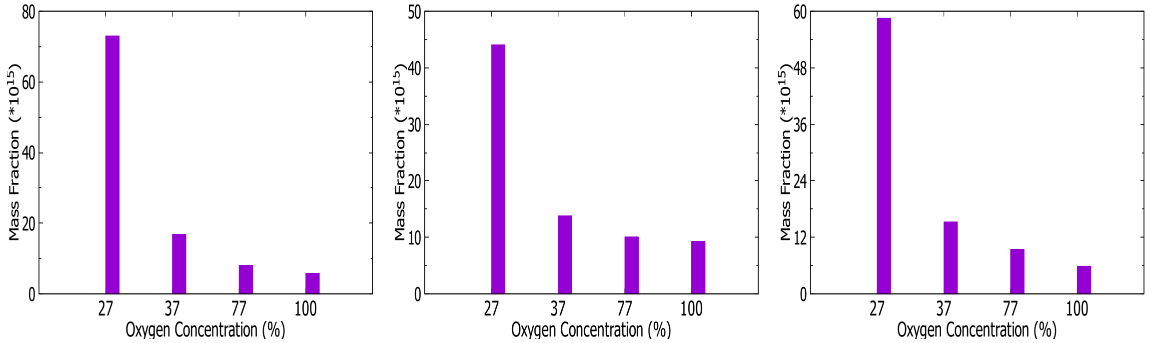

(a) Case 1 (b) Case 2 (c) Case 3

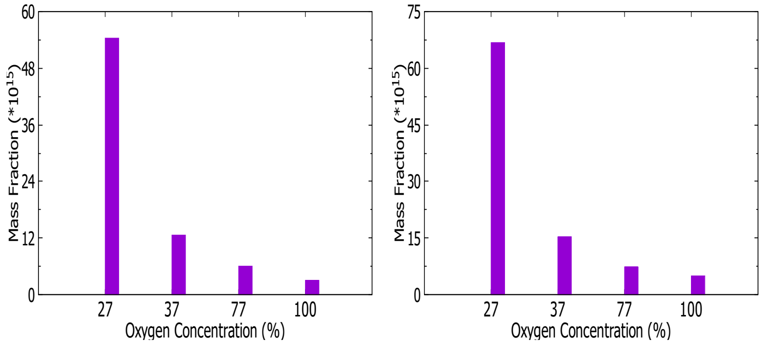

(d) Case 4 (e) Case 5

Figure B.2: Mass fraction of SO_2 in O_2/CO_2 environments with partition assumptions (*t*=100ms).

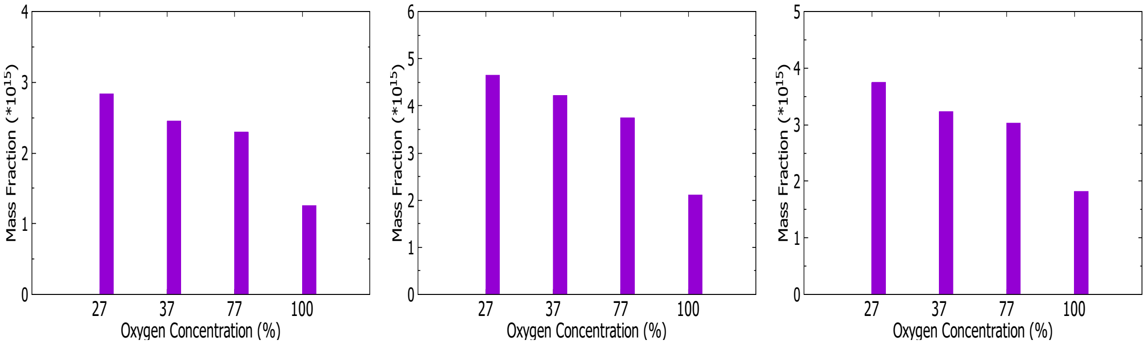

(a) Case 1 (b) Case 2 (c) Case 3

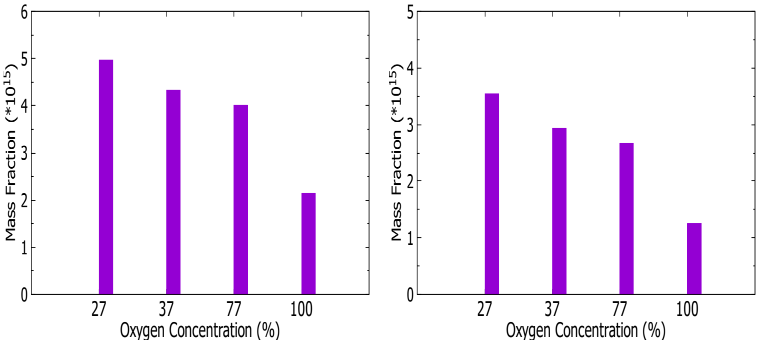

(d) Case 4 (e) Case 5

Figure B.3: Mass fraction of H_2S in O_2/N_2 environments with partition assumptions (t=100ms).

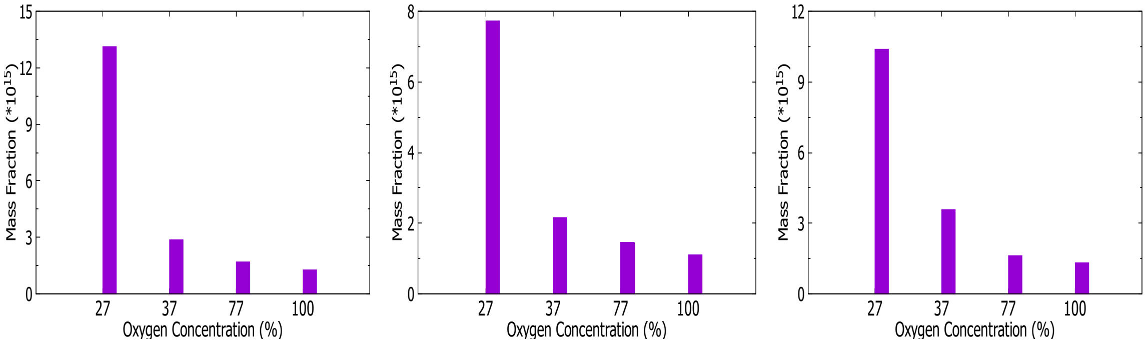

(a) Case 1 (b) Case 2 (c) Case 3

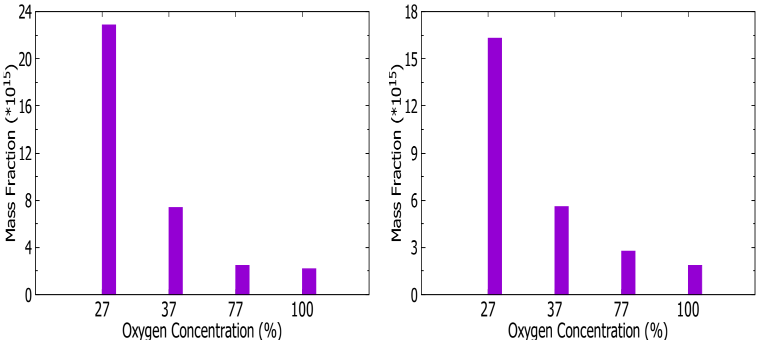

(d) Case 4 (e) Case 5

Figure B.4: Mass fraction of H_2S in O_2/CO_2 environments with partition assumptions (t=100ms).

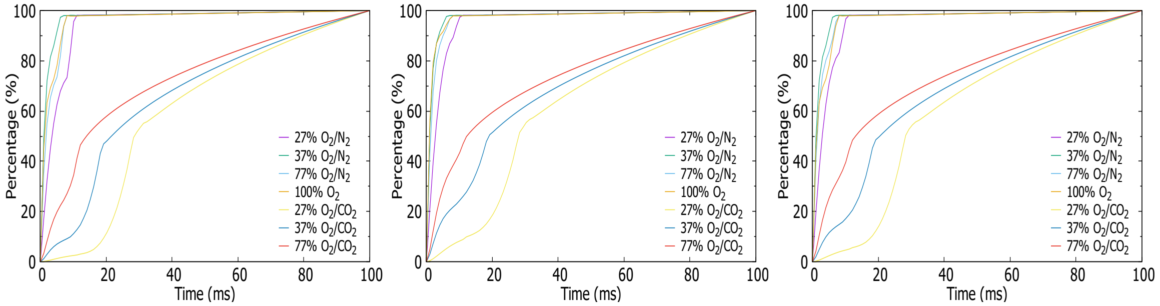

(a) Case 1 (b) Case 2 (c) Case 3

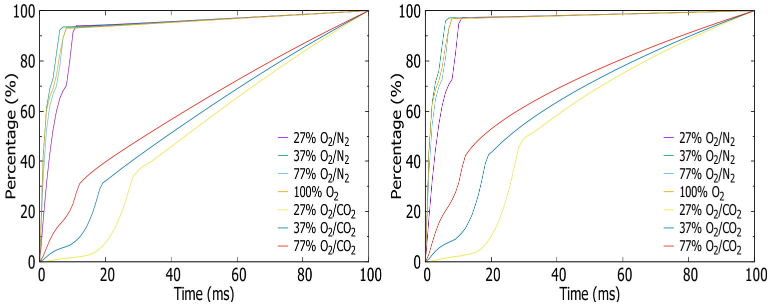

(d) Case 4 (e) Case 5

Figure B.5: Percentage of SO_2 formation during combustion process under varying gas conditions with partition assumptions.

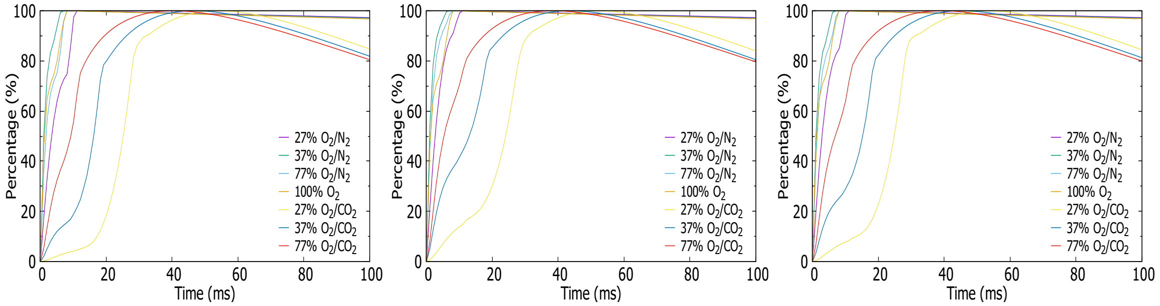

(a) Case 1 (b) Case 2 (c) Case 3

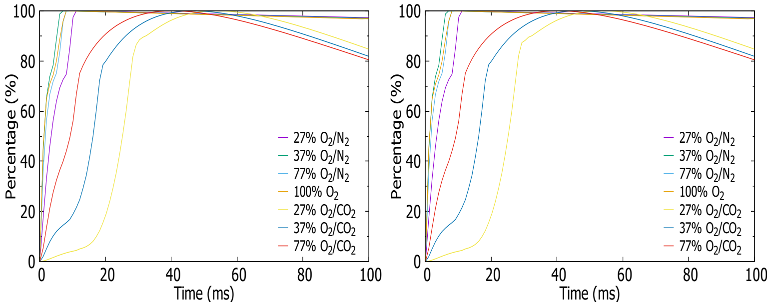

(d) Case 4 (e) Case 5

Figure B.6: Percentage of H_2S formation during combustion process under varying gas conditions with partition assumptions.